ANALYSIS OF ONE AND TWO DIMENSIONAL BANDGAP STRUCTURES USING AUTOMATED METHOD OF LINES WITH ARBITRARY LONGITUDINAL DISCONTINUITIES

BY

MOHAMMED ZAHED MUSTAFA KHAN

A Thesis Presented to the

DEANSHIP OF GRADUATE STUDIES

KING FAHD UNIVERSITY OF PETROLEUM & MINERALS

DHAHRAN, SAUDI ARABIA

In Partial Fulfillment of the
Requirements for the Degree of

MASTER OF SCIENCE

In

ELECTRICAL ENGINEERING

March 2004

UMI Number: 1420924

INFORMATION TO USERS

The quality of this reproduction is dependent upon the quality of the copy submitted. Broken or indistinct print, colored or poor quality illustrations and photographs, print bleed-through, substandard margins, and improper alignment can adversely affect reproduction.

In the unlikely event that the author did not send a complete manuscript and there are missing pages, these will be noted. Also, if unauthorized copyright material had to be removed, a note will indicate the deletion.

UMI®

UMI Microform 1420924

Copyright 2004 by ProQuest Information and Learning Company.

All rights reserved. This microform edition is protected against unauthorized copying under Title 17, United States Code.

KING FAHD UNIVERSITY OF PETROLEUM AND MINERALS

DHAHRAN 31261, SAUDI ARABIA

DEANSHIP OF GRADUATE STUDIES
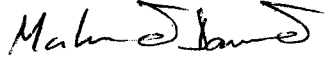
This thesis, written by

MOHAMMED ZAHED MUSTAFA KHAN

under the direction of his Thesis Advisor and approved by his Thesis Committee,

has been presented to and accepted by the Dean of Graduate Studies, in partial

fulfillment of the requirements for the degree of

MASTER OF SCIENCE IN ELECTRICAL ENGINEERING

<u>THESIS COMMITTEE</u>

3/5/2004

Dr. Hussain A. Al – Jamid (Chairman)

3/5/04

Dr. Mahmoud M. Dawoud (Member)

4/5/04

Dr. Husain M. Masoudi (Member)

Dr. Jamil M. Bakhashwain
(Department Chairman)

Prof. Osama A. Jannadi
(Dean of Graduate Studies)

11/5/2004
Date

Dedicated to my family and my grand mother

Acknowledgements

In the beginning, I must thank Allah the Almighty and the Most Beneficent and Merciful for His blessings throughout my life in general and in the course of this thesis in particular.

I am indebted to King Fahd University of Petroleum and Minerals for supporting my M.S. studies and this research work.

The most influential and constructive assistance in developing many of the ideas in this thesis came from my thesis advisor Dr. Hussain A. Al-Jamid. My thesis's quality is a result of the many tiring hours he has spent in helping to refine it. His appreciation and words of encouragement gave a new life to my efforts in hard times. I am thankful to him.

I would also like to express my deep appreciation to my committee members, Dr. Mahmoud M. Dawoud and Dr. Husain M. Masoudi, for their constant help and encouragement. Their suggestions and critiques were most appreciated.

My acknowledgement also goes to Dr. Jamil Bakshashwain, Chairman Electrical Engineering Department for his support.

All I have achieved could not have been possible without the undying love and

Contents

List of Tables

List of Figures

xiii

Nomenclature

English Symbols

E	electric field vector, volts/meter
H	magnetic field vector, amperes/meter
N	diagonal matrix of refractive-index squared at mesh grids
I	identity matrix
P	time-averaged power per unit length in the y-direction, watts/m
Q	matrix of the eigen-value equation
n	refractive index
k_o	free space wavenumber, radians/meter
h	mesh size, meter
d, w	thickness of a layer, meter
j	$\sqrt{-1}$
t	time, sec

Greek Symbols

ψ	general field component of the **E** or **H** field
Ψ	general field component of the **E** or **H** sampled field, column vector
ϵ_o	free space permittivity, $4\pi \cdot 10^{-7}$ Vs/Am
ϵ_r	relative permittivity
μ_o	free space permeability, $8.8541 \cdot 10^{-12}$ As/Vm
μ_r	relative permeability
$\omega = 2\pi f$	angular frequency, rad/sec
α_m	mth modal field coefficient
β	propagation constant. radians/meter
λ	wavelength, meter
∇	nabla operator, $\frac{\partial}{\partial x}\hat{a}_x + \frac{\partial}{\partial y}\hat{a}_y + \frac{\partial}{\partial z}\hat{a}_z$
∇^2	Laplace operator, $\frac{\partial^2}{\partial x^2} + \frac{\partial^2}{\partial y^2} + \frac{\partial^2}{\partial z^2}$

Abbreviations

TE	Transverse Electric
TM	Transverse Magnetic
MOL	Method of Lines
PML	Perfectly Matched Layer
BPM	Beam Propagation Method
ABC	Absorbing Boundary Condition
SIT	Semi Infinite Termination

WDM	Wavelength Division Multiplexing
n_{eff}	Modal Effective Index
λ_B	Bragg Wavelength
Re	Real part of a complex number
Im	Imaginary part of a complex number

Subscripts

A_x, A_y, A_z	x, y, z components of a vector $\mathbf{A}$
$\psi_i, \psi_{i-1}, \psi_{i+1}$	sample number of field ψ
$\psi_{i\pm}, \psi_{i-1\pm}, \psi_{i+1\pm}$	field immediately to the left or to the right of a sample point

Superscript

$\psi^{(1)}$	first derivative of ψ
$\psi^{(2)}$	second derivative of ψ
$\psi^{(3)}$	third derivative of ψ
$\psi^{(4)}$	fourth derivative of ψ
$\psi^{(5)}$	fifth derivative of ψ
$\psi^{(6)}$	sixth derivative of ψ
A^*	complex conjugate of A

THESIS ABSTRACT

Name: MOHAMMED ZAHED MUSTAFA KHAN

Title: ANALYSIS OF ONE AND TWO DIMENSIONAL BANDGAP STRUCTURES USING AUTOMATED METHOD OF LINES WITH ARBITRARY LONGITUDINAL DISCONTINUITIES.

Degree: MASTER OF SCIENCE

Major Field: ELECTRICAL ENGINEERING

Date of Degree: MARCH 2004

In this thesis work, various one dimensional and two dimensional bandgap structures are analyzed. In the one dimensional case, we analyzed a deep grating, symmetrically coupled deep grating and asymmetrically coupled deep grating structures. In the two dimensional case, we analyzed the presence of line defects and point defects as well as a U-turn line defect. In all the above bandgap structures, we calculated the spectral response including modal reflectivity, modal transmissivity and the loss due to radiation. Due to the fact that, we need to analyze very different structures, an automated Method of Lines (MOL) program has been developed for this purpose. This automaticated user-friendly computer program which accounts for arbitrary longitudinal discontinuities in a numerically efficient manner, is used in the thesis work. The MOL with improved features is also discussed in this thesis work. Improved implementation of the transverse second derivative operator and the Perfectly Matched Layer (PML) are discussed.

In general, the spectral response of these structures give rise to interesting features such as the presence of transmission resonances within the bandgap, which make them potential candidates for use as compact wavelength filters.

Keywords: Method of Lines (MOL), Perfectly Matched Layer (PML), Bandgap Structures, Wavelength Filters.

Master of Science Degree

King Fahd University of Petroleum and Minerals, Dhahran.
MARCH 2004

ملخص الرسالة

الاسم: محمد زاهد مصطفى خان

عنوان الرسالة: تحليل بنيات فجوة المجال الأحادية البعد والثنائية البعد باستخدام طريقة الخطوط التلقائية مع إنقطاعات طولية عشوائية

الدرجة: ماجستير

التخصص: الهندسة الكهربائية

تاريخ الرسالة: مارس 2004 م.

في هذه الرسالة تم تحليل عدة بنيات تعتمد على فجوة المجال الأحادية و الثنائية البعد. في حالة البعد الواحد، قمنا بتحليل الهيئات التالية: محزوز عميق منفصل ومحزوزان عميقان منفصلان تناظرياً ومحزوزان عميقان متصلان لا تناظرياً. أما في الحالة الثنائية البعد، فقد درسنا أثر وجود نواقص خطية ونقطية والتي على شكل U. في جميع بنيات فجوة المجال السابقة الذكر، تم حساب طيف الاستجابة بما في ذلك معامل إنعكاس النمط ومعامل إرسال النمط والخسارة الناجمة عن التشتت. ونظراً لأن غرضنا في هذا البحث القيام بتحليل بنيات مختلفة، فقد قمنا لهذا الغرض بتطوير طريقة الخطوط بحيث تكون تلقائية. إن برنامج الحاسوب الذي تم تطويره واستخدامه في هذه الرسالة تلقائي وسهل الاستعمال كما أن له القدرة على التعامل مع إنقطاعات طولية عشوائية بطريقة فعالة من الناحية الرقمية. كذلك قمنا في هذا البحث بإضافة بعض التعديلات على طريقة الخطوط منها تعديل في معامل المشتقة الثانية العرضي و كذلك تعديل في الطبقة الماصة المثالية. وبصورة عامة، فإن طيف الإستجابة لهذه البنيات يحتوي على خصائص مهمة منها وجود مجال إرسال داخل فجوة المجال، مما يجعل هذه البنيات قابلة للإستعمال لبناء مرشحات طول موجية صغيرة الحجم.

درجة الماجستير

جامعة الملك فهد للبترول والمعادن، الظهران

مارس 2004

Chapter 1

Introduction

1.1 Integrated Optics

Integrated Optics is a relatively new and exciting field of activity which is primarily

based on the fact that light can be guided and confined in very thin films (with

dimensions on the order of the wavelength of light) of transparent materials on

suitable substrates. The term Integrated Optics was first proposed in 1969, by S.E.

Miller of Bell Labs [1, 2]. By a proper choice of the substrate, film and a proper

configuration of the waveguide, one can perform a wide range of operations such as

modulation, switching, multiplexing, filtering or generation of optical waves. Due

to the miniature size of these components, it is possible to obtain a high density of

optical components in space unlike the case of bulk optics. Thus, integrated optics is

the name given to a generation of opto-electronic systems in which wires and cables

are replaced by waveguiding optical fibers, respectively and conventional integrated

1

circuits replaced by optical integrated circuits (OIC).

An optical integrated circuit (OIC) is a thin-film circuit that provides enhanced stability and compactness by integrating optical sources, detectors, switches or modulators, and interconnection of optical waveguides on a single substrate. All these devices are guided wave devices and operate on guided waves only. From the point of view of wave optics, OIC's represent the third generation of optical devices, and have numerous advantages over previous technologies [3]. These devices are expected to be rugged in construction, have good mechanical and thermal stability, be mass producible with high precision and reproducibility, and have a small power consumption.

One of the most promising applications of the integrated optics is in the field of optical fiber communications. The optical fiber has assumed importance because of its high information carrying capacity; it is here that integrated optics will play an important role in optical signal processing at the transmitting and receiving ends and on regeneration at the repeaters [4]. Other important applications are envisaged to be spectral analysis, optical signal processing and wavelength division multiplexing (WDM).

An optical waveguide is a structure which confines and guides the light beam by the process of total internal reflection (TIR). The most extensively used optical waveguide is the optical fiber which consists of a central cylindrical core and cladding. The refractive index of the cladding material is always chosen to be lower than the refractive index of the core material (in order to trap the field energy inside

the core by the phenomenon of TIR).

Longitudinal discontinuity problems in the optical waveguide are also of considerable theoretical and practical interest. They play an important role in designing practical devices such as tapers, bends, y-junctions, couplers, mode converters, filters, connections of different waveguides, etc. Much effort has been made in the understanding of the reflection and transmission phenomena at a discontinuity interface. The present thesis focusses on such waveguides with longitudinal discontinuities.

In integrated optics, two types of waveguides are used; these are the planar waveguides and the channel (or strip) waveguides. In planar waveguides, the confinement of light energy is achieved only along one transverse dimension and the light energy can diffract in the other direction. In contrast to planar waveguides, strip or channel waveguides confine the light energy in both transverse dimensions.

Depending on the refractive index profile, the waveguides can be classified into two main categories, namely, step-index and graded index waveguides. A waveguide with a uniform refractive index profile in each layer comes under the first category whereas a waveguide with a continuously varying refractive index profile comes under the second category.

Due to the difficulty in modeling (both theoretical and numerical) waveguides having two dimensional confinement, the work in this thesis will only address waveguide structures having one dimensional confinement.

1.2 Numerical Techniques to Model Waveguide Structures

Analysis and modeling of guided optical waveguide problems have been an important research topic since the last two decades. Several numerical methods have been developed to model waveguide structures. Among these methods are the Beam Propagation Method (BPM) [5, 6, 7], the Finite Difference Time Domain (FDTD) Method [7, 8], the Collocation Method [9], the Mode Matching Method (MMM) [10] and the Method of Lines (MOL) [7, 11, 12].

1.2.1 Different Numerical Methods

The FDTD is one of the most widely used numerical technique methods. It is universal, robust, methodologically simple and descriptive. The wave propagating through the structure is found by a direct integration in the time domain of Maxwell's equation in discretized form. Discretization is done both in time and in space using a staggered grid (or a cubic grid). The main shortcoming of the FDTD method is its high computational demand.

The BPM is the most widely used numerical method for the modeling of integrated and fiber-optic devices. It also involves a discretization of the electromagnetic field. It is computationally efficient, and methodologically even simpler than the FDTD. The main underlying assumption in the BPM is the use of the slow varying

envelope approximation along the direction of the field propagation, leading to the parabolic form of the wave equation. In addition, the BPM generally assumes slow changes in the waveguide profile.

The Collocation Method is based on the Helmholtz equation and does not require the Fresnel approximation for its implementation [13]. In this method, the field is expanded into a set of suitable orthogonal basis functions $\phi_n(x)$ in the transverse direction. The choice of the basis functions depend on the problem geometry. Since these basis are not eigen-modes of the problem, we need a larger number of basis functions to achieve accurate results.

1.2.2 The Method of Lines (MOL)

The Method of Lines is a well-established and efficient numerical procedure for the analysis of a variety of optical and microwave waveguides. Its advantages stems from the fact that it is a semi-analytical approach that leads to a comparatively small numerical effort and high calculational accuracy. The MOL can easily account for both, the backward reflected field and the forward transmitted field as well as its ability to account for optical structures with large refractive index contrast. This is an important advantage leading to the popularity of the MOL in analyzing longitudinally inhomogeneous structures. Detailed formulation of the MOL is presented in chapter 3.

1.3   Overview of the Thesis

The section briefly states the objective of the research work that has been carried out in this thesis and the organization of the thesis in a comprehensive manner.

1.3.1   Objectives of the Thesis

The work to be addressed in this thesis includes

- Developing an automated user-friendly MOL (Method of Lines) program that accounts for arbitrary longitudinal discontinuities in an efficient manner.

- Improving the accuracy of the automated MOL program by employing improved higher-order approximations of the transverse second derivative operator with appropriate interface conditions. Employing the Perfectly Matched Layer (PML) absorber that utilizes a non-uniform loss profile in order to effectively terminate the problem space.

- Applying the program for the analysis of 1D guided wave deep grating structures (or bandgap structures) and their use as wavelength filters. The work includes the analysis of periodic waveguide deep gratings and the effect of the groove depth and the number of periods on its spectral response, using the automated program.

- Analysis of symmetrically and asymmetrically coupled 1D bandgap structures. The effect of the filling factor (i.e. the ratio of width of the air region and the

grating period) on the spectral response is studied. The effect of the uniform distance which separates the two coupled structures is also studied.

- Analysis of 2D bandgap structures. Defects such as the line defect, point defect, are studied. A device which bends the light wave by 180 degrees (using two 90° bends)(called as the U-turn waveguide) with small radiation loss is also studied towards the end of this thesis.

1.3.2 Thesis Organization

This thesis is organized in a comprehensive manner so that the reader may easily follow the progress of the work. It starts from a brief review of basic slab waveguide theory and then proceeds in a comprehensive manner to our results and discussions of the optical devices that we assume would be helpful in the Wavelength Division Multiplexing (WDM).

Chapter one is an introductory chapter, which surveys the historical background of integrated optics. Then, an overview of the different numerical techniques to model optical structures is given throwing light on the MOL technique.

Chapter two is completely devoted to the quantitative understanding of a simple planar optical waveguide (dielectric slab waveguide). The theory is presented briefly along with the eigen value equation of both the TE and TM guided modes.

Chapter three starts with the introduction to Method of Lines (MOL), which is applied for the solution of the wave equation in the present thesis. The complete

mathematical formulation of the MOL is also presented. Later in the chapter, extensions to the basic MOL is discussed. The necessary interface conditions for the structures with longitudinal index discontinuities is presented briefly. The improved five-point approximation of the transverse second derivative operator with appropriate interface conditions is discussed. The implementation of the Perfectly Matched Layer (PML) absorber with graded loss profile is explained. The above mentioned extensions to the MOL are applied and are used in the later work to calculate the spectral response of various guided wave structures.

In chapter four, MOL analysis of waveguides exhibiting longitudinal discontinuities are discussed. The chapter starts by considering a waveguide with a single longitudinal discontinuity. Comparison with published work is done to confirm the accuracy of implementation. Later, multiple longitudinal discontinuities are discussed. The algorithms that are used to simulate such structures are presented and the results are compared with published work. Chapter five ends with the discussion of the development of the automated program along with an example.

In chapter five, the guided wave grating structure is analyzed and the effect of the number of periods and the depth of the groove, on the spectral response is studied. Both TE and TM guided modes are discussed.

Chapter six and seven are devoted to optical devices that are formed by coupling the basic guided wave grating structure (discussed in chapter 6). Symmetrical and asymmetrical coupled structures are discussed in chapter six and seven, respectively.

Chapter eight throws light on the analysis of an optical waveguide structure that

bend the incident wave by 180 degrees (in the form of a U-turn utilizing two 90° bends) within small space with small radiation loss.

In the final chapter (chapter nine), the presented work is summarized along with the conclusions and some suggestions for future extensions.

Chapter 2

Planar Optical Waveguide

2.1 Introduction

Since the waveguide forms the backbone of all integrated optical devices, a very brief introduction to the three layer step index slab waveguide is going to be given in this chapter for reference. The reader may refer to [14, 15, 16] for detailed analysis. The waveguide selected for analysis is an asymmetric one because almost all waveguides used in integrated optics are asymmetric in nature (the refractive indices of all the layers are different) and thereby making it easier to understand the physical principles of the more complicated guiding structures. The slab waveguide is also used for light guidance in integrated optical circuits [14, 17, 18, 19, 20].

2.2 The Three Layer Step-Index Dielectric Slab Waveguide

In this section, a brief idea about the derivation of the scalar wave equation and its application to the planar waveguide and its guided modes will be discussed.

2.2.1 The Wave Equation

A simple planar three-layer step-index dielectric slab waveguide structure is shown in fig.2.1 which has a core of refractive index n_2, superstrate and substrate with refractive indices n_1 and n_3 ($n_1 > n_2 > n_3$), respectively. The coordinate system used throughout in this thesis is also shown in the same figure. The material of each layer is assumed to be non-magnetic and homogeneous. A time-harmonic field of the form $e^{-j\omega t}$ is assumed. The time harmonic, three dimensional vector wave equation which is derived from the Maxwell's equations, is shown below

$$\nabla^2 \mathbf{E} + k_o^2 n^2 \mathbf{E} = 0 \qquad (2.1)$$

Where $\mathbf{E}$ is the electric field (equation 2.1 is equally applicable for the magnetic field $\mathbf{H}$), k_o (equal to $2\pi/\lambda_0$) is the free space wave number and n is refractive index of any layer (n_1, n_2 or n_3). On employing a further assumption of a 2D structure, i.e. infinitely wide and uniform structure in the y-direction, we may use $\frac{\partial}{\partial y} = 0$. In order to obtain modal solutions corresponding to wave propagation in the z direction, the field is assumed to vary as $e^{j\beta z}$ in the z direction (β is the longitudinal propagation

n_3 *Superstrate*
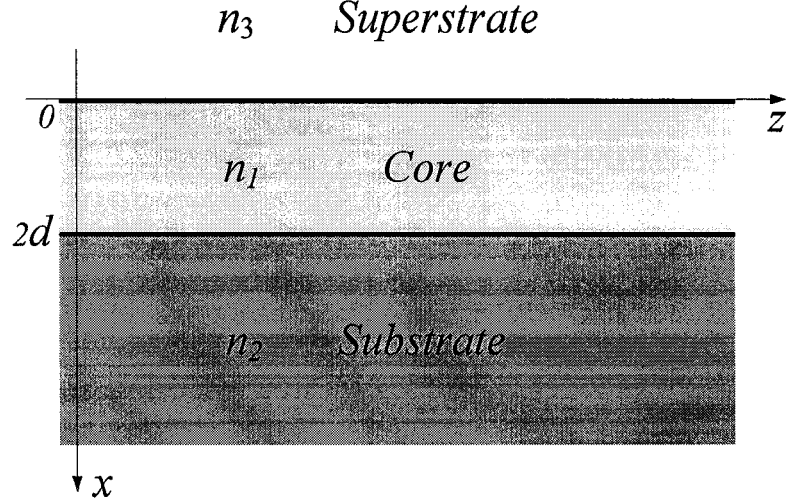
Figure 2.1: The Three Layer Step Index Slab Waveguide.

constant). In this case, equation 2.1 reduces to the well known Helmholtz equation

given below [14]

$$\frac{d^2\mathbf{E}}{dx^2} + (k_o^2 n^2 - \beta^2)\mathbf{E} = 0 \qquad (2.2)$$

Using equation 2.2 and imposing appropriate boundary conditions at each interface

[superstrate/core (x = 0) and core/substrate (x = 2d)], the modal solutions (guided

modes) of the structure as well as the corresponding propagation constants can be

obtained.

2.2.2   Transverse Electric (TE) Guided Modes

For TE-polarized waves, the electric field has a single component in the y-direction,

namely: $\overrightarrow{\mathbf{E}} = E_y \overrightarrow{a_y}$. The magnetic field **H** has two components so that $\overrightarrow{\mathbf{H}} =$

$H_x \overrightarrow{a_x} + H_z \overrightarrow{a_z}$. By solving equation 2.2 in each layer of the slab waveguide (along

with the application of the boundary condition that E_y is continuous at the interface), E_y can be obtained. Using Maxwell's equations, the corresponding two non-zero components of the magnetic field H_x and H_z can also be obtained. These components are given below

$$E_y = \begin{cases} Ae^{-rx} & , x \geq 0 \\ A\cos(qx) + B\sin(qx) & , 0 \geq x \geq 2d \\ (A\cos(2dq) - B\sin(2dq))\, e^{p(x+2d)} & , x \leq 2d \end{cases} \tag{2.3}$$

$$H_x = -\frac{\beta}{\omega\mu_o}E_y \tag{2.4}$$

$$H_z = -\frac{j}{\omega\mu_o}\frac{\partial E_y}{\partial x} \tag{2.5}$$

where $q^2 = n_1^2 k_o^2 - \beta^2$, $p^2 = \beta^2 - n_2^2 k_o^2$ and $r^2 = \beta^2 - n_3^2 k_o^2$. Substituting equation 2.3 in equation 2.5, to obtain H_z and again applying boundary conditions for the continuity of H_z, the following TE eigenvalue equation can be obtained.

$$\tan(2aq) = \frac{q(p+r)}{q^2 - pr} \tag{2.6}$$

Equation 2.6 relate the wavelength, refractive indices, core thickness and propagation constant. The longitudinal propagation constant β is the only unknown quantity in equation 2.6, and hence it can be easily obtained using zero finding programs (see appendix D). An example of the TE mode patterns for a three-layer symmetric slab waveguide is shown in fig.2.2.
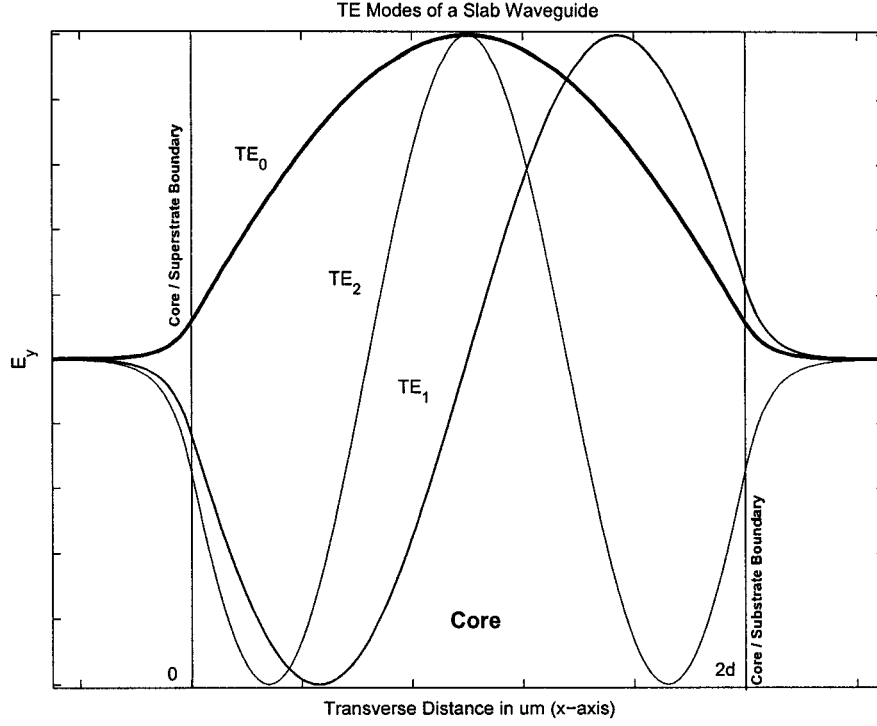
Figure 2.2: *TE* Modal Field Patterns of a Symmetric Slab Waveguide.

2.2.3 Transverse Magnetic (TM) Guided Modes

Solving equation 2.2 (when it is in terms of the magnetic field **H**), the only non zero magnetic field component H_y of the TM-polarized waves can be obtained in the three regions as

$$H_y = \begin{cases} Ce^{-rx} & , x \geq 0 \\ C\cos(qx) + D\sin(qx) & , 0 \geq x \geq 2d \\ (C\cos(2dq) - D\sin(2dq))\, e^{p(x+2d)} & , x \leq 2d \end{cases} \qquad (2.7)$$

Again using Maxwell's equations, the two non-zero components of the electric

field namely E_x and E_z are obtained as

$$E_x = -\frac{\beta}{\omega n_i^2 \epsilon_o} H_y \tag{2.8}$$

$$E_z = -\frac{j}{\omega n_i^2 \epsilon_o} \frac{\partial H_y}{\partial x} \tag{2.9}$$

In a similar fashion as done in the TE case, an eigenvalue equation for the TM modes can also be obtained and is given below

$$\tan(2aq) = \frac{qn_1^2 \left(n_3^2 p + n_2^2 r\right)}{n_2^3 n_3^2 q^2 - n_1^4 pr} \tag{2.10}$$

The guided mode patterns for the TM polarized modal field for a symmetric slab waveguide ($n_1 = n_3$) are found to be in general similar to the TE mode patterns (fig2.2) except that a sudden change in the slope of the magnetic field occurs at material interfaces.

Chapter 3

The Method of Lines (MOL) and

its Extensions

3.1 Introduction

The Method of Lines is a partial discretization technique. This numerical method

forms a versatile tool for the analysis of optical and microwave waveguides. Due

to its semianalytical approach, the computational effort is much less than other

methods applied to the same problem. In MOL, the equations are discretized only

as far as necessary and all other calculations are done analytically. As interface

conditions can be easily employed in this method, discontinuous filed curves can be

described accurately. This leads to the popularity of this method for solving more

complicated problems. Later in the chapter, extensions to the MOL are presented.

16

3.2 MOL Formulation

In order to solve the two dimensional wave equation using the MOL, the field is discretized in one dimension (the transverse dimension, x in our case) and solved analytically in the direction of wave propagation (the z direction) [15, 16, 21, 22]. The MOL has been used to analyze waveguides exhibiting longitudinal discontinuities. Waveguide structures with a single [23, 24] and multiple discontinuities [25, 26, 27, 28, 29] using the MOL have been reported in the literature. Non-linear waveguide problems [30] and the diffraction problem from waveguide ends [31], has also been analyzed by this method.

The waveguide's interfaces are kept parallel to the direction of propagation (z-axis) and then discretized along the transverse direction (x-axis). The field will be calculated along these discretized lines (known as mesh lines or points) which are kept equidistant from each other. The structure is considered to be bounded by electric or magnetic walls (in order to terminate the problem space). The resulting system of difference equations is then decoupled and manipulated through algebraic expressions.

Consider the two dimensional wave equation

$$\frac{\partial^2 \psi(x,z)}{\partial x^2} + \frac{\partial^2 \psi(x,z)}{\partial z^2} + k_o^2 n^2 \psi(x,z) = 0 \qquad (3.1)$$

where

ψ = Electric or Magnetic Field (E_y or H_y)

$k_o = 2\pi/\lambda_o$
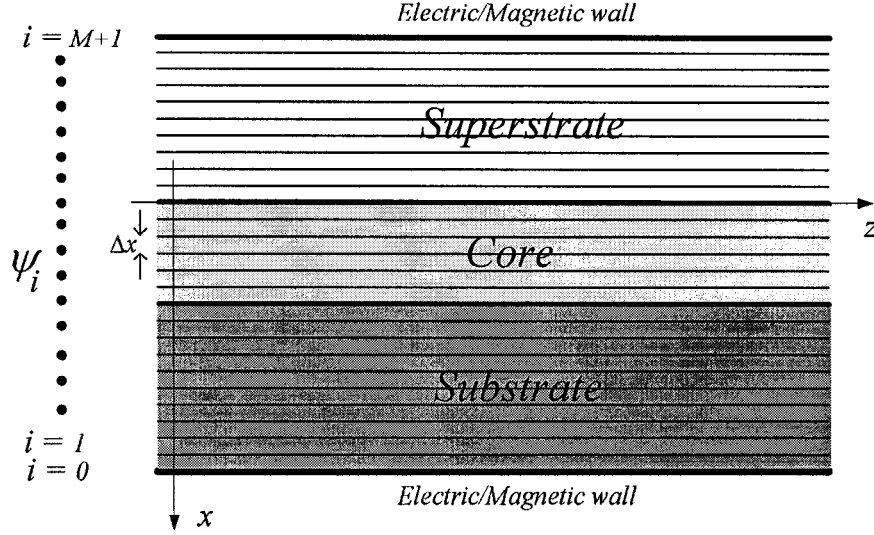
Figure 3.1: Mesh Discretization used in the MOL.

λ_o = Free space wavelength

n = Refractive index of the medium

The refractive index is assumed to be locally uniform in the z-direction, i.e. $n(x, z) = n(x)$. The field $\psi(x, z)$ and the refractive index $n(x)$, are discretized along the x-axis. On applying the three-point central difference approximation to the transverse second derivative operator (refer to appendix A) of ψ with respect to x (equation 3.1), we obtain a system of ordinary differential equations. Each equation can be written as (at the ith grid)

$$\frac{\psi_{i+1}(z) - 2\psi_i(z) + \psi_{i-1}(z)}{(\Delta x)^2} + \frac{d^2\psi_i(z)}{dz^2} + k_o^2 n_i^2 \psi_i(z) = 0 \qquad (3.2)$$

where Δx is the mesh size (fig. 3.1).

If the field in the x-direction is discretized into M points, then equation 3.2 yields

the following M equations:

$$i = 1: \qquad \frac{1}{(\Delta x)^2} [\psi_2 - 2\psi_1 + \psi_0] + \frac{d^2}{dz^2} [\psi_1] + k_o^2 n_1^2 [\psi_1] = 0 \qquad (3.3)$$

$$i = 2: \qquad \frac{1}{(\Delta x)^2} [\psi_3 - 2\psi_2 + \psi_1] + \frac{d^2}{dz^2} [\psi_2] + k_o^2 n_2^2 [\psi_2] = 0 \qquad (3.4)$$

$$i = 3: \qquad \frac{1}{(\Delta x)^2} [\psi_4 - 2\psi_3 + \psi_2] + \frac{d^2}{dz^2} [\psi_3] + k_o^2 n_3^2 [\psi_3] = 0 \qquad (3.5)$$

$$\vdots$$

$$i = M: \qquad \frac{1}{(\Delta x)^2} [\psi_{M+1} - 2\psi_M + \psi_{M-1}] + \frac{d^2}{dz^2} [\psi_M] + k_o^2 n_M^2 [\psi_M] = 0 \qquad (3.6)$$

The above system of equations can be assembled in matrix form as

$$\frac{1}{(\Delta x)^2} \begin{bmatrix} -2 & 1 & & & & \\ 1 & -2 & 1 & & & \mathcal{O} \\ & 1 & -2 & 1 & & \\ & & \ddots & \ddots & \ddots & \\ \mathcal{O} & & & 1 & -2 & 1 \\ & & & & 1 & -2 \end{bmatrix} \begin{bmatrix} \psi_1(z) \\ \psi_2(z) \\ \psi_3(z) \\ \vdots \\ \vdots \\ \psi_M(z) \end{bmatrix} + \frac{d^2}{dz^2} \begin{bmatrix} \psi_1(z) \\ \psi_2(z) \\ \psi_3(z) \\ \vdots \\ \vdots \\ \psi_M(z) \end{bmatrix}$$

$$+ k_o^2 \begin{bmatrix} n_1^2 & & & & & \\ & n_2^2 & & & \mathcal{O} & \\ & & n_3^2 & & & \\ & & & \ddots & & \\ & \mathcal{O} & & & \ddots & \\ & & & & & n_M^2 \end{bmatrix} \begin{bmatrix} \psi_1(z) \\ \psi_2(z) \\ \psi_3(z) \\ \vdots \\ \vdots \\ \psi_M(z) \end{bmatrix} = \begin{bmatrix} 0 \\ 0 \\ 0 \\ \vdots \\ \vdots \\ 0 \end{bmatrix}$$

or, can be cast into the more compact form:

$$\frac{1}{(\Delta x)^2}C\Psi + \frac{d^2}{dz^2}\Psi + k_o^2 N\Psi = 0 \tag{3.7}$$

and finally

$$\frac{d^2}{dz^2}\Psi + Q\Psi = 0 \tag{3.8}$$

The resulting vector $\Psi = [\psi_1(z), \psi_2(z), ..., \psi_M(z)]^t$ represents the discretized field. The square matrix Q is given by

$$Q = \frac{1}{(\Delta x)^2}C + k_o^2 N \tag{3.9}$$

where C represents the tri-diagonal central difference approximated transverse second derivative matrix , N is a diagonal matrix containing the discrete values of the square of the refractive indices in the transverse direction.

Thus, the solution to the above 2nd-order ordinary matrix differential equation (equation. 3.8) is simple, given as [12]

$$\Psi = e^{j\sqrt{Q}z}A + e^{-j\sqrt{Q}z}B \tag{3.10}$$

where A and B are constant vectors having the same dimensions as Ψ. The terms $e^{\pm j\sqrt{Q}z}$ represent field propagation in the $\pm z$, respectively. The $M \times M$ matrices

$e^{j\sqrt{Q}z}$ and $e^{-j\sqrt{Q}z}$ are evaluated by first diagonalizing matrix Q to find the eigenvalues and eigenvectors as shown below

$$Q = UVU^{-1} \tag{3.11}$$

where the diagonal matrix V contains the eigenvalues of Q and the square matrix U contains the corresponding eigenvectors. Hence the term $e^{\pm j\sqrt{Q}z}$ can be evaluated using the following expression:

$$e^{\pm j\sqrt{Q}z} = U e^{\pm j\sqrt{V}z} U^{-1} \tag{3.12}$$

3.3 Extensions to the MOL

Important extensions to the MOL which results in an increase of its numerical efficiency will be discussed in this section. Those extensions include, improvement to the transverse second derivative operator using an improved higher order finite difference approximation. The use of Perfectly Matched Layer to absorb the radiative field effectively. The results to be presented in this section confirm the accuracy of our implementation.

3.4 Improved Higher Order Finite Difference Approximation of the Transverse Second Derivative Operator

The central difference approximation of the second derivative operator $\frac{\partial^2}{\partial x^2}$ (see equation 3.2) has some major drawbacks. It is a 3-point central difference formula with an accuracy of $\mathcal{O}(h^2)$ in regions of uniform refractive index. Its accuracy decreases at index discontinuities. Because central difference is used to derive equation 3.2, a non uniform mesh size cannot be used in this case. Equation 3.2 also does not account properly for the TE and TM boundary conditions at material (refractive index) discontinuities. Thus, equation 3.2 is limited to the case of low index contrast in the transverse direction. If applied to TM polarized waves in high index contrast waveguides, equation 3.2 fails and gives erroneous results. In addition, it requires very fine mesh size (small Δx) to give an acceptable level of accuracy which leads to increased matrix size in the MOL and hence much increased runtime. The numerical accuracy of $\frac{\partial^2}{\partial x^2}$ can be improved without an excessive number of discretization lines by using higher order approximations of the transverse second derivative operator.

A higher order approximation scheme discussed in [32], will be implemented in this thesis. This technique is more efficient and more flexible than the one reported in [33]. It accounts for both TE and TM polarized waves and uses a non-uniform meshing scheme for added efficiency. This results in a much reduced matrix size in

the MOL, faster computational speed and lower memory usage.

In the subsequent sections, a brief idea about the interface conditions (I.Cs.) for an arbitrary mesh size and index discontinuities is given followed by final expressions of the higher order approximation of the transverse second derivative operator algorithm.

3.4.1 Interface Conditions

Before moving to the approximation algorithm, a clear idea about the behavior of the field at the interface (where refractive index discontinuity occurs) is required. This can be achieved by reviewing in brief, the interface conditions (I.C's).

The I.C's can be derived using equations 2.5 and 2.9 for TE and TM modes, respectively and are shown in detail in [15, 16]. Using the above equations and applying the boundary condition i.e. continuity of electric field E_y, E_z and magnetic field H_y, H_z, on the either side of the interface results in the following equations

$$E_y^{0^+} = E_y^{0^-} \tag{3.13}$$

$$\frac{\partial E_y^{0^+}}{\partial x} = \frac{\partial E_y^{0^-}}{\partial x} \tag{3.14}$$

$$H_y^{0^+} = H_y^{0^-} \tag{3.15}$$

and

$$\frac{1}{n_2^2} \frac{\partial H_y^{0^+}}{\partial x} = \frac{1}{n_1^2} \frac{\partial H_y^{0^-}}{\partial x} \tag{3.16}$$

Equations 3.13,3.14 and 3.15, 3.16 corresponds to the TE and TM modes, respectively.

Therefore, from the above equations it can be concluded that the tangential electric field E_y and its first derivative is continuous across an interface and that the tangential magnetic field H_y is continuous but its first derivative is discontinuous at the interface. All the higher order derivatives of both E_y and H_y are discontinuous at an interface.

3.4.2 Higher Order Transverse Second Derivative Operator Algorithm

There are many algorithms reported in the literature that discuss higher order approximation of the second derivative operator [33, 34]. Although these algorithms give sufficiently high accuracy of the modal field profile and the effective indices, there are some limitations. The approach of [33] inspite of having an advantage by utilizing non uniform mesh and handles both TE and TM modes efficiently at the interfaces, it requires the presence of a uniform mesh size and a uniform refractive index on both sides of a discontinuity point (discontinuity due to mesh size, refractive index, or both). Due to this limitation, the number of points in the MOL has to be increased thereby decreasing the efficiency of the MOL.

The algorithm that will be presented here [32] does not suffer from such limitations. Therefore, this algorithm will be used throughout this thesis. This improved

algorithm allows both the mesh size and refractive index to change in a completely arbitrary manner from one layer to the next, without any restrictions. This basic difference leads to a number of advantages, which includes flexibility, efficiency and accuracy of the results. The approach used in this reference, for obtaining higher order approximation of the transverse second derivative operator, can be easily extended from the 3-point to the 5-point, the 7-point etc. Contrary to the approach presented in [33], which requires separate treatments for the points surrounding a discontinuity point, the present approach treats all point equally.

The algorithm will not be derived here and only the relevant final expressions will be given approximating the transverse second derivative operator ψ with respect to x is presented. The reader is referred to [32] for detail derivation. Only the results of the 5-point approximation will be presented. Referring to fig.3.2, the following is the final expression for the 5-point approximation technique approximation

$$
\begin{bmatrix} \psi_i \\ \psi_{i^-}^{(1)} \\ \psi_{i^-}^{(2)} \\ \psi_{i^-}^{(3)} \\ \psi_{i^-}^{(4)} \end{bmatrix} = C^{-1} \begin{bmatrix} \psi_{i-2} \\ \psi_{i-1} \\ \psi_i \\ \psi_{i+1} \\ \psi_{i+2} \end{bmatrix} \tag{3.17}
$$

where ψ_i is the field at the ith interface of thickness h_i and uniform refractive index n_i. The minus and plus signs in $\psi_{i-(+)}$ represents the field immediately to the left (right) of the ith mesh point, respectively. The superscript in $\psi^{(d)}$ denotes the dth derivative of ψ with respect to x. $\psi_{i-(+)1}$ represents the field at previous mesh
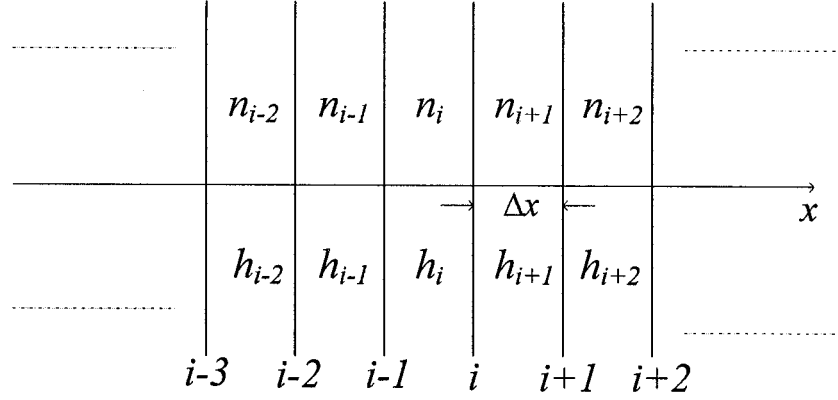
Figure 3.2: Generalized refractive index and mesh size distribution.

point (next mesh point). The elements of third row of C^{-1} provide the required finite difference coefficients for approximating the second derivative operator. The matrix C in equation.3.17 is defined as

$$
C = \begin{bmatrix}
q_{i-1}^{-} M_{i-1}^{-1} N_i^{-} \\
\\
q_i^{-} \\
\\
1 \quad 0 \quad 0 \quad 0 \quad 0 \\
\\
q_{i+1}^{+} M_i \\
\\
q_{i+2}^{+} M_{i+1} N_{i+1}^{+} M_i
\end{bmatrix}
\tag{3.18}
$$

where the matrices M, q and N are given below

$$
M_i^{\pm 1} = \begin{bmatrix}
1 & 0 & 0 & 0 & 0 \\
0 & \rho_i^{\pm 1} & 0 & 0 & 0 \\
\mp \delta_i & 0 & 1 & 0 & 0 \\
0 & \mp \rho_i^{\pm 1} \delta_i & 0 & \rho_i^{\pm 1} & 0 \\
\delta_i^2 & 0 & \mp 2\delta_i & 0 & 1
\end{bmatrix}
\tag{3.19}
$$

$$q_i^\pm = \begin{bmatrix} 1 & \pm h_i & \frac{h_i^2}{2!} & \frac{\pm h_i^3}{3!} & \frac{h_i^4}{4!} \end{bmatrix} \tag{3.20}$$

$$N_i^\pm = \begin{bmatrix} 1 & \pm h_i & \frac{h_i^2}{2!} & \frac{\pm h_i^3}{3!} & \frac{h_i^4}{4!} \\ 0 & 1 & \pm h_i & \frac{h_i^2}{2!} & \frac{\pm h_i^3}{3!} \\ 0 & 0 & 1 & \pm h_i & \frac{h_i^2}{2!} \\ 0 & 0 & 0 & 1 & \pm h_i \\ 0 & 0 & 0 & 0 & 1 \end{bmatrix} \tag{3.21}$$

where $\rho_i = 1$ for the TE waves and $\rho_i = \frac{n_{i+1}^2}{n_i^2}$ for the TM waves, and $\delta_i = k_0^2(n_{i+1}^2 - n_i^2)$.

The expressions corresponding to the 3-point and the 7-point approximation are presented in appendix B for reference.

3.4.3 Numerical Results

High Contrast Asymmetrical Waveguide

The developed algorithm for the three-point, five-point and seven-point approximation of the transverse second derivative operator $(\frac{\partial^2}{\partial x^2})$ are used to model the high-contrast asymmetric waveguide shown in the inset of fig. 3.3. The effective index of the TE_0 mode of this slab waveguide is calculated using the 3, 5 and 7-point approximation as a function of the mesh size (that is increasing the number of discretization points M) in the problem space at $\lambda_0 = 1.00\mu m$. The outer layers thickness is kept sufficiently large so that the modal field decays to a sufficiently

small value before it reaches the exterior wall of the problem space.

The exact value of the effective index of the TE_0 mode, calculated by STF1 program (see Appendix D), is given by $n_{eff,TE_0} = 3.0708680179441$. The absolute error $|n_{eff,exact} - n_{eff,calc}|$, as a function of the number of mesh points M is shown in the same figure (fig.3.3). The error is seen to decrease smoothly with M and the error order is very close to $O(h^2)$, $O(h^4)$ and $O(h^6)$ for 3,5 and 7-point approximations, respectively. The corresponding absolute error in the effective refractive index of the TM_0 mode (for the same waveguide) is shown in fig.3.4, which appears to be similar to the TE_0 mode case. The exact value of the effective index up to 14 digits is given by $n_{eff,TM_0} = 2.5237142996534$. It is observed that the 7-point formula gives a better estimate of n_{eff} with relatively few sample points when compared to the 5-point and the 3-point formulas.

3.5 Absorbing Boundary Conditions

For the analysis of any waveguide structure, the waveguide has to be enclosed in a box called "the computational window" or "the problem space". This is done in order to limit the computational effort and model an open space problem using a finite width window. The truncation of the field at the edges of the computational window is usually obtained by assuming an electric wall ($E_y = 0$) or a magnetic wall ($H_y = 0$) at both edges of the computational window. The presence of these walls is undesirable, causing the radiative waves to completely reflect backwards
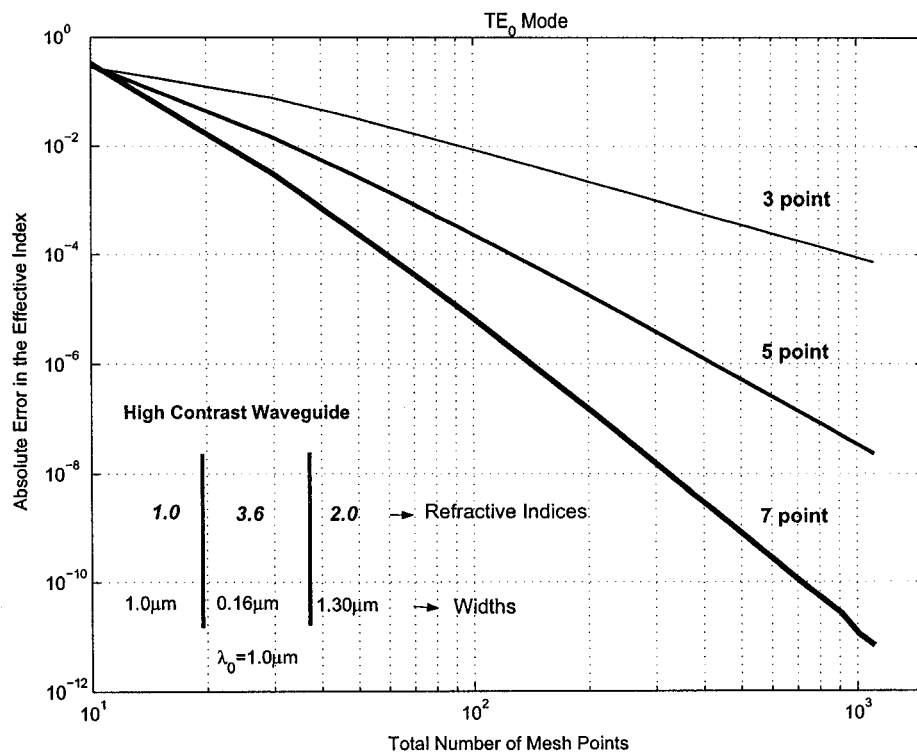
Figure 3.3: Variation of the error with the total number of mesh points (TE_0 Mode).
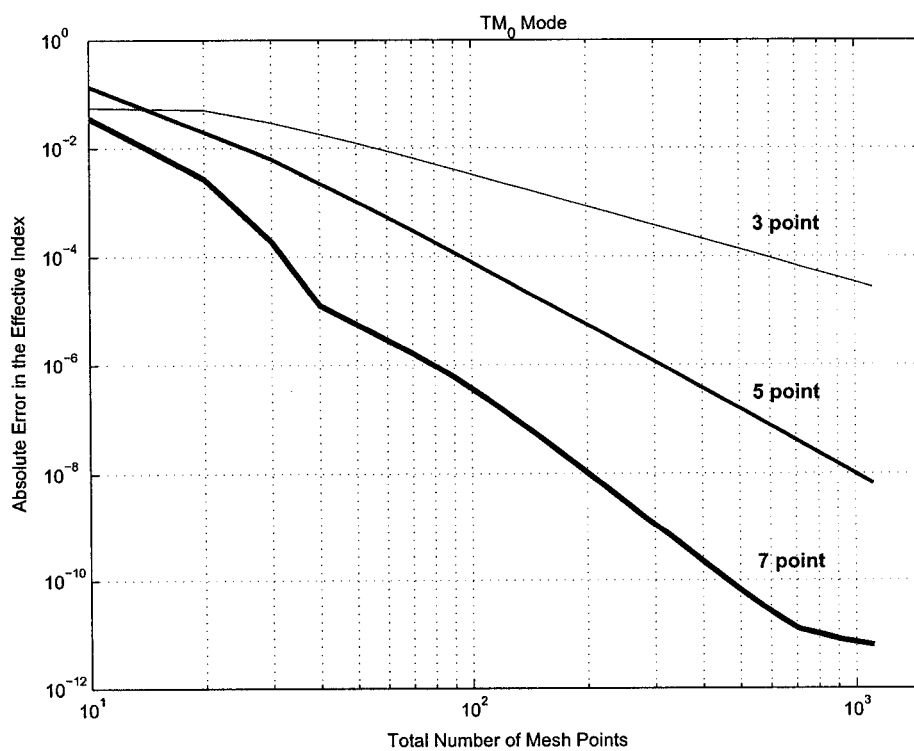
Figure 3.4: Variation of the error with the total number of mesh points (TM_0 Mode).

into the computational window. These reflected waves interfere with the field inside the computational window, leading to erroneous results. In order to improve the accuracy of the MOL, absorbing boundary condition are used for the purpose of absorbing the radiated field.

3.5.1   Perfectly Matched Layer (PML)

Perfectly matched layer (PML) is an example of an absorbing boundary condition. If the PML region (assumed to exist near the boundaries of the computational window) is made sufficiently wide, only negligible electromagnetic reflections at the extreme edges of the computational window may occur [35] (see fig.3.5)(because most of the field will be absorbed by the PML).

Background

The PML used in this work is based on transforming real space into the complex domain [35, 36]. The distance x within the PML is mapped into the complex domain according to $x \rightarrow x(1 + j\sigma)$ $[\triangle x \rightarrow \triangle x(1 + j\sigma)$ in discretized form]. This results in the formation of an attenuation factor in the PML (towards the inside of the PML) followed by a termination of the mesh points. The parameter σ $(\sigma > 0)$ controls the rate of decay within the PML. The radiative wave e^{+jkx} propagating in the $+x$ direction in the real space will be transformed to

$$e^{+jkx(1+j\sigma)} = e^{+jkx}e^{-k\sigma x} \tag{3.22}$$
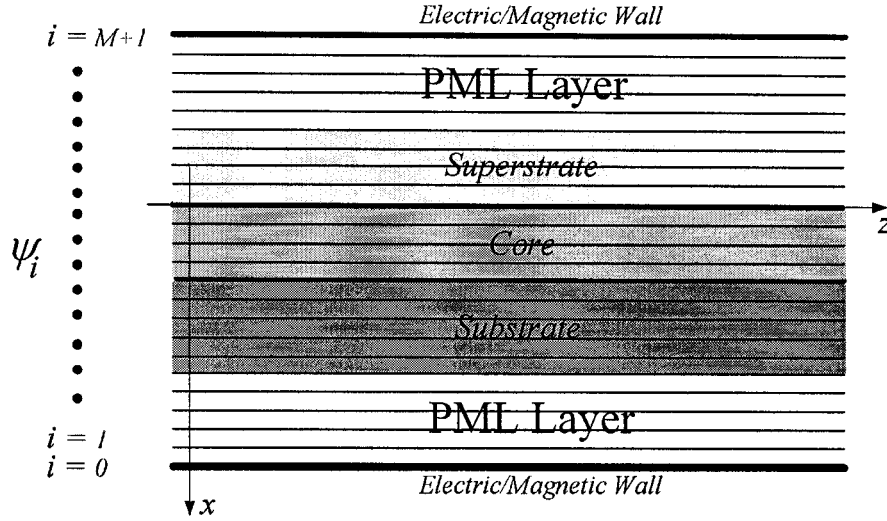
Figure 3.5: PML incorporated in Mesh Discretization.

in the complex space. Hence, the term $e^{-k\sigma x}$ causes wave attenuation in the $+x$ direction. The choice of the decay factor σ is discussed in reference [36].

If the term $\triangle x\sigma$ remains unchanged throughout the PML, then we have a uniform PML. If this term is gradually increased into the PML, following a certain profile, then the PML is termed non-uniform or graded PML. In general, the graded loss profile is superior in performance to the uniform profile [37]. This will be shown by considering an example in the next subsection. The present work utilizes a PML with a graded loss profile. Therefore, more explanation will be provided which which should be sufficient to general understanding. The reader is refered to [37] for details.

For a graded PML, we define first

$$x_i = \frac{i\,\pi/2}{M_p + 1} \qquad (i = 1, 2, 3, \dots M_p) \tag{3.23}$$
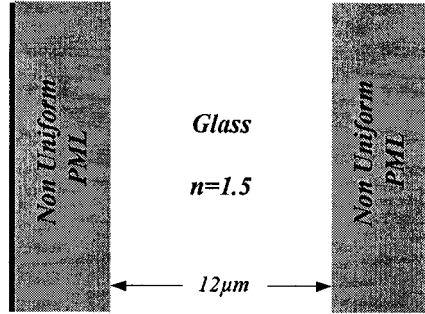
Figure 3.6: Illustration of the PML Scheme used. The White Region between the PML corresponds to Glass with $n = 1.5$.

where M_p is the number of mesh points in the PML region. Then, the parameters

η and x_i are used to define the the non uniform loss profile as $\frac{\eta}{M_p} f(x_i)$. Where $f(x_i)$

is a function that defines the loss profile (for instance, tangent, exponential, secant,

cubic, linear, etc). The present thesis utilizes the tangent graded loss profile and

therefore, its performance will be evaluated and compared with the uniform loss

profile in the subsequent section.

3.5.2   Numerical Results

Gaussian Field Propagation in Glass

In order to asses the performance of the PML, the propagation of a two-dimensional

Gaussian beam in glass is simulated using the MOL. The beam has a spot size of

$w = 2\mu m$ and the operating wavelength $\lambda_0 = 1.0\mu m$ is launched at z=0. Glass

occupies the region ($|x| < 6\mu m$)(shown in fig.3.6). Two identical PML layers are

placed on either side of the problem space having $\eta = 1.0$ and $M_p = 12$. Glass is

discretized into 60 mesh points. Both PML follow the Tangent loss profile [i.e. $f(x_i)$

$= \frac{\eta}{M_p} Tan(x_i)]$. The analytical results (obtained from [37, 38]) are compared with the calculated results which are shown in fig.3.7. The beam propagation is shown at z=0, 30, 60, 90 and $120\mu m$, respectively. The curves are displaced successively by 0.7 on the vertical scale for clarity. From this figure, it can be seen that the simulated results agree with the analytical results, thus establishing the accuracy of of PML.

In figure 3.8, comparison of the graded tangent loss profile and the Uniform loss profile is made with the same parameters mentioned above, at $z = 100\mu m$. As seen in the figure, good agreement between the theoretical and the calculated fields when the tangent profile is used. However, relatively strong reflection is seen to develop at the glass/PML interface, when the uniform loss profile is used. Thus, from this result it can be concluded that the graded PML has a better performance compared to the uniform PML.
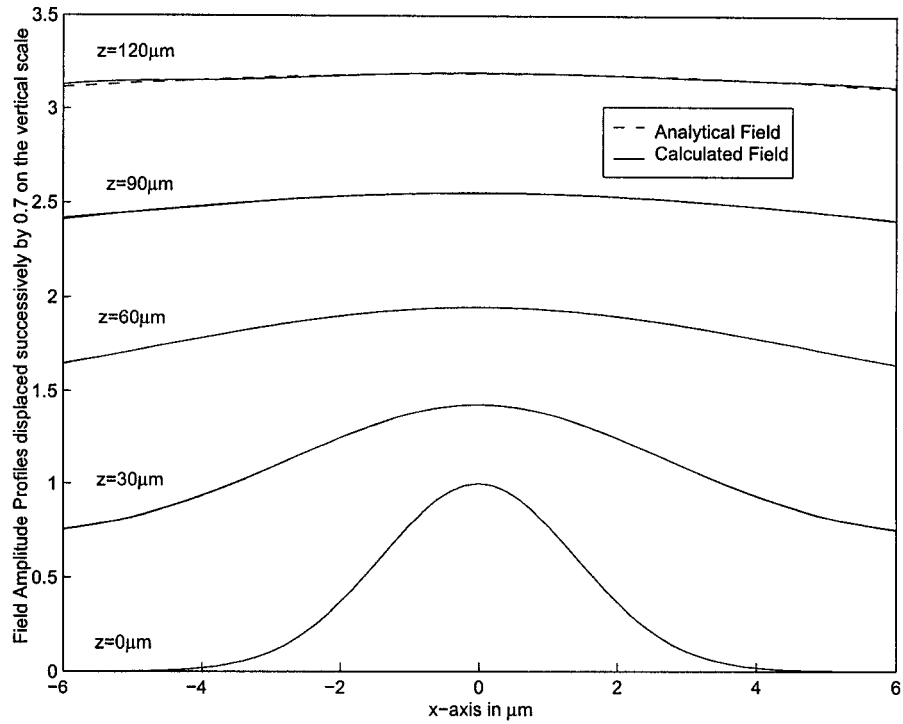
Figure 3.7: Theoretical and Calculated Gaussian Beam Propagation in Glass using a Graded PML with a Tangent Loss Profile.
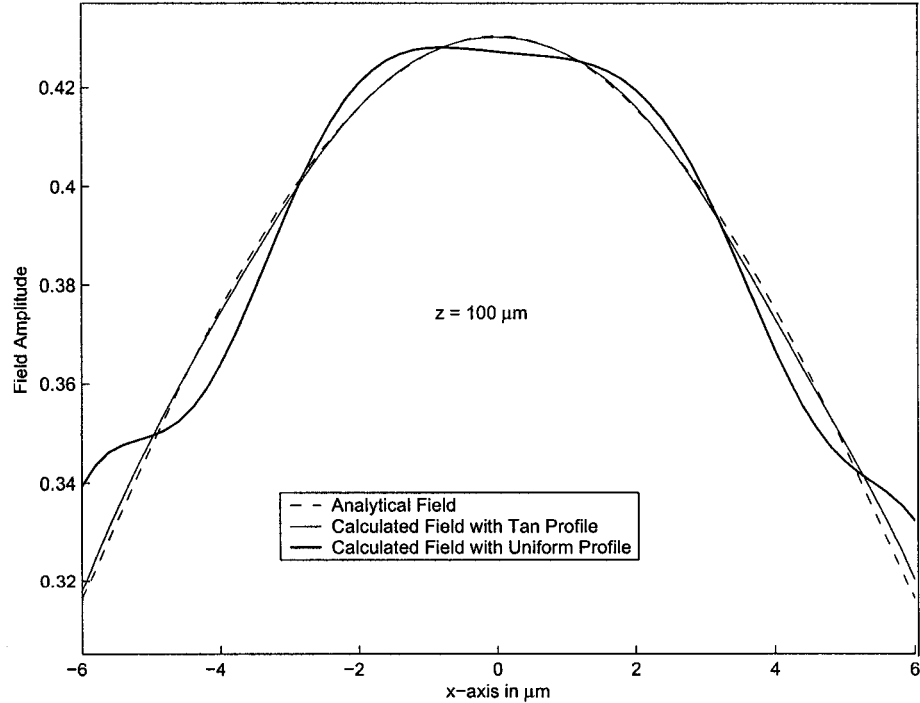
Figure 3.8: Comparison of the Graded PML with a Tangent loss Profile and the PML with a Uniform loss Profile.

Chapter 4

MOL Analysis of Longitudinal

Discontinuities

4.1 Introduction

Discontinuity problems in the optical guided-wave devices are of considerable the-
oretical and practical interests. They play an important role in designing practical
devices such as tapers, bends, y-junctions, couplers, mode converters, wavelength
filters, connections of different waveguides, etc. Much effort has been made towards
the understanding of the reflection and transmission phenomena at a discontinuity
interface.

Fig.4.1 illustrates some examples of guided wave grating structures exhibiting
longitudinal discontinuities. These structures may be broadly classified into pe-
riodic corrugated structures (see fig.4.1(a)) and arbitrary or aperiodic corrugated

35

structures (see fig.4.1(b)). A more complex structure which exhibits both periodic and arbitrary longitudinal discontinuities is shown in fig.4.1(c).

The periodic structure consists of rectangular periodic gratings of groove depth h and period T. The structure is usually composed of thousands of such periods. Each period consists of two discontinuities. The total reflected and the total transmitted field of the structure is the phasor sum of all the individual reflected and transmitted fields at each discontinuity.

The arbitrary waveguide structure shown in fig.4.1(b) consists of five distinct regions. Each region may have a different refractive index contrast and the width can also varies in an arbitrary fashion.

The third example (fig.4.1(c)) is a more complex structure consisting of two periodic structures with widths T_1, T_2 and depths h_1, h_2 respectively. These are combined with different arbitrary regions. MOL analysis of such a guided structure is a relatively laborious task. In this thesis we have developed a program that can handle such complex structures in a numerically efficient way. The program is developed with an eye on reducing the human effort required to program such a structure, efficiently.

Gratings applications also include, wavelength dispersion, conversion, modulation and control of guided wavefronts in optical integrated circuits [39]. The gratings structures have dimensions which are suitable for fabrication and integration process. On the basis of applications, they can be classified as active and passive device components. Distributed Feedback (DFB) [40] and Distributed Bragg Reflector (DBR)
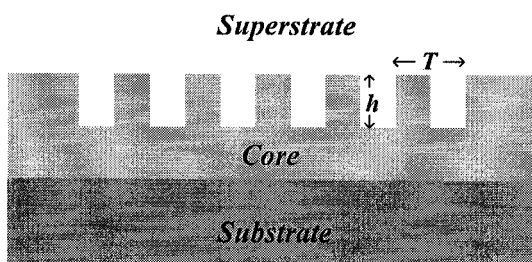
Guided Wave Grating Structure
exhibiting Periodic Longitudinal
Discontinuities

(a)
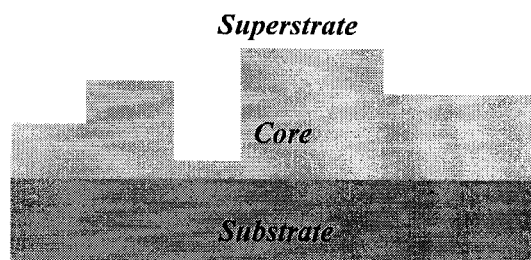
Guided Wave Grating Structure
exhibiting Arbitrary Longitudinal
Discontinuities

(b)
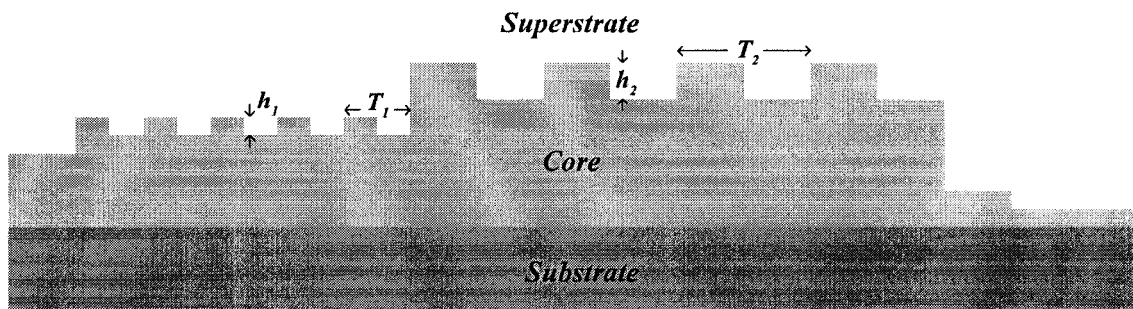
Guided Wave Grating Structure
exhibiting Periodic and Arbitrary
Longitudinal Discontinuities

(c)

Figure 4.1: Waveguide Grating Structures.

lasers [41, 42] are examples of corrugation-based active devices. [3] gave some examples of passive grating components, which includes grating couplers, deflectors, reflectors, mode converters, wavelength filters, etc. They can also be classified on the bases of structure as index modulation and relief types [3]. Gratings are also used as couplers for coupling the electromagnetic field into and out of integrated optical waveguides and devices [43, 44]. This application relies on electromagnetic coupling through phase matching of the different fields by the corrugated region.

The MOL is especially suitable for the analysis of discontinuities in optical waveguides [23, 24, 26], because it can account for both the transmitted and reflected fields. The MOL has been applied to solve non-linear scattering problem from a single discontinuity [45] and surface-plasmon mode scattering [46, 47]. Apart from the MOL, many other numerical techniques has been adopted by the researchers to analyze the waveguide discontinuities such as the Mode Matching method [48], the Ritz-Galerkin variational technique [49], the Equivalent Transmission-Line Network Method [50], the Beam Propagation method [5, 6], etc.

4.2 Single Longitudinal Discontinuity

A single longitudinal discontinuity is shown in Fig.4.2, which consists of two longitudinally uniform regions, region 0 and region 1. The field is incident from region 0 resulting in a reflected field back into region 0 and a transmitted field in region 1. The total field in each region is the sum of the forward field, e^{+jSz}, and the

Interface

$e^{+jS_0 z} A_0$

→

Incident Wave

$e^{+jS_1 z} A_1$

→

Transmitted Wave

$e^{-jS_0 z} B_0$

←

Reflected Wave

Region 0 *Region 1*

$z=0$

Single Longitudinal
discontinuity
(a)

$n_2=3.24$ *Cladding* *Air*

0

$n_1=3.6$ *Core* D *z*

$n_0=1.0$

$n_2=3.24$ *Cladding*

x

Waveguide Structure
(b)
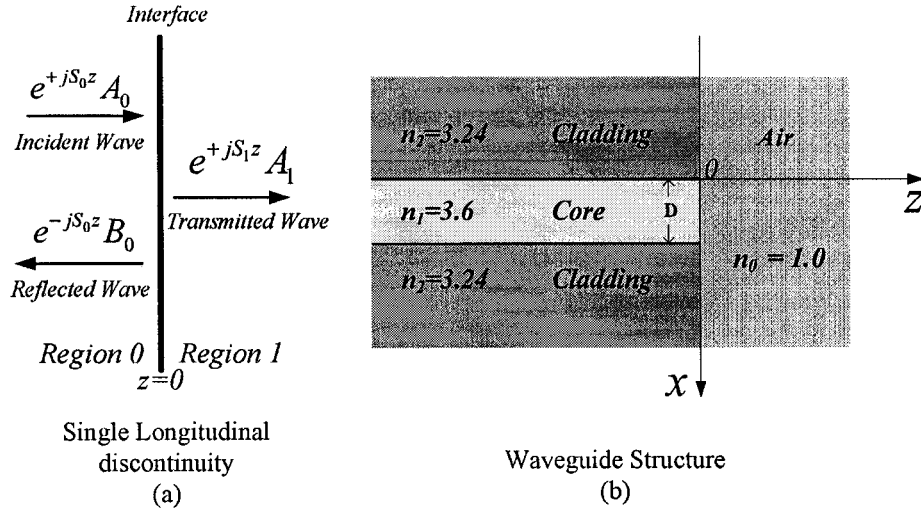
Figure 4.2: Single Longitudinal Discontinuity and the simulated Structure.

backward field, e^{-jSz}, where $S = \sqrt{Q}$. The total field Ψ_0 in region 0 is the sum of the incident and the reflected fields whereas the total field in region 1 consists of only the transmitted field.

By applying the appropriate boundary conditions at the discontinuity, it is possible to express B_0 (reflected field) and A_1 (transmitted field) in terms of A_0 (incident field). For the TE polarization, the resulting relations are [15, 16]

$$A_1 = 2(I + S_0^{-1} S_1)^{-1} A_0 = T A_0 \tag{4.1}$$

$$B_0 = (I - S_0^{-1} S_1)(I + S_0^{-1} S_1)^{-1} A_0 = R A_0 \tag{4.2}$$

and for the TM polarization

$$A_1 = 2(I + S_0^{-1} N_0 N_1^{-1} S_1)^{-1} A_0 = T A_0 \tag{4.3}$$

$$B_0 = (I - S_0^{-1} N_0 N_1^{-1} S_1)(I + S_0^{-1} N_0 N_1^{-1} S_1)^{-1} A_0 = R A_0 \tag{4.4}$$

where N_0 and N_1 are the diagonal matrices containing the square of the refractive

indices of region 0 and region 1, respectively. The terms A_0, B_0 and A_1 respectively represents the incident field, reflected field, and the transmitted field at $z = 0$, which is the assumed location of the discontinuity. The square matrices T and R are the transmission and reflection matrices respectively. The above equations can also be written as

$$A_1 \;=\; B_0 + A_0 \tag{4.5}$$

$$=\; RA_0 + A_0 \tag{4.6}$$

$$=\; (R + I)A_0 = TA_0 \tag{4.7}$$

The above results are valid for the symmetric as well as asymmetric single longitudinal waveguide discontinuities.

4.2.1 Modal Power and Coefficients Calculation using MOL

Before moving to the numerical results of a single waveguide discontinuity, an idea about the modal power calculation is given in this section which has been used throughout the thesis. The mode power can be calculated by the basic method of squaring the amplitude of the modal field. The modal field amplitude calculation can be done using the overlap integral method. This method has been explained and derived in appendix C. In this section, the general expression of the overlap integral (equation C.7) is used to obtain the expression for the modal field amplitude of a single waveguide discontinuity (see fig.4.2(a)).

Considering TM modes, the incident magnetic field is given by

$$H_y = e^{+jS_0z}A_0 \tag{4.8}$$

where the $M \times 1$ column matrix, A_0, represents the incident field at $z = 0$ and the $M \times M$ matrix $S_0 = \sqrt{Q_0}$ where Q_0 is defined in chapter 3. Using Maxwell's equations, the x component of the incident electric field for TM modes is given by:

$$E_x = \frac{j}{\omega\epsilon_o n_i^2}\frac{\partial H_y}{\partial z} \tag{4.9}$$

where n_i is the sampled refractive index on the ith discretization line. Substituting equation 4.8 into equation 4.9, we have:

$$E_x = \frac{j}{\omega\epsilon_o N_0}\frac{\partial}{\partial z}(e^{+jS_0z}A_0) \tag{4.10}$$

$$= -\frac{1}{\omega\epsilon_o N_0}S_0 e^{+jS_0z}A_0 \tag{4.11}$$

where the matrix N is defined in chapter 3. Hence, the incident electric and the incident magnetic field components, E_x and H_y, at $z = 0$ are given by:

$$E_x|_{z=0} = -\frac{1}{\omega\epsilon_o N_0}S_0 A_0 \tag{4.12}$$

$$H_y|_{z=0} = A_0 \tag{4.13}$$

The average power flow (per unit length in the y-direction) in the z direction is given by:

$$P_z = \frac{1}{2}Re\int_{-\infty}^{\infty} E_x H_y^* dx \tag{4.14}$$

For discrete field, integration is replaced by summation over the index of the array.

$$P_z = \frac{1}{2}Re\left[\sum_{m=1}^{M} E_{xm}H^*_{ym}(\Delta x)_m\right] \tag{4.15}$$

Substituting E_x and H_y from equations 4.12 and 4.13 into equation 4.15, we obtain expression for calculating the input power:

$$P_z = \frac{1}{2\omega\epsilon_o}Re\left[N_0^{-1}S_0A_0A_0^*\right]\Delta x \tag{4.16}$$

The above equation can be used for the calculation of the reflected and transmitted power of the waveguide. The modal field amplitude can also be obtained by calculating the modal expansion coefficient α_m of the waveguide by using the modal coefficient formula C.6, that is

$$\alpha_m = \frac{A^t N_0^{-1} F_m}{F_m^t N_0^{-1} F_m} \tag{4.17}$$

where the $M \times 1$ vector F_m represents the discretized modal field distribution of the mth mode, A is the discretized field and the superscript t represents transpose of a vector. The above formula can be used for the TE modes by replacing matrix N with the identity matrix I.

On squaring the modal expansion coefficient one can obtain the required mode power. Since the thesis is emphasized on obtaining the modal reflectivity and transmissivity of various guided-wave structures, the definitions of these terms are given below

Modal Reflectivity (**R**) is defined as the ratio of the modal reflected power to the modal incident power and modal transmissivity (**T**) is defined as the ratio of the modal transmitted power to the modal incident power, satisfying the conversation of power **R** + **T** = 1. The fraction of the power radiated can be calculated using the above formula i.e. **Ra** (Radiation loss) = 1 - **R** - **T**.

4.2.2 Numerical Results

The formulation of a single longitudinal discontinuity has been evaluated and compared with published results [51]. The chosen structure is shown in fig.4.2(b), which represents a simple laser-facet. The structure is modeled at $\lambda_0 = 0.86\,\mu m$. The core width D is varied from 0.05 to $1.00\mu m$ and the fundamental modal reflectivity of the TE wave is calculated as a function of D. The computational window is made large enough so that the field is negligible at the electric walls. The TE_0 modal field is assumed to be incident on the laser facet from the left. Our results are shown in fig.4.3 along with the results of reference [51]. From the figure we can see that our results are in close agreement with that of reference [51], thereby establishing the accuracy of implementation.

Fig.4.4 shows the reflectivity of the fundamental TE and TM waves for different index contrast. The cladding refractive index is first expressed as $3.6(1-\triangle)$, with $\triangle$ selected to be 10% and 3%. Our results and the results of [51] show good agreement with slight deviation in the curves for the TM_0 case.
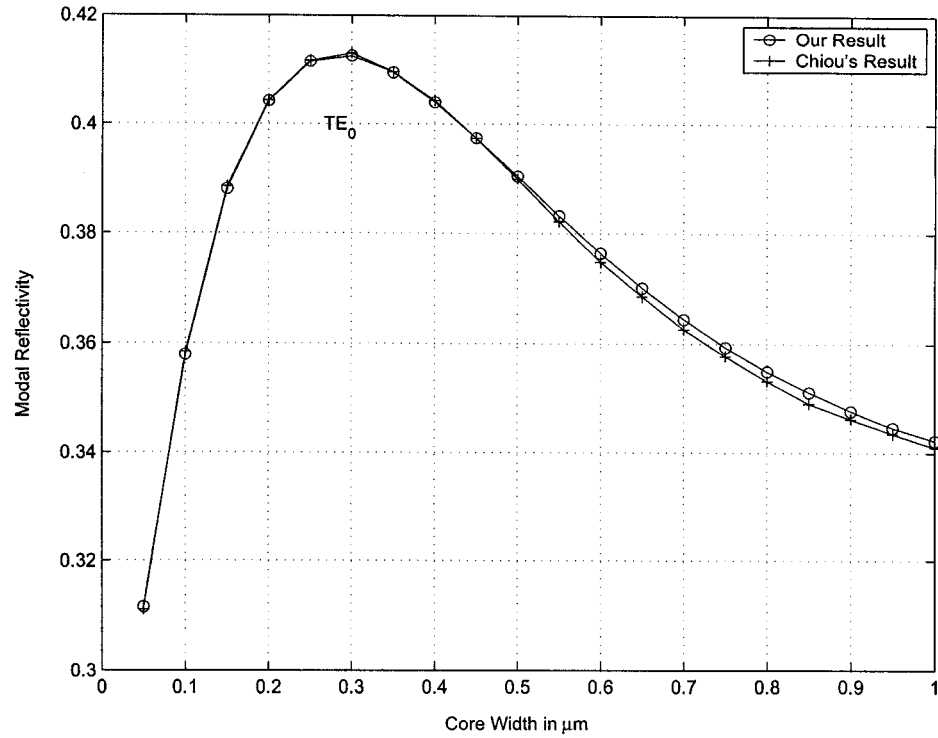
Figure 4.3: Fundamental TE mode Reflectivity of the Waveguide Structure shown in fig.4.2(b).
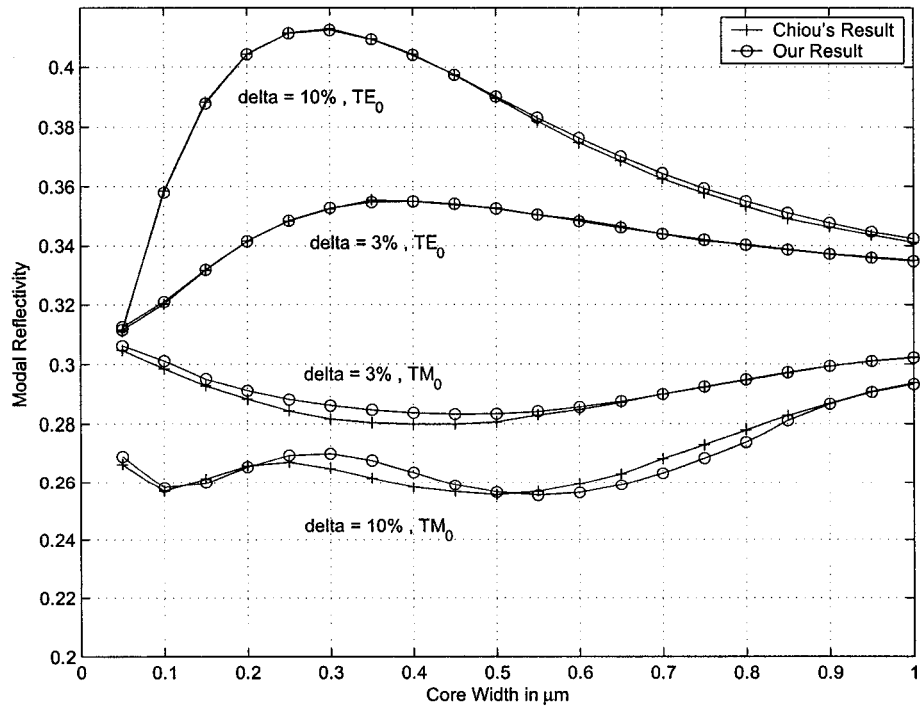
Figure 4.4: Modal Reflectivity of the Waveguide Structure shown in fig.4.2(b).

4.3 Analysis of Multiple Longitudinal Discontinuities

A number of theoretical methods have been reported in the literature for the analysis of waveguides with periodic corrugations. Marcuse [20] used coupled-mode theory to analyze a slab waveguide with sinusoidal deformation on one of its interfaces. The spectral response of a grating filter using the coupled-mode theory was calculated and compared with experimental work in [52]. In reference [53], the Effective-Index method was used to model a waveguide grating and the results were compared with coupled-mode theory. A major limitation of the coupled-mode theory is that it can only model small waveguide perturbations which is due to its approximate formulation.

The Method of Lines is widely used for the analysis of periodic as well as aperiodic finite length gratings. There are a number of algorithms that utilizes the MOL for the analysis of such waveguides [28, 54, 55]. In this thesis two such algorithms are discussed and will be used throughout the work.

The first algorithm is called the Layer by Layer method [28], which is a recursive procedure that accounts for multiple discontinuities by accounting for a discontinuity at a time. We start this procedure at the last discontinuity (at the output side of the structure) and work backwards layer by layer, until the first discontinuity is reached. This procedure is a simple one. However it requires much computational time and memory when the number of discontinuities is large. However, the main

advantage of this approach is that the field within the structure can be obtained in addition to the overall transmitted and reflected fields.

The second algorithm which will be used in this work is called the Cascading and Doubling procedure [54]. It is a stable approach that can be used to account for multiple waveguide discontinuities. It is very efficient when applied to periodic structures with a large number of discontinuities. However, this procedure can only be used to obtain the overall reflected and transmitted field. The field inside the discontinuous structure cannot be obtained by this procedure.

In the current chapter, a brief review of the MOL formulation of these algorithm is explained and compared.

4.4 The Layer By Layer Algorithm

Consider the multi-discontinuities layer structure shown in figure 4.5. It consists of N discontinuities divided in $N + 1$ regions (from $1, 2......, N, N + 1$), $d_i = z_i - z_{i-1}$ (i=$0, 1, 2......, N$), represents the distance between the two successive discontinuity. The total field is composed of forward and backward fields. Thus, the total field in the layers is expressed as:

$$\Psi_0 \quad = \quad e^{+jS_0 z}A_0 + e^{-jS_0 z}B_0 \tag{4.18}$$

$$\Psi_1 \quad = \quad e^{+jS_1 z}A_1 + e^{-jS_1(z-z_1)}B_1 \tag{4.19}$$

$$\vdots$$
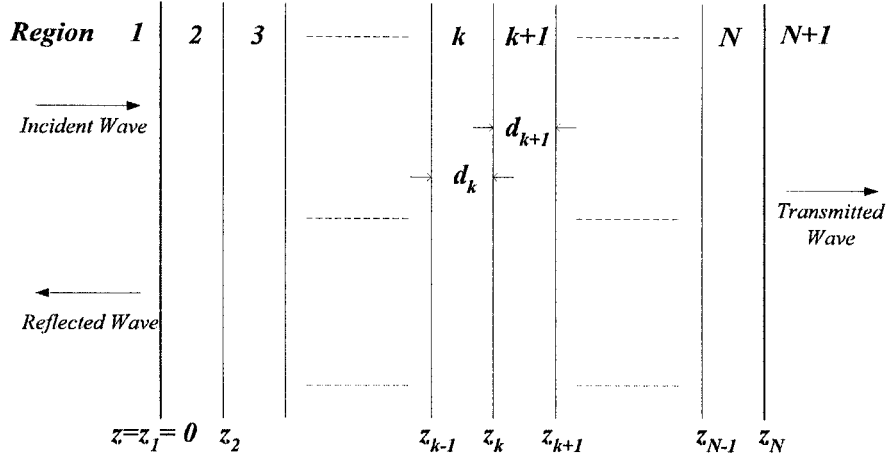
Figure 4.5: Multiple Waveguide Discontinuities in the z direction.

$$\Psi_k \quad = \quad e^{+jS_k(z-z_{k-1})}A_k + e^{-jS_k(z-z_k)}B_k \tag{4.20}$$

$$\vdots$$

$$\Psi_{N+1} \quad = \quad e^{+jS_{N+1}(z-z_N)}A_{N+1} \tag{4.21}$$

The subscript k in Ψ_k and S_k denotes the column vector Ψ_k and the matrix S_k in k region. In figure 4.5, the wave is incident on the interface located at $z = 0$ from the left. In region $N + 1$, the transmission region, the wave is assumed to propagate without reflection in the $+z$ direction. At each discontinuity, the boundary condition for TE waves requires the continuity of the tangential fields, E_y and H_z. In other words, the continuity of Ψ and $\frac{d\Psi}{dz}$ must be satisfied at the interfaces.

Application of these conditions at $z = z_k$ (i.e. to equation 4.20), results in the following relationships [28]

$$e^{jS_k d_k} A_k + B_k = A_{k+1} + e^{jS_{k+1} d_{k+1}} B_{k+1} \tag{4.22}$$

and

$$U_k(e^{jS_k d_k} A_k - B_k) = U_{k+1}(A_{k+1} - e^{jS_{k+1} d_{k+1}} B_{k+1}) \tag{4.23}$$

Where U_k is defined in chapter 4, that is $U_k = S_k$ for TE waves and $U_k = N_k^{-1} S_k$ for the TM waves. Using the above two equations and after simple mathematical manipulation, it can be shown that [28]

$$B_k = 0.5[(I - U_k^{-1} U_{k+1}) A_{k+1} + (I + U_k^{-1} U_{k+1}) D_{k+1} B_{k+1}] \tag{4.24}$$

and

$$D_k A_k = 0.5[(I + U_k^{-1} U_{k+1}) A_{k+1} + (I - U_k^{-1} U_{k+1}) D_{k+1} B_{k+1}] \tag{4.25}$$

where $D_k \equiv e^{jS_k d_k}$ and I is the identity matrix (whose size is same as that of U_k). By introducing a square reflection matrix (for simplicity) Γ_k, the relation between the incident and the reflected field in region $z = z_k$ may be expressed as

$$B_k \equiv \Gamma_k(e^{jS_k d_k} A_k) = \Gamma_k(D_k A_k) \tag{4.26}$$

Substituting equation 4.26 in equations 4.24 and 4.25 and after some manipulation we obtain

$$\Gamma_k = [(I - U_k^{-1}U_{k+1}) + (I + U_k^{-1}U_{k+1})D_{k+1}\Gamma_{k+1}D_{k+1}] \times$$

$$[(I + U_k^{-1}U_{k+1}) + (I - U_k^{-1}U_{k+1})D_{k+1}\Gamma_{k+1}D_{k+1}]^{-1} \qquad (4.27)$$

where $k = 0, 1, 2, ..., N$. For $k = 0$, $d_0 = d_{-1} = 0$ and for $k = N$, $B_{N+1} = 0$. This is a recursive relationship which expresses the reflection matrix of layer k in terms of the reflection matrix of layer $k + 1$. We start from the last layer, in which there is only a forward wave ($B_{N+1} = 0$), where $\Gamma_{N+1} = 0$. With this initial value, we use equation 4.27 recursively in the backward direction. Once Γ_1 is known, using equation 4.26, we have

$$B_1 \equiv \Gamma_1(e^{jS_1 d_1} A_1) = \Gamma_1(A_1) \qquad (4.28)$$

where z = 0, i.e. $d_0 = 0$, so that $d_1 = 0$, which gives $e^{jS_1 d_1} = I$ (A_1 corresponds to the incident field). Using the above procedure, we can find the total reflected field in terms of the incident field for any number of discontinuities in the z-direction. Similar procedure can be adopted to find the reflected field in the intermediate layers. The transmitted field in each layer, or the total transmitted field of any number of layers in terms of the incident and the reflected field can be calculated using the following equation.

$$A_{k+1} = 0.5[(I + U_{k+1}^{-1}U_k)D_k A_k + (I - U_{k+1}^{-1}U_k)B_k] \qquad (4.29)$$

Using equation 4.29 along with the stored values of Γ_k, one can find A_{k+1} and hence the field inside the layers or the overall transmitted field.

4.4.1 Numerical Results

A waveguide with periodic gratings is considered to show the effectiveness of the algorithm. The waveguide grating is shown in the inset of fig.4.6. It is a high index contrast with a groove depth of $0.04\mu m$ and a total of 50 periods. The TE_0 mode field is launched in the waveguide and the modal reflectivity is plotted in the same figure (fig.4.6), as a function of wavelength. The results show a central main lobe in the modal reflectivity centered at $0.9\mu m$ and several side lobes can be observed.

In another simulation, the results obtained by our algorithm is compared with those of reference [56]. The waveguide structure which consists of 64 periods, is shown in the inset of fig.4.7. The waveguide is excited using the fundamental TE mode and the modal reflectivity is calculated as a function of wavelength. As seen in fig.4.7, our results almost coincide with those of [56], thereby establishing the effectiveness of our algorithm and implementation.

4.5 The Cascading and Doubling Algorithm

The Cascading and Doubling procedure discussed in detail in [15, 16, 54] offers an efficient way of calculating the transmitted and the reflected fields of waveguides with many multiple discontinuities. This can be applied provided knowledge of the field in the intermediate regions is not required. Referring to figure 4.8, the two regions 'A' and 'B' represent two asymmetric distributed discontinuities, which are separated by
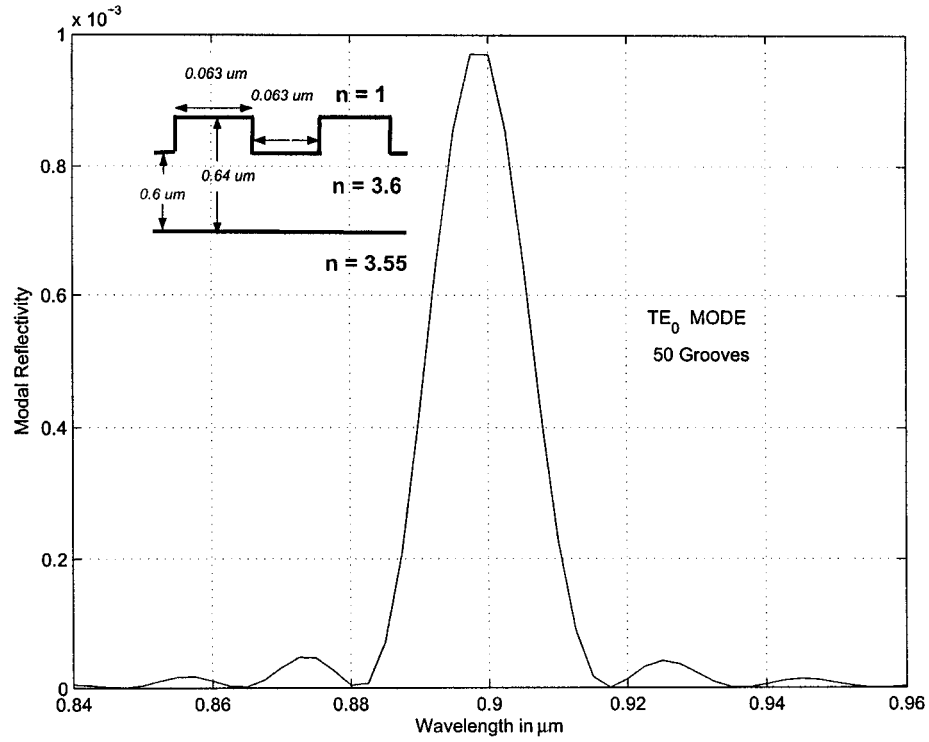
Figure 4.6: TE_0 Modal Reflectivity of the Waveguide Structure shown in the inset.
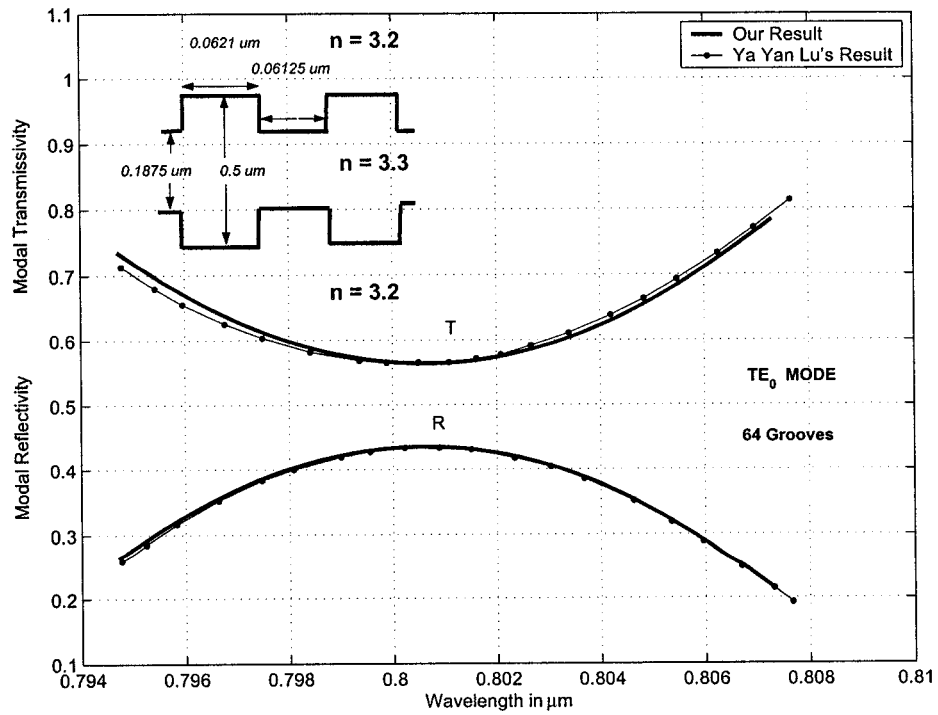
Figure 4.7: Spectral Response of the Waveguide Structure shown in the inset.
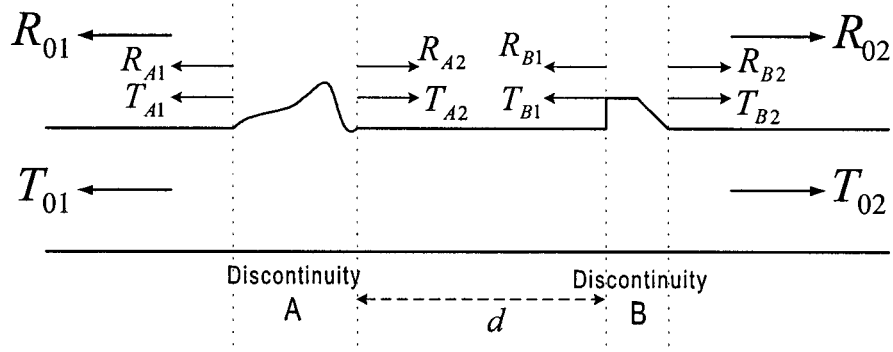
Figure 4.8: Two Waveguide Discontinuities Cascaded Together.

a uniform region of width d. The field reflection and transmission coefficients of both regions are assumed to be known, therefore, the quantities $[R_{A1}, T_{A2} \ (R_{A2}, T_{A1})]$, of the first region (i.e. discontinuity 'A', when the field is incident from left(right) of the discontinuity) and $[R_{B1}, T_{B2} \ (R_{B2}, T_{B1})]$, of the second region, are assumed to be known. When both discontinuities are joined together (see Fig.4.8) then, the reflection and transmission coefficients of the combined structure are given by [54]

$$T_{02} \ = \ T_{B2} \left(I - e^{jSd} R_{A2} e^{jSd} R_{B1} \right)^{-1} e^{jSd} T_{A2} \tag{4.30}$$

$$R_{01} \ = \ R_{A1} + T_{A1} e^{jSd} R_{B1} \left(I - e^{jSd} R_{A2} e^{jSd} R_{B1} \right)^{-1} e^{jSd} T_{A2} \tag{4.31}$$

The matrix S is associated with the uniform region separating the two discontinuities. Thus equations 4.30 and 4.31 gives the Cascading Algorithm which gives the net reflection and transmission matrices of a cascaded structure composed of two sub-structures in terms of their individual reflection and transmission matrices. The relations for R_{02} and T_{01} are as seen from the right-hand side are easily obtained from 4.30 and 4.31 by interchanging $A \rightleftharpoons B$ and $1 \rightleftharpoons 2$ [54].

When A and B are symmetric discontinuities, i.e. $R_1 = R_2 = R$ and $T_1 = T_2 = T$, equations 4.30 and 4.31 reduce to

$$R_{01} \;=\; R_A + T_A e^{jSd} R_B \left(I - e^{jSd} R_A e^{jSd} R_B\right)^{-1} e^{jSd} T_A \qquad (4.32)$$

$$T_{02} \;=\; T_B \left(I - e^{jSd} R_A e^{jSd} R_B\right)^{-1} e^{jSd} T_A \qquad (4.33)$$

If structures 'A' and 'B' are identical and symmetric, then $R_A = R_B = R$ and $T_A = T_B = T$. So the relations are further simplified to:

$$R_{01} \;=\; R + T e^{jSd} R \left(I - e^{jSd} R e^{jSd} R\right)^{-1} e^{jSd} T \qquad (4.34)$$

$$T_{02} \;=\; T \left(I - e^{jSd} R e^{jSd} R\right)^{-1} e^{jSd} T \qquad (4.35)$$

Finally, in the important special case, in which the above two identical and symmetric discontinuities, are attached directly to each other, such that $d = 0$, then we end up with the very simplified relationship

$$R_{01} \;=\; R + T R \left(I - R^2\right)^{-1} T = R_{02} \qquad (4.36)$$

$$T_{02} \;=\; T \left(I - R^2\right)^{-1} T = T_{01} \qquad (4.37)$$

The above equations 4.36 and 4.37 can be used to model a periodic waveguides with a large number of periods in an efficient manner. This can be done by combining two periods using the above equations, then the two periods are again be combined using the same equation to find the reflection and transmission matrices of four periods. The same process is continued for the whole structure. Therefore, as can be seen, this algorithm works in a power of 2. For 2^N periods, it requires repeated

use of equations 4.36 and 4.37, N times only, thus improving the efficiency of the procedure. To get a better understanding of the procedure, the reader is referred to references [15, 16, 54].

4.5.1 Numerical Results

The algorithm discussed above is applied to calculate the spectral response of waveguide gratings and a comparison is done with published results. Fig.4.9 shows the modal reflectivity curve as a function of wavelength for the same waveguide structure (shown in the inset of fig.4.7) but having 256 periods instead of 64 periods. The TE_0 polarized wave is incident on the left of the waveguide and the reflected field is calculated. Using equation 4.17, the modal reflectivity is calculated. Our results are compared with those of reference [57]. From the results we can infer that our results and those of [57], are same.

Figure 4.10 shows the modal reflectivity of an asymmetric waveguide grating having 262144 periods. The parameters of the waveguide are $n_{sup} = 1$, $n_{core} = 1.53$, $n_{sub} = 1.52$, core width $d = 2.4\mu m$, groove depth $h = 0.5\mu m$ and $l_0 = 0.106456\mu m$, $l_1 = 0.106553\mu m$ (where $l_0 + l_1$ is the period of the grating). As seen from the figure, the modal reflectivity has an asymmetric central main lobe and densely packed side lobes. Thus the algorithm is valid for waveguide grating structures with large number of periods.
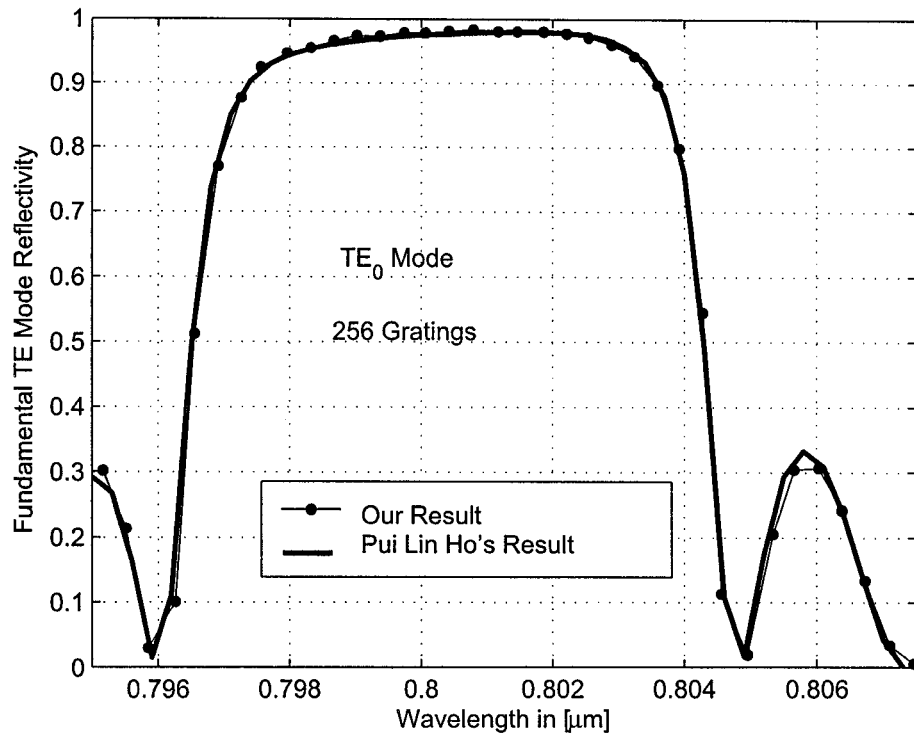
Figure 4.9: Deep Grating TE Modal Reflectivity.
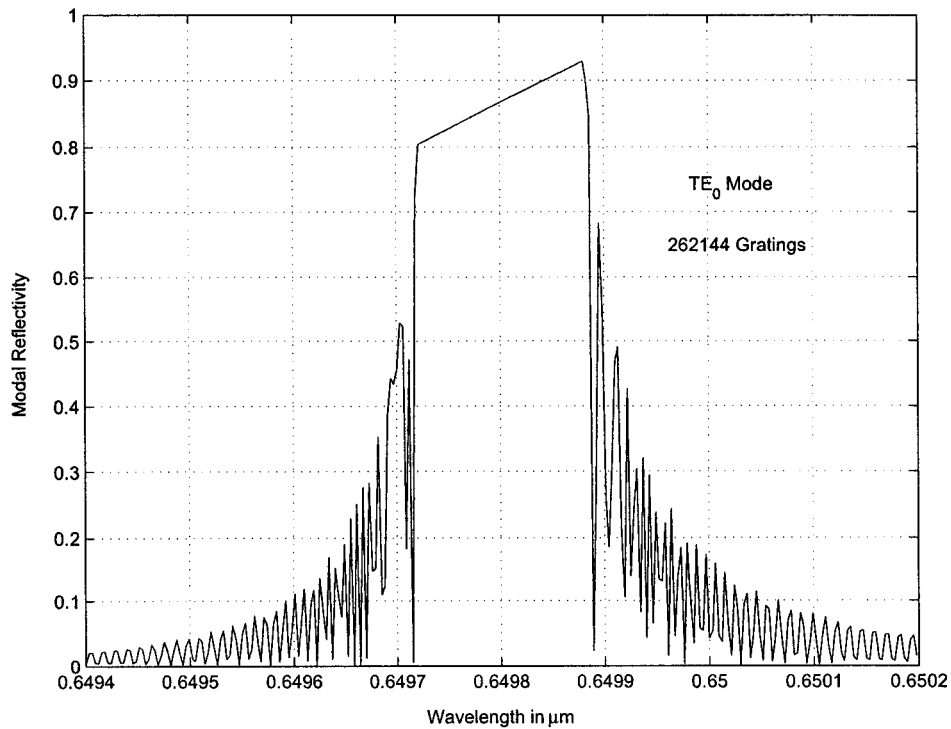
Figure 4.10: Deep Grating TE Modal Reflectivity, Semi-Infinite.

4.6   Comparison of Both Algorithms

The algorithms presented above, namely the layer by layer algorithm and the cascading and doubling algorithm are used to calculate the modal reflectivity of the grating structure shown in the inset of fig.4.11. From the figure (fig.4.11) it can be inferred that the results of both the algorithms are identical. The cascading and doubling algorithm took 2.5 second per wavelength where as the layer by layer method took 5.5 second per wavelength, to calculate the modal reflectivity.

Both the algorithms can model periodic and aperiodic gratings structures or combination of both. The cascading and doubling algorithm handles a large periodic gratings in an efficient manner. Doubling algorithm and then cascading algorithm can be applied to the periodic structure for numerical efficiency. The same periodic gratings can also be analyzed using only the cascading algorithm with the expense of numerical efficiency because the algorithm treats each discontinuity as an arbitrary discontinuity and calculates the modal reflectivity and transmissivity. The layer by layer method is a straightforward algorithm which treats aperiodic as well as periodic structures in a similar manner (i.e. arbitrary discontinuity). Therefore numerical efficiency cannot be achieved from the layer by layer method for large periodic grating structures. For a grating structure with small number of periods, both the algorithms are efficient where as for large number of periods, the cascading and doubling algorithm serves superior than the layer by layer method (it requires lot of human effort and memory as well).
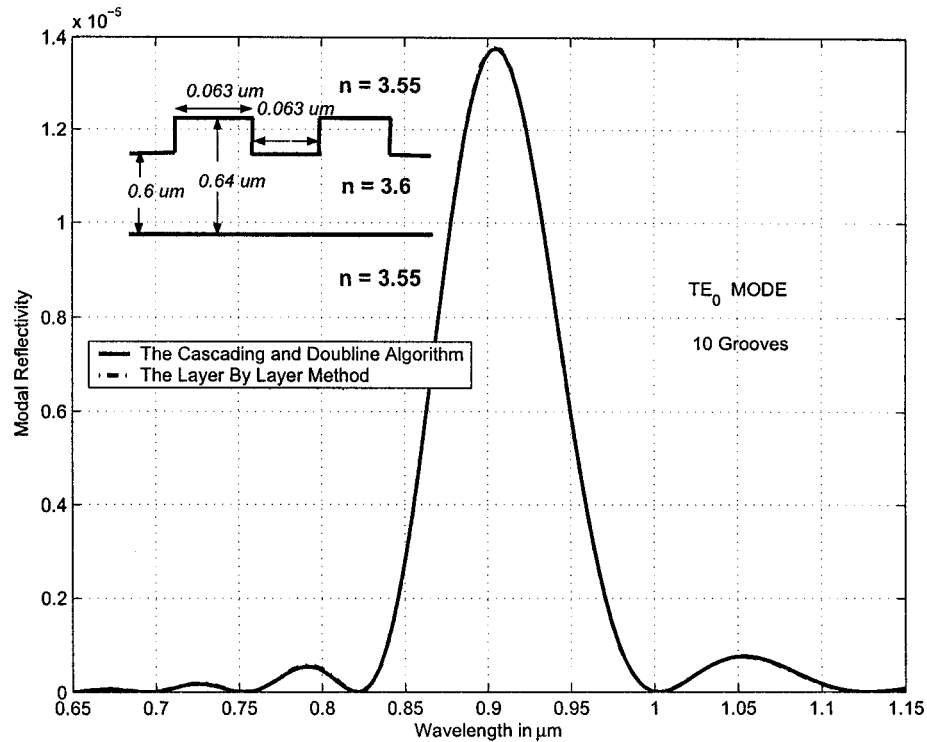
Figure 4.11: Comparison of the Layer by Layer method and the Cascading and Doubling Algorithm.

Therefore the cascading algorithm and the cascading and doubling algorithm are used to develop an automated program whereas the layer by layer algorithm is kept as a verification tool.

4.7 Development of the Automated Program

Application of the MOL into a multilayered structure in an efficient manner is not straightforward. It requires calculation of reflection and transmission matrices of each arbitrary region , and then using the cascading and doubling procedure in a correct way in order to obtain the overall response. A program is thus needed to

reduce the human effort for this task in a numerically efficient manner. Therefore we have developed a semi automatic program that is based on the single discontinuity formula, the cascading algorithm and the cascading and doubling algorithm.

The speciality of the program is that it handles the periodic region of the guided-wave grating structure in a numerically efficient manner. The program utilizes the doubling and cascading procedure to get its spectral response. If the program sees an aperiodic or arbitrary region in the guided-wave grating structure, then the transmission and reflection matrices of that individual region are calculated using the single discontinuity expressions (equations.4.2) and then cascading algorithm is applied to get the end results. This procedure is explained in detailed with reference to fig.4.12. The development of the program took more than three months because of the complexity of programming.

Fig.4.12 represents a guided wave grating structure with periodic and arbitrary discontinuities. The detailed specifications of the structure is shown in the figure. The structure is divided into seven distinct regions with region 1 and 7 to be the beginning and the terminating region, respectively. Regions 2 and 3 constitutes the first periodic part of the structure with five periods and regions 4 and 5 constitutes the other independent periodic part of the structure with four periods. Region 6 is an arbitrary region.

The waveguide structure is defined in the form of a vector with the term '[-1]' separating the arbitrary and periodic regions (or parts) of the waveguide structure. The vector is terminated by the last region of the structure without the term '[-1]'.
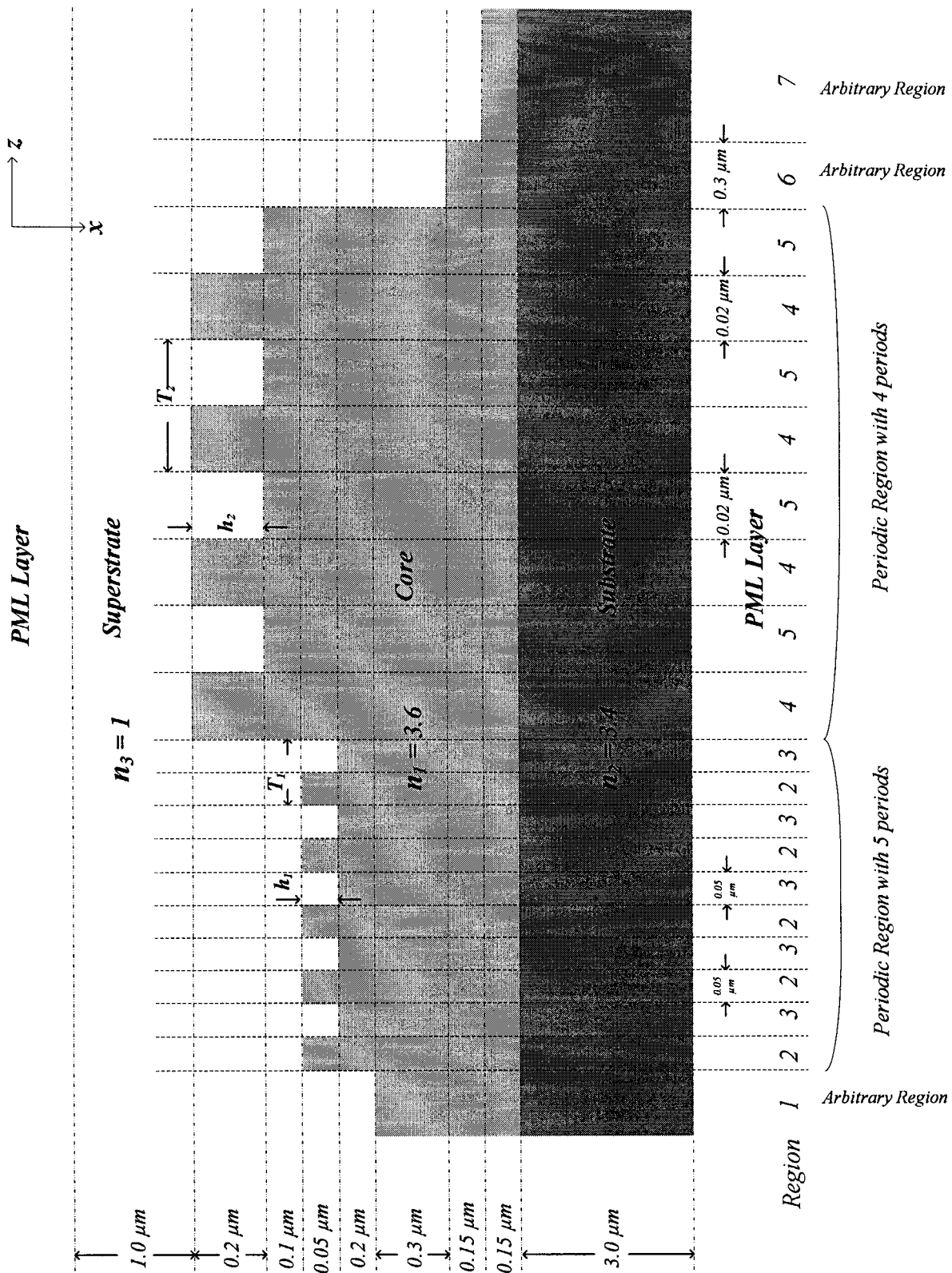
Figure 4.12: Detailed Specifications of the Waveguide Grating Structure.

Therefore, this represents the end of the waveguide structure and no further regions are available. An example of the vector defining the waveguide structure of fig.4.12 is given

$$st=[\ 1 \quad [\text{-}1]$$
$$2 \quad 0.05 \quad 3 \quad 0.05 \quad 5\ [\text{-}1]$$
$$4 \quad 0.02 \quad 5 \quad 0.02 \quad 4\ [\text{-}1]$$
$$6 \quad 0.3 \quad [\text{-}1]$$
$$7\ ];$$

The first line of the vector contains only one term that corresponds to the region 1 of the waveguide, which indicates the starting of the waveguide structure. This is an arbitrary region. The second line constitutes five terms which represents a periodic part in the waveguide structure. It can be noted that the terms of the first line and the second lines are separated by '[-1]' which indicates that these two line represents two different regions of the waveguide (first line represents the arbitrary part and the second line represents the periodic part of the waveguide, respectively). The first and second term of the second line represents the region number and width of the region, respectively. The third and fourth term of the second line represents the other region number and width, respectively. Both these regions constitutes the period of the waveguide and the fifth term of the second line represents the number of periods in that periodic part of the waveguide structure, which in our case is five. The third line of the vector constitutes the other independent periodic part of the grating structure. Therefore these two lines are again separated by '[-1]' indicating

that these represents different regions or part of the waveguide structure. The fourth line of the vector constitutes of only two terms which represents an arbitrary region in the waveguide structure. The first and the second term represents the region number and the width of the region respectively. Finally the last line of the vector (line number five) contains only one term with out '[-1]' which indicates the termination of the vector i.e. the end of the waveguide structure.

The developed program first calculates the reflection and transmission matrices of the first region [or the first arbitrary part of the waveguide (i.e. simulates the first line of the vector 'st')] using equation.4.2. The program then scans the number of terms of the second line of the vector (or the number of terms between two '[-1]' indicators). If it happens to be five, then the program identifies the part of the waveguide structure as the periodic part and applies the doubling and cascading procedure to obtain the reflection and transmission matrices of the periodic part. Then the program calculates the overall reflection and transmission matrices of the combined first arbitrary part and the periodic part by using the cascading algorithm. When the program sees only two terms in any line of the vector (fourth line in our case) it identifies as an arbitrary part and applies equation.4.2 to get the reflection and transmission matrices of that part. In a similar fashion the program calculates the spectral response of the waveguide structure as it moves from left to the right of the waveguide structure and every time it sees a periodic or aperiodic part on its way, it calculates the reflection and transmission matrices of that part independently and then combines with the available reflection and transmission matrices (that it has

calculated till now) using cascading algorithm to get the overall result. When the program sees only one term in the vector, it identifies it as the last region, calculates the reflection and transmission matrices of the last arbitrary region, combines with the available results and gives the end result.

Defining the refractive index matrix in a correct way is also important for the program to give correct results. The refractive indices of each region is written in a form of row as given below

$$
n = \begin{bmatrix}
1 & 1 & 1 & 1 & 1 & 3.6 & 3.6 & 3.6 & 3.4; \\
1 & 1 & 1 & 3.6 & 3.6 & 3.6 & 3.6 & 3.6 & 3.4; \\
1 & 1 & 1 & 1 & 3.6 & 3.6 & 3.6 & 3.6 & 3.4; \\
1 & 3.6 & 3.6 & 3.6 & 3.6 & 3.6 & 3.6 & 3.6 & 3.4; \\
1 & 1 & 3.6 & 3.6 & 3.6 & 3.6 & 3.6 & 3.6 & 3.4; \\
1 & 1 & 1 & 1 & 1 & 1 & 3.6 & 3.6 & 3.4; \\
1 & 1 & 1 & 1 & 1 & 1 & 1 & 3.6 & 3.4
\end{bmatrix}
$$

The first row corresponds to region one scanned vertically from the superstrate to the substrate of the waveguide structure. The second row corresponds to the the second region. In a similar way the last row of the matrix corresponds to the last region of the waveguide structure (region seven). Therefore the row indicates the change in the refractive index along the x-direction and the column represents the change in the refractive index along the z-direction.

The other predefined parameters that are required by the program are as follows

M1 : Used to assign the number of mesh point in the waveguide structure.

w1 : Used to assign the width of the waveguide structure.

lambda1 : Used to assign the working wavelength. If a single wavelength is given then the program returns the transmitted and reflected field as the output, else the modal reflectivity and transmissivity are given as the output.

TE : Used to define the field polarization. TE=1 for TE modes and TE=0 for TM modes.

n1 : Used to assign the refractive index contrast matrix of the waveguide structure discussed above.

st : Used to define the Waveguide structure discussed above.

npml_sub, npml_sup : Used to assign the number of mesh points in the substrate and superstrate PML region, respectively.

eta_sub, eta_sup : Used to assign the PML parameter η of the substrate and superstrate PML region, respectively.

order : Used to defines the order of the approximation for approximating the transverse second derivative operator. If order $= 3$, then the 3-point approximation is used. For order $= 5$ or 7, the program employs the 5-point or the 7-point approximation technique.

pml_profile : Holds the PML profile string that has to be used in the program. The program can accept any of the profiles given below

tan : respresents the tangent profile [i.e. $f(x_i) = \frac{\eta}{M_p} Tan(x_i)$].

sec : respresents the secant profile [i.e. $f(x_i) = \frac{\eta}{M_p} Sec(x_i)$].

sin : respresents the sine profile [i.e. $f(x_i) = \frac{\eta}{M_p} Sin(x_i)$].

exp : respresents the exponential profile [i.e. $f(x_i) = \frac{\eta}{M_p} e^{x_i}$].

sqr : respresents the square profile [i.e. $f(x_i) = \frac{\eta}{M_p}(x_i)^2$].

lin : respresents the linear profile [i.e. $f(x_i) = \frac{\eta}{M_p}(x_i)$].

unf : respresents the uniform profile [i.e. $f(x_i) = \frac{\eta}{M_p}$].

The terms η, x_i and M_p are defined in chapter 3. There are some limitation to our automated program. For instance, it does not account for periodic parts of the waveguide structure that has a periodicity of more than two regions, it cannot recognize the format of input other than the specified one.

4.7.1 Example

All the parameters mentioned above are assigned appropriately according to the specifications of the waveguide structure shown in figure 4.12. These parameters are written in a matlab file. The contents of the file are given below

lambda = 0.7 : 0.02 : 3;

TE = 1;

w = [1   0.2   0.1   0.05   0.2   0.3   0.15   0.15   3];

M = [10   7   4   3   7   10   6   6   20];

$$n = [\,1 \quad 1 \quad 1 \quad 1 \quad 1 \quad 3.6 \quad 3.6 \quad 3.6 \quad 3.4;$$
$$1 \quad 1 \quad 1 \quad 3.6 \quad 3.6 \quad 3.6 \quad 3.6 \quad 3.6 \quad 3.4;$$
$$1 \quad 1 \quad 1 \quad 1 \quad 3.6 \quad 3.6 \quad 3.6 \quad 3.6 \quad 3.4;$$
$$1 \quad 3.6 \quad 3.6 \quad 3.6 \quad 3.6 \quad 3.6 \quad 3.6 \quad 3.6 \quad 3.4;$$
$$1 \quad 1 \quad 3.6 \quad 3.6 \quad 3.6 \quad 3.6 \quad 3.6 \quad 3.6 \quad 3.4;$$
$$1 \quad 1 \quad 1 \quad 1 \quad 1 \quad 1 \quad 3.6 \quad 3.6 \quad 3.4;$$
$$1 \quad 1 \quad 1 \quad 1 \quad 1 \quad 1 \quad 1 \quad 3.6 \quad 3.4\,];$$

st = [1 [-1]

2 0.05 3 0.05 5 [-1]

4 0.02 5 0.02 4 [-1]

6 0.3 [-1]

7];

npml_sup = 4;

npml_sub = 8;

eta_sub = 0.35;

eta_sup = 0.5;

pml_profile = 'tan';

order = 5;

Range of the wavelengths used for obtaining the modal reflectivity is assigned to the variable 'lambda'. TE guided field is selected for analysis, therefore 'TE' is assigned 1. The width distribution or width of each layer in the x-direction

is assigned to 'w' in the form of a vector. The first and last term of the vector represents the width of the superstrate and substrate, respectively. 'M' holds the number of mesh points used for the analysis, in the form of a vector (a total of 73 points in the waveguide). The refractive index matrix is assigned to the variable 'n' and the vector defining the complete waveguide structure in the z-direction, is assigned to 'st'. The number of points used in the superstrate PML region is 4 (assigned to 'npml_sup') with η value of 0.35 (assigned to 'eta_sup'). Substrate PML region with 8 mesh points and η value of 0.5 is used. The profile selected for the PML is the tangent profile ('profile'='tan') with 5-point approximation ('order'= 5). The file is named 'example'. The file is then called by the automated program (named 'mainap') in the following format, in the command window of Matlab.

mainap('example')

The effective implementation of the automated program is checked by the verification tool (the layer by layer method). The results from both, the automated program and the layer by layer method, are shown in fig.4.13. It can be seen that the automated program results overlaps with the layer by layer method results, thus establishing the effectiveness of our implementation. The layer by layer method took 5 seconds per wavelength and the automated program also took 5 seconds per wavelength. However, the automated program becomes much more efficient than the layer by layer method when the number of periods in the periodic part of the structure is relatively large. This is demonstrated in fig.4.14, where the same complex structure (of fig.4.12) is simulated with different number of periods in the
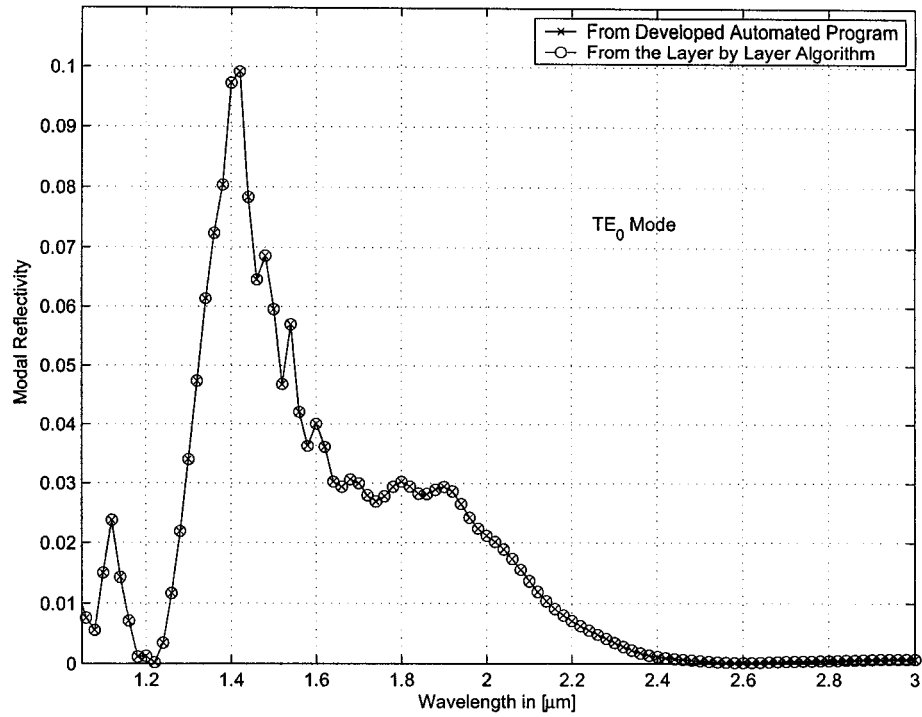
Figure 4.13: Fundamental TE Modal Reflectivity of the Guided wave grating structure shown in fig.4.12
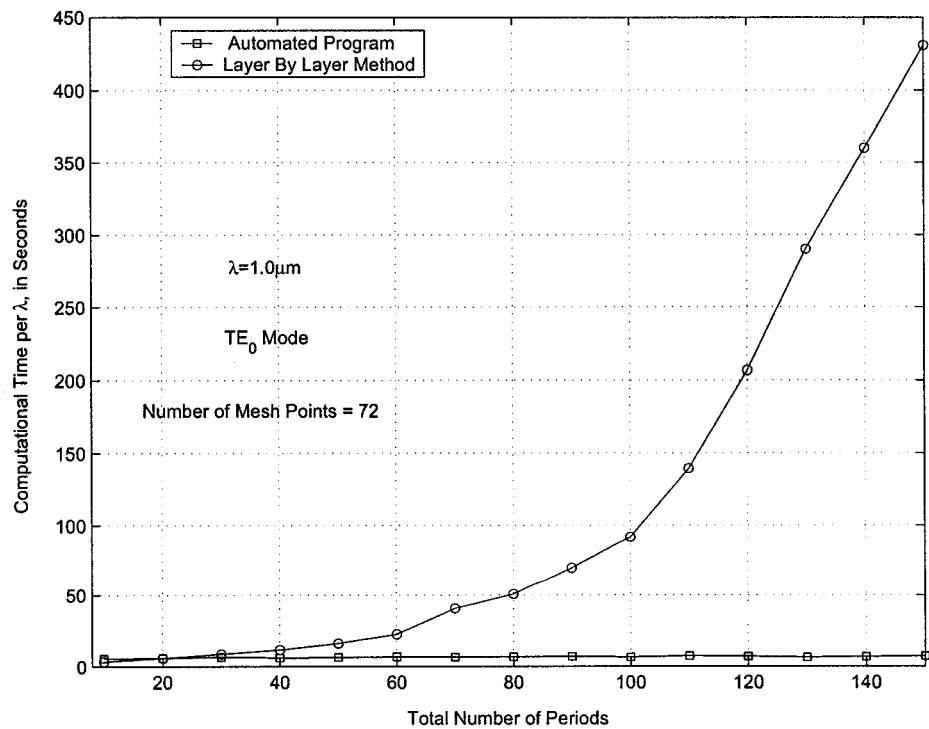
Figure 4.14: Time required per wavelength of the structure shown in fig.4.12 versus the total number of periods in the periodic part of the structure.

periodic part of the structure. The number of periods in both the periodic regions of the structure is assumed to be same. The TE_0 modal reflectivity is calculated at $\lambda = 1.0 \mu m$ with 72 mesh points within the waveguide. The time required per wavelength is plotted on the vertical axis with the total number of periods shown on the horizontal axis (P4 machine with 256MB RAM running under Windows XP Operating System, has been used). It is seen that, with increase in the number of periods in the periodic part of the waveguide, the time required by the automated program is much less than the time required by the layer by layer method. The time taken for the automated program to simulate 150 periods in the structure is only 7.18 seconds per wavelength whereas the layer by layer method has done the same problem in 430.76 seconds. This demonstrates the efficiency of our automated program.

Chapter 5

Analysis of Guided Wave Grating Structure

5.1 Introduction

The waveguide gratings are of considerable importance in Integrated Optics. They are used as wavelength filters, couplers etc. Active research is being done for the analysis and application of these devices. The concept and evolution of photonic bandgap and photonic crystals and their realization and analysis can be considered as extensions to grating structures. Gratings can be broadly classified into shallow and deep gratings. Shallow gratings are the gratings in which the depth of the grooves is assumed to be less than 10% of the width of the core . Gratings with more than 10% of the core width are classified as deep waveguide gratings. The present thesis focusses on deep waveguide gratings.

In this chapter, a guided wave grating structure is introduced and analyzed in detail. The fundamental mode spectral response of the structure is analyzed using the Automated Method of Lines program developed earlier using the five point approximation. A PML layer is used on both sides of the computational window utilizing a graded loss profile. The graded PML loss profile results in high PML efficiency, which results in reduced reflectivity from the PML with relatively small number of points in the PML layer.

5.2   The Deep Grating Structure

The structure shown in fig.5.1 will be analyzed. This waveguide grating is known to exhibit wavelength selective filtering due to the multiple reflections from each discontinuity along the waveguide grating. The core thickness of the structure is chosen so that only the fundamental TE mode is supported. The depth of the waveguide gratings is chosen to be infinite. Numerically, this is implemented by allowing the groove depth h to extend to the bottom of the computational window (i.e. $h = 8.3\mu m$ or relatively infinity). In practical devices the bottom wall of the groove penetrates deep into the substrate. Later in this thesis, the effect of the groove depth on the spectral response of the grating structure will also be analyzed by considering the groove depth to be finite. A total of 75 mesh points is used in the computational window excluding the PML. A graded tangent loss profile for the PML with 6 points on the top (superstrate PML layer) with $\eta = 1$, and 10 points at
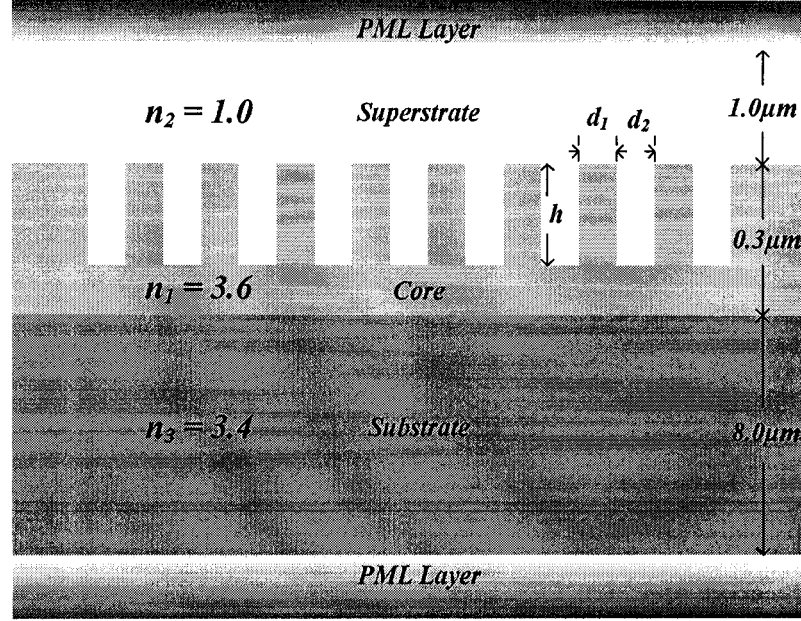
Figure 5.1: Guided Wave Grating Structure with half grating period, $d_1 = d_2 = 0.175854778\mu m$, h, the groove depth, is variable, taking values from 0 to 8.3 μm, and N is the number of Gratings.

the bottom (substrate PML layer) with $\eta = 0.35$ is used. The structure is designed to be single mode at the resonant wavelength of $\lambda_c = 1.55\mu m$. This wavelength approximately satisfies the Bragg's formula

$$n_{1eff}d_1 + n_{2eff}d_2 \simeq \lambda_c/2 \tag{5.1}$$

where n_{1eff} and n_{2eff} are the effective indices of the TE_0 mode of the waveguide and the air (hole) regions, respectively. d_1 and d_2 are the widths of waveguide and air regions, respectively. In the present case, we have chosen $d_1 = d_2 = T/2$ for simplicity, later we will show the effect of changing d_1 and d_2 on the spectral response of the grating structure. Substituting all the required values in the above equation, one can obtain the half grating period $T/2$ (n_{2eff} is taken as 1 in this

case).

The Bragg's formula is not accurate in this case because it is applicable to only grating structures with shallow grooves. Therefore, the center wavelength of the structure is expected to differ from the designed center wavelength.

The width of the substrate is selected large enough, based on the highest wavelength to be scanned, so that the guided field strength at the inner walls of the PML is very small (on the order of 10^{-5}) compared to its value at the core-substrate interface. This is done in order to avoid any interaction between the guided mode and the PML layer. In a similar fashion, the width of the superstrate is also taken to be sufficiently large.

5.2.1   Effect of the Number of Grating Periods

The fundamental TE mode is excited on the left of the structure shown in fig.5.1 and the spectral response is calculated for different number of periods N. The spectral response of the deep grating structure for $N=$ 2, 8 and 30 grating periods are shown in figs.5.2, 5.3 and 5.4, respectively. Three dimensional views of the reflectivity spectrum, transmissivity spectrum and fraction of radiated power, of the same structure for different number of periods are respectively shown in figs.5.5, 5.6 and 5.7.

By comparing figs.5.2, 5.3 and 5.4, it is observed that there is a large change in the shape of the main lobe for the first few periods. The main lobe becomes
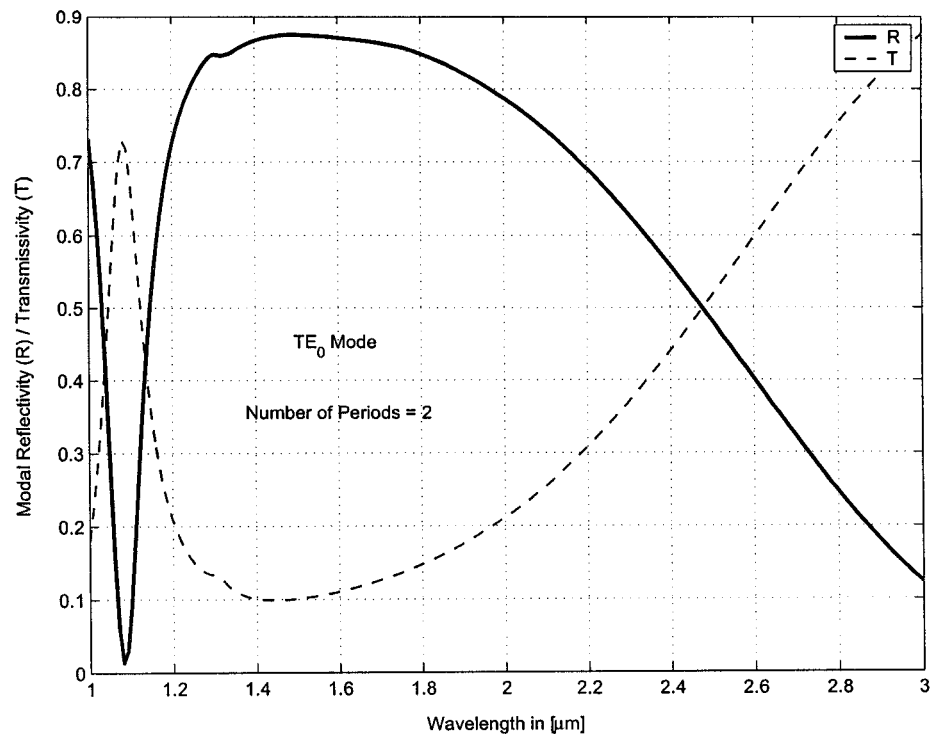
Figure 5.2: Spectral Response of the Deep Grating Structure with 2 grating periods.
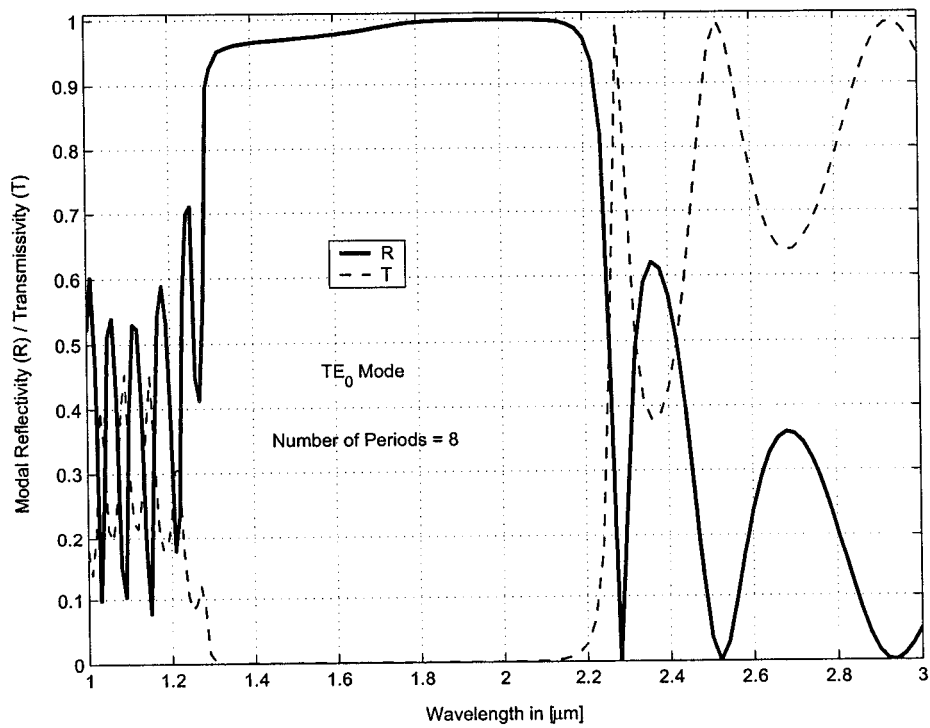
Figure 5.3: Spectral Response of the Deep Grating Structure with 8 grating periods.
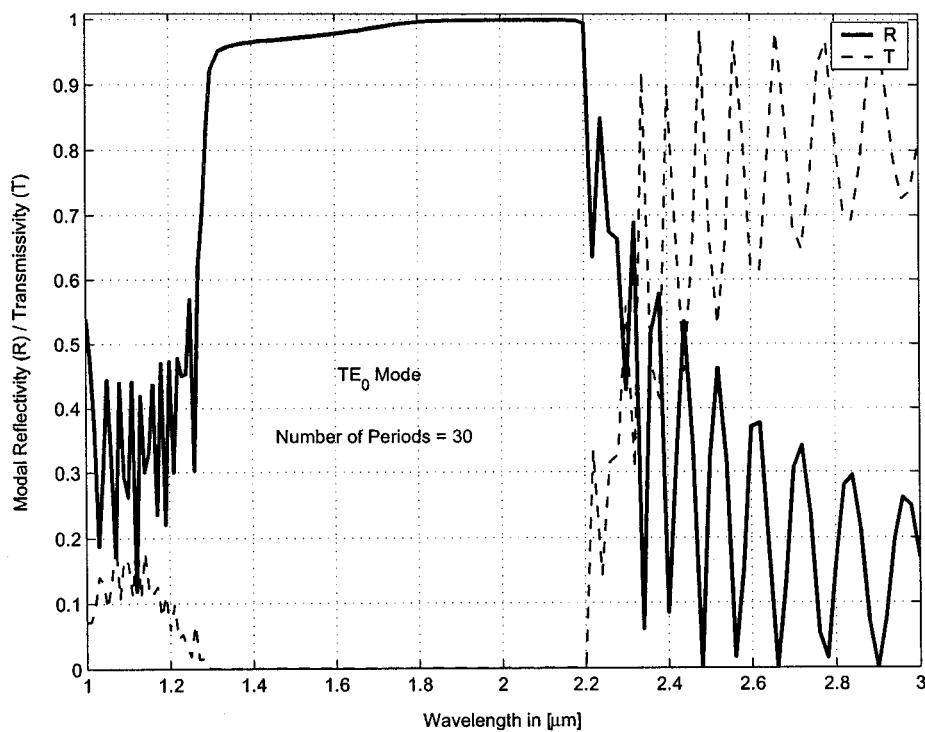
Figure 5.4: Spectral Response of the Deep Grating Structure with 30 grating periods.
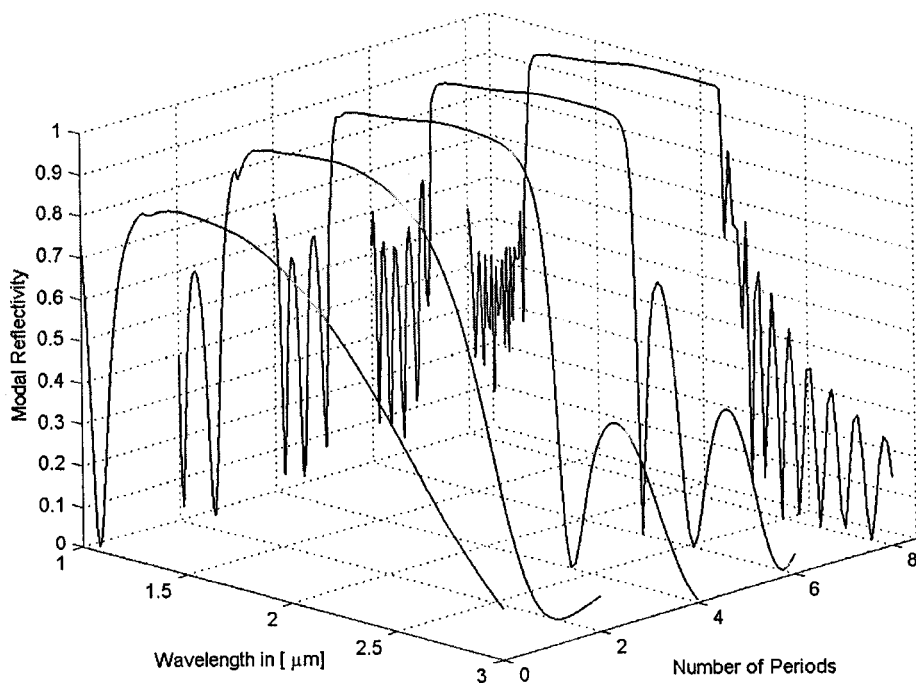
Figure 5.5: A Three Dimensional View of the Fundamental TE Mode Reflectivity Spectrum of a Deep Grating Structure. The number of grating periods are displaced successively by '2' on the z-axis (0 to 8 corresponds to N=2,3,5,8 and 30, respectively).
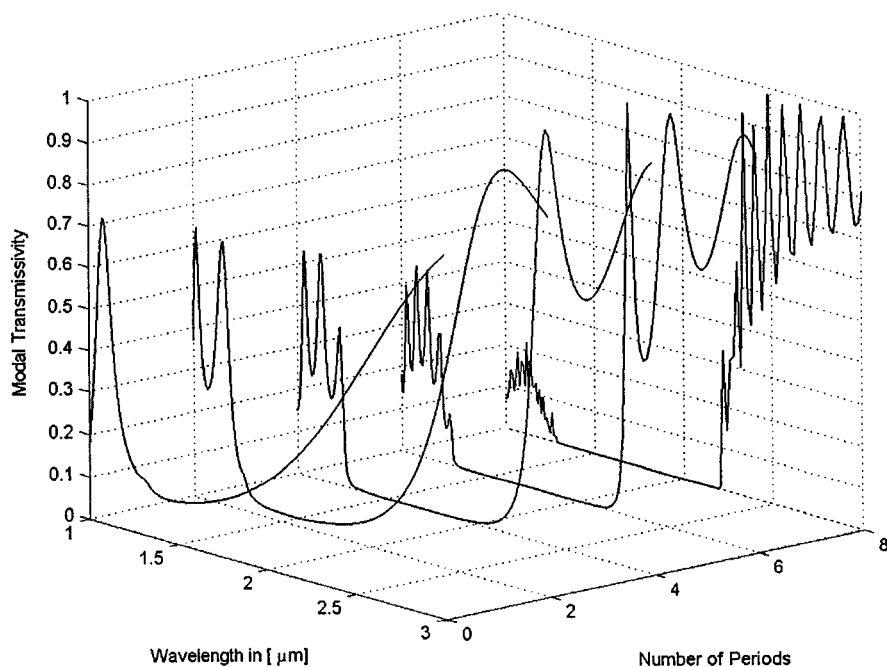
Figure 5.6: A Three Dimensional View of the Fundamental TE Mode Transmissivity Spectrum of a Deep Grating Structure. The number of grating periods are displaced successively by '2' on the z-axis (0 to 8 corresponds to N=2,3,5,8 and 30, respectively).
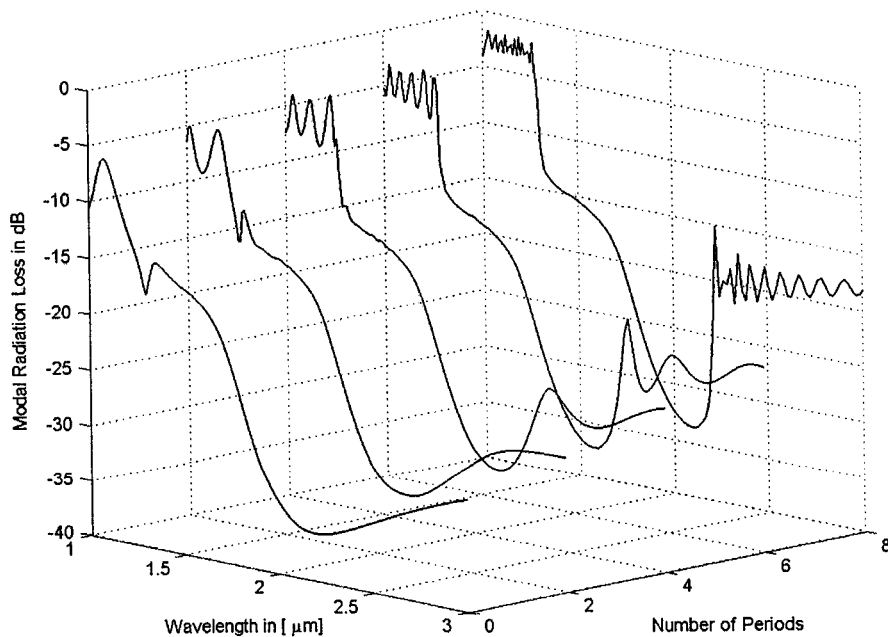
Figure 5.7: A Three Dimensional View of the Fundamental TE Mode Radiation Spectrum of a Deep Grating Structure. The number of grating periods are displaced successively by '2' on the z-axis (0 to 8 corresponds to N=2,3,5,8 and 30, respectively).

steady and the peak reflectivity increases (and peak transmissivity decreases) when the number of periods increases. In addition, the width of the main lobe tends to decrease as N increases (nearly a flat response as N increases). Figs.5.5, 5.6 can be used to better visualize the effect of the increasing N. As N increases, the width of the main lobe becomes narrower and when exceeds 8 periods, it remains the same. Any increase in the number of periods beyond this value has a small effect on the main lobe. However, as N increases, the side lobes become more dense and the radiated power (out side the main lobe) increases (see fig.5.7).

Figs.5.8 and 5.9 respectively show the reflectivity and transmissivity spectrum variation with N at five different wavelengths selected to be within the main lobe. These figures also provide the same conclusion that there is no transmission beyond approximately 8 periods. The band of frequencies where there is no transmission (transmissivity=0) is called a bandgap and the structures exhibiting such property are called bandgap structures. The bandgap depends on the index contrast, depth of the grating and the width of the grating. In the later analysis of the deep grating structure, the number of grating periods will be fixed to 8 periods. This choice is made because the bandgap remains constant afterwards (increasing N beyond 8).

5.2.2   Effect of the Filling Factor

The choice of d_1 and d_2 effects the band gap to a very large extent in a deep grating structure. In this section the effect of changing d_1 and d_2 for the same structure (i.e.
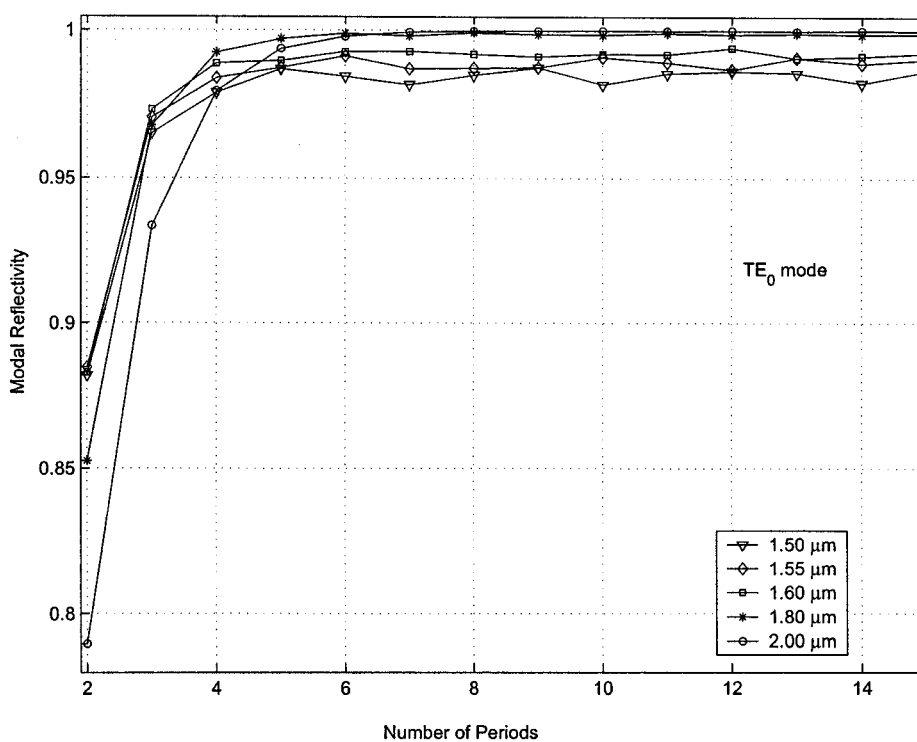
Figure 5.8: Fundamental Mode Reflectivity Verses the Number of Periods at five different wavelengths.
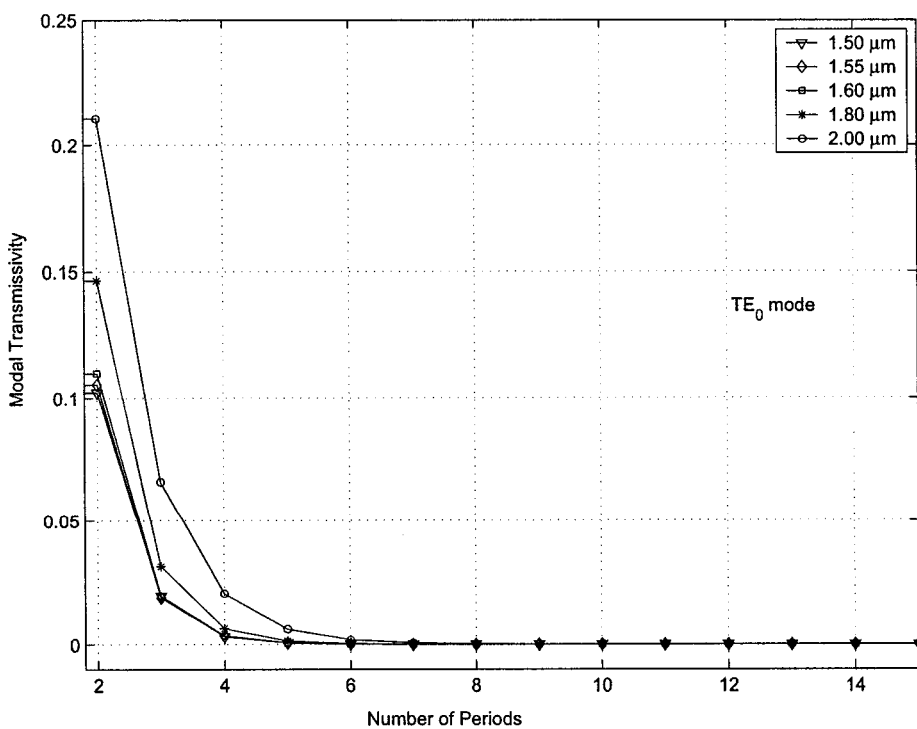
Figure 5.9: Fundamental Mode Transmissivity Verses the Number of Periods at five different wavelengths.

fig.5.1) is analyzed. A new parameter known as the filing factor f is introduced. This parameter is an important parameter for such a waveguide and characterizes its behavior (i.e. the formation of bandgap). It is defined as

$$f = \frac{Width\ of\ Air\ Region}{Grating\ Period} = \frac{d_2}{d_1 + d_2} = \frac{d_2}{T} \qquad (5.2)$$

where d_1 and d_2 are defined at the beginning of this chapter. In the previous analysis of the effect of the number of grating periods, we assumed $d_1 = d_2$, which corresponds to a filling factor of $f=0.5\%$. In this section the previously studied deep grating structure with 8 periods is used in the analysis.

Refereing to figs.5.3, 5.10 and 5.11, there is a large change in the width of the main lobe with the change in the filling factor. Figs.5.10, 5.3 and 5.11 correspond to filling factors of $f = 0.25$, 0.5 and 0.65, respectively. The reflectivity curve become more asymmetric when f is increased. The reflection from each period increases with f due to the increase in the air gap width, and hence the peak reflectivity increases causing the transmissivity to decrease. A better visualization of the effect of the filling factor on the spectral response can be seen from figs.5.12, 5.13 and 5.14. When f increases, the main lobe shifts towards the lower wavelengths and the peak reflectivity increases. Thus, the center wavelength also shifts towards the lower wavelengths. Both inside and outside the main lobe, towards the lower wavelength, the fraction of radiated power is observed to be very high when compared to the fraction of the radiated power at the higher wavelengths (see fig.5.14). The widths of the main lobe (bandgap) and center wavelength, for different filling factors are
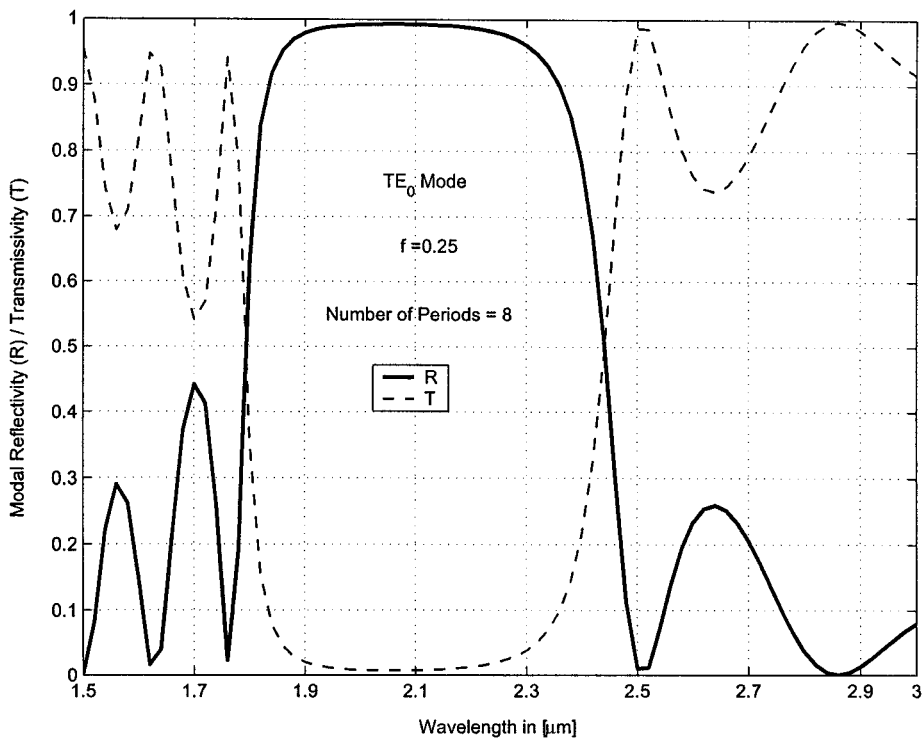
Figure 5.10: Spectral Response of a Deep Waveguide Grating with f=0.25.
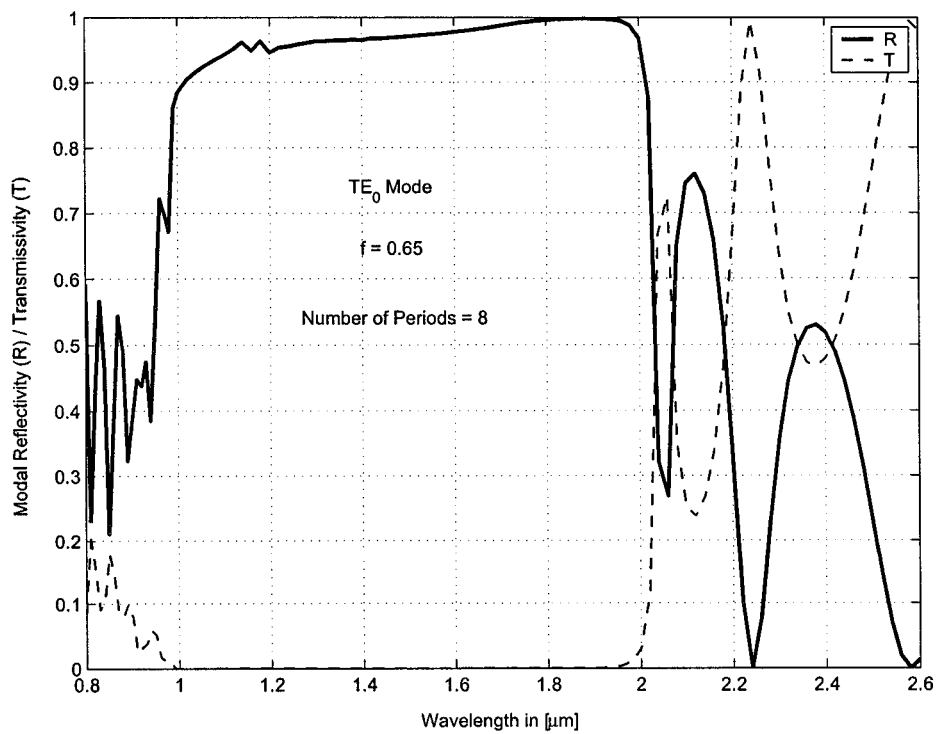
Figure 5.11: Spectral Response of a Deep Waveguide Grating with f=0.65.
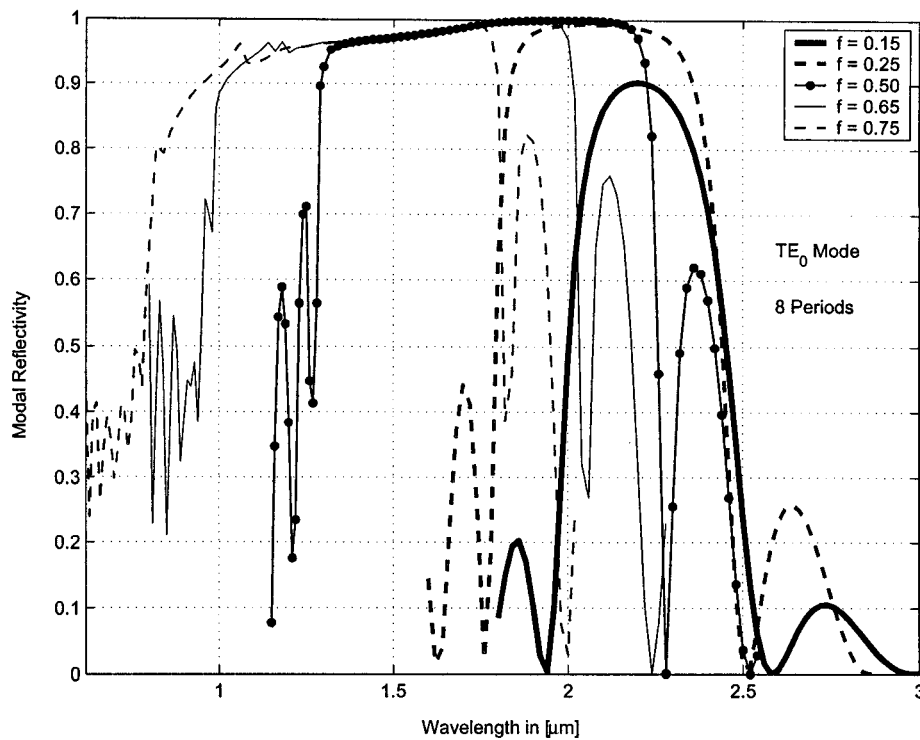
Figure 5.12: Fundamental TE Mode Reflectivity of the a Deep Waveguide Grating for different Filling Factors.
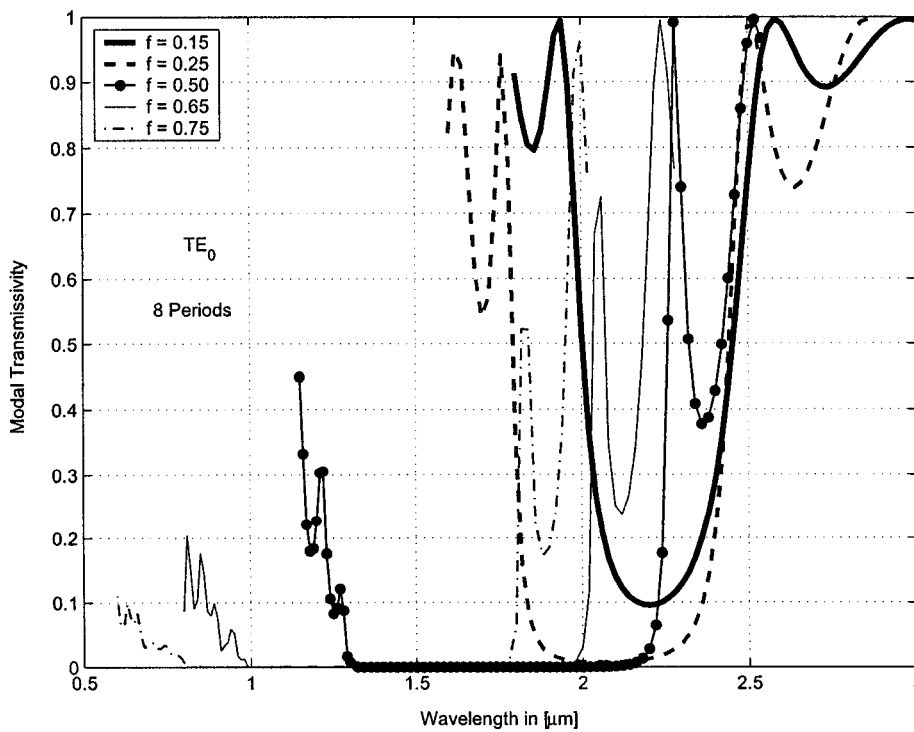
Figure 5.13: Fundamental TE Mode Transmissivity of the a Deep Waveguide Grating for different Filling Factors.
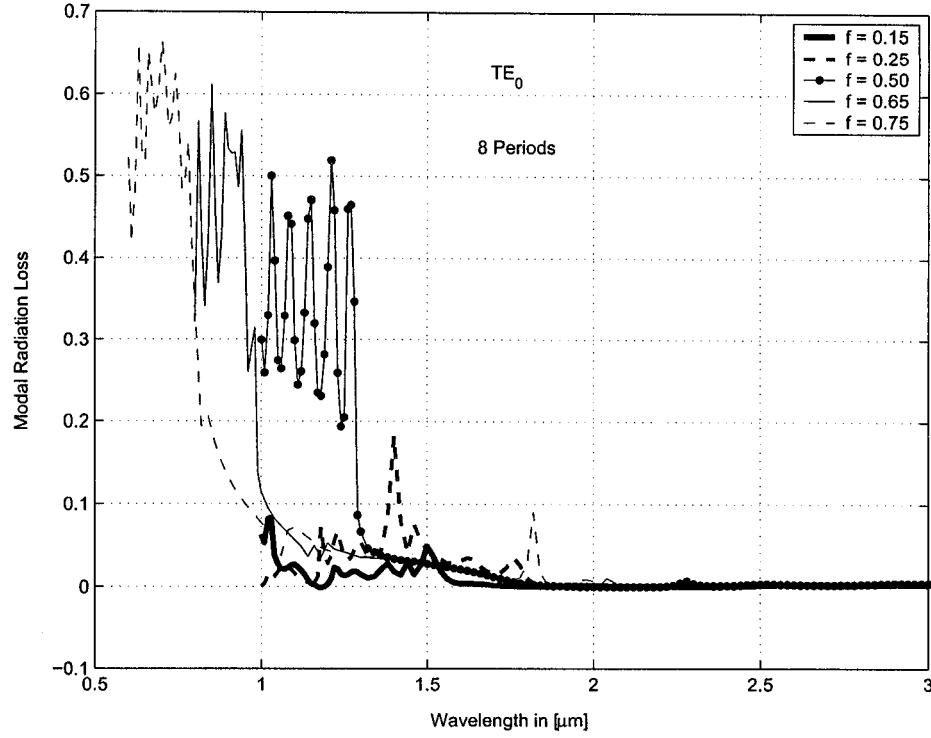
Figure 5.14: Radiation Loss of the a Deep Waveguide Grating for different Filling Factors.

tabulated in table 5.1 below

Filling Factor f	Spectral Width $\triangle\lambda(\mu m)$	Center Wavelength $\lambda_c(\mu m)$	Fractional Spectral Width $\frac{\triangle\lambda}{\lambda_c}$
0.15	0.48	2.26	0.2124
0.25	0.65	2.14	0.3037
0.50	0.97	1.76	0.5511
0.65	1.05	1.48	0.7094
0.75	1.06	1.30	0.8154

Table 5.1: Spectral Width of the Deep Grating Structure for different Filling Factors

From table 5.1 it is clear that when f increases, both the band gap width and the fractional spectral width $\frac{\triangle\lambda}{\lambda_c}$ increases.

5.2.3 Effect of the Groove Depth

In this section, we will study the effect of the groove depth 'h', of the guided wave structure (fig.5.1) on the spectral response of the structure. The groove depth h takes values ranging from $0\mu m$ to ∞. All simulations are done for the fundamental TE mode excited on the left of the structure. The spectral response for groove depths of $h = 2.77w$ (277%), $8.3w$ (830%), $13.83w$ (1383%) and $19.36w$ (1936%), calculated based on waveguide core width, are plotted in figs.5.15 to 5.18, respectively. As the grating depth is increased, the main lobe becomes wider and the peak reflectivity increases. This stems from the fact that, as the depth increases, the field encounters an increasing effective index discontinuity (i.e. n_{1eff}/n_{2eff} value increases) and hence high reflection occur. The main lobe becomes wider as h increases. A good view of the development of the band gap can be obtained from figs.5.19 and 5.20.

Figs.5.21 and 5.22 show the modal reflectivity and transmissivity as a function of the grating depth at six different wavelengths. The wavelengths are selected from within the main lobe (these wavelengths covers the complete main lobe). It is seen that, lower wavelengths acquire maximum reflectivity at $14w$ (1400%) groove depth where as the higher wavelengths acquire peak reflectivity of one, when the groove depth is infinity. Similar behavior is observed in the transmissivity figure where the lower wavelengths reaches zero transmissivity at a groove depth of $1.2w$ (120%) and higher wavelengths acquire zero transmissivity at infinite groove depth.

The effect of the groove depth on the radiation loss for $h = 2.77w$ (277%), $8.3w$
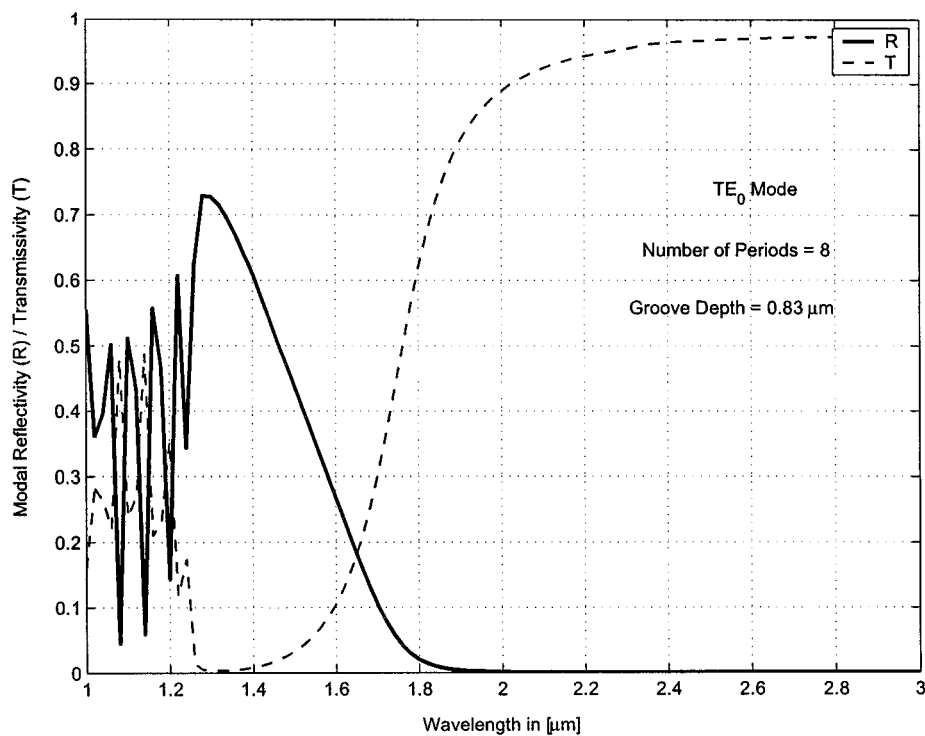
Figure 5.15: Spectral Response of the Grating Structure with a Groove Depth of $2.77w$.
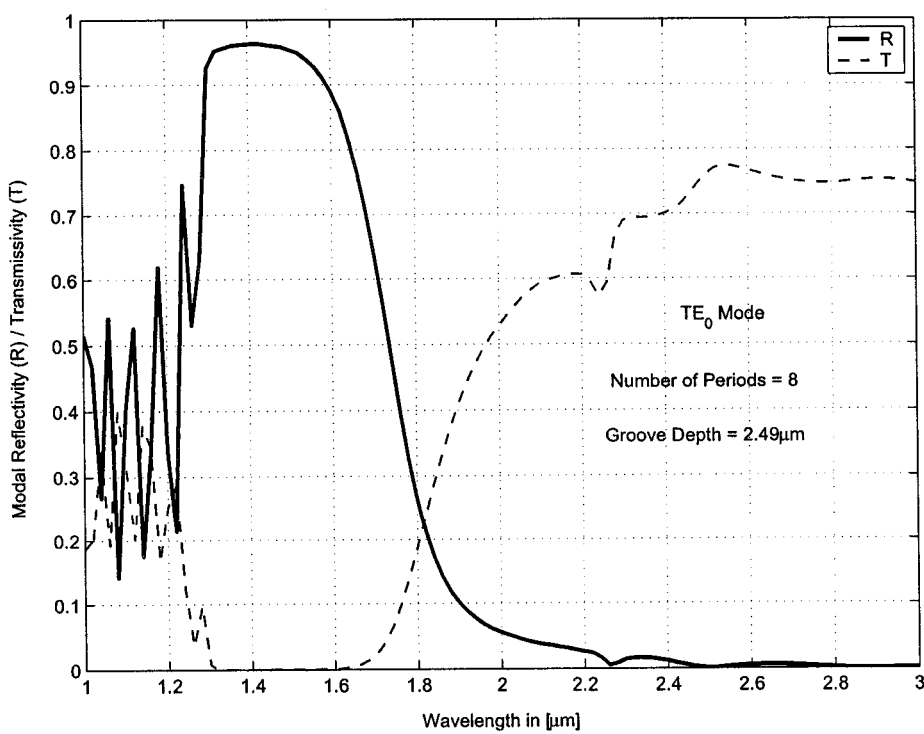
Figure 5.16: Spectral Response of the Grating Structure with a Groove Depth of $8.30w$.
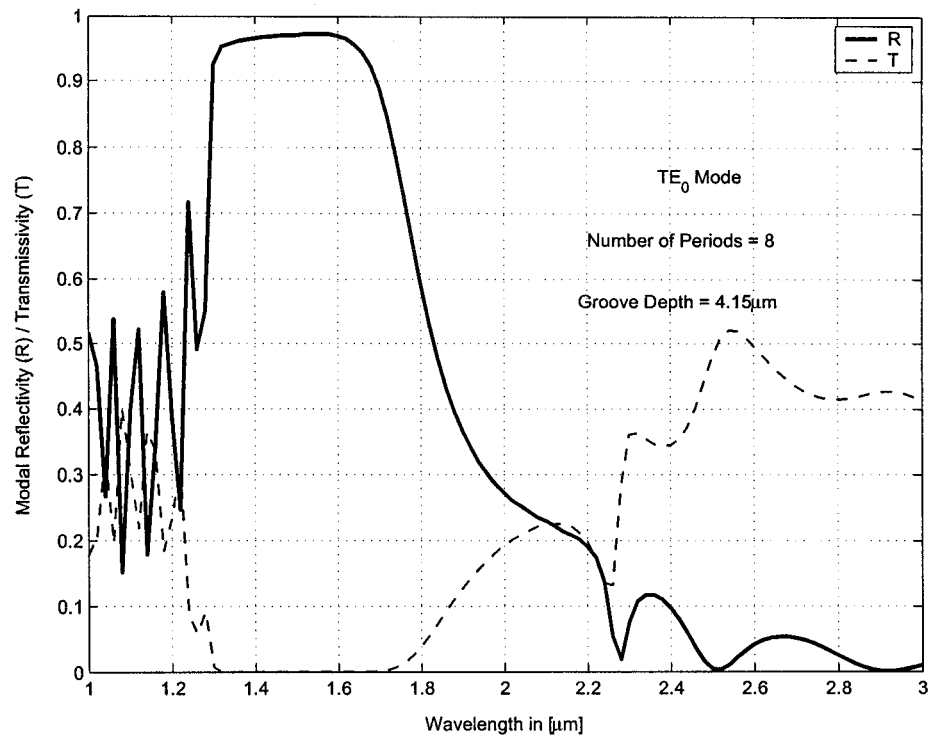
Figure 5.17: Spectral Response of the Grating Structure with a Groove Depth of 13.83w.
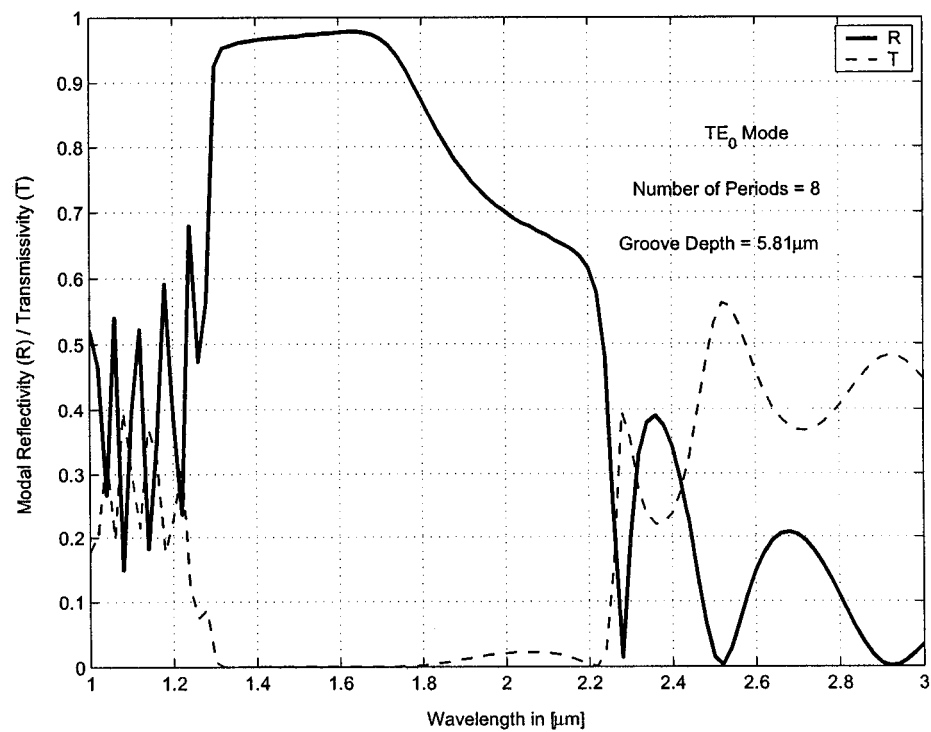
Figure 5.18: Spectral Response of the Grating Structure with a Groove Depth of 19.36w.
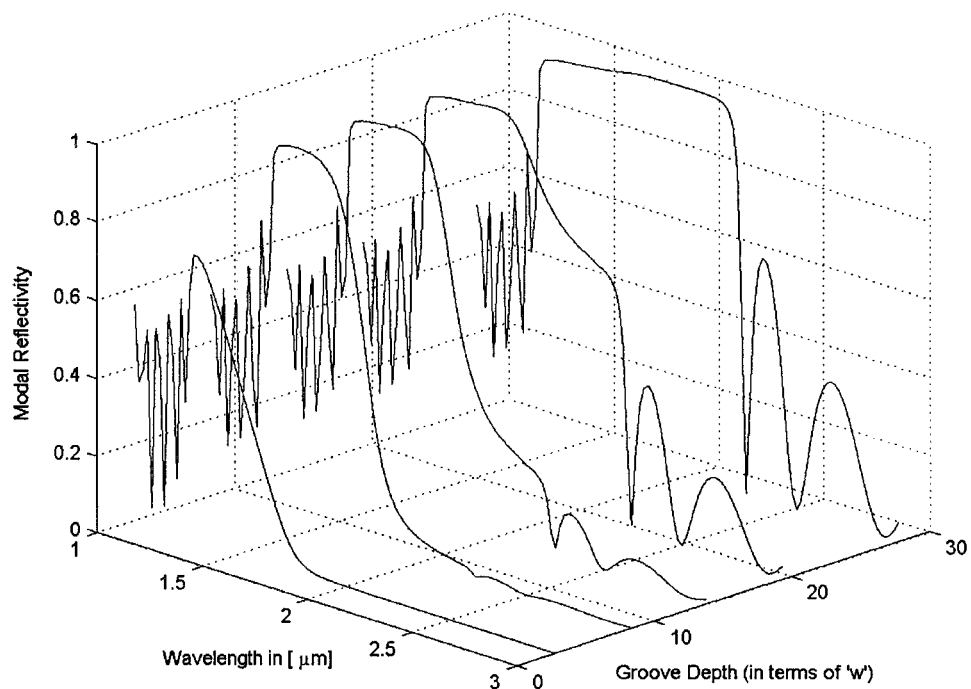
Figure 5.19: Fundamental TE Mode Reflectivity of of the Grating Structure at different Groove Depths.
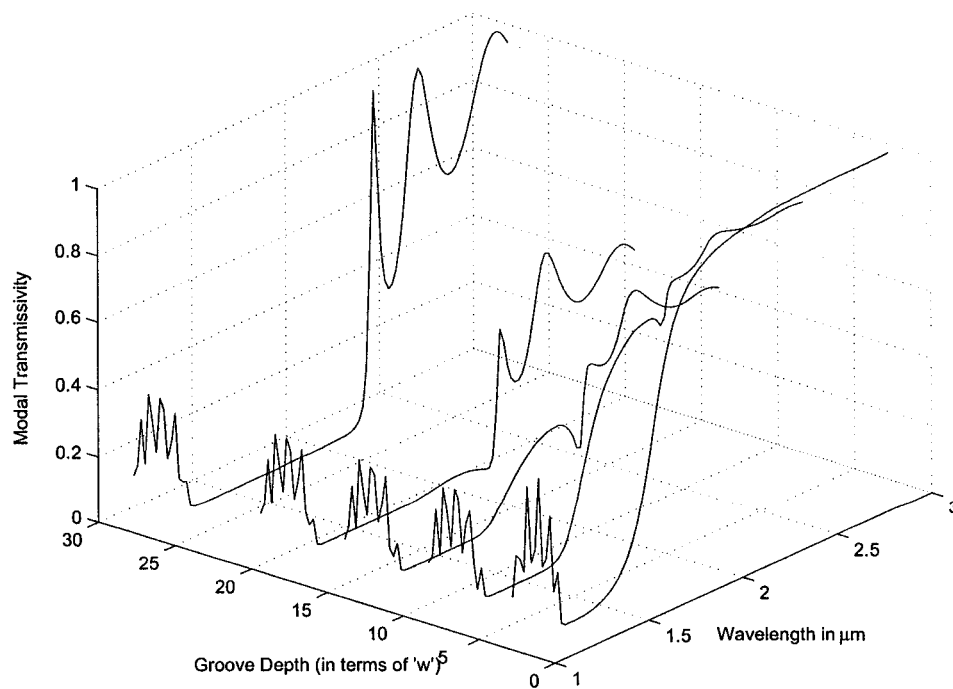
Figure 5.20: Fundamental TE Mode Transmissivity of of the Grating Structure at different Groove Depths.
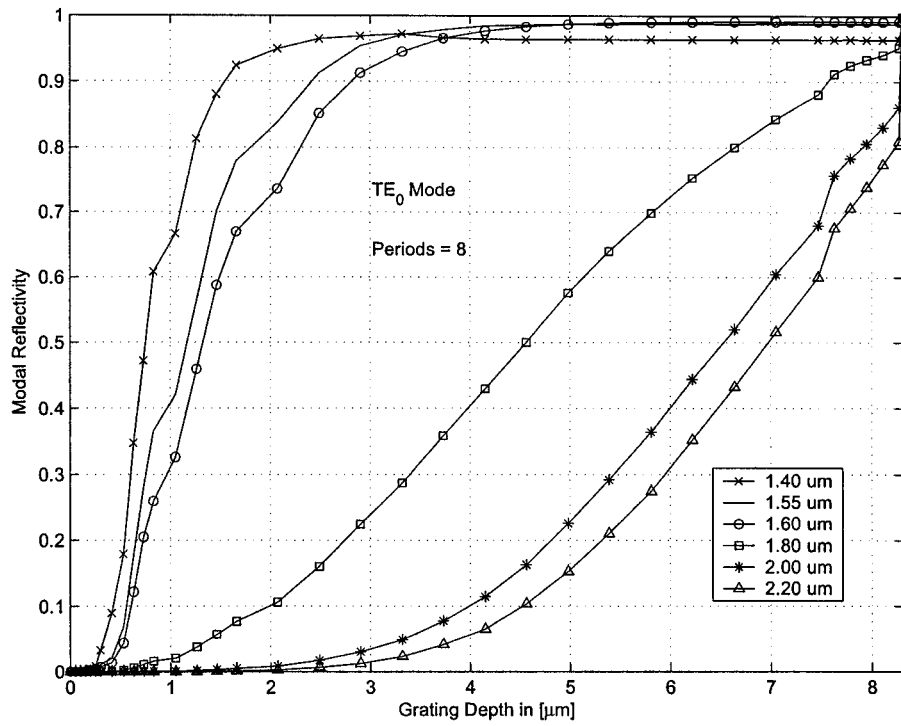
Figure 5.21: Fundamental TE Mode Reflectivity of the Waveguide Gratings at six different wavelengths.
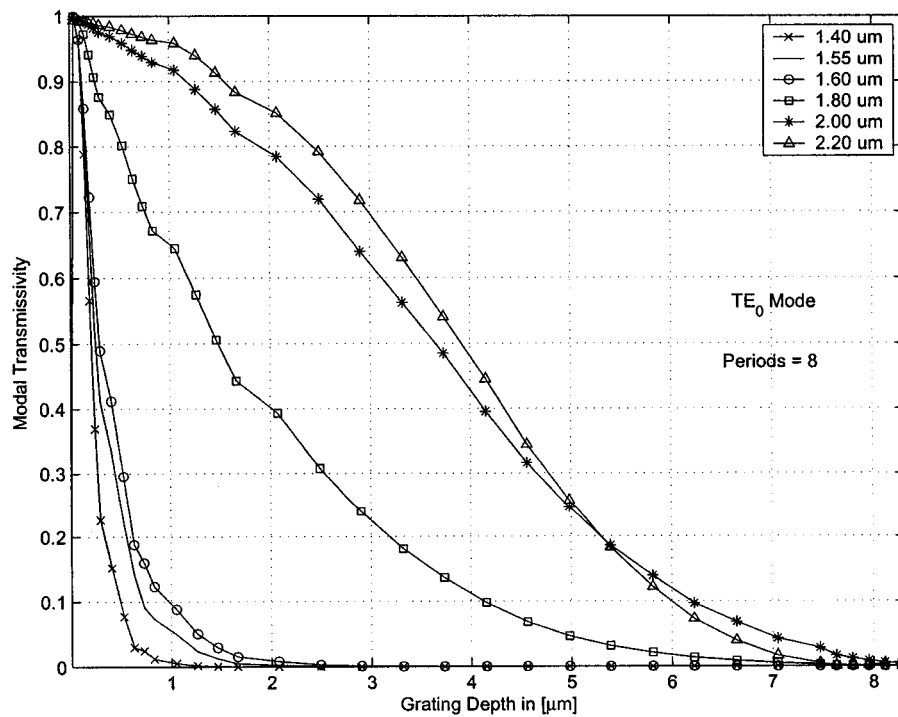
Figure 5.22: Fundamental TE Mode Transmissivity of the Waveguide Gratings at six different wavelengths.
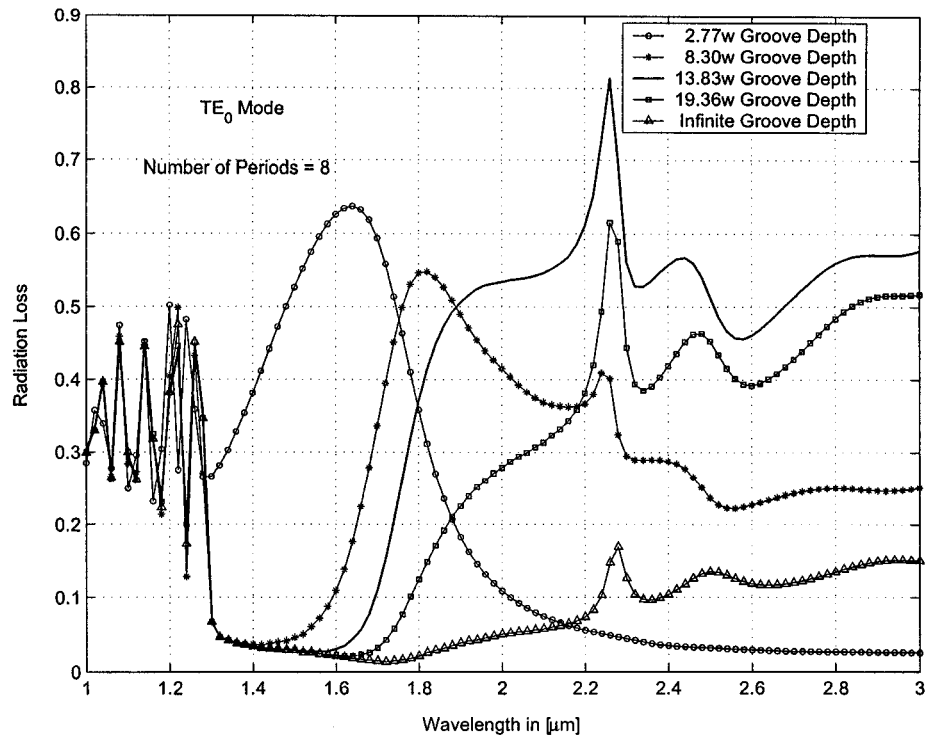
Figure 5.23: The Radiation loss of the Grating Structure at different Groove Depths.

(830%), 13.83w (1383%) and 19.36w (1936%), is illustrated in fig.5.23. It can be observed that the radiation loss decreases within the bandgap as h is increased. A good understanding and visualization of the above mentioned fact can be obtained from figs.5.24 to 5.25.

5.2.4 TM Guided Mode

The analysis of the deep grating structure discussed in this chapter was based on the fundamental TE mode case. The same structure is now analyzed when excited by the fundamental TM modal field on the left of the structure. The parameters chosen
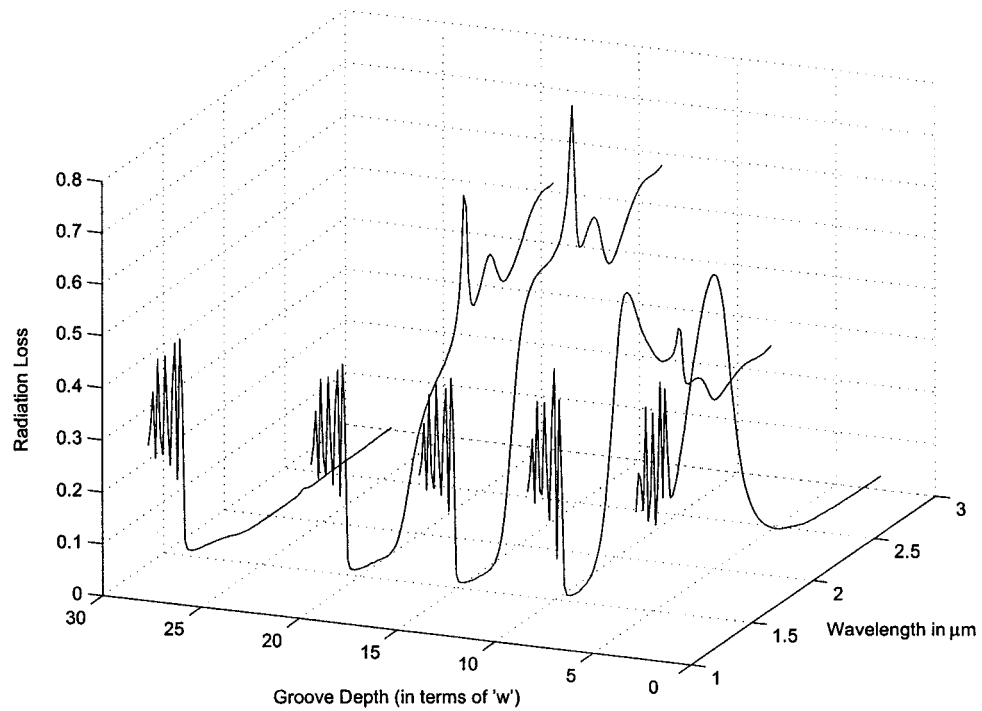
Figure 5.24: A Three Dimensional view of the Radiation loss of the Grating Structure at different Groove Depths.
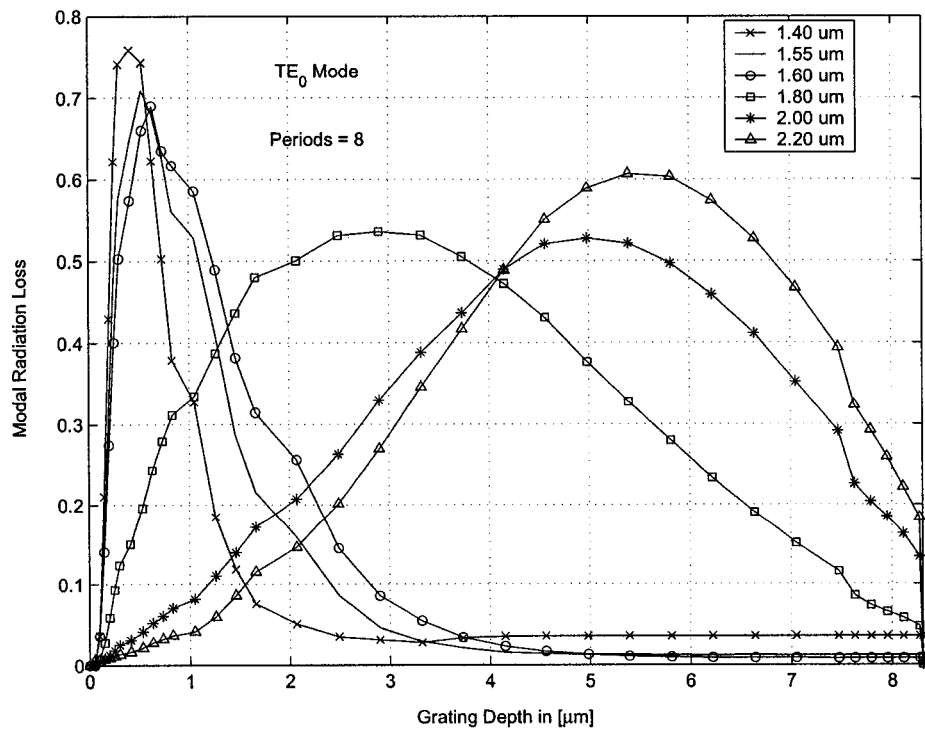
Figure 5.25: Fundamental TE Mode Radiation Loss of the Waveguide Gratings at six different wavelengths.
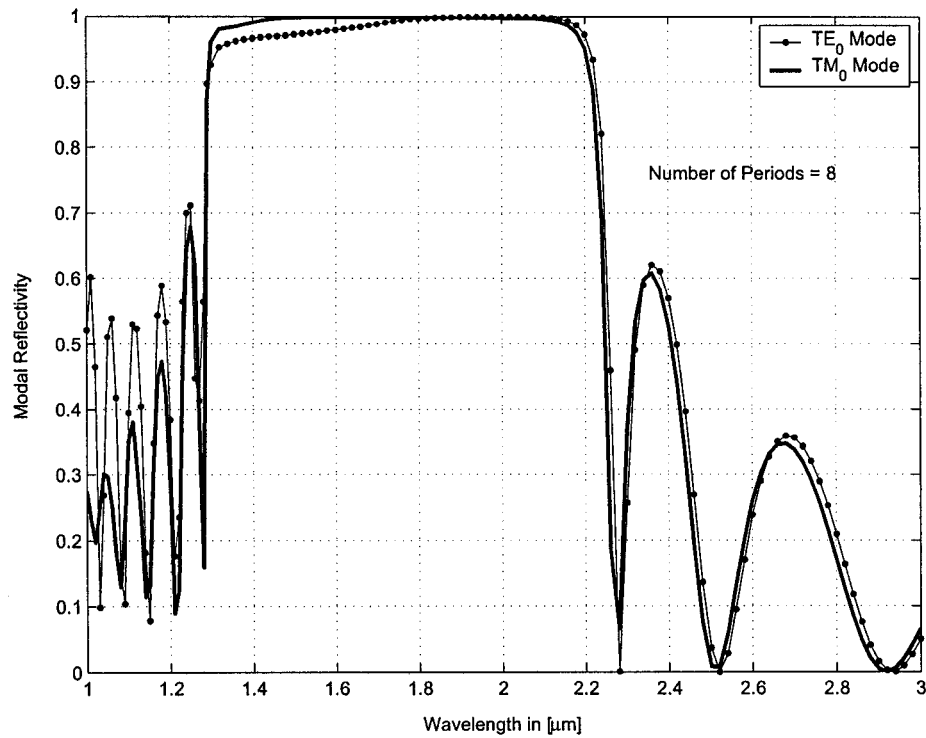
Figure 5.26: Fundamental Mode Reflectivity of the Infinitely Deep Grating Structure.

in this case are the same, as used previously (i.e. with 8 grating periods, groove depth $h = \infty$ and $f = 0.5$). The modal reflectivity, transmissivity and fraction of radiated power are shown in figs.5.26, 5.27 and 5.28, respectively. Comparison with the TE case is done in the same figures. The reflectivity spectrum is more symmetric in the TM case. It appears that the structure's behavior is similar for both TE and TM modes. An increase in the radiated power is observed in the TM case, at higher wavelengths but at lower wavelengths the radiated power is much less than the TE case (i.e. the radiated power is less than TE within the bandgap). In the later work to follow, the analysis of guided wave grating structures will be limited only to TE
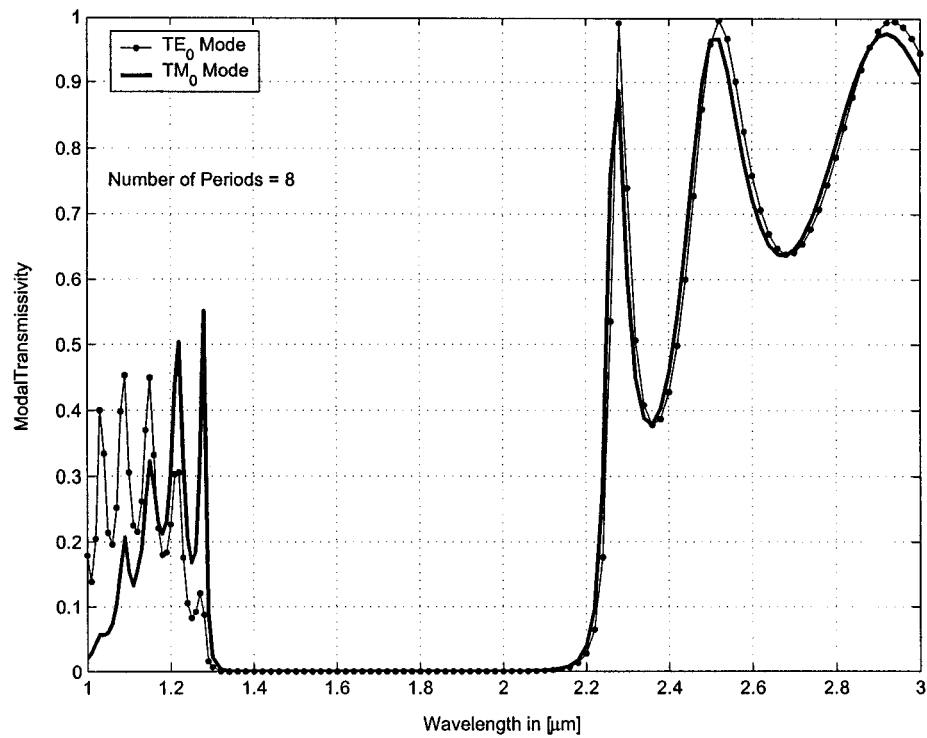
Figure 5.27: Fundamental Mode Transmissivity of the Infinitely Deep Grating Structure.
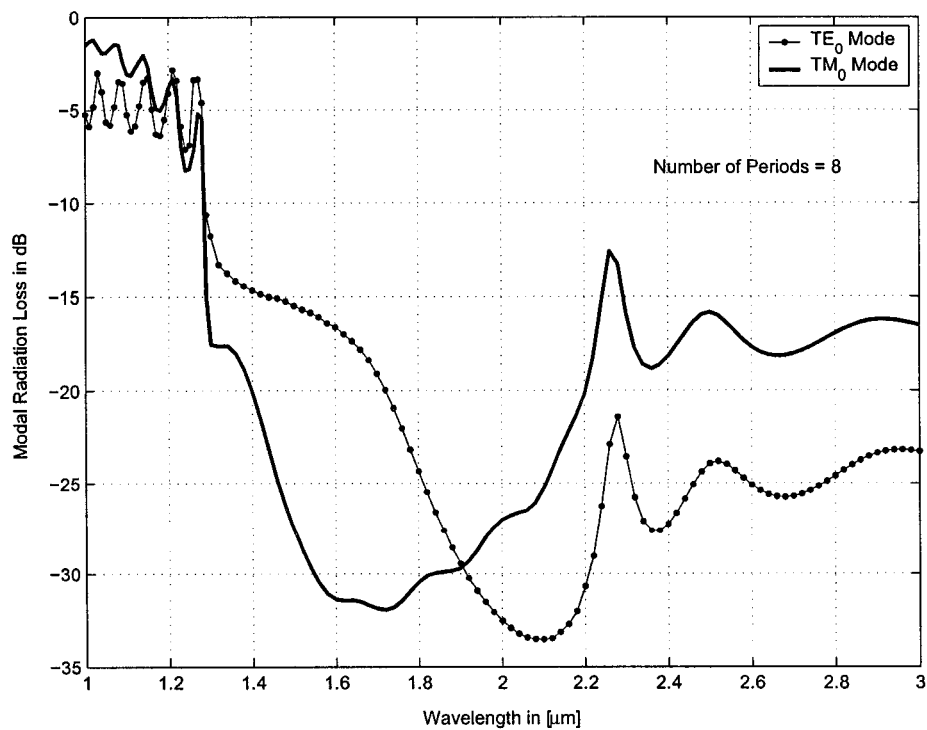
Figure 5.28: Fundamental Mode Radiation Loss of the Infinitely Deep Grating Structure.

modes.

5.3   Discussion

A guided-wave deep grating structure is studied in this chapter and the effect of the number of grating periods, the filling factor and the groove depth, on the spectral response of the structure was analyzed. It is seen that, with eight grating period, a bandgap between the wavelength range of 1.3 μm and 2.2 μm is formed, in which there is no transmission of electromagnetic wave. It has been shown that, an increase in the filling factor shifts the bandgap towards lower wavelengths and that the main lobe becomes wider. It is also seen that, with an infinite groove depth, the bandgap is formed with minimal radiation loss whereas for a finite groove depth, leakage within the bandgap occurs. The results of the TM guided mode are similar to that of the TE guided mode, for the deep grating structure that has been considered in this chapter.

Chapter 6

Analysis of Symmetrical Coupled Grating Structure

6.1   Introduction

In the previous chapter, a finite length periodic deep grating structure has been studied with reasonable depth. In the present chapter, two finite-length periodic deep grating structures are coupled together to form a microcavity (see fig.6.1). Similar kind of structures have been reported in literature [58, 59, 60]. We will study the spectral response of these coupled structures. As will be seen later, one feature of extreme importance is the appearance of the narrow transmission band with in the stop band of the structure. This narrow transmission band may be utilized in the Wavelength division multiplexing (WDM) optical systems, as a channel drop filter.
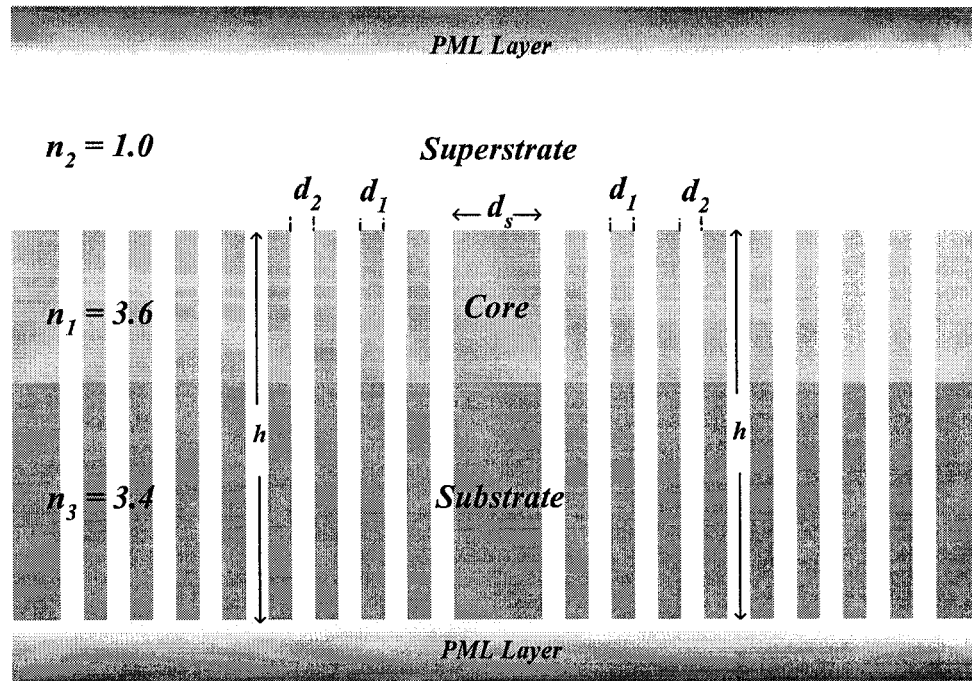
Figure 6.1: Symmetrical Coupled Grating Structure. $d_1 = 0.75T$, $d_2 = 0.25T$. T is the period of grating equals $0.2495\mu m$. $h \to \infty$, d_s is the length of the microcavity. $N = 16$ and core width $w = 0.3\mu m$.

6.2 The Symmetrical Coupled Guided Wave Grating Structure

Optical filters with very high selectivity are becoming key elements in wavelength division multiplexing (WDM) optical systems. Such filters can be obtained by coupling the deep grating structures studied in the previous chapter, by a uniform region of length d_s, forming an optical resonant microcavity (see fig.6.1). It will be shown that, by controlling the length of the microcavity (also called as defect layer), it is possible to obtain a transmission resonance in the bandgap.

The coupled structure consists of 16 periods with a microcavity half way through

it, with infinitely deep gratings i.e. $h \rightarrow \infty$ (finite depth behave as ∞ if h goes very deep into the substrate), etched in it. A grating period $T= 0.2495\mu m$ and a filling factor of $f=0.25$ are assumed. Therefore, the air gap width $d_2=0.0624\mu m$ and the waveguide region, $d_1=0.1871\mu m$. These parameters are calculated based on a transmission resonance at the center wavelength 1.09965 μm. These values are obtained using the Bragg's formula given in equation.5.2. This equation overestimates the center wavelength, therefore with this period T (which is calculated at lower wavelength of 1.09965 μm), the device produces transmission resonance at a center wavelength of approximately $1.5\mu m$.

The length of the cavity is varied and and its effect is observed on the transmission resonance and radiation. Also the effect of the filling factor on the transmission resonance is analyzed.

6.2.1 Effect of the length of the Microcavity 'd_s'

The calculated spectral response for $d_s = 1.1T$ (T is the period of the structure) is shown in fig.6.2. The figure shows a wide bandgap extending from 1.3 to $1.7\mu m$ and a sharp transmission resonance peak near $1.443\mu m$. The transmission peak is situated towards the lower wavelengths thereby making the narrow bandgap to the left and a wider bandgap to the right. At resonant wavelength, the structure has a transmissivity of 55%. The fraction of radiated power (shown as a circle marker line in fig.6.12) is very high (approximately 39%). Therefore, a large fraction of

Figure 6.2: Spectral Response of the Symmetrical Coupled Grating Structure with $d_s = 1.1T$.
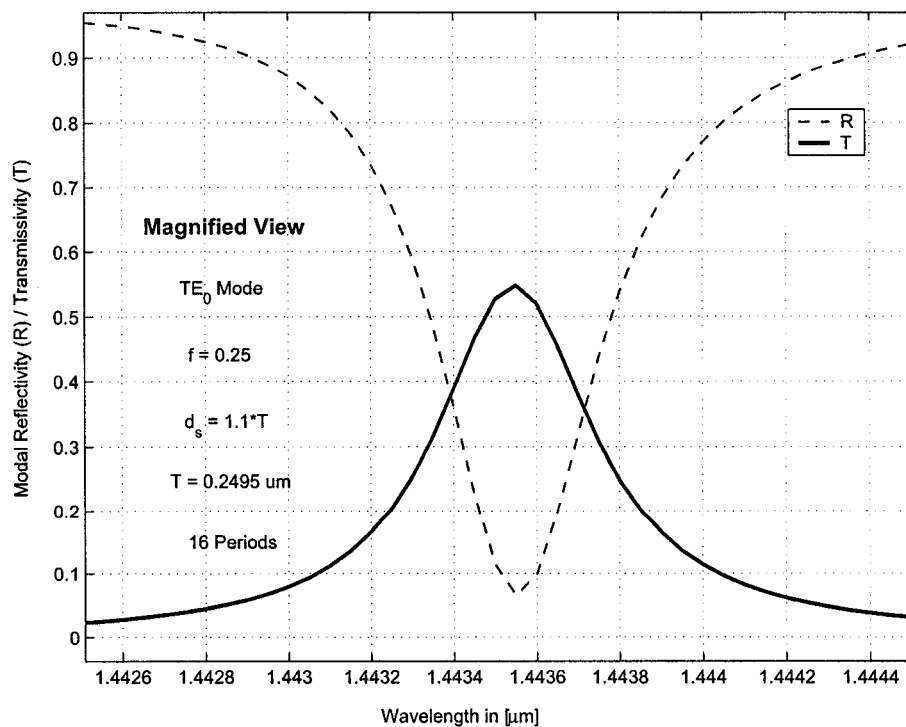
Figure 6.3: Magnified View of the Spectral Response of the Symmetrical Coupled Grating Structure with $d_s = 1.1T$.

the power is lost due to radiation from the structure. A magnified view of the transmission resonance is shown in fig.6.3.

Next, the dimensions of the microcavity (d_s) is altered and its effect on the position of the transmission resonant wavelength and the peak transmission and radiation, is analyzed. Considering fig.6.4 and its magnified view (fig.6.5), we see that increasing the microcavity length, causes an increase in the transmission resonance of the microcavity. The resonant wavelength shifts towards longer wavelength with an increase in the percentage of transmission (80%) and a decrease in the radiation loss by a factor of 2. Similar behavior is seen on lengthening the microcavity even further (figs.6.6 to 6.11). As expected, the transmission resonance moves towards the longer wavelengths accompanied with an increase in the modal transmissivity. The fraction of the radiated power of the structure decreases considerably, thereby making the structure more efficient (see fig.6.12).

Fig.6.6 (see fig.6.7 for magnified view) is of particular interest. The structure has a transmission resonance at the center wavelength of $1.55\mu m$ with a considerable bandgap on either side of the resonant wavelength. The structure is thus a good candidate for use as filter in wavelength division multiplexing operating at $\lambda = 1.55\mu m$.

The spectral response with $d_s = 1.6\mu m$ shown in figs.6.10 and 6.11, reveals that the structure in this case exhibits a dual transmission resonance in the bandgap. One is situated at the lower wavelength and the other is situated at the higher wavelength sides of the bandgap. The higher wavelength resonance has high transmission when
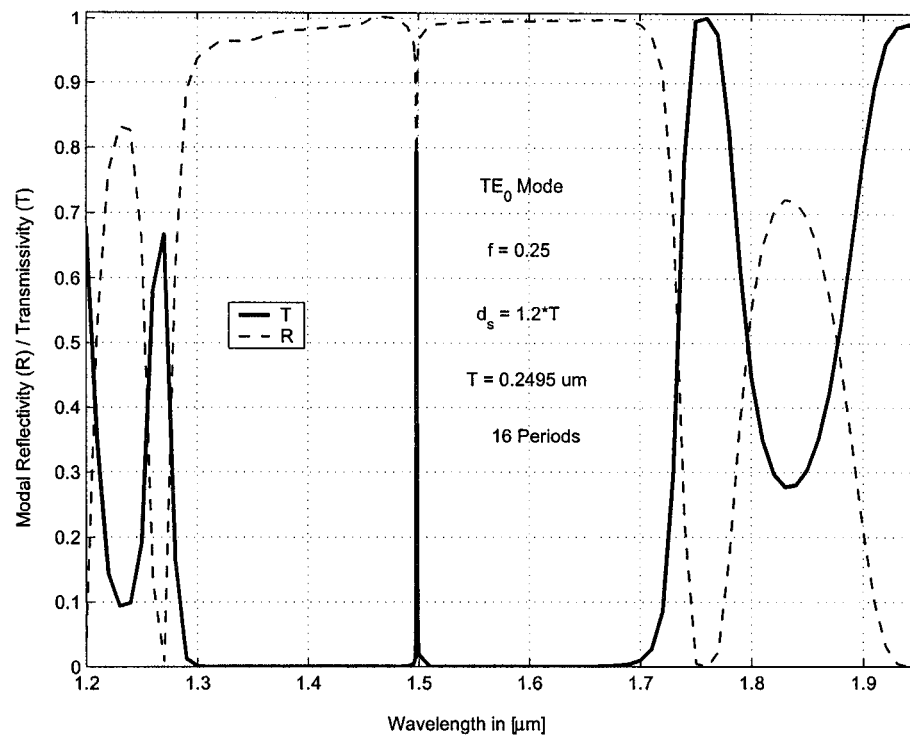
Figure 6.4: Spectral Response of the Symmetrical Coupled Grating Structure with $d_s = 1.2T$.
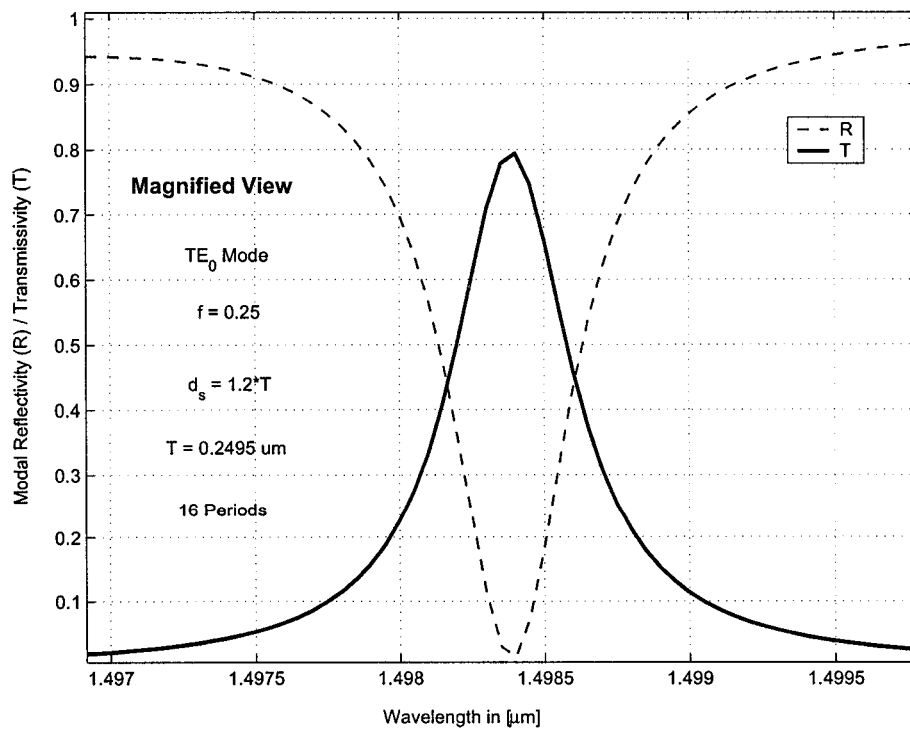
Figure 6.5: Magnified View of the Spectral Response of the Symmetrical Coupled Grating Structure with $d_s = 1.2T$.
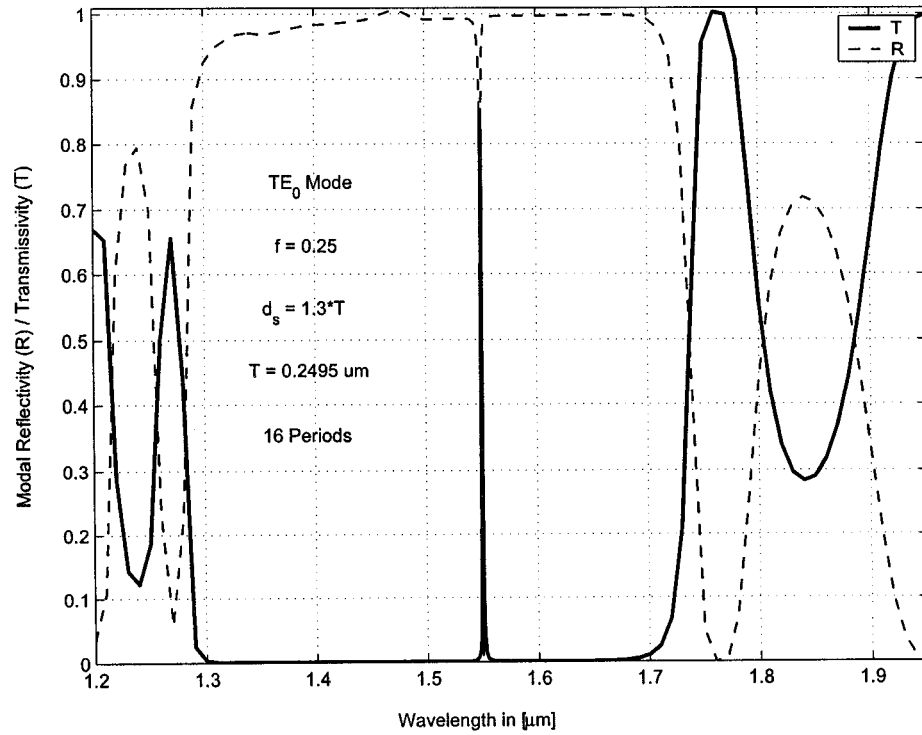
Figure 6.6: Spectral Response of the Symmetrical Coupled Grating Structure with $d_s = 1.3T$.
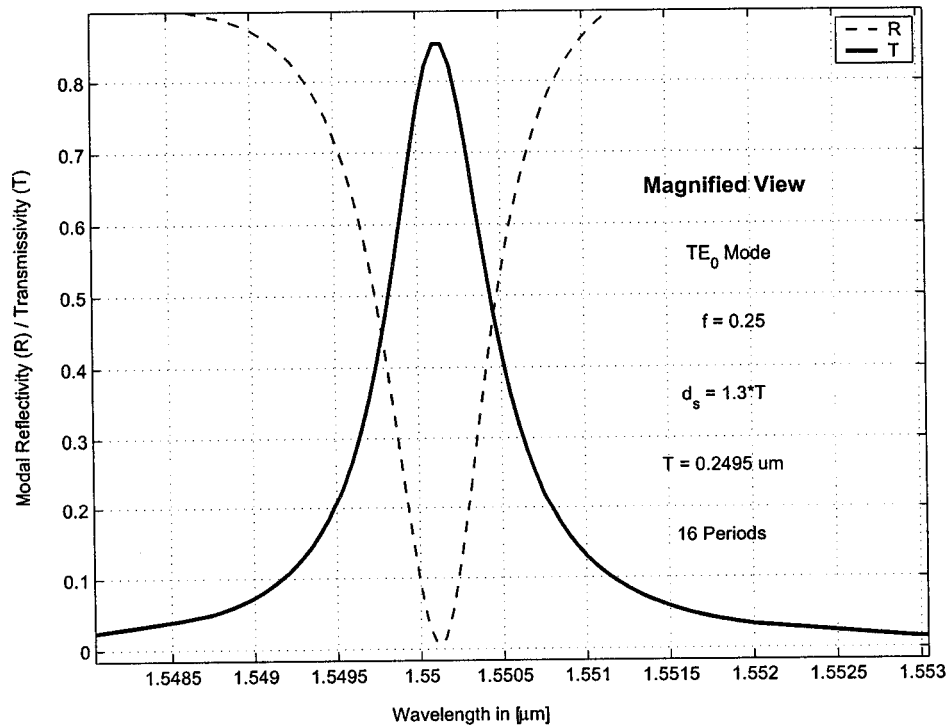
Figure 6.7: Magnified View of the Spectral Response of the Symmetrical Coupled Grating Structure with $d_s = 1.3T$.
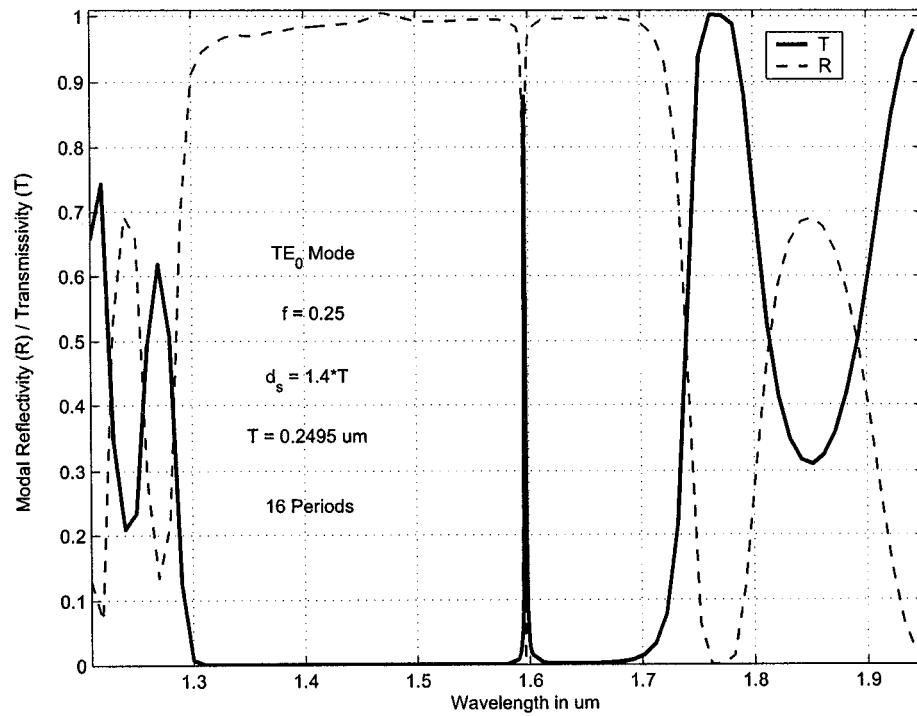
Figure 6.8: Spectral Response of the Symmetrical Coupled Grating Structure with $d_s = 1.4T$.

Figure 6.9: Magnified View of the Spectral Response of the Symmetrical Coupled Grating Structure with $d_s = 1.4T$.

Figure 6.10: Spectral Response of the Symmetrical Coupled Grating Structure with $d_s = 1.6T$.

Figure 6.11: Magnified View of the Spectral Response of the Symmetrical Coupled Grating Structure with $d_s = 1.6T$.

compared to the lower wavelength resonance. The radiation is negligible in the former case and as much as 40% of the power is radiated form the structure in the latter case. The appearance of the pair of transmission resonance in this particular case is obviously due to the increase in the length of the microcavity.

The observations obtained from the above figures are summarized in table 6.1 so that the reader better appreciates the behavior of the structure.

d_s	R (%)	T (%)	Ra (%)	$\Delta\lambda(nm)$	$\lambda_c(\mu m)$	$\frac{\Delta\lambda}{\lambda_c}$ (10^{-3})
1.1T	6.4	55.0	38.6	0.53	1.4435	0.37
1.2T	1.0	79.5	19.5	0.61	1.4984	0.41
1.3T	0.6	85.2	14.2	0.73	1.5501	0.47
1.4T	0.4	87.6	12.0	1.4	1.5965	0.88
1.6T	0.1	99.3	0.6	5.0	1.6672	2.99

Table 6.1: Calculated Spectral Width of the Transmission Resonance, in case of Symmetrical Coupled Grating Structure, for different lengths of the microcavity. (R, T and Ra corresponds to the Peak Reflectivity, Peak Transmissivity and Peak Radiation Loss, respectively).

The table shows that minimum fractional spectral width $(\frac{\Delta\lambda}{\lambda_c})$ is obtained when $d_s = 1.1T$. This quantity increases monotonically with microcavity length d_s.

Fig.6.13 shows the tuning capability of the structure. Here the length of the microcavity is varied in terms of the grating period T of the structure, and the transmission resonant wavelength is calculated in each case. From the figure we see that the resonant wavelength increases with d_s. Tuning the structure at any of the resonant wavelength is possible. Unfortunately, the radiation loss comes into picture. If a lower resonant wavelength is desired, large radiation is experienced resulting in reduced transmission.
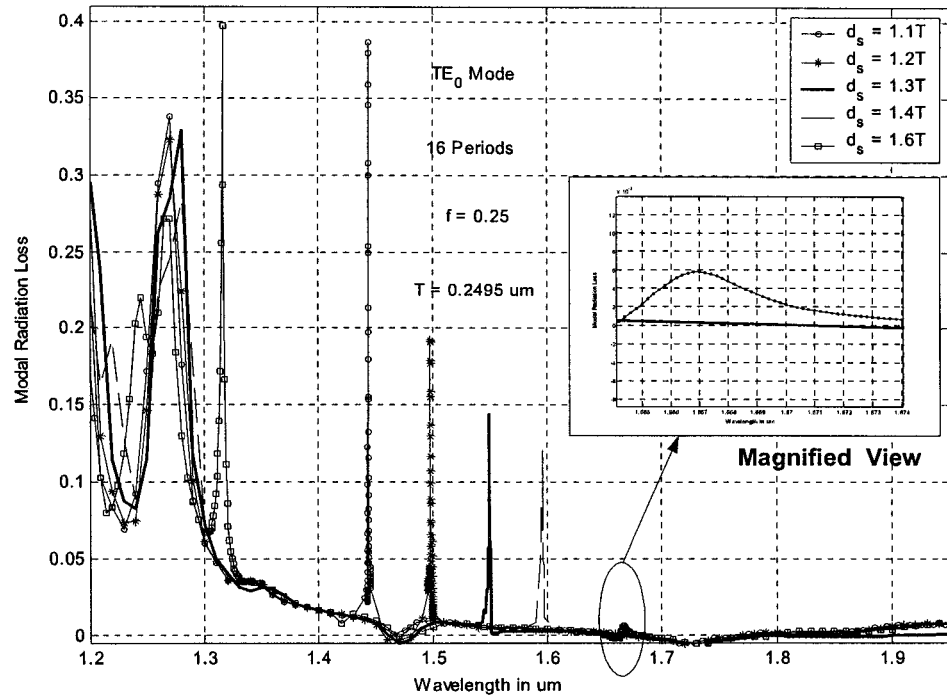
Figure 6.12: The Radiation Loss of the Symmetrical Coupled Grating Structure for different values of d_s.
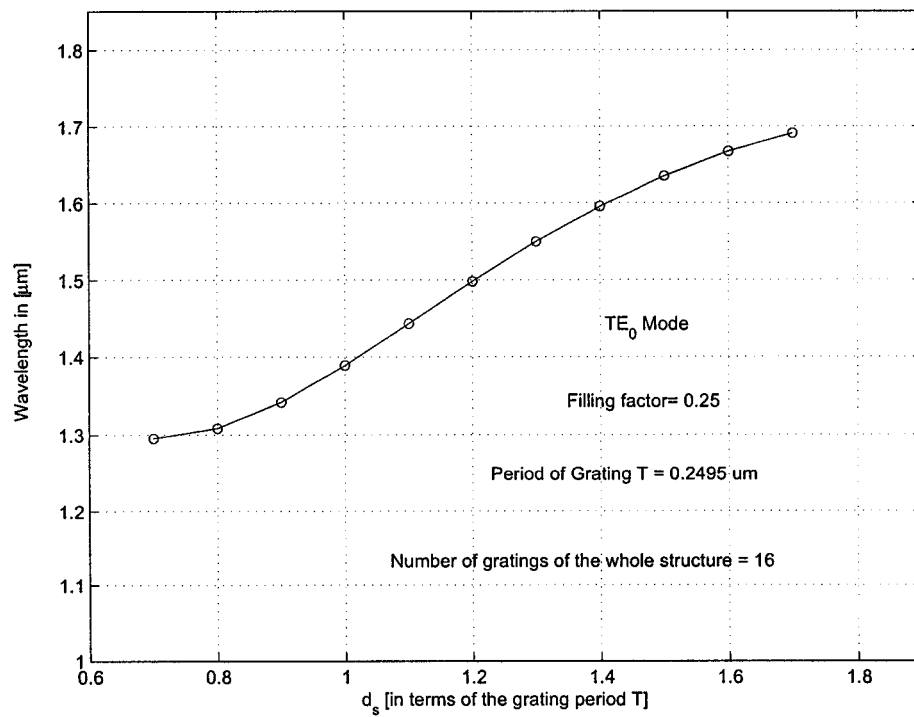
Figure 6.13: Transmission Resonance Wavelength Verses the Mocrocavity Length, of the Symmetrical Coupled Structure.

6.2.2 Effect of the the Filling Factor

The effect of the filling factor on the position of the band edges and transmission resonant wavelength can be seen in figs.6.14, 6.6 and 6.15, keeping the length of the microcavity constant at $d_s = 1.3T$. All the other parameters are kept same as those used above.

From the figs.6.16 and 6.17, which gives a good visualization of the effect of f, we see that the filling factor has a very small effect on the position of the transmission resonance, causing small shift towards the lower wavelength. However, a large increase in the width of the bandgap is seen, with f.

The fig.6.18, which is a magnified view of the transmissivity curve, reveals that the spectral width decreases with f. Hence, the fractional spectral width (calculated at half power)is decreased making the structure more wavelength selective. The corresponding numerical values are tabulated in table 6.2 for reference.

f	R (%)	T (%)	Ra (%)	$\triangle\lambda(nm)$	$\lambda_c(\mu m)$	$\frac{\triangle\lambda}{\lambda_c}$ (10^{-3})
0.15	0.3	95.0	4.7	6.70	1.5725	4.2607
0.25	0.6	85.2	14.2	0.73	1.5501	0.4709
0.50	1.2	79.5	19.3	0.35	1.5358	0.2279

Table 6.2: Calculated Spectral Width of the Transmission Resonance, in case of Symmetrical Coupled Grating Structure, at different Filling Factors. (R, T and Ra corresponds to the Peak Reflectivity, Peak Transmissivity and Peak Radiation Loss, respectively).

Fig.6.19 shows the radiated power dependence on the filling factor f. It is clearly seen that the radiated power at the transmission resonance wavelength increases
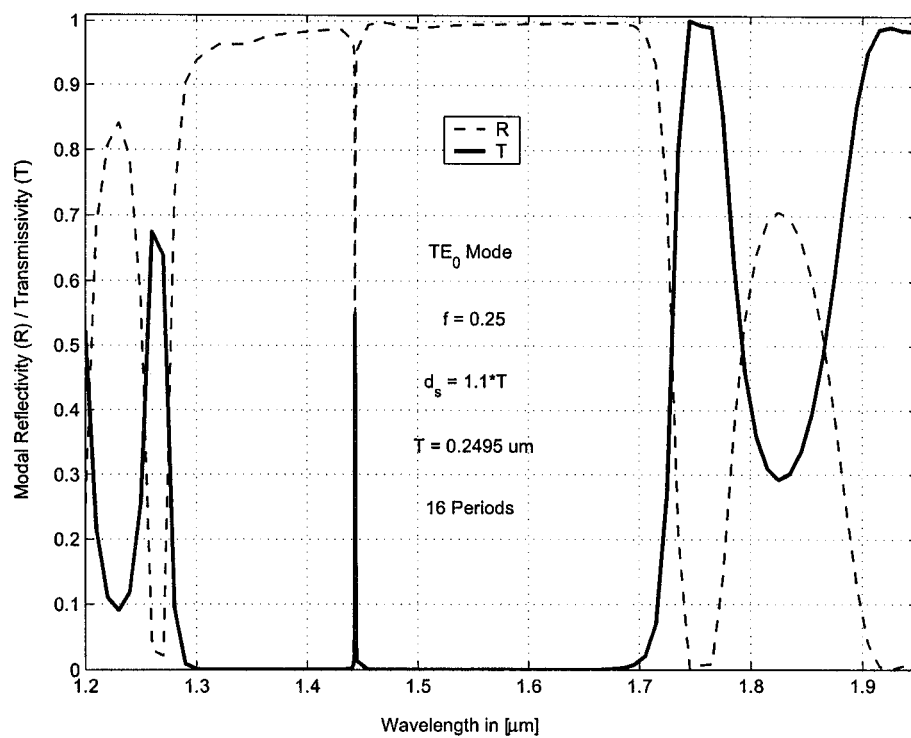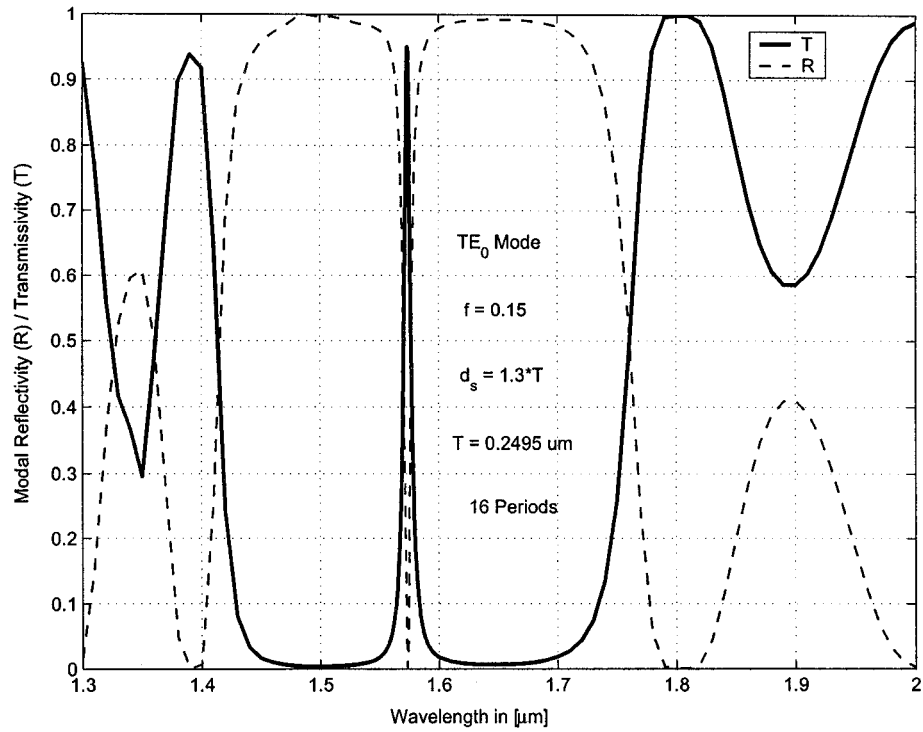
Figure 6.14: Spectral Response of the Symmetrical Coupled Grating Structure at $f = 0.15$.
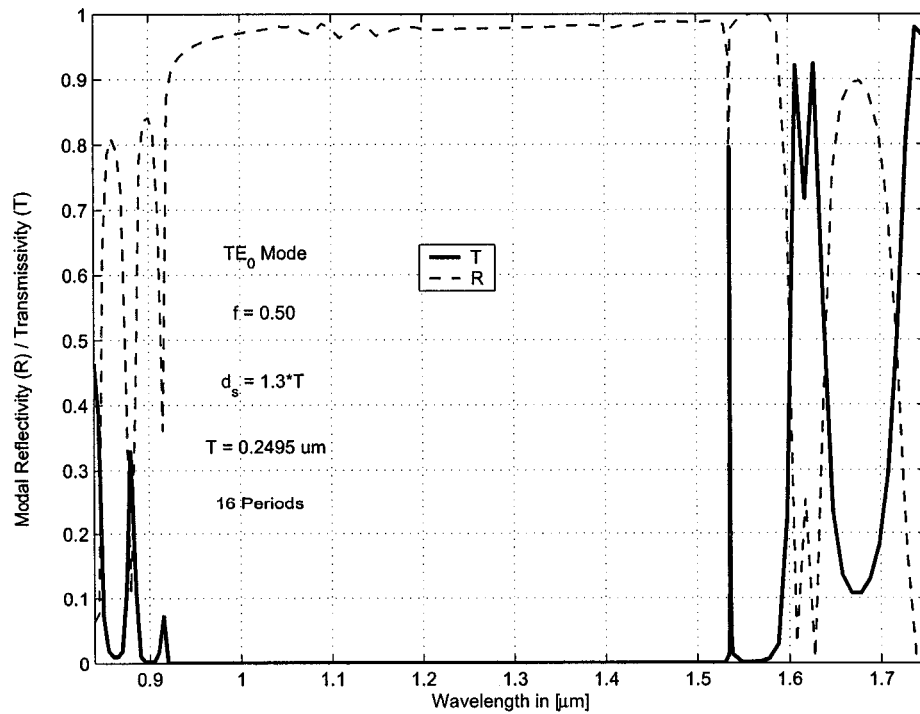
Figure 6.15: Spectral Response of the Symmetrical Coupled Grating Structure at $f = 0.50$.
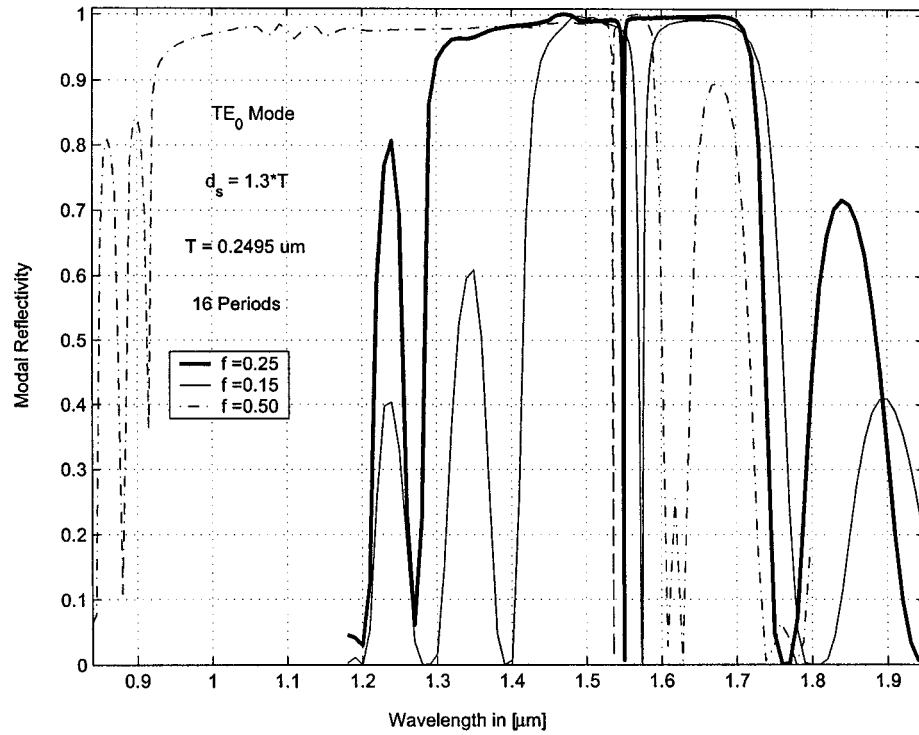
Figure 6.16: Fundamental TE Mode Reflectivity of the Symmetrically Coupled Grating Structure at different Filling Factors.
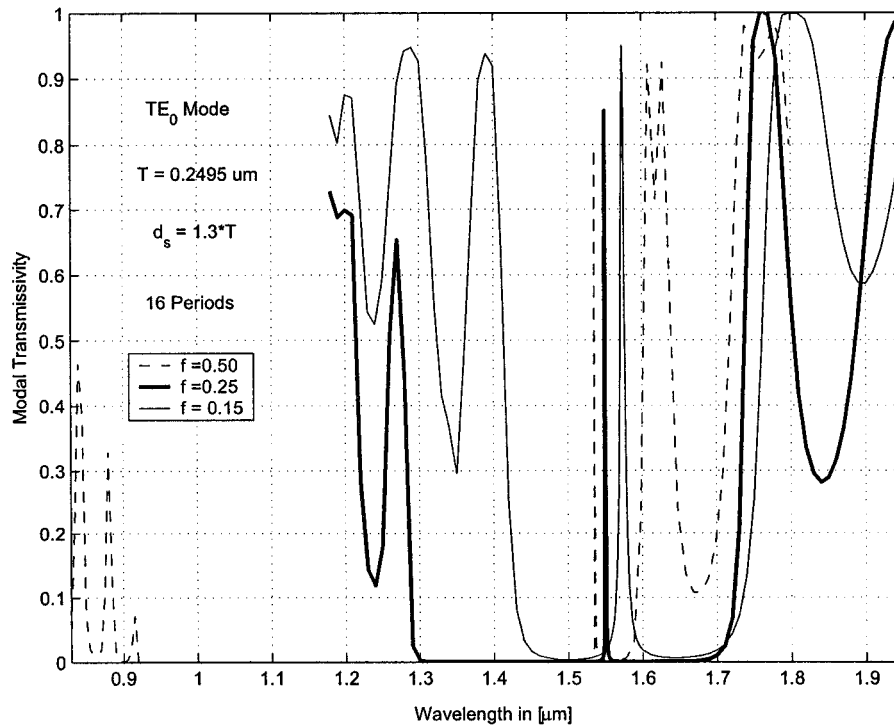
Figure 6.17: Fundamental TE Mode Transmissivity of the Symmetrically Coupled Grating Structure at different Filling Factors.
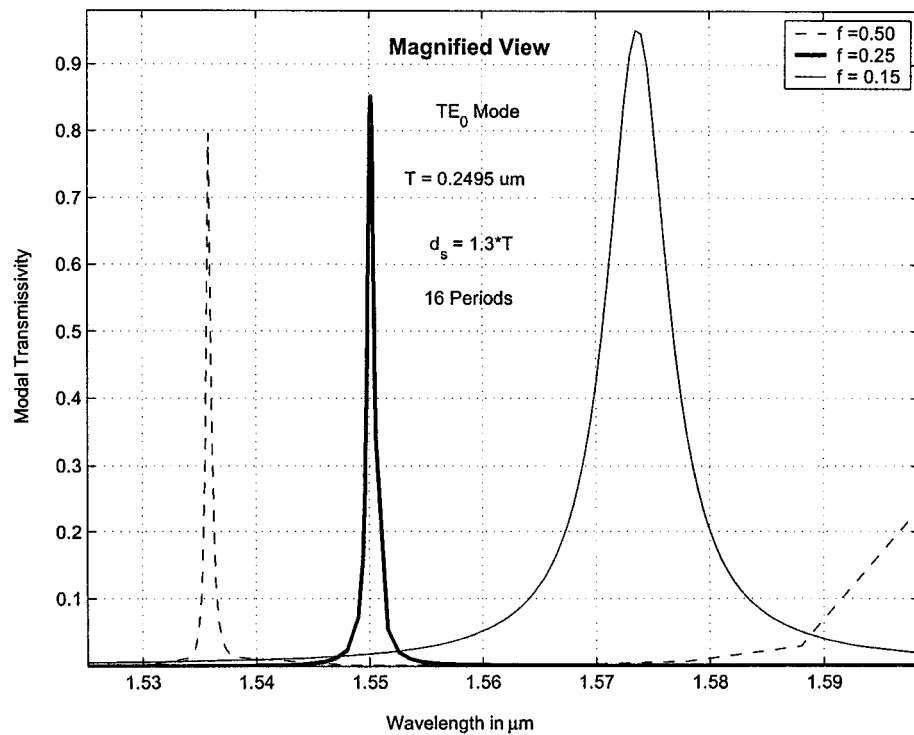
Figure 6.18: Magnified Views of the Transmission Resonance of the Symmetrically Coupled Grating Structure at different Filling Factors.
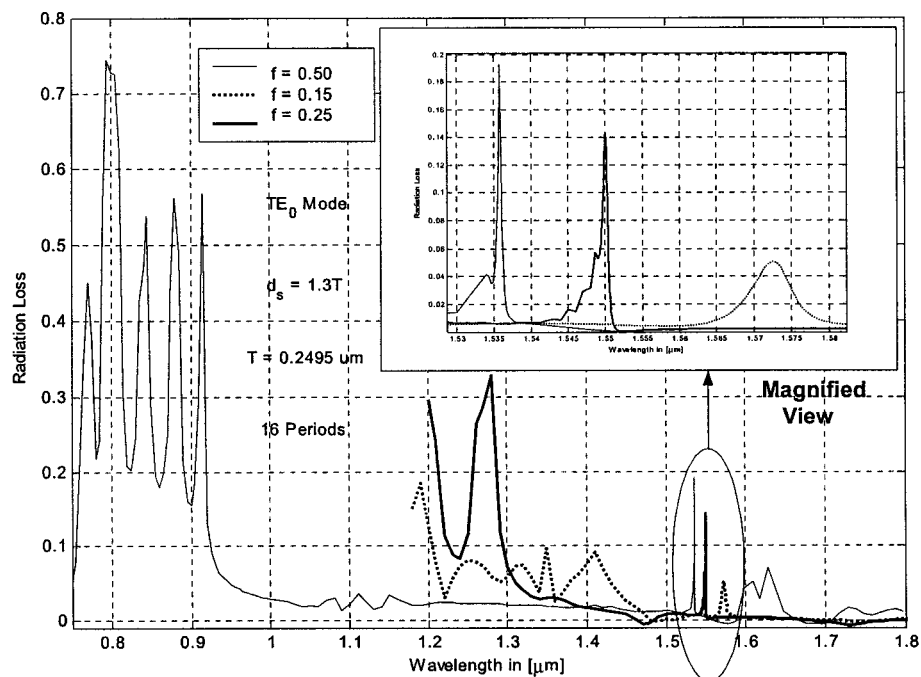
Figure 6.19: Fundamental TE Mode Radiation Loss of the Symmetrically Coupled Grating Structure at different Filling Factors.

with f (see the inset of the fig.6.19).

6.3 Discussion

A symmetrically coupled deep grating structure is studied in this chapter. The effect of the length of the microcavity and the filling factor, has been investigated for the symmetrically coupled grating structure, using the automated program. A narrow null is seen to develop in the reflection band thereby forming a narrow transmission resonance within the bandgap. The position and width of the transmission resonance is seen to vary with the length of the microcavity. The resonance wavelength is seen to move towards the higher wavelengths with a decrease in radiation, upon increasing the length of the microcavity. The filling factor has a very small effect on the position of the transmission resonance. However, the fractional spectral width of the transmission resonance is seen to decrease or a decreasing function of the filling factor.

Chapter 7

Analysis of Asymmetrical Coupled Grating Structure

7.1 Introduction

In the previous chapter, an optical filters with high wavelength selectivity was presented and analyzed in detail. This narrow band transmission filter is based on the coupling between two identical finite-length periodic structures. In this chapter, we study the coupling between dissimilar finite-length periodic structure. This is done with an eye on the application in wavelength filtering.
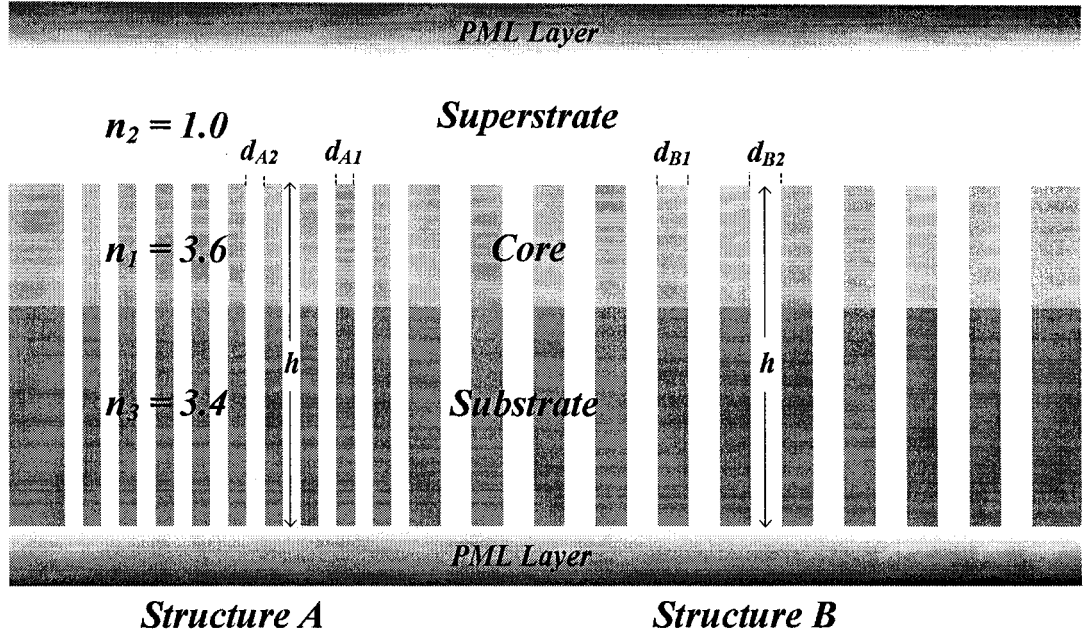
Figure 7.1: Asymmetrical Coupled Grating Structure. Structure A parameters: $d_{A1} = 0.75T_1$, $d_{A2} = 0.25T_1$. $T_1 = 0.2495\mu m$, Structure B parameters: $d_{B1} = 0.75T_2$, $d_{B2} = 0.25T_2$. T_2 is variable. $h \to \infty$, $N = 20$ and width of the core $w = 0.3\mu m$, for both the Structures.

7.2 The Asymmetrical Coupled Guided Wave Grating Structure

An asymmetrically coupled structure is shown in fig.7.1. The structure consists of two corrugated guided-wave structures of different periods cascaded together. The left hand structure (structure A) has a grating period of $T_1 = d_{A1} + d_{A2}$ (will be kept constant through out the analysis) with f=0.25. The right hand structure (structure B) has a grating period of $T_2 = d_{B1} + d_{B2}$ (will be varied) with same filling factor f=0.25. The groove depth ($h \to \infty$) and the number of periods ($N = 10$) will be fixed for both the structures. The Fundamental TE mode is excited on the left

hand side of the structure. It will be shown later that, by controlling the period of structure B, it is possible to create a very wide bandgap (in the order of 1 *micron*) and also a wideband transmission resonance in the bandgap. The values of the different parameters are shown in fig.7.1.

For this asymmetrically coupled structure, two analyses are done. First by directly coupling the two structures and second, by coupling the two structures with non zero separation, forming a microcavity (as done in the previous chapter).

7.2.1   Effect of Direct Coupling

The two structures (structures A and B) are coupled directly and analyzed.

Effect of Coupling Structure A and Structure B

Figs.7.2, 7.3 and 7.5 shows the spectral response of the asymmetrical guided wave grating structure at $T_2 = 0.3176, 0.3425$ and 0.3993 μms, respectively. By examining the first figure (fig.7.2), we see that the width of the stop band has increased to by a large extent. The width of the stop band is around $0.9\mu m$. This value is about twice that obtained in the symmetrical case (the bandgap width is about $0.46\mu m$ in the symmetrical case).

By further increasing the period of the second structure (structure B). A wide band transmission resonance is developed within the bandgap as seen in fig.7.3 (for a magnified view refer to fig.7.4). A high transmissivity at resonance (approximately
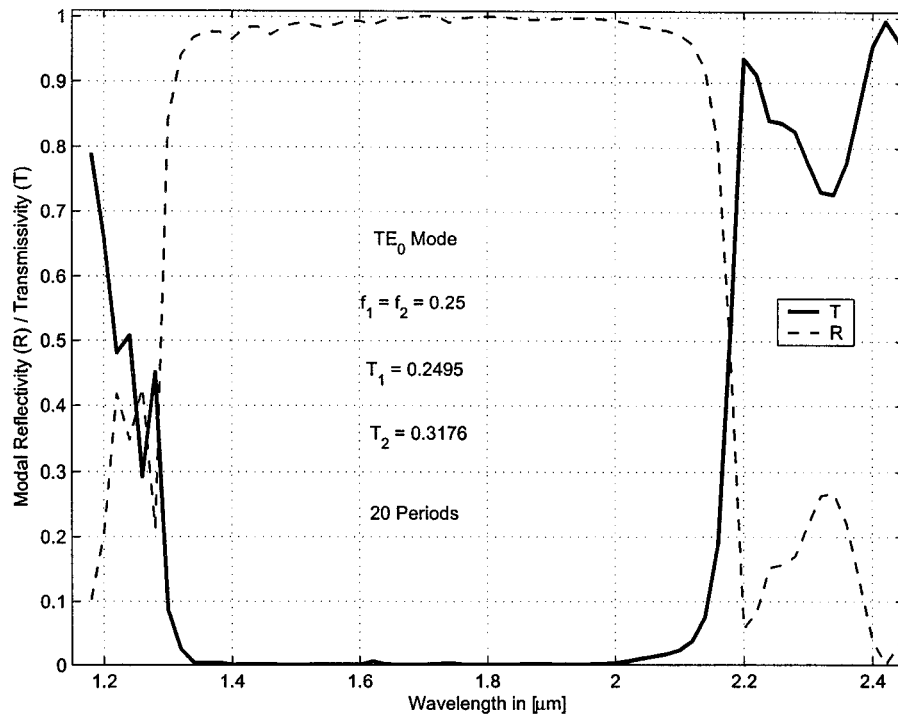
Figure 7.2: Spectral Response of the Asymmetrical Coupled Grating Structure with $T_2 = 0.3176\mu m$.
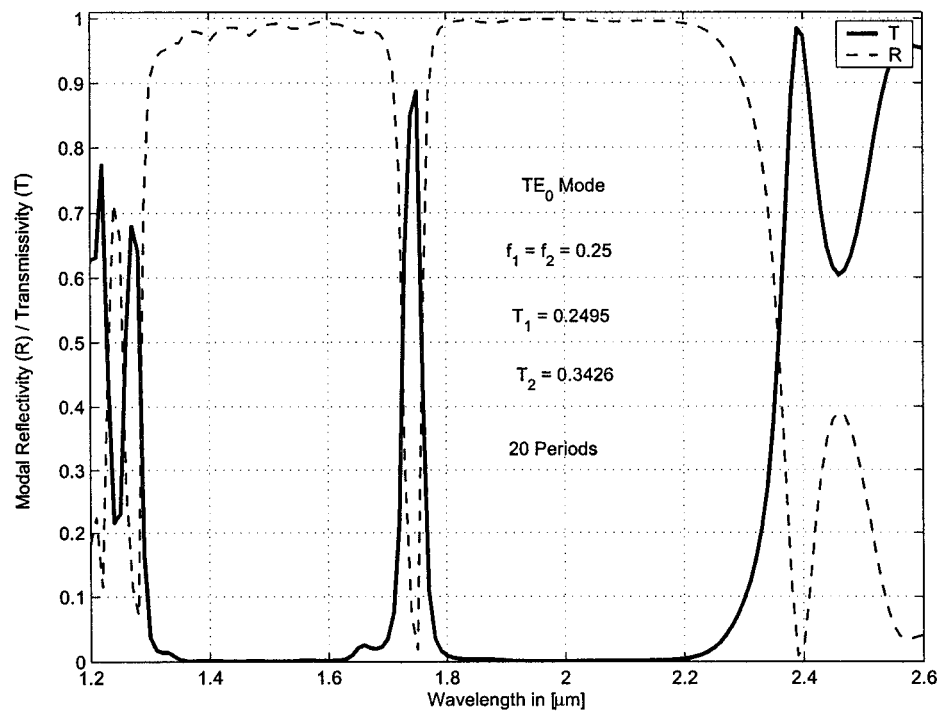
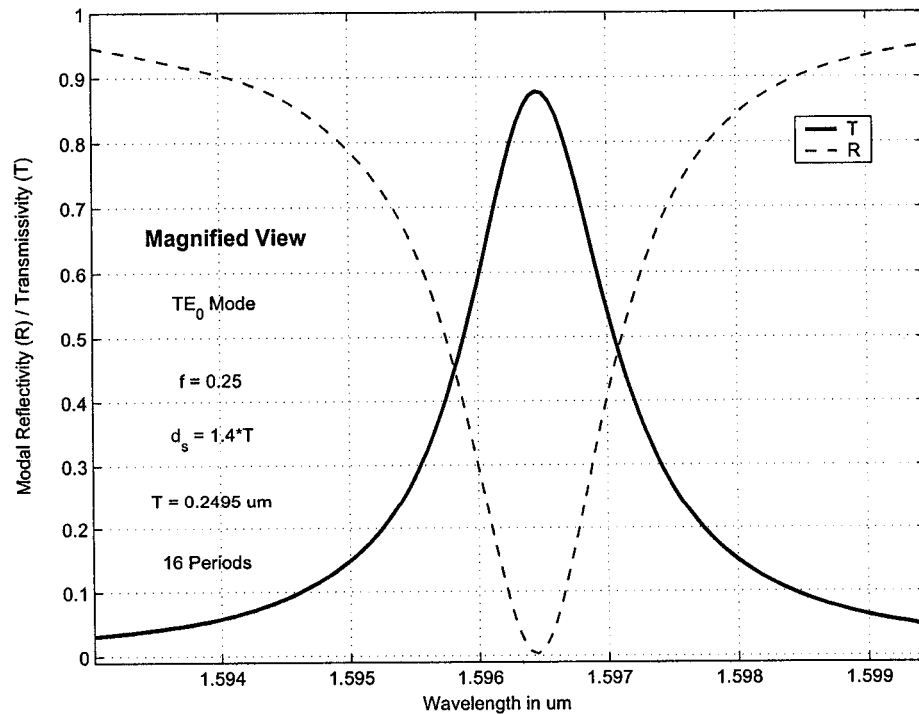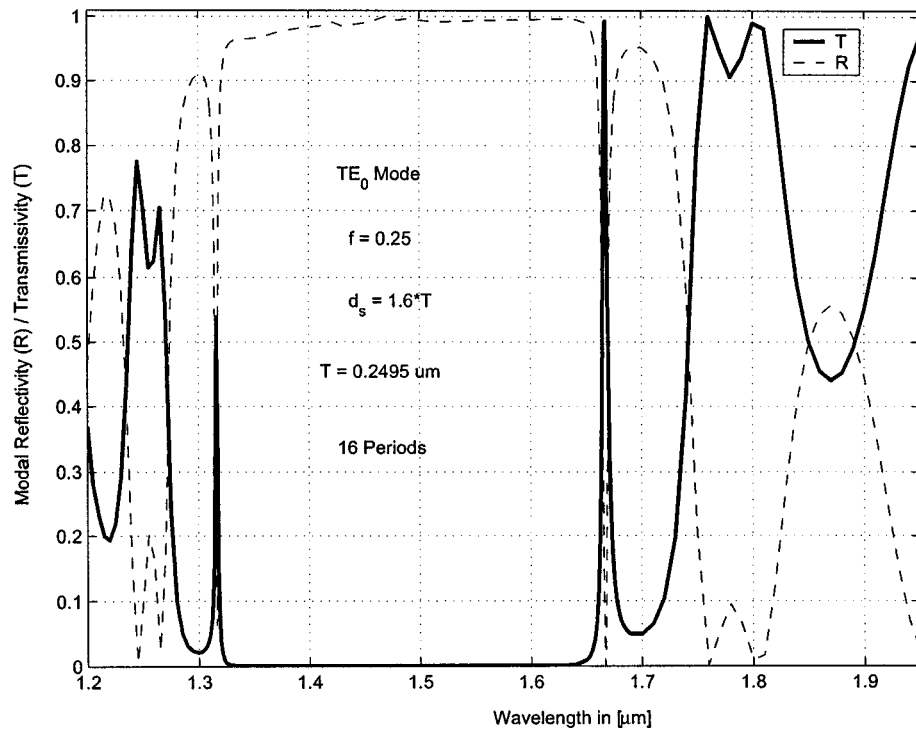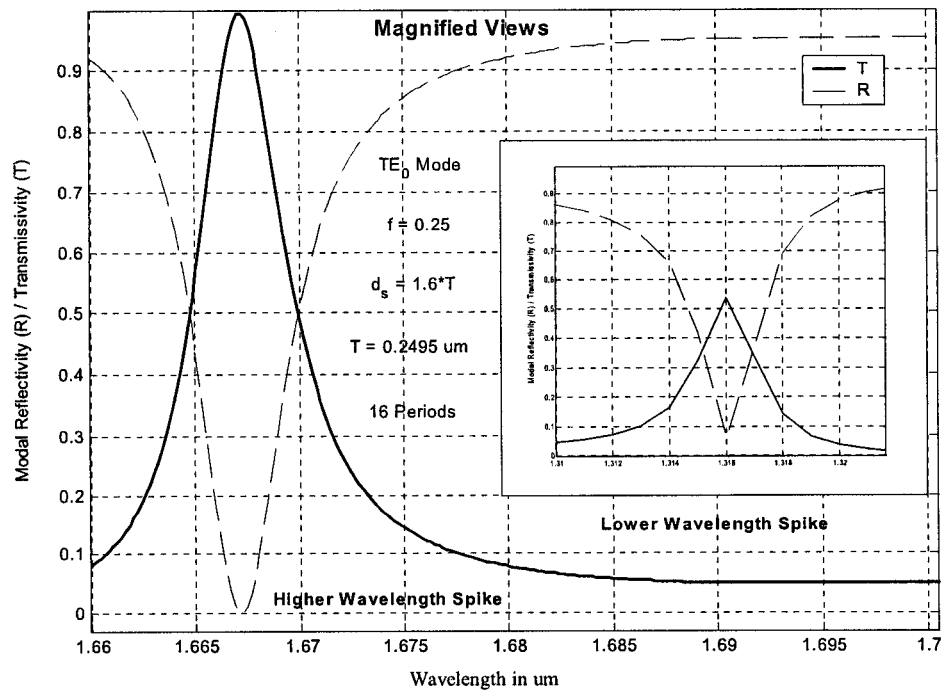Figure 7.3: Spectral Response of the Asymmetrical Coupled Grating Structure with $T_2 = 0.3425\mu m$.
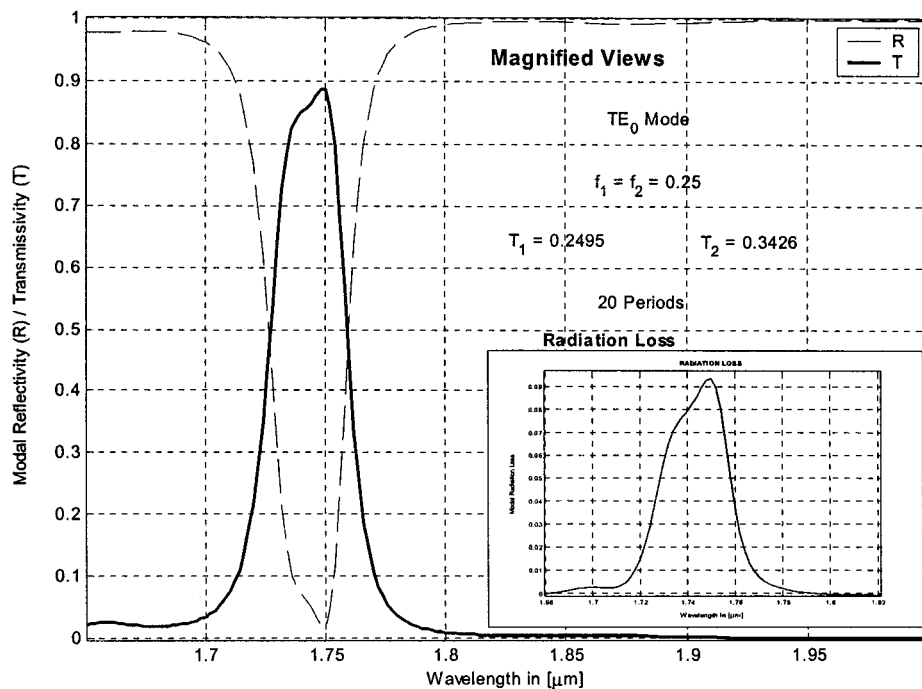
Figure 7.4: Magnified View of the Transmission Region of the Asymmetrical Coupled Grating Structure with $T_2 = 0.3425\mu m$.
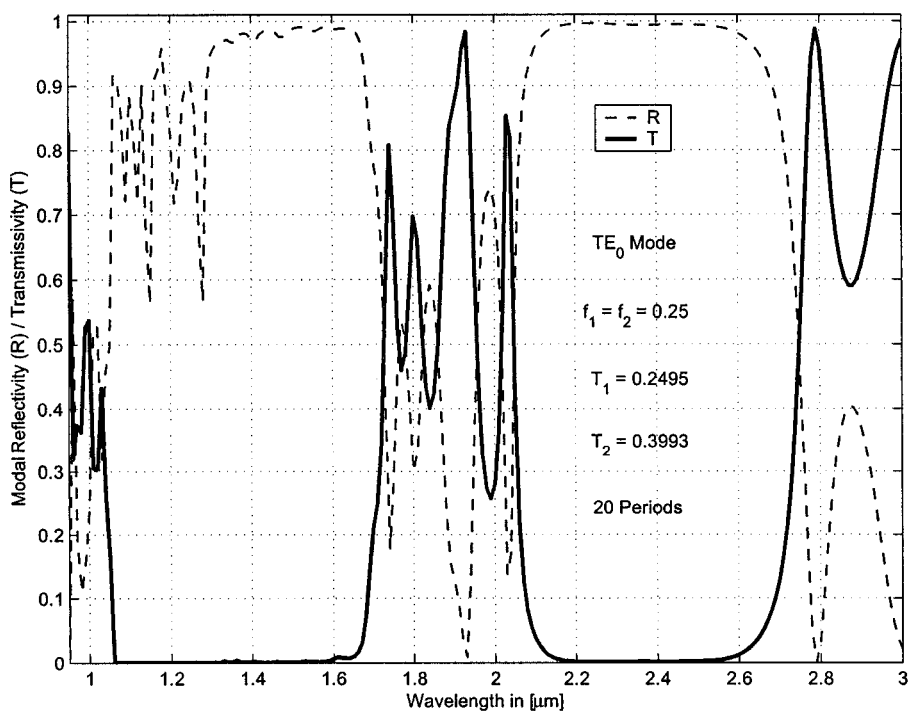
Figure 7.5: Spectral Response of the Asymmetrical Coupled Grating Structure with $T_2 = 0.3993\mu m$.

89%) is obtained. From the magnified view it can be seen that the transmission band is relatively wide (approximately $34.9nm$) when compared to the symmetrical case, where the transmission resonance width obtained is about $0.53nm$ to $5nm$. The center wavelength is situated at $1.750\mu m$ with fractional spectral width of approximately 19.9×10^{-3} which is much large than the corresponding symmetrical case. Thus, with the current set of parameters, the asymmetrically coupled structure behaves as a wideband filter.

Fig.7.5 shows a very wideband transmission resonance in the stop band. Ripples are observed in the transmission band with transmissivity varying approximately from 30% to 95%. Figs.7.6 and 7.7 show the effect of T_2 on the over all spectral response of the structure. From fig.7.6(7.7), we can see how the transmission dip (the corresponding transmission resonance) is developed when T_2 is increased.

Effect of Coupling Structure B and Structure A

Because the combined structure under present consideration is asymmetric, its response is expected to be different due to excitation from the left and the right hand sides. We denote the excitation from the left hand side by AB and excitation from the right hand side by BA. We are interested in comparing the spectral responses in those two cases.

The asymmetrical coupled structure with $T_2 = 0.3426\mu m$ is used for the above analysis. The coupling in done in the opposite way (structures BA). Calculated results for both the possibilities are shown in figs. 7.8, 7.9 and 7.10. Ripples are ob-
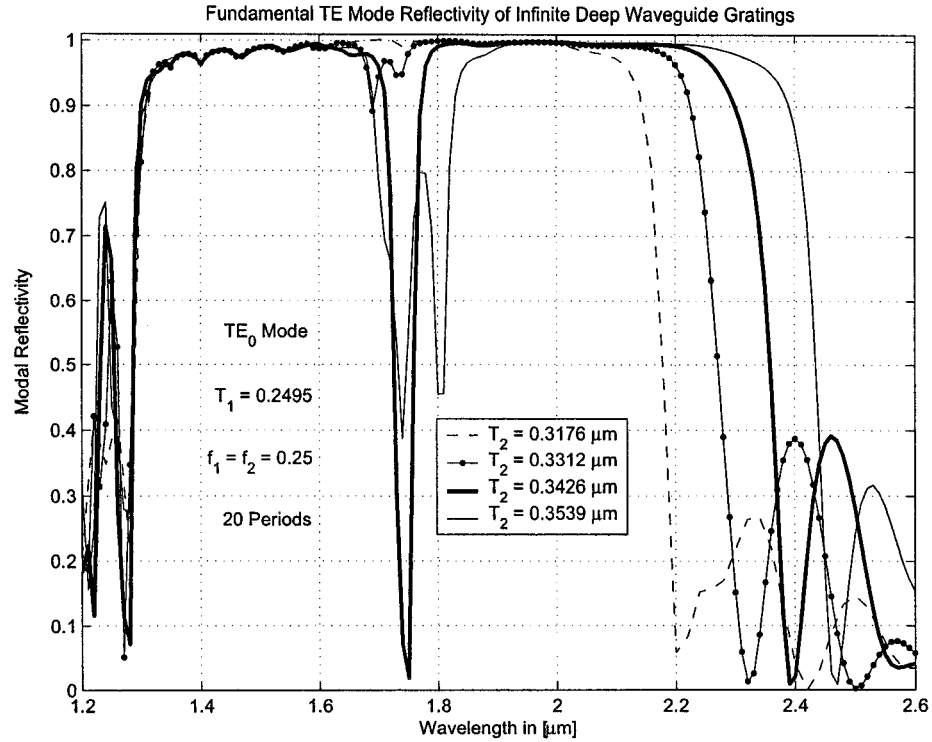
Figure 7.6: Fundamental TE Mode Reflectivity of the Asymmetrical Coupled Grating Structure for different values of T_2.
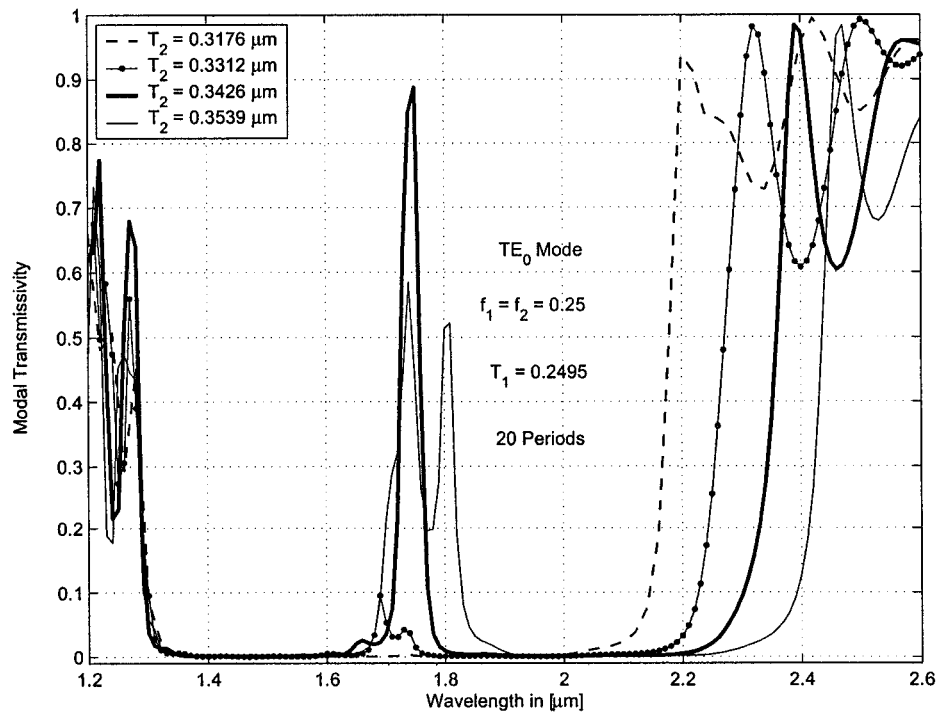
Figure 7.7: Fundamental TE Mode Transmissivity of the Asymmetrical Coupled Grating Structure for different values of T_2.
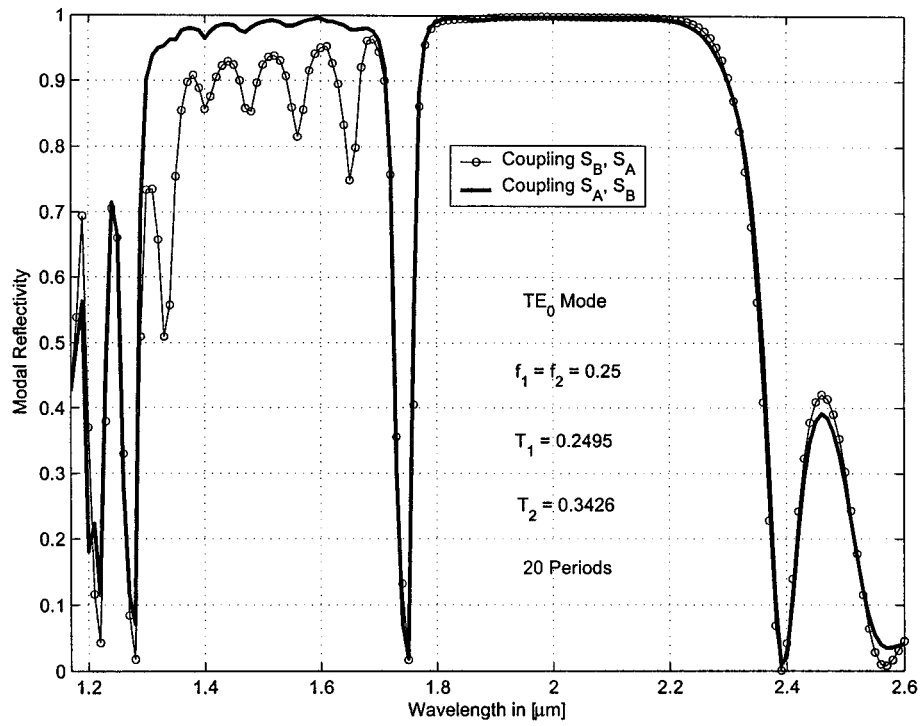
Figure 7.8: Comparison of Coupling Structures AB and BA. TE_0 Modal Reflectivity.
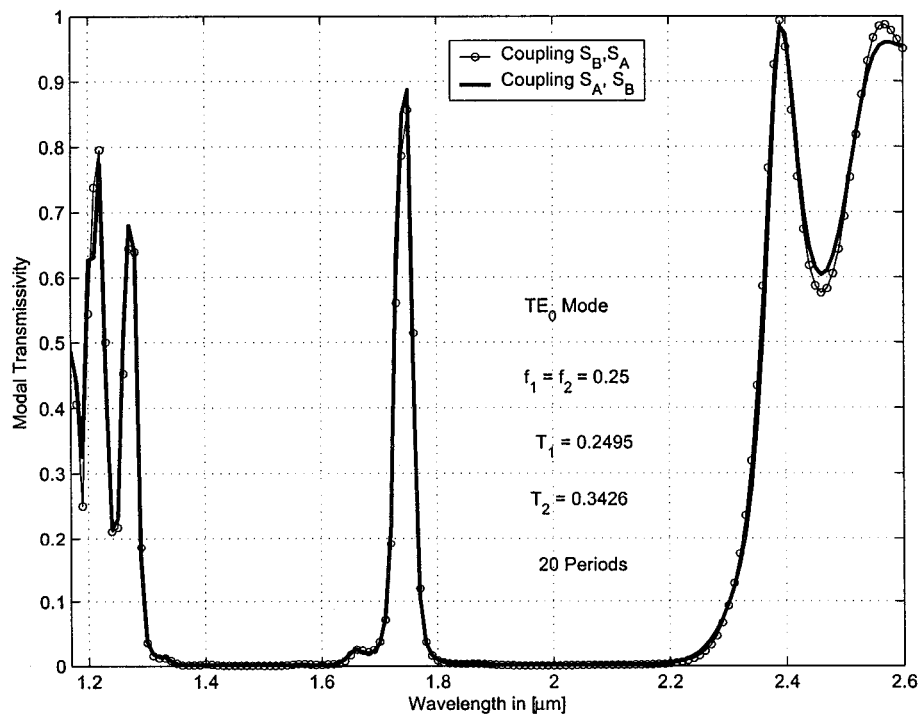
Figure 7.9: Comparison of Coupling Structures AB and BA. TE_0 Modal Transmissivity.
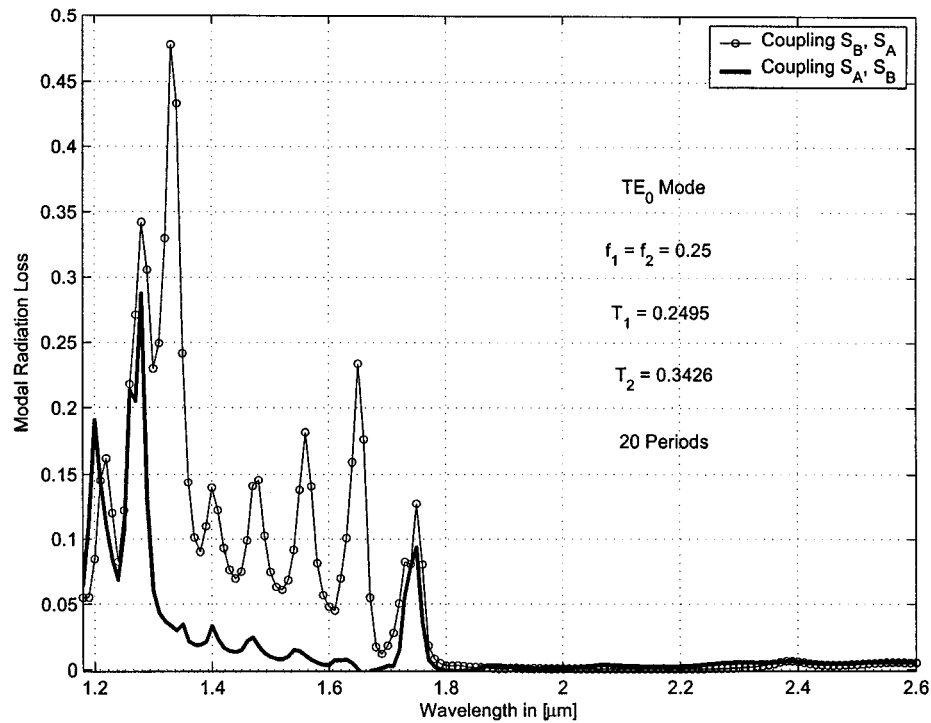
Figure 7.10: Comparison of Coupling Structures AB and BA. TE_0 Mode Radiation Loss.

served towards the lower wavelengths in the reflectivity curve of the combined structure (on the left of the resonant wavelength) where as there is almost no difference in the transmissivity curve, in both the cases. The coupled structure experiences more radiation when coupling structures B and A when compared to the results of coupling structures A and B. This can be very well visualized from fig.7.10

7.2.2 Effect of the length of the Microcavity 'd_s'

The two structures (A and B) are coupled by a uniform region of the same waveguide material (forming a microcavity) of length d_s. The effect of d_s on the transmission

resonance is studied in this case (microcavity length d_s is varied in terms of the period of structure A, i.e. T_1).

Figs.7.11, 7.13 and 7.15 shows the calculated spectral response of the asymmetrical structure corresponding to $d_s = 1.3T_1, 1.33T_1$ and $1.4T_1$, respectively, keeping the period of the structure B,i.e. $T_2 = 0.3176\mu m$ is constant. A transmission resonance appears in all these cases. Table 7.1 gives a summary to some of the important results corresponding to theses figures.

d_s	R (%)	T (%)	Ra (%)	$\triangle\lambda(nm)$	$\lambda_c(\mu m)$	$\frac{\triangle\lambda}{\lambda_c}$ (10^{-3})
$1.3T_1$	25	40	35	3.80	1.6630	2.2850
$1.33T_1$	5	46	50	3.90	1.6702	2.3350
$1.4T_1$	28	27	45	4.45	1.6865	2.6386

Table 7.1: Calculated Spectral Width of the Transmission Resonance, in case of Asymmetrical Coupled Grating Structure, for different length of microcavity d_s. The period of Structure B is selected to be $T_2 = 0.3176\mu m$.(R, T and Ra corresponds to the Peak Reflectivity, Peak Transmissivity and Peak Radiation Loss, respectively).

From the table 7.1, we see that the maximum transmissivity that can be achieved in this case is only 40% (for $d_s = 1.33T_1$). Any change in d_s (increase or decrease) results in reduced transmission. The radiation loss is very high for this structure (50% for $d_s = 1.33T_1$). Therefore $d_s = 1.33T_1$ is the best length of the microcavity to obtain optimal results. Better visualization of the spectral width can be seen in the magnified figures (shown in figs.7.12, 7.14 and 7.16). When we increase the period T_2 of structure B, there is small shift in the position of the transmission resonant wavelength towards the higher wavelengths. The results summarized in table 7.1 supports the conclusion. The amount of transmission is seen to vary with
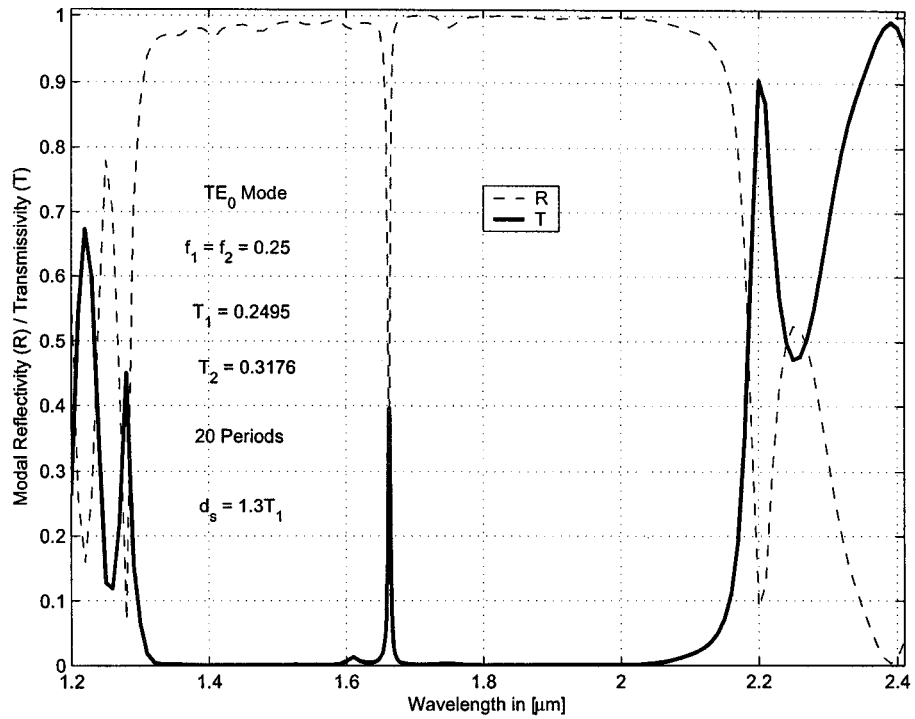
Figure 7.11: Spectral Response of the Asymmetrically Coupled Grating Structure for $d_s = 1.3T_1$.
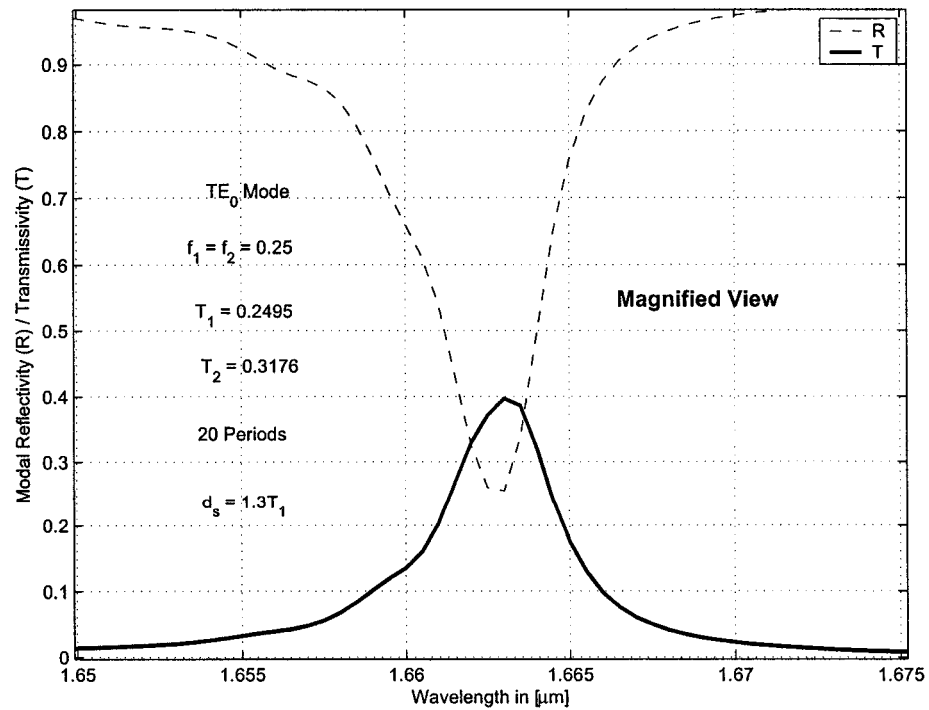
Figure 7.12: Magnified view of the Spectral width of the Asymmetrically Coupled Grating Structure for $d_s = 1.3T_1$.
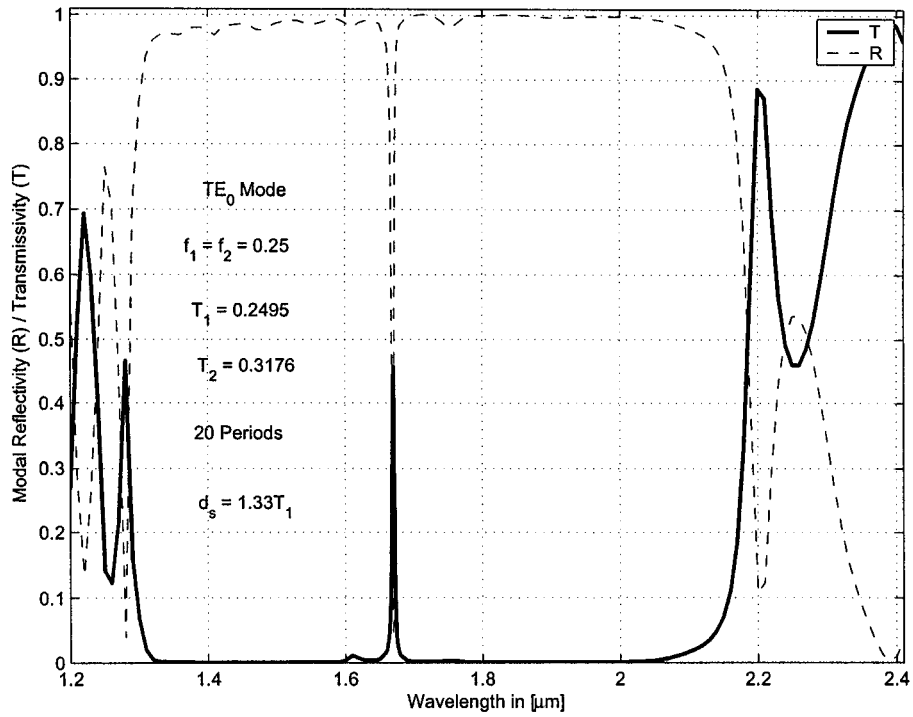
Figure 7.13: Spectral Response of the Asymmetrically Coupled Grating Structure for $d_s = 1.33T_1$.
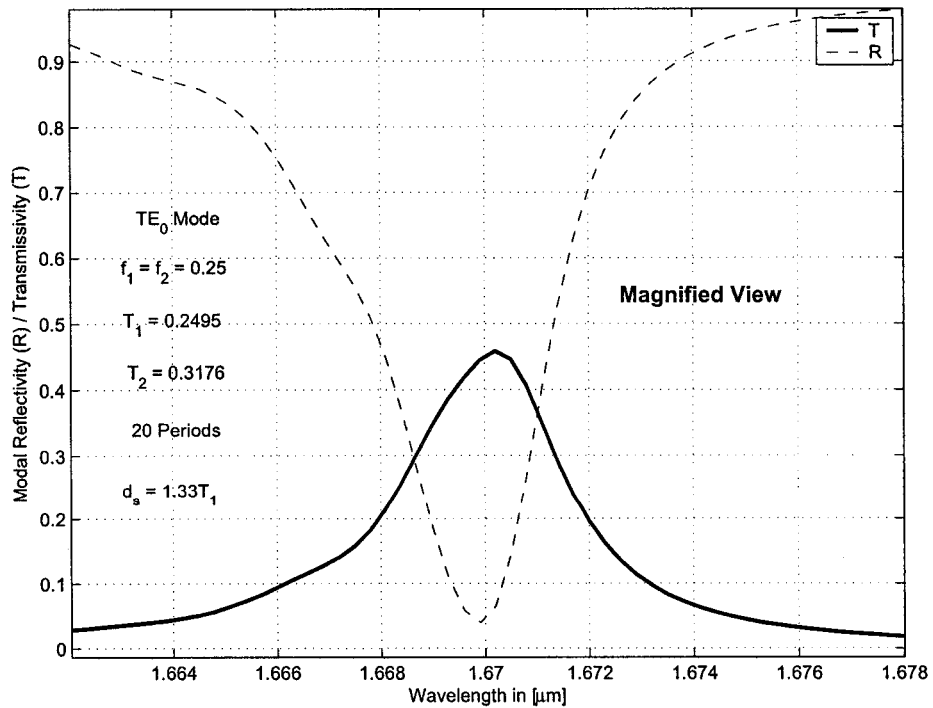
Figure 7.14: Magnified view of the Spectral width of the Asymmetrically Coupled Grating Structure for $d_s = 1.33T_1$.
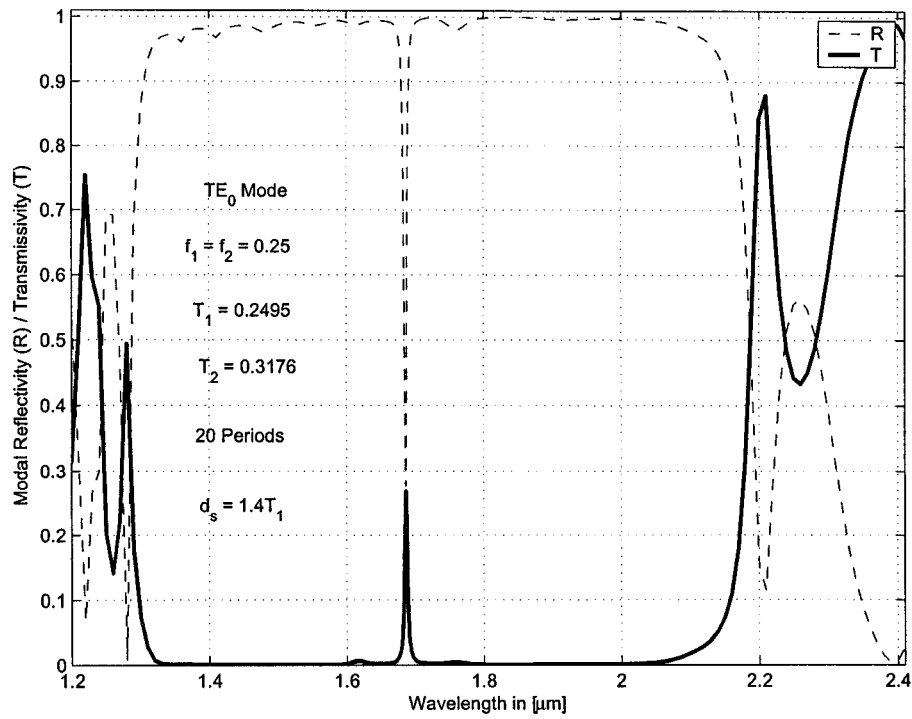
Figure 7.15: Spectral Response of the Asymmetrically Coupled Grating Structure for $d_s = 1.4T_1$.
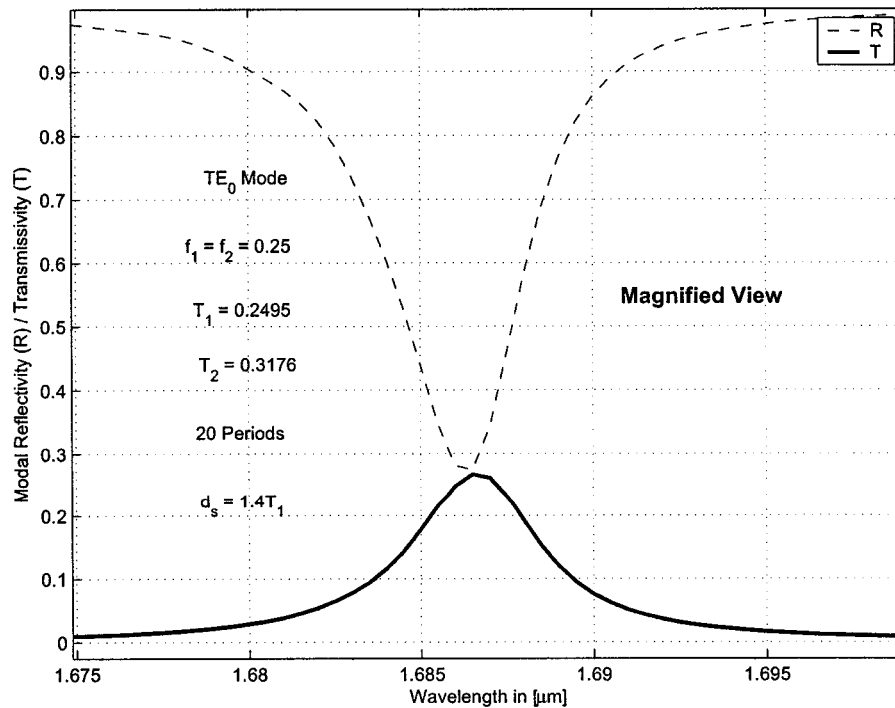
Figure 7.16: Magnified view of the Spectral Response of the Asymmetrically Coupled Grating Structure for $d_s = 1.4T_1$.
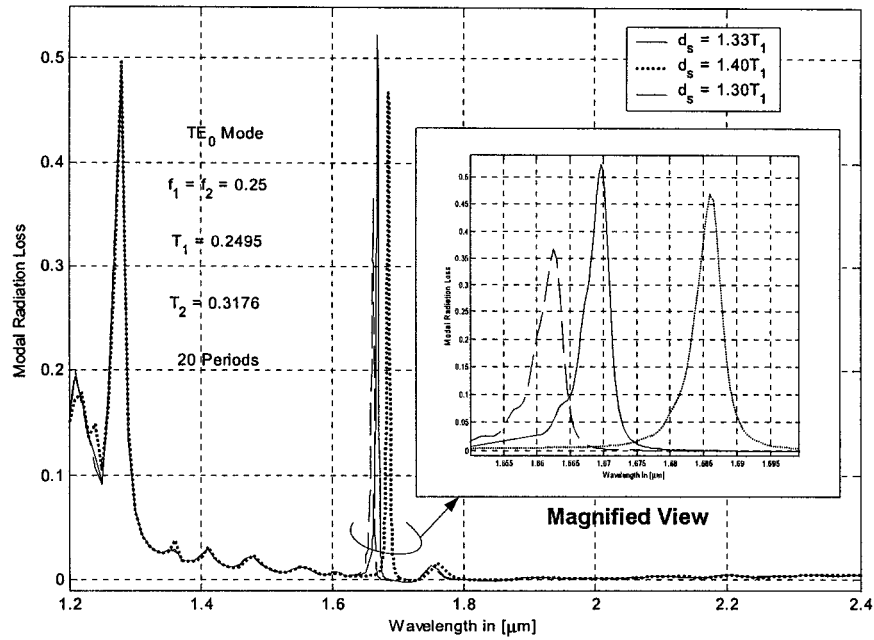
Figure 7.17: The Fundamental TE Mode Radiation Loss of the Asymmetrical Coupled Grating Structure at different d_s.

the length of the microcavity. The maximum transmission that can be achieved for the asymmetrical coupled structure is 46%. Fig.7.17 represents the fraction of radiated power. It is seen that the amount of radiated power is high (40 to 50%). Therefore, around half of the power is lost in radiation.

The other set of figures (figs.7.18 and 7.19), represents the spectral response of the asymmetrically coupled structure with $T_2 = 0.3312\mu m$ and $d_s = 1.4T_1$, and its magnified view. The results shows a formation of transmission resonance. The curve resembles the one without the microcavity, except that of the formation of the transmission resonance (see the curve with dots in fig.7.6 and 7.7). The fractional
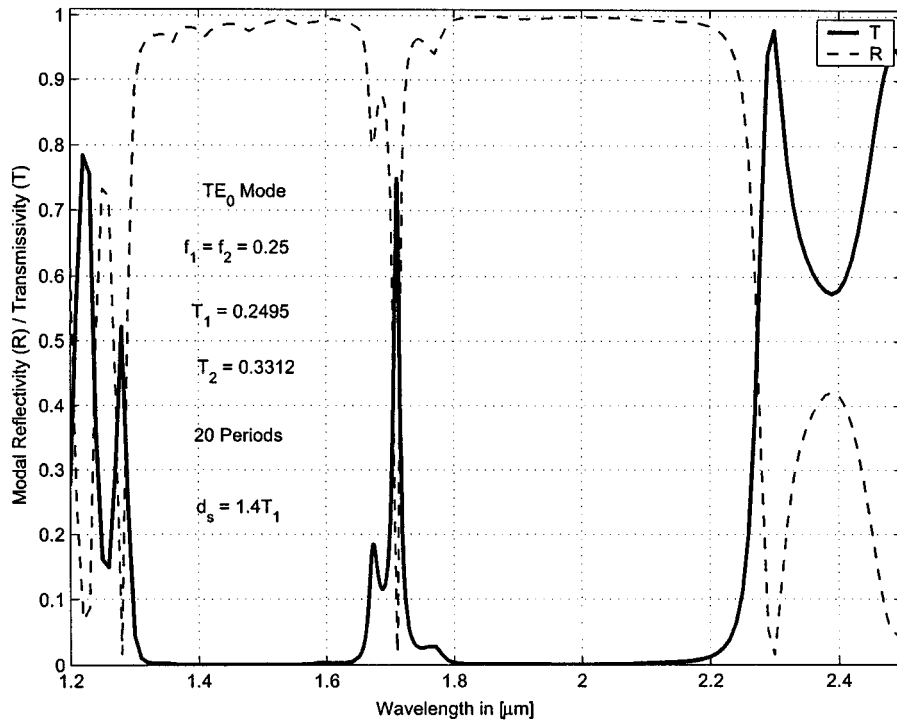
Figure 7.18: Spectral Response of the Asymmetrically Coupled Grating Structure for $d_s = 1.4T_1$ and $T_2 = 0.3312\mu m$.
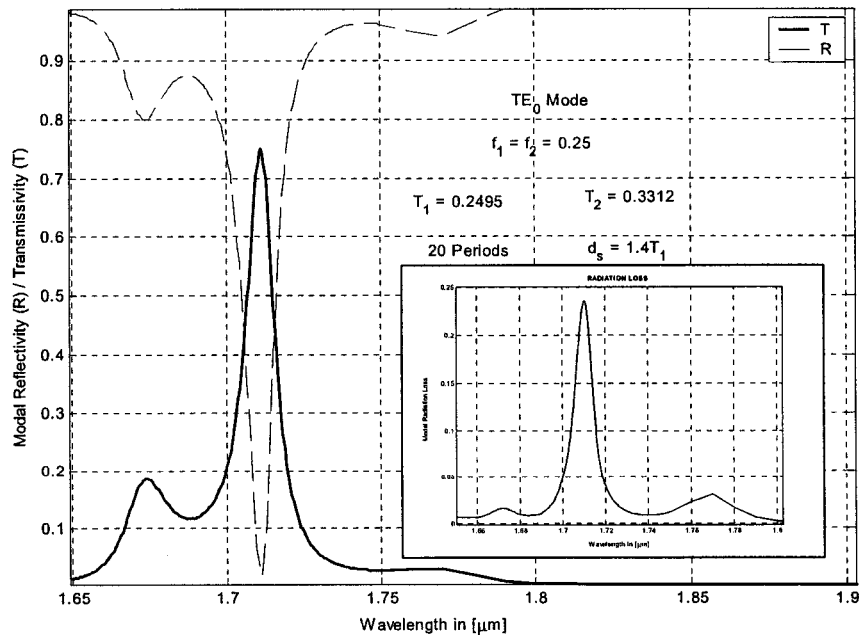
Figure 7.19: Magnified view of the Spectral Response of the Asymmetrically Coupled Grating Structure for $d_s = 1.4T_1$ and $T_2 = 0.3312\mu m$.

spectral width is seen to be wider than the previous results (figs.7.13, 7.11 and 7.15)

obtained, when $T_2 = 0.3176\mu m$. The amount of transmission is also high compared

to the previous results with less radiation. The results are summarized in table 7.2

for quick reference.

d_s	R (%)	T (%)	Ra (%)	$\triangle\lambda(nm)$	$\lambda_c(\mu m)$	$\frac{\triangle\lambda}{\lambda_c}$ (10^{-3})
$1.4T_1$	2	75	23	12	1.7110	7.0134

Table 7.2: Calculated Spectral Width of the Transmission Resonance, in case of an Asymmetrical Coupled Grating Structure, at different d_s. Structure B period is selected to be $T_2 = 0.3312\mu m$.(R, T and Ra corresponds to the Peak Reflectivity, Peak Transmissivity and Peak Radiation Loss, respectively).

From the table it can be inferred that the structure gives relatively superior performance with $T_2 = 0.3312\mu m$ and $d_s = 1.4T_1$, when compared to the performance with $T_2 = 0.3176\mu m$ and $d_s = 1.3T_1, 1.33T_1$ and $1.4T_1$.

7.3 Discussion

An asymmetrically, directly coupled waveguide deep grating structure has been analyzed in this chapter. It is seen that beyond a certain value of the grating period of structure B, a wide band transmission region is seen to develop, which becomes wider with further increase in the grating period. The spectral response of the asymmetrically coupled structure is studied due to left-side and right-side excitations. It has been observed that there is an increase in the radiation towards the lower wavelength for the latter case whereas the transmissivity curve remains the same for both

forms of excitations. The presence of a microcavity in the case of the asymmetrically coupled structure is also studied. As expected, a transmission resonance has been seen to occur within the bandgap. The resonance wavelength varies with the length of the microcavity. The radiation is seen to be high in the asymmetrically coupled case with lower peak transmissivity at the resonance wavelength, when compared to a symmetrically coupled structure. However, with an increase in the grating period of structure B, better higher transmission is observed, but with an increase in the fractional spectral width.

Chapter 8

Analysis of 2D Bandgap Structures

8.1 Introduction

Low-loss bends in the integrated optical circuits are essential to connect various parts of the circuits in order to realize more complex circuit arrangements. Conventional bends are done usually over a curved path with relatively large radius of curvature in order to reduce radiation loss. In some cases however, it is possible to realize 90° turns. These sharp turns help in the relaization of compact integrated optical circuits.

In this chapter, we will study the effect of the formation of a periodic hole pattern in the solid material. The unit period of such structures is commonly known as photonic crystals and the corresponding pattern is known as photonic bandgap

structures [61, 62]. These periodic hole pattern can give rise to a transmission bandgap, which can be used to produce interesting effects, as will be seen in this chapter. We will use these bandgap structures to form a U-turn waveguide, which consists of two 90° turns, and apply the previously developed program to analyze it.

8.2 Analysis of the Air Hole Pattern

A two dimensional composite structure consisting of a square air hole pattern in the solid material, which under appropriate condition can form a 2D bandgap structure, is shown in fig.8.1. The structure and the field are assumed to be uniform in the x-direction and hence this corresponds to a 2D structure. The structure consists of a waveguide at the input and the output ends of the air hole pattern. The shaded regions of the waveguide corresponds to air whereas the white region corresponds to the solid material which is assumed to be GaAs having a refractive index $n =$ 3.6. The length of the pattern comprises of 10 air hole rows (in the direction of propagation of the wave i.e. 10 longitudinal periods L_p) and width of 13 air hole columns (in the transverse direction i.e. 13 transverse periods T_p)(shown in the same figure i.e. fig.8.1). A unit cell or the period (or a photonic crystal) of the periodic air hole pattern (or photonic bandgap structure) is shown in fig.8.2. It is known that with $d_p = 0.364 \mu m$ and $d_a = 0.6 d_p = 0.2184 \mu m$, the structure experiences a full bandgap in the range of $\lambda =$1.49 to 1.62μm, centered at approximately 1.55μm, for the TM waves [63]. For the TE waves, the bandgap is very narrow and therefore the
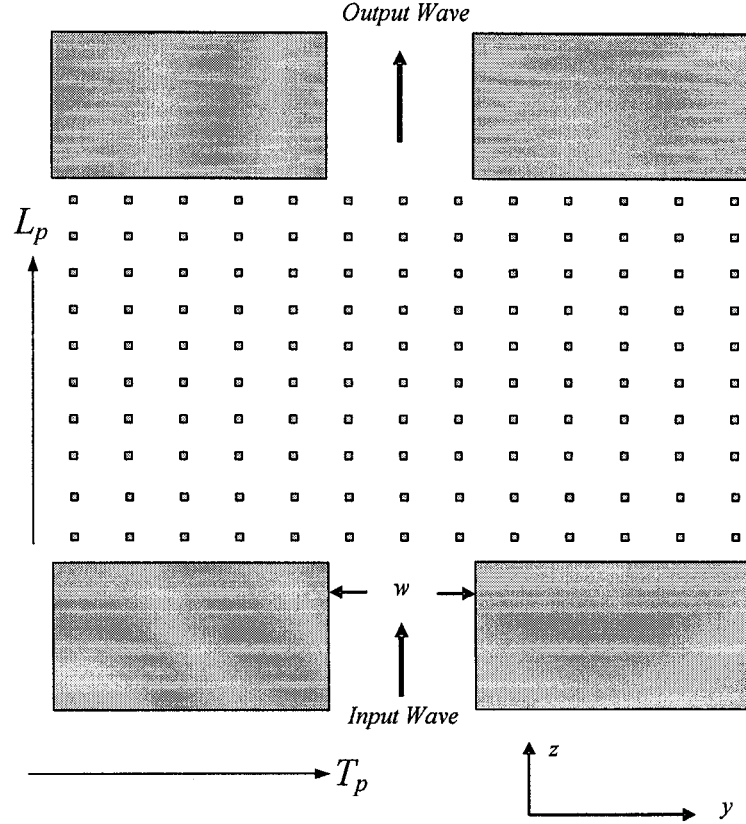
Figure 8.1: The 2D Bandgap Structure (or the Air Hole Pattern) with Input and Output waveguide. The shaded region is air with $n = 1$, the white background corresponds to GaAs with $n = 3.6$ and the waveguide width $w = 0.25\mu m$.

TE response of the structure will not investigated in this thesis. It can be observed that the waveguide width $w = 0.25\mu m$ is approximately same as the width of the air hole. in the figure, the width of the waveguide is drawn wider for clarity. In order to verify the formation of bandgap, the structure is simulated with 1, 2, 4 and 10 longitudinal periods keeping the number of transverse periods constant at 10, using the developed automated program. The results are shown in figs.8.3 to 8.6, respectively. With 1 and 2 longitudinal periods, the bandgap is not fully formed because small number of longitudinal periods, which allows wave transmission in
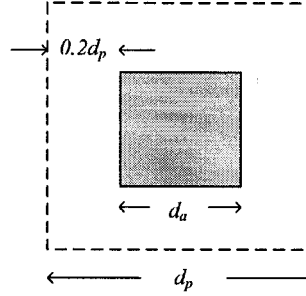
Figure 8.2: A unit cell or period of the Air Hole Pattern. $d_p = 0.364\mu m$ and $d_a = 0.6d_p = 0.2184\mu m$. The shaded region is air whereas the white background corresponds to GaAs with $n = 3.6$.

that wavelength range. However, the formation of a complete bandgap can be observed in fig. 8.6, when the number of longitudinal periods is sufficiently large. In this case, we observe negligible or no power transmission within that range of wavelengths. The two vertical lines in the graph represents the bandgap region with the center wavelength roughly at $\lambda = 1.55\mu m$.

Fig.8.7 shows the effect of the number of longitudinal periods separating the input and output waveguides, on the TM_0 transmissivity. It can be observed that as the number of longitudinal periods increases, the transmissivity drops within the bandgap. From the results it can be concluded that that transmissivity becomes negligible when the number of periods exceeds roughly eight.

8.3 Defects in the Air Hole Pattern

Defects introduced in the air hole pattern can alter the spectral response significantly. A defect corresponds to the absence of an air hole or a group of air holes in
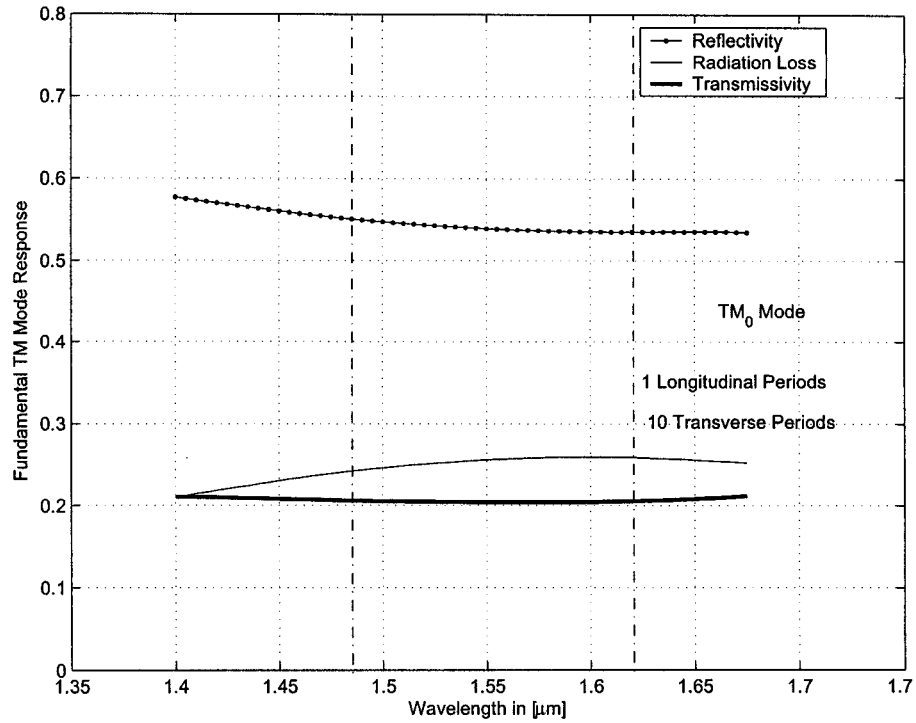
Figure 8.3: Fundamental TM Mode Spectral Response in the case of $1L_p$ separation between the Input and the Output Waveguides.
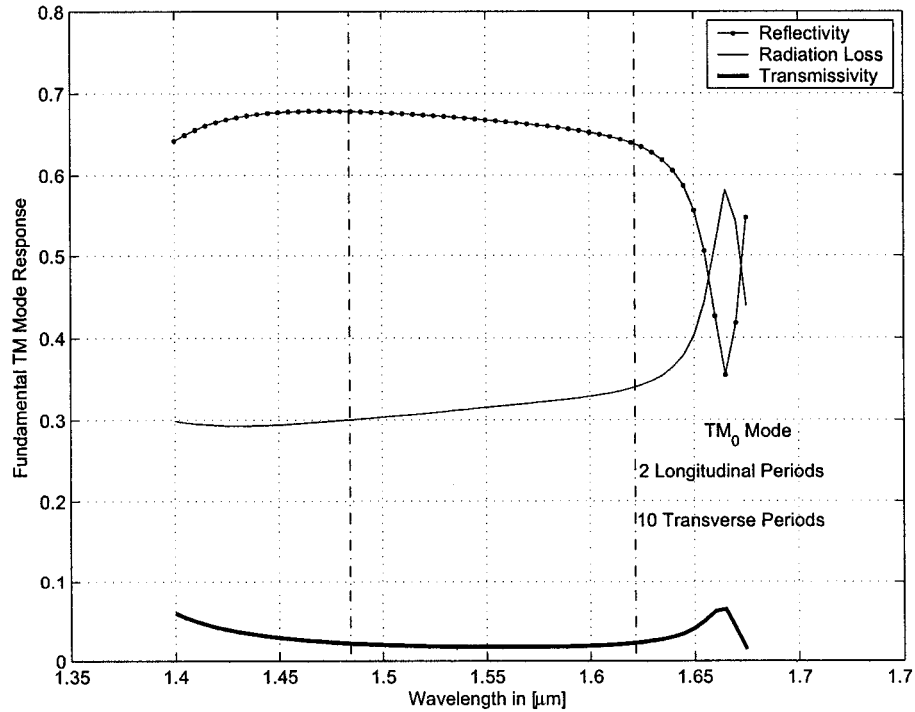
Figure 8.4: Fundamental TM Mode Spectral Response in the case of $2L_p$ separation between the Input and the Output Waveguides.
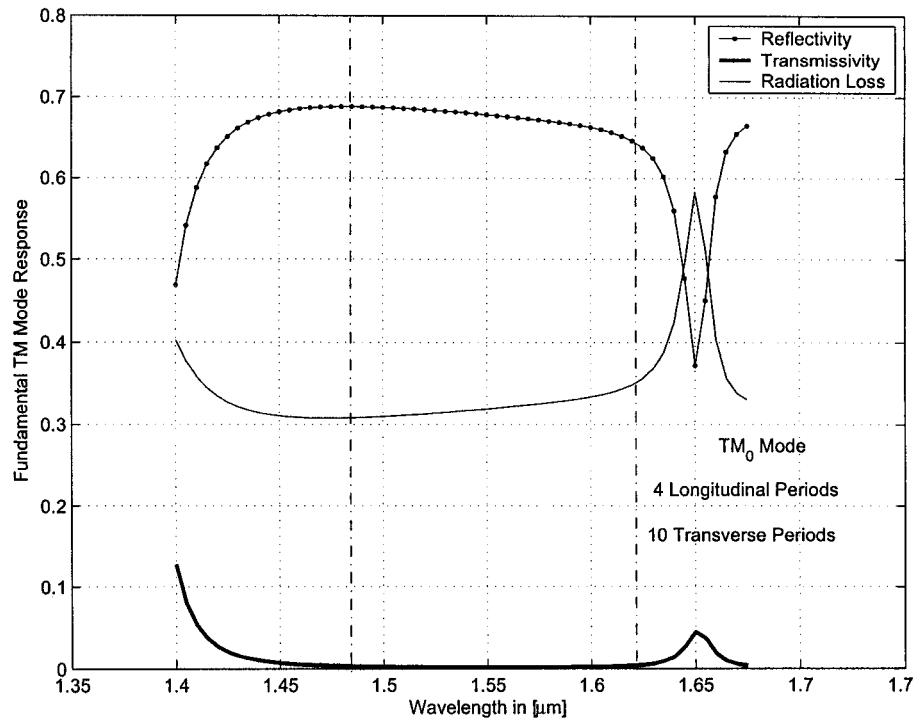
Figure 8.5: Fundamental TM Mode Spectral Response in the case of $4L_p$ separation between the Input and the Output Waveguides.
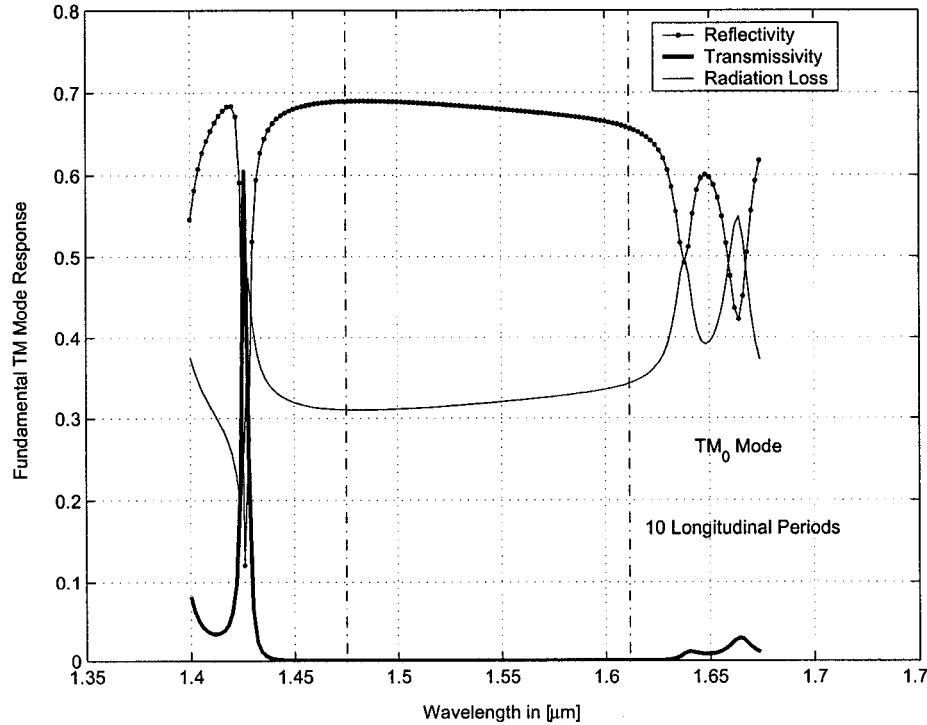
Figure 8.6: Fundamental TM Mode Spectral Response in the case of $10L_p$ separation between the Input and the Output Waveguides.
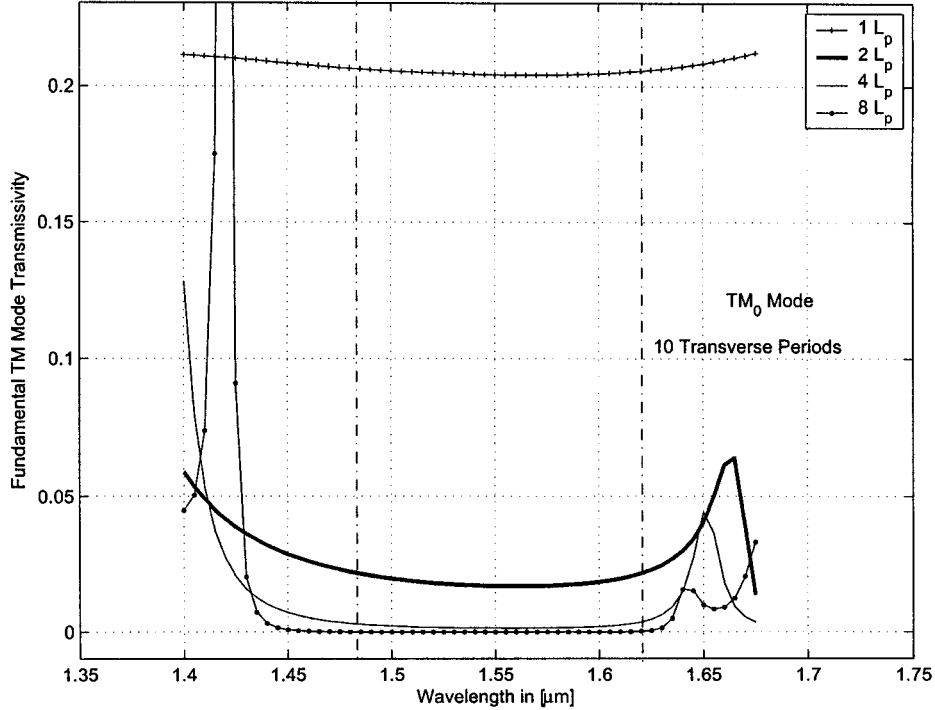
Figure 8.7: Fundamental TM Mode Transmissivity corresponding to different number of periods L_p separating the Input and the Output Waveguides.

the periodic hole pattern. There are various types of defects that can be examined such as a straight line defect and a point defect. We will examine the effect of both types of defects.

8.3.1 The Straight Line Defect

Fig.8.8 shows a straight line defect at the center of the air hole pattern. This defect is constructed by removing all the air holes from the central column. The spectral response of this structure is shown in fig.8.9. There is large increase in the transmissivity suggesting that the line defect is acting as a waveguide which
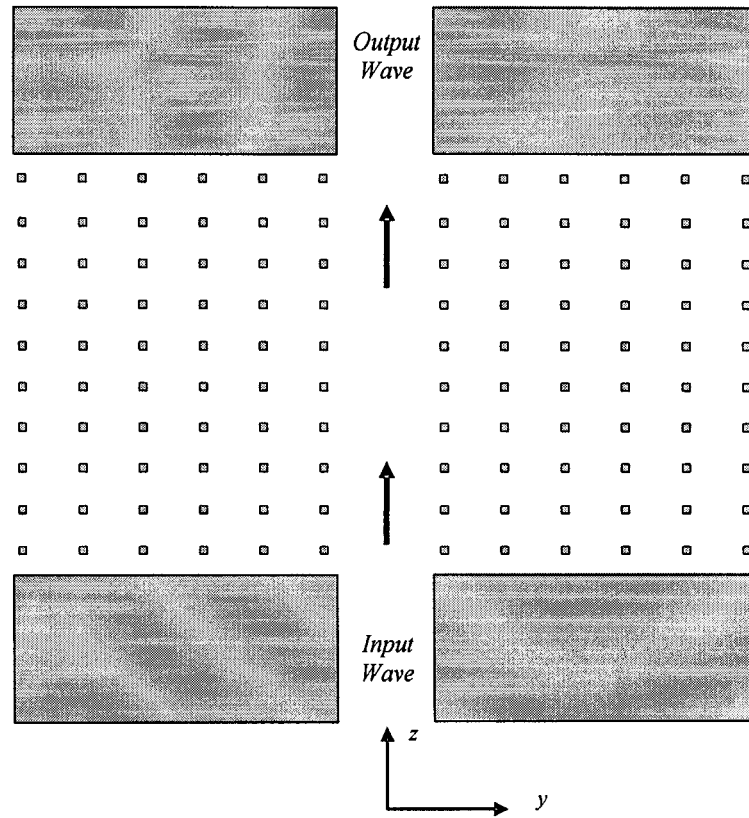
Figure 8.8: Single Line Defect at the Center of the Air Hole Pattern.
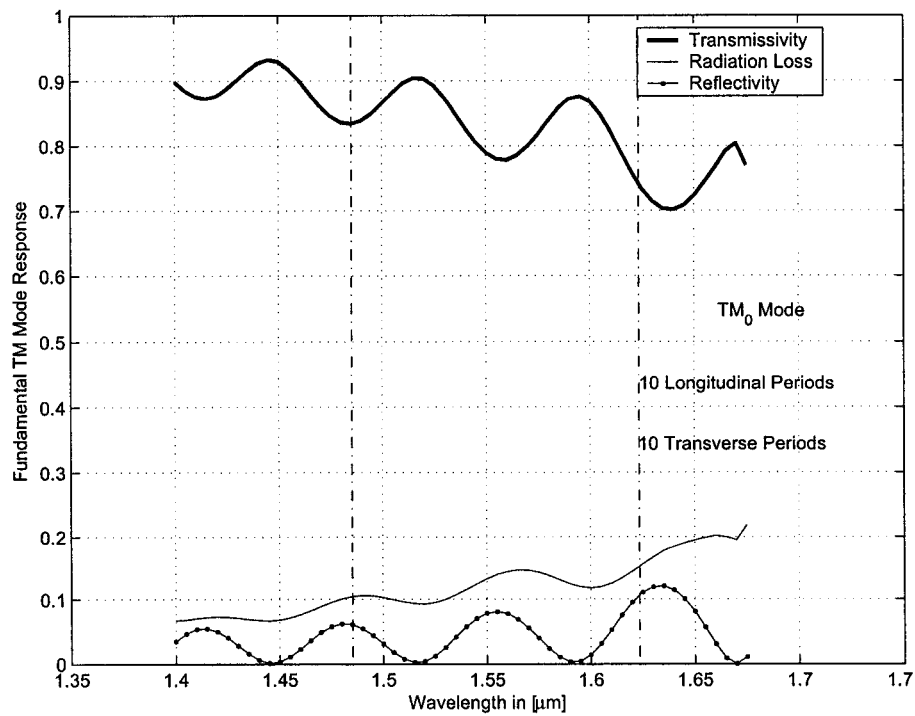
Figure 8.9: Fundamental TM Mode Spectral Response of the Air Hole Pattern with a Straight Line Defect at the Center.

is transmitting the wave from the input to the output ends. Oscillation are seen in the transmissivity and reflectivity curves. The oscillatory behavior reveals that the air hole pattern between the input and output waveguide is acting as a cavity. This cavity effect is due to the reflections due to mismatch between the conventional waveguide and the waveguide formed by the straight line defect (at both the input and output ends).

Figs.8.10 and 8.11 corresponds to the same line defect, but with different number of longitudinal and transverse periods, respectively. Fig.8.10 shows the results of the simulation using different number of longitudinal periods, keeping the number of transverse periods constant. It can be inferred from the figure that the transmissivity remains high with oscillatory behavior, even when the number of longitudinal period is very high (2000). It can also be observed that the oscillations in the curve increases as the cavity length increases. Fig.8.11 corresponds to the results of the single line defect for various number of transverse periods, keeping the longitudinal periods same. It can be seen that, with 2 and 4 transverse periods, the modal transmissivity is reduced. This suggests that the waveguide formed from the line defect is highly lossy due to leakage in the transverse direction. But with five and above transverse periods, the line defect produces a substantially lossless guidance.
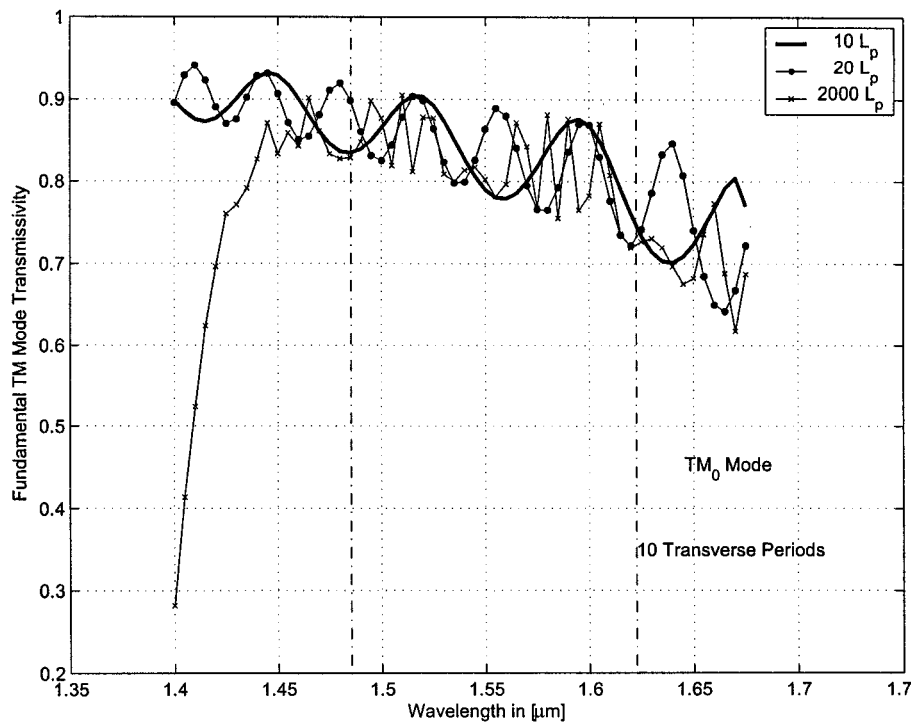
Figure 8.10: Fundamental TM Mode Transmissivity of the Air Hole Pattern with a Straight Line Defect at the Center. Effect of Limiting the number of Longitudinal Periods.
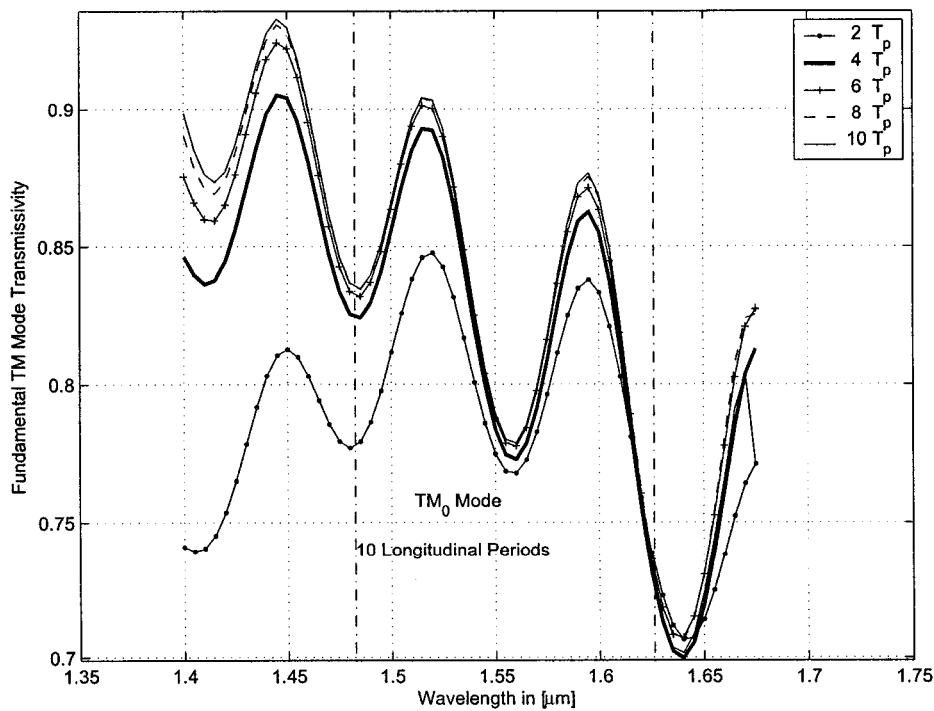
Figure 8.11: Fundamental TM Mode Transmissivity of the Air Hole Pattern with a Straight Line Defect at the Center. Effect of Limiting the number of Transverse Periods.

8.3.2   Effect of the Complete Absence of Air Hole Pattern

In order to have a good understanding of the effect of the lossless waveguide forma-
tion by the single line defect between the input and output waveguides, the structure
is simulated again by removing all the air holes from the air hole pattern. The results
of the resulting transmissivity and radiation loss at different longitudinal periods are
shown in figs.8.12 and 8.13, respectively. It can be seen that the transmissivity is
very low and becomes negligible as the separation (length) between the input and
the output waveguides is increased. The transmissivity becomes zero when the sep-
aration becomes very large (2000 longitudinal periods). Thus, it can be concluded
that the air hole pattern in this case acts as an unbound medium and hence, the
input beam expands very rapidly resulting in very low transmissivity and high ra-
diation loss. The energy of the input beam is almost completely radiated when
the separation between the input and the output waveguide is large, as depicted
in fig.8.13. In this case, the remaining power is reflected and coupled to the input
waveguide. Again due to the cavity effect, oscillatory behavior is observed which
increases in spatial frequency with the increase in the cavity length.

8.3.3   A Single Point Defect

A single point defect is introduced within the straight line defect, as shown in fig.8.14.
The resulting structure is simulated in order to calculate the modal transmissivity
as shown in fig.8.15. A narrow reflection resonance or transmission null is seen close
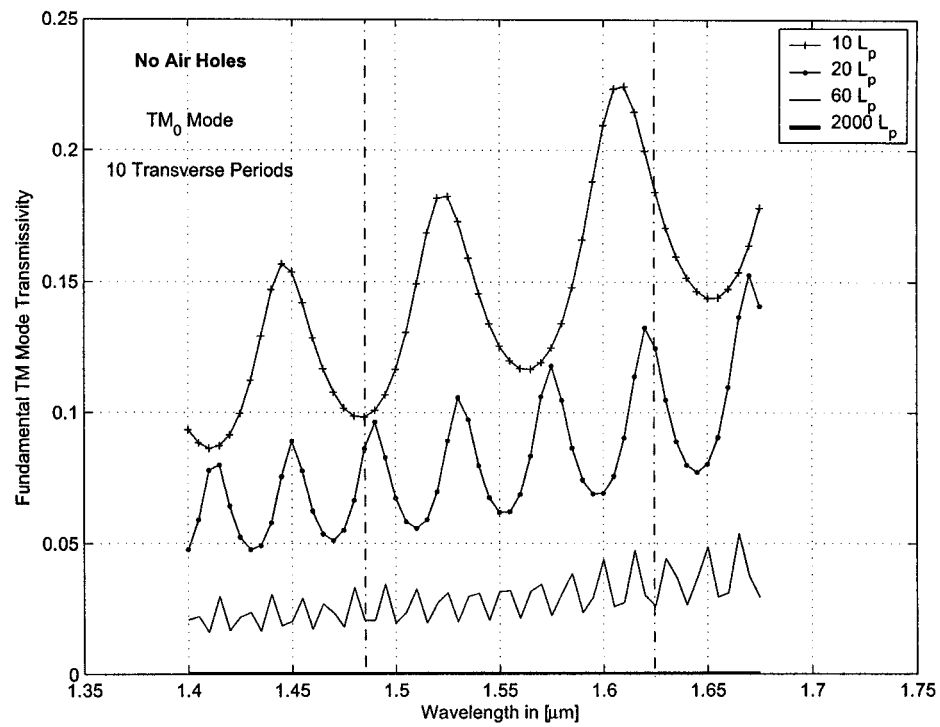
Figure 8.12: Fundamental TM Mode Transmissivity of the Structure in the Absence of the Air Hole Pattern.
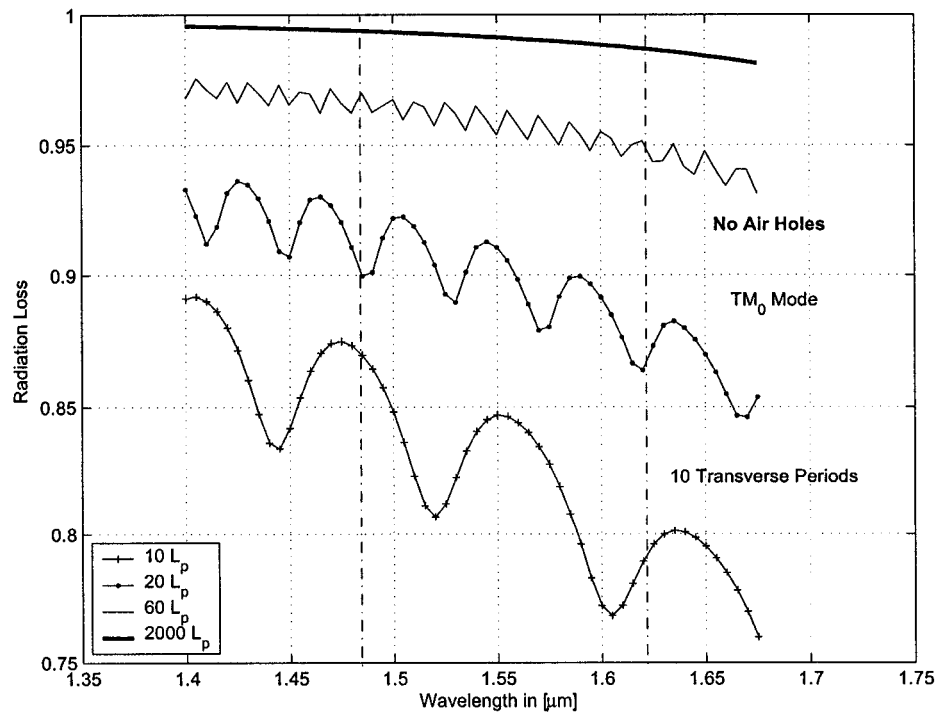
Figure 8.13: Fundamental TM Mode Radiation Loss of the Structure in the Absence of the Air Hole Pattern.
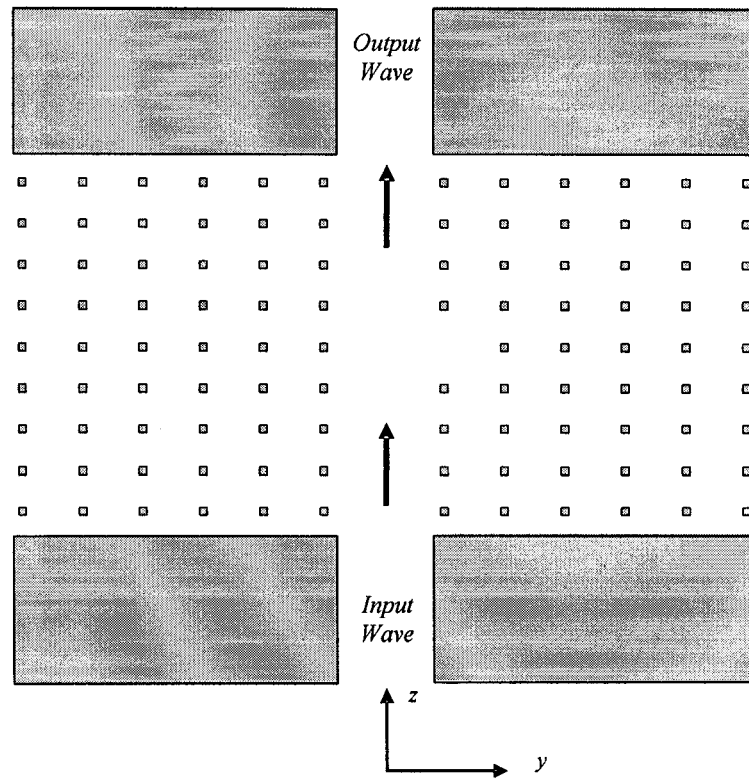
Figure 8.14: A Single point Defect introduced at the Center of the Straight Line Defect.
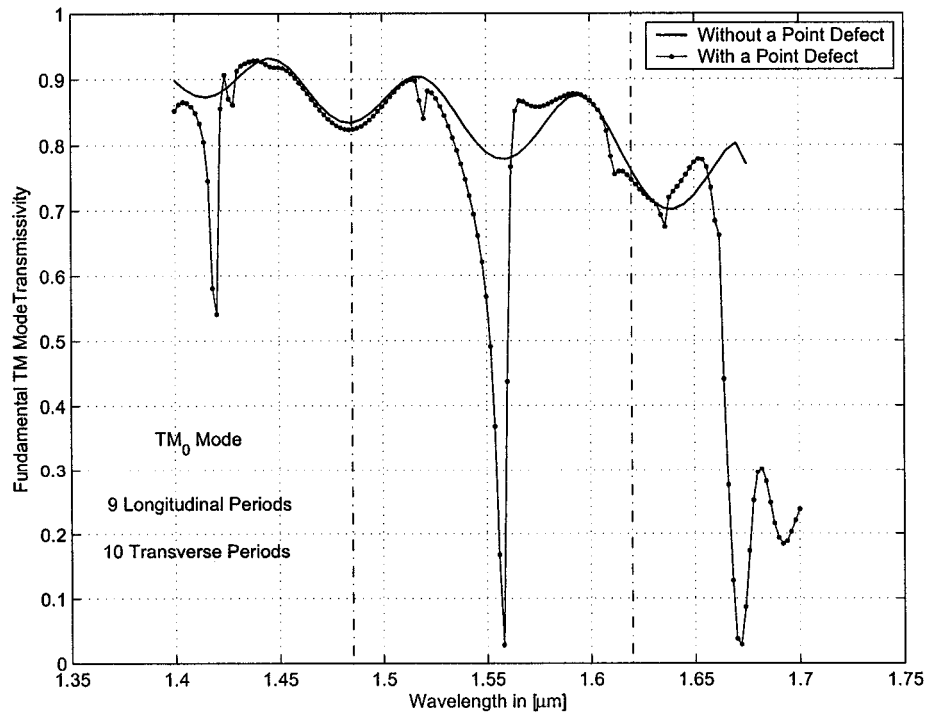
Figure 8.15: Fundamental TM Mode Transmissivity due to a Single Point Defect at the Center of the Line Defect.
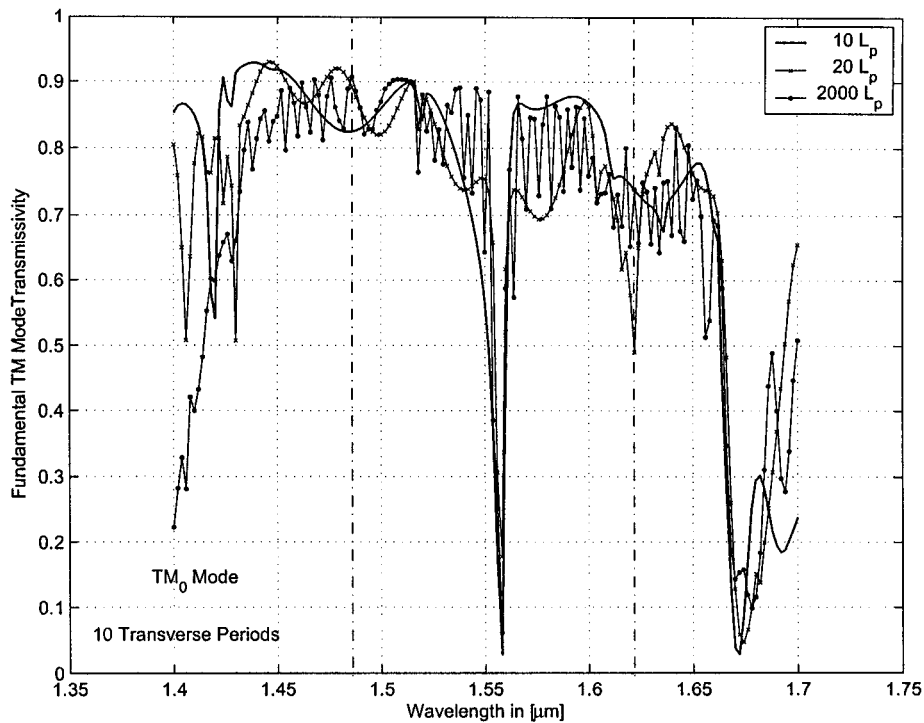
Figure 8.16: Fundamental TM Mode Transmissivity due to a Single Point Defect at the Center, for Different Longitudinal Periods.

to the center wavelength $1.55\mu m$ within the bandgap. Fig.8.16 shows the response of the structure simulated using different number of longitudinal periods. It can be observed that the position and width of the transmission null is almost independent of the length of the cavity, provided, the point defect remains at the middle of the straight line defect.

8.4 The Semi Infinite Air Hole Pattern

Fig.8.17 shows an example of the structure, where the output slab waveguide does not exist and instead, the input waveguide is coupled to a semi-infinite air hole
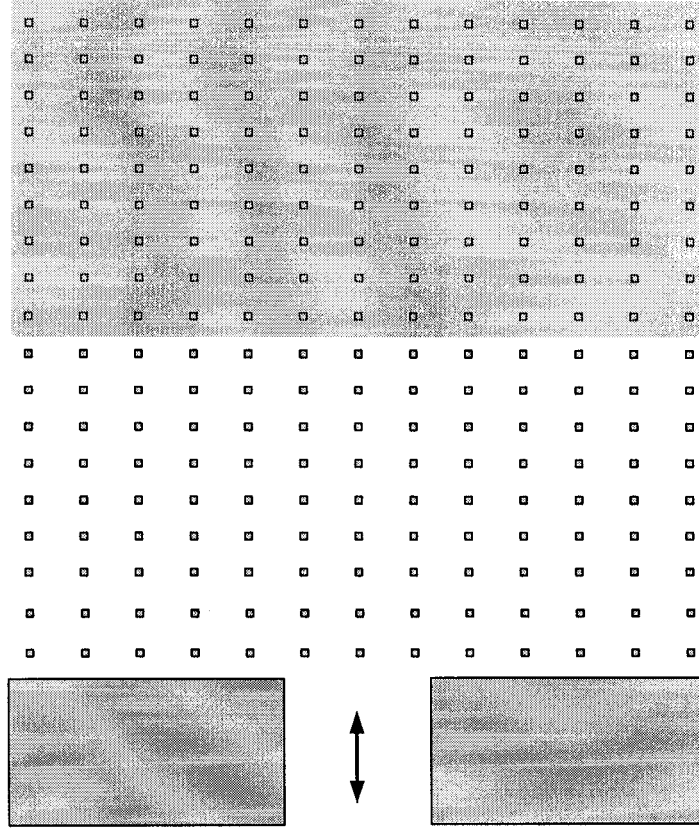
Figure 8.17: The Air Hole Pattern with Input waveguide and Semi-Infinite Termination.

pattern in the z-direction. The semi-infinite air hole patterns or the semi-infinite termination (SIT) is shown with the light gray shading. This part of the structure is made lossy while the other part (unshaded part) is lossless. The SIT is implemented numerically by assuming very small material loss in the SIT, so that the wave does not experience a discontinuity when it crosses the lossless side and enters into the lossy side. The number of longitudinal periods in the SIT is made very large, so that the field becomes negligible at the output end, thus simulating a semi-infinite termination. For this purpose, we used $2^{16} = 65536$ lossy longitudinal periods within the SIT. A suitably small uniform loss is introduced into the corresponding air and
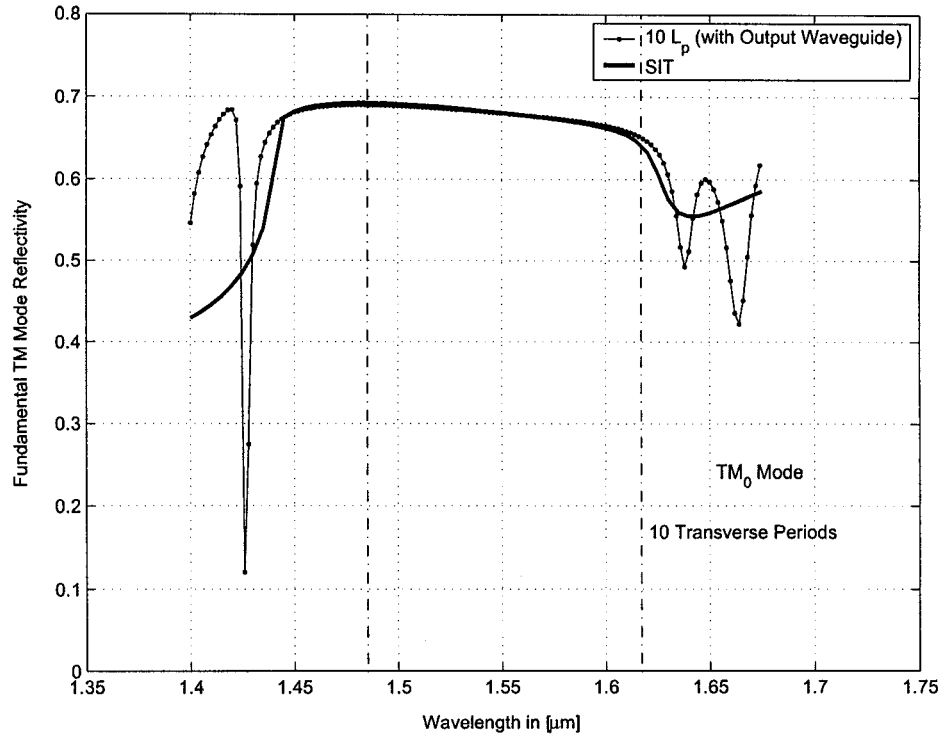
Figure 8.18: Fundamental TM Mode Reflectivity of the Structure (fig.8.17) with a Semi-Infinite Termination.

GaAs materials, resulting in $n_{air}^2 = 1.00^2 + j5 \times 10^{-4}$ and $n_{GaAs}^2 = 3.60^2 + j5 \times 10^{-4}$ within the SIT. The tuning of the SIT (namely, the selection of the appropriate number of longitudinal periods and the loss) will not be discussed in this thesis, the reader is referred to [63] for details. The material outside the SIT remains lossless.

The modal reflectivity of the structure (fig.8.17) is shown in fig.8.18. It can be noted that there is no oscillatory behavior outside the bandgap now because of the absence a mismatch at the output section (the absence of the cavity).

A straight line defect with SIT at the output side is shown in fig.8.19. The finite length straight line is terminated by the semi-infinite termination without a line
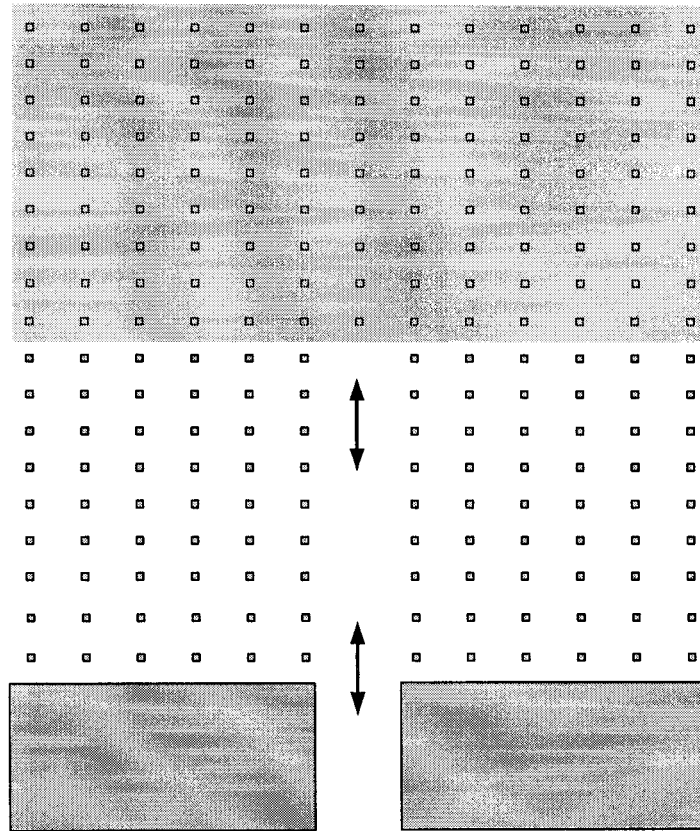
Figure 8.19: The Air Hole Pattern with Straight Line Defect and Semi-Infinite Termination.
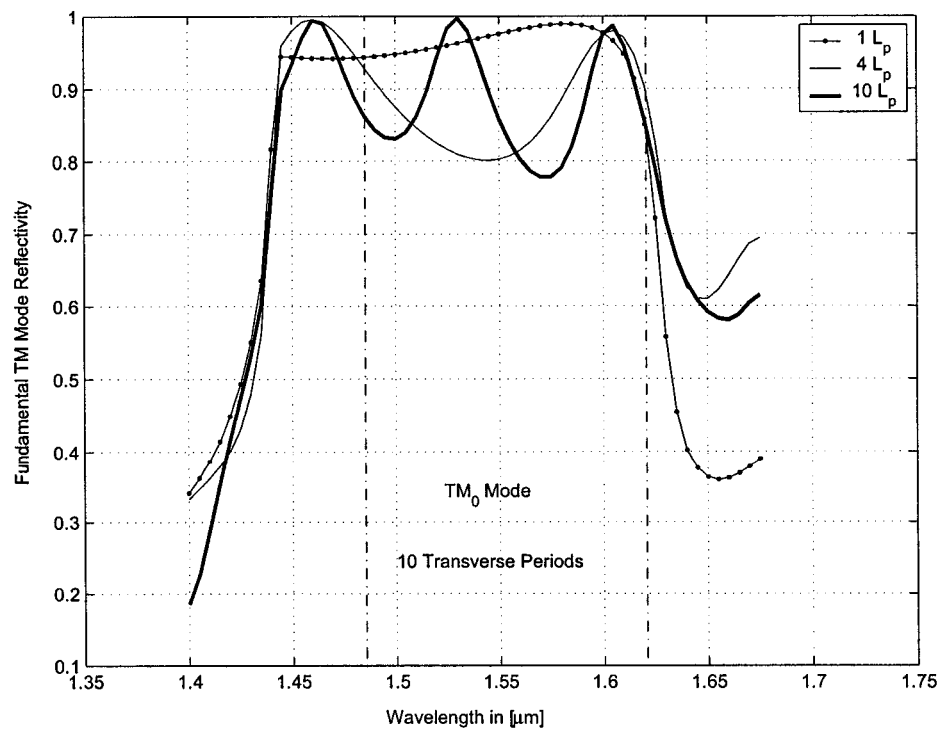
Figure 8.20: Fundamental TM Mode Reflectivity of the Structure (fig.8.19) with a Semi-Infinite Termination, for various Cavity Lengths.
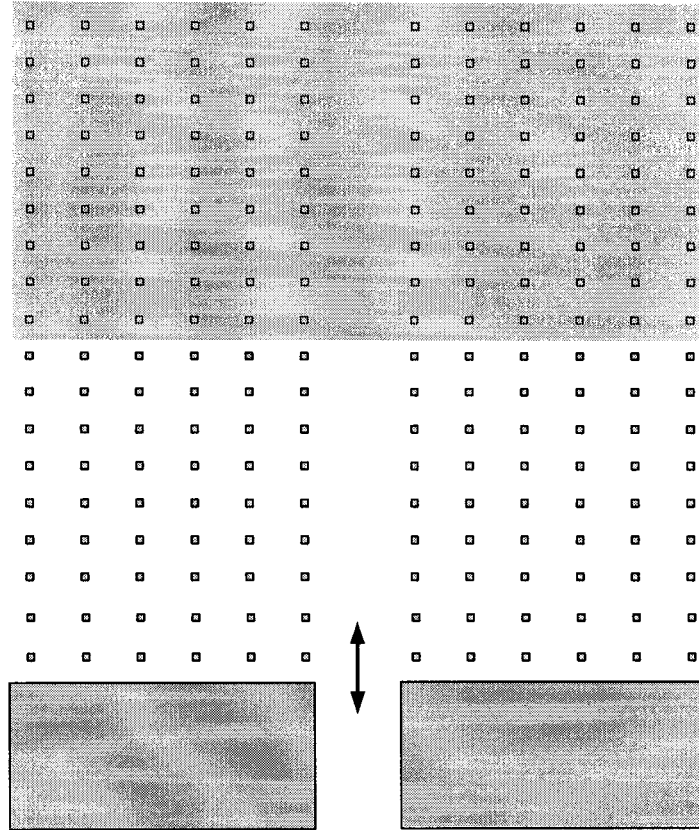
Figure 8.21: A Straight Line Defect and a Straight Line Defect within the Semi-Infinite Termination.

defect. The length of the straight line (i.e. the number of longitudinal periods) is varied and the modal reflectivity is calculated and shown in fig.8.20. The reflectivity curve remains relatively high within the bandgap when the line defect is very short $(1L_p)$. There is no oscillations in the curve because of very short cavity length. However, when the length of the straight line is increased, the oscillatory behavior is clearly observed.

Fig.8.21 corresponds to a straight line defect, using SIT with a matching straight line defect. The arrangement simulates as semi-infinite straight line defect. Here the wave also does not experience any discontinuity upon transition from the loss-
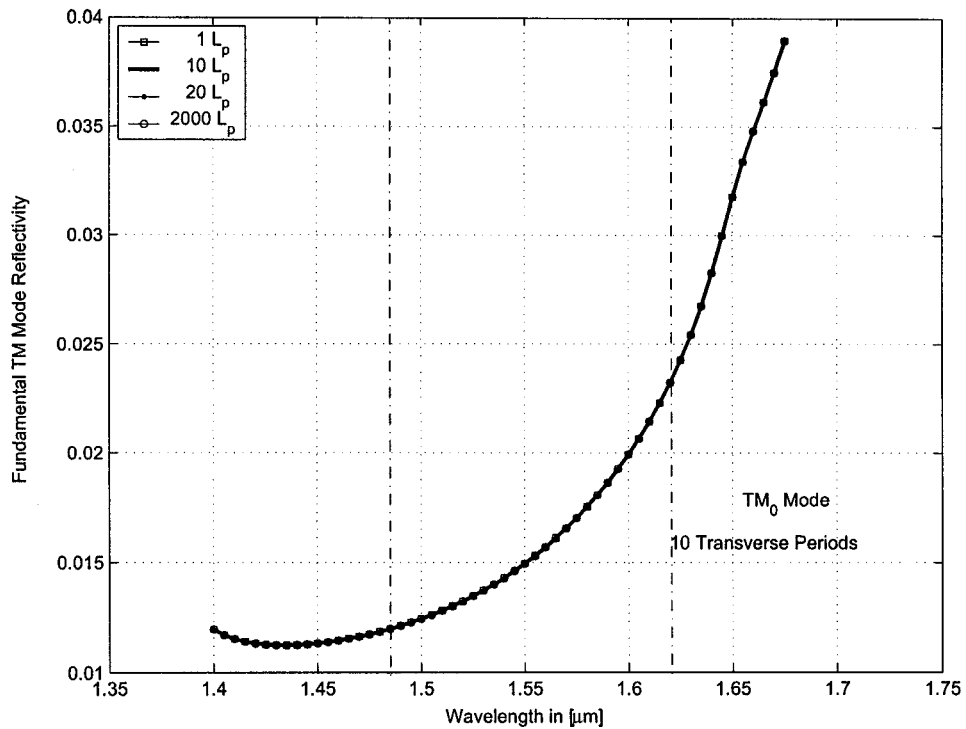
Figure 8.22: Fundamental TM Mode Reflectivity due to a Semi-Infinite Termination Line Defect.

less to the lossy region. The wave thus experiences only a single mismatch at the input waveguide/line defect interface. The results are summarized in fig.8.22. The reflectivity is very small and is only due to the reflections at the input waveguide and the line defect interface. The reflectivity curve remains unchanged (and without any oscillations) when the length of the line defect in the lossless region is varied, confirming zero reflection at the lossless/lossy interface and thus confirming the applicability of the current method of SIT implementation .
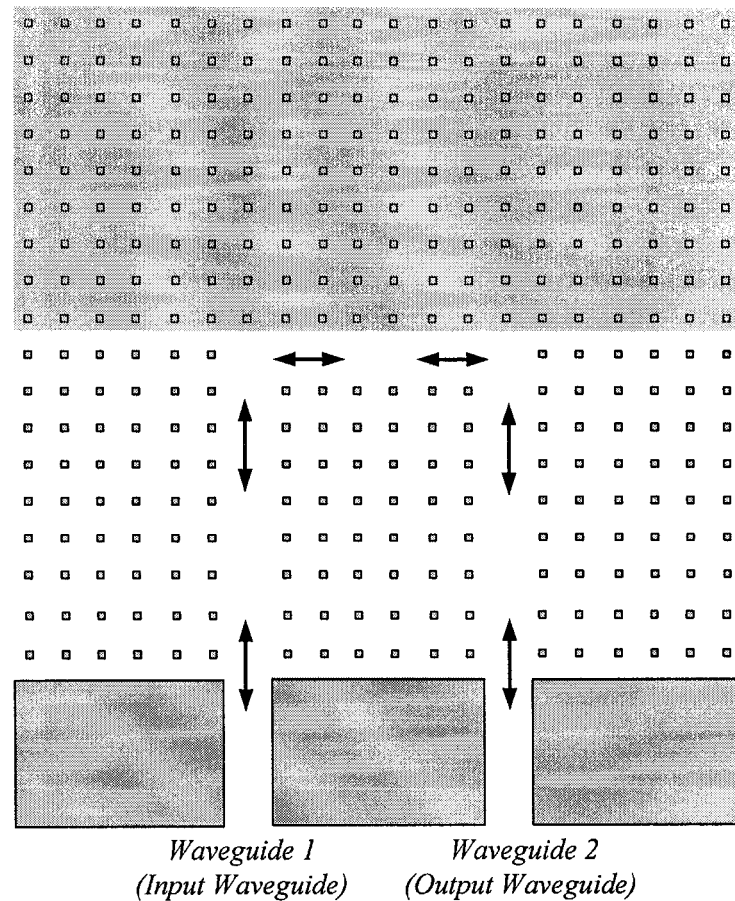
Figure 8.23: The Line Defect that forms a U-turn.

8.5 Response of a U-Turn Defect Waveguide

Fig.8.23 shows a line defect that forms a U-turn. The two slab waveguides at the input plane are sufficiently separated by the air region. The input power is injected into the waveguide on the left hand side (waveguide-1). The field is guided by the straight line defect before it encounters a sharp 90-degree turn. Part of the field will in general be reflected at this turn and the remaining part will be transmitted. In a similar fashion part of the field is transmitted through the second sharp 90-degree turn. In this manner, it is possible for the field to make a U-turn and exits out of the
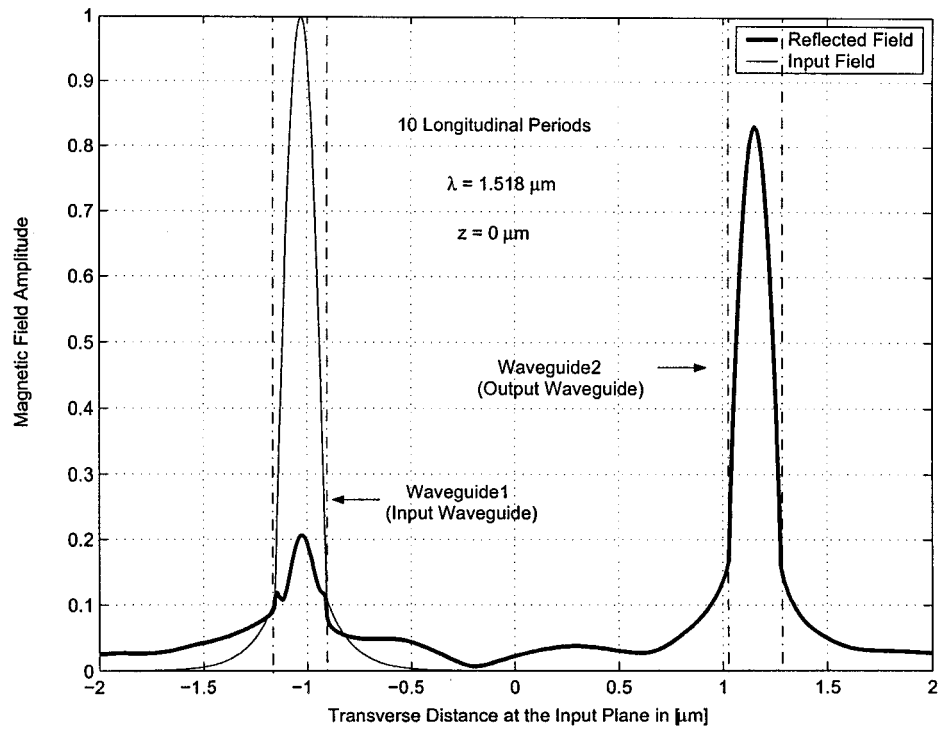
Figure 8.24: Incident and the Reflected Magnetic Field at the Input Plane. The right hand part of the Reflected Field represents the Field that exits out of the Output Waveguide. The vertical lines indicate the input and the output waveguide boundaries.

slab waveguide on the right-hand side of the input plane (waveguide-2). Therefore, waveguide-1 is the input waveguide and waveguide-2 is the output waveguide.

Fig.8.24 represents the magnetic field amplitude at the input plane at $\lambda = 1.518\mu m$. The input magnetic field pattern is also shown in the figure, whose center occurs just below $y = -1\mu m$ which corresponds to the center of the input waveguide (waveguide-1). The reflected field is also shown in the same figure. As seen in the figure, most of the reflected field exits out of the output slab waveguide (the right-hand side of the waveguide i.e. waveguide-2) and some of the reflected field exits out

of the input waveguide (the left-hand side of the waveguide i.e. waveguide-1). For clarity vertical lines are shown in the figure which corresponds to the waveguide-1 (input waveguide) and waveguide-2 (output waveguide). In other terms the output field, available on the right hand side (centered near $y = 1.15 \mu m$) is the transmitted field or the output field from the U-turn. The U-turn waveguide is 10 longitudinal periods long and 5 transverse periods wide (5 transverse periods between each line defect).

Fig.8.25 shows the reflected field at different wavelengths. The transmission is maximum at $\lambda = 1.518 \mu m$ which corresponds to the resonance wavelength. The transmitted field at this wavelength is relatively large, suggesting near matched conditions of reflectionless transmission through the two 90 degrees sharp turns. The transmitted field below and above $\lambda = 1.518 \mu m$ is less than the maximum possible.

The return power in waveguide-2 (output waveguide) or in other words the output power of waveguide-2 or fraction of the power transmitted, as a function of wavelength is shown in fig.8.26. It can be seen that two transmission resonance are observed which are close to the bandgap edges. The transmitted power at the center wavelength of the bandgap ($\lambda = 1.55 \mu m$) is seen to be almost zero. Thus, the U-turn waveguide transmits the electromagnetic field with minimum loss for only certain wavelengths, to the output end, thereby making this configuration potentially useful in optical communication systems, serving as a wavelength filter.

The CPU (P4 machine with 256MB RAM running under Windows XP Operating
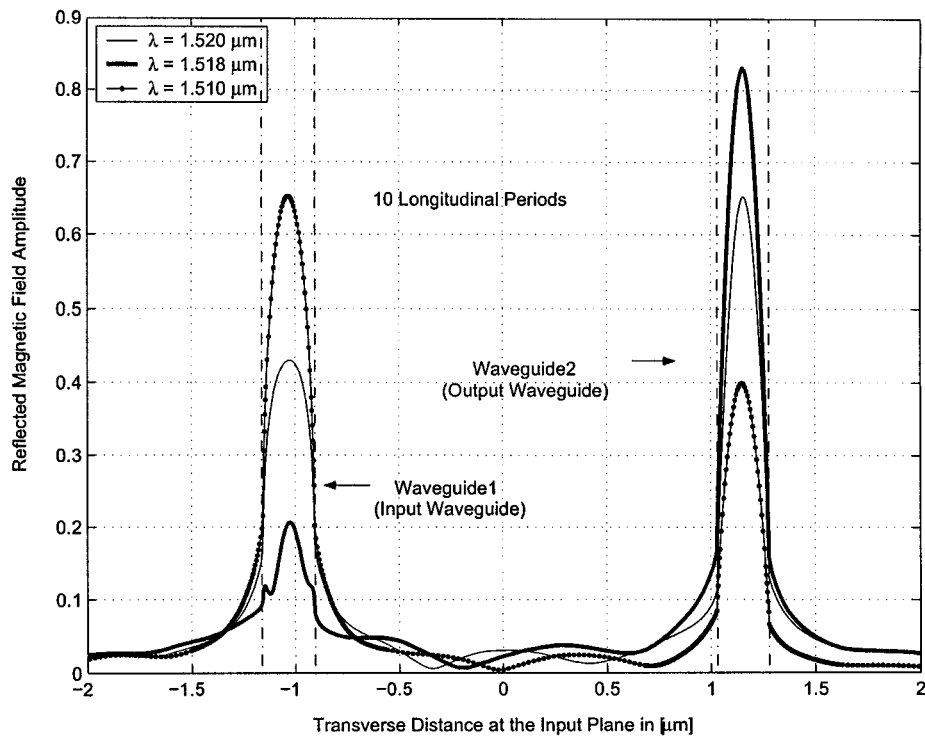
Figure 8.25: Reflected Field Patterns below, at, and above the Resonance Wavelength. The right hand side of the Reflected Field constitutes the Transmitted Field. The vertical lines indicate the input and the output waveguide boundaries.
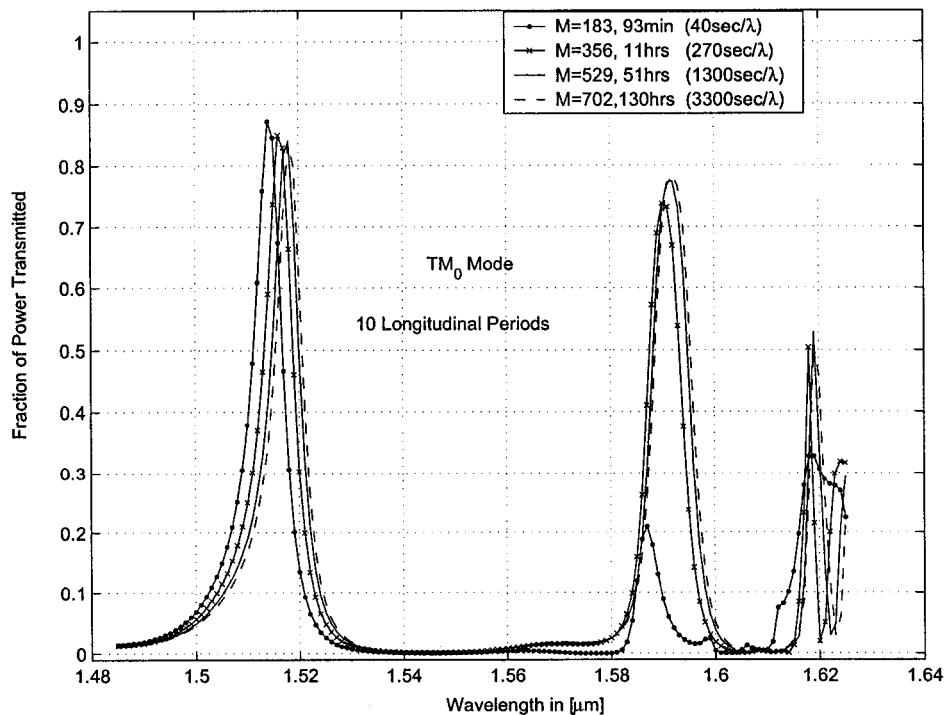
Figure 8.26: Fraction of Power Transmitted through the U-Turn Line Defect.

System) runtime to obtain the curves of the fraction of the transmitted power, is shown in the legend of the same figure. The program took 1300 seconds per wavelength, to simulate the structure, with 529 mesh points within the waveguide (excluding the PML points) where as, for 702 mesh points (excluding the PML points), the CPU took 3300 seconds per wavelength.

8.6   Discussion

Our simulation has confirmed the formation of 2D bandgap in the periodic hole pattern. The effect of the number of longitudinal periods on the bandgap has been examined. The straight line defect, the point defect, the complete absence of air-hole pattern, has been considered in the chapter. It is seen that with a straight line defect, the structures acts as a lossless waveguide within the bandgap. A sharp transmission null is seen, when a point defect occurs at the center of the line defect. In the third case, i.e. in the complete absence of air-hole pattern, the transmission decreases and becomes negligible with the increase in the distance between the input and the output waveguide, which is due to the loss of guidance.

The concept of semi-infinite termination is introduced and demonstrated. A U-turn defect has also been considered. This type of defect results in a U-turn waveguide with two 90 degrees turns. The calculated results of the of the U-turn waveguide, reveals two transmission resonances within the bandgap with relatively high power transmission.

Chapter 9

Summary, Conclusion and Future

Work

The numerical technique for the analysis of guided-wave structures used in this thesis is the Method of Lines (MOL). Enhancements to the MOL has been carried out in this thesis by use of improved higher order approximation of the transverse second derivative operator and absorbing boundary conditions. An efficient, general and user friendly program has been developed. This program has been used for the analysis of the symmetrical and asymmetrical 1D deep grating structures as well as 2D deep grating structures. In the subsequent sections, a brief summary of the work that has been carried out in the thesis, is presented followed by conclusions and some future extensions to the work.

149

9.1   Summary

- The improved higher order approximation of the transverse second derivative operator has been incorporated in the MOL. The three-point, five-point and seven-point approximations were implemented and evaluated for a waveguide structure with a high index contrast.

- The absorbing boundary condition (Perfectly Matched Layer) has been successfully incorporated into the MOL with improved performance. The PML with a non-uniform loss profile has been simulated and tested. The PML has been used extensively throughout the thesis for absorbing the radiative field.

- Longitudinal waveguide discontinuities has been studied using the improved MOL. The single and multiple discontinuities results have been compared with published results. The layer by layer method and the cascading and doubling algorithms were used to analyze multiple longitudinal discontinuities.

- A numerically efficient program using the enhanced MOL, is developed based on the cascading and doubling algorithm. The program can calculate the spectral response of optical waveguides with arbitrary longitudinal discontinuities in an efficient manner. It is made user friendly so that the user does not require an in depth knowledge of the program. The results of the automated program were checked with the layer by layer method, which served as a verification tool in this thesis.

- Various interesting deep grating structures were considered in this thesis. The spectral response of the symmetrically and asymmetrically coupled guided-wave 1D deep grating structures were obtained and analyzed. The spectral response of 2D deep grating structures were also obtained. The effect of the straight line defect and the point defect were considered. The spectral response of a U-turn waveguide formed within the 2D periodic hole pattern has been calculated.

9.2 Conclusions

- The improved higher order approximation of the transverse second derivative operator gives good accuracy of the effective index with relatively small number of mesh points. The approach used in the approximation allows the refractive index and the mesh size to vary in an arbitrary manner from one layer to the other, resulting in a flexible and numerically efficient routine. The program treats all the mesh points in a unified manner irrespective of the location of the mesh point. The results of the calculated and exact values are compared by simulating a high index contrast waveguide, which revels the high accuracy of the approach.

- An improved PML utilizing a non-uniform loss profile is shown to give relatively superior performance when compared to the PML with uniform loss profile, using a smaller number of mesh points in the PML layer. The effective

implementation of the improved PML has been demonstrated by launching gaussian beam in glass and comparing the calculated results with analytically available ones. The results almost coincide with each other.

- The layer by layer and the cascading and doubling algorithms were used to calculate the spectral response of the optical waveguide with longitudinal discontinuities. The results of both methods were compared with the published results. The results show excellent agreement with published results. The two algorithms give identical results. This fact has been demonstrated by simulating periodic optical waveguides using both methods.

- The automated program is developed successfully and its results were compared with the verification tool. Excellent agreement is seen between the two approaches, establishing the accuracy of our programming. The program is made user friendly with a high degree of freedom in selecting the order of approximation, the loss profile of the PML layer, the number of mesh points in the PML layer, etc.

- A guided-wave deep grating structure is studied and the effect of the number of grating periods, the filling factor and the groove depth, on the spectral response of the structure were analyzed. It is seen that, with eight grating period, a bandgap in the wavelength range of 1.3 μm to 2.2 μm is produced, in which there is no transmission of electromagnetic wave. It has been shown that, an increase in the filling factor shifts the bandgap towards lower wavelengths and

that the main lobe becomes wider. It is concluded that, with an infinite groove depth, the bandgap is formed with minimal radiation loss whereas for a finite groove depth, leakage within the bandgap occurs.

- The effect of the length of the microcavity and the filling factor is investigated for the symmetrically coupled deep grating structure. As a result, a narrow transmission resonance is seen to occur within the bandgap. The position and width of the transmission resonance varies with the length of the microcavity. The filling factor has a very small effect on the position of the transmission resonance.

- In the case of asymmetrically coupled deep grating structure, the bandgap become wider, as the grating period of structure B increases. It has been shown that beyond a certain value of the grating period of structure B, a wide band transmission window is seen to develop, which become wider with further increase in the grating period. The spectral response of the asymmetrically coupled structure is studied due to left-sided and right-sided excitations. It has been observed that there is an increase in the radiation for the latter case whereas the transmissivity curve remain the same for both type of excitations. Similar behavior is observed for an asymmetrical structure, when coupled by a microcavity, as in the symmetrically coupled structure case. A transmission resonance occurs within the bandgap and the resonance wavelength varies with the length of the microcavity. The radiation is seen to be high in the

asymmetrically coupled case when compared to the symmetrically coupled structure.

- In general, the symmetrically coupled structure results in a higher transmissivity at resonance than the asymmetrically coupled structure.

- Simulation of the 2D bandgap structures confirms the formation of a bandgap for TM polarized waves. The semi infinite termination (SIT) has been introduced at the output end of the 2D bandgap structure in order to simulate a semi-infinite periodic structure. The effectiveness of the SIT has been demonstrated.

- A U-turn waveguide formed by defects in the air hole pattern has been simulated. It is seen that this waveguide allows electromagnetic waves of a certain wavelength range to pass through it and become available at the output with minimum reflections at the two sharp 90 degree turns forming the U-turn waveguide. Two transmission resonances were seen within the bandgap with about 80% relative power transmission.

9.3 Future Prospects

The following are some possible future research activities:

- The periodic guided-wave deep grating structures were analyzed in this thesis work. One can look into the behavior of an aperiodic guided wave deep grat-

ing structures and subsequently to symmetrically coupled and asymmetrically coupled structures constructed from them.

- Extension of this work to three dimensional guided-wave grating structures is also of importance, since simulation based on a 3D waveguide model is more realistic than that based on the 2D model. However, extension of the MOL to the 3D space is known to result in prohibitive computational time and memory requirements. Calculation of the eigenvalues and eigenvectors are computationally very demanding in the 3D case and prohibitive in most cases. An alternative approach in the implementation of the MOL need to be developed. A recently reported approach based on Pade approximants appears to be a good candidate for this task.

- The grating structures which were analyzed in this thesis utilizes a single mirocavity separating the waveguide gratings. A structure with two or more mocrocavities may prove to have interesting features and thus may be a subject of investigation.

Appendix A

The Three-Point Central

Difference Approximation

To obtain an expression for the discretized second derivative of a certain function, we express the function in terms of a power series. We can have a good approximation of the given function in terms of a polynomial by neglecting all except the first few terms of the resulting series. One of the most convenient power series is the Taylor's Series which can be expressed as:

$$f(x) = \sum_{n=0}^{\infty} \frac{f^{(n)}(a)}{n!} (x - a)^n \tag{A.1}$$

where $f^{(n)}$ is the nth derivative of $f(x)$ with respect to x.

If Taylor's series is expanded about $x = 0$, the resulting series is often called a Maclaurin's Series expansion. Expanding $\psi(x)$ about $x = 0$ using equation A.1:

$$\psi(x) = \psi(0) + \frac{\psi'(0)}{1!}x + \frac{\psi''(0)}{2!}x^2 + \frac{\psi'''(0)}{3!}x^3 + \frac{\psi''''(0)}{4!}x^4 + \dots \tag{A.2}$$

Evaluating the above equation at $x = \pm\Delta x$ results in:

$$\psi_1 = \psi(0) + \frac{\psi'(0)}{1!}\Delta x + \frac{\psi''(0)}{2!}(\Delta x)^2 + \frac{\psi'''(0)}{3!}(\Delta x)^3 + \frac{\psi''''(0)}{4!}(\Delta x)^4 + ... \quad (A.3)$$

$$\psi_{-1} = \psi(0) - \frac{\psi'(0)}{1!}\Delta x + \frac{\psi''(0)}{2!}(\Delta x)^2 - \frac{\psi'''(0)}{3!}(\Delta x)^3 + \frac{\psi''''(0)}{4!}(\Delta x)^4 + ... \quad (A.4)$$

Adding equations A.3 and A.4, we have:

$$\psi_1 + \psi_{-1} = 2\psi(0) + \psi''(0)(\Delta x)^2 + \frac{\psi''''(0)}{12}(\Delta x)^4 + ... \quad (A.5)$$

this equation leads to:

$$\psi''(0) = \frac{\psi_1 - 2\psi(0) + \psi_{-1}}{(\Delta x)^2} - \frac{\psi''''(0)}{12}(\Delta x)^2 - ... \quad (A.6)$$

which can be approximated as:

$$\psi''(0) \approx \frac{\psi_1 - 2\psi(0) + \psi_{-1}}{(\Delta x)^2} \quad (A.7)$$

It is apparent from equation A.7 that the leading error resulting from the approximation is proportional to $(\Delta x)^2$.

Appendix B

Improved Higher-Order

Approximations

B.1   The Three-Point Formulation

Referring to fig.3.2, the following is the final expression for the 3-point approximation technique:

$$
\begin{bmatrix} \psi_i \\ \psi_{i-}^{(1)} \\ \psi_{i-}^{(2)} \end{bmatrix} = C^{-1} \begin{bmatrix} \psi_{i-1} \\ \psi_i \\ \psi_{i+1} \end{bmatrix}
\tag{B.1}
$$

Where:

$$C = \begin{bmatrix} q_i^- \\ 1 \quad 0 \quad 0 \\ q_{i+1}^+ M_i \end{bmatrix} \tag{B.2}$$

$$M_i^{\pm 1} = \begin{bmatrix} 1 & 0 & 0 \\ 0 & \rho_i^{\pm 1} & 0 \\ \mp \delta_i & 0 & 1 \end{bmatrix} \tag{B.3}$$

$$q_i^\pm = \begin{bmatrix} 1 & \pm h_i & \frac{h_i^2}{2!} \end{bmatrix} \tag{B.4}$$

$$N_i^\pm = \begin{bmatrix} 1 & \pm h_i & \frac{h_i^2}{2!} \\ 0 & 1 & \pm h_i \\ 0 & 0 & 1 \end{bmatrix} \tag{B.5}$$

where $\rho_i = 1$ for the TE waves and $\rho_i = \frac{n_{i+1}^2}{n_i^2}$ for the TM waves, and $\delta_i = k_0^2(n_{i+1}^2 - n_i^2)$.

B.2 The Seven-Point Formulation

The 7-point transverse second derivative approximation can also be found in a similar manner. The relevant matrices in this case are given below:

$$
\begin{bmatrix} \psi_i \\ \psi_{i-}^{(1)} \\ \psi_{i-}^{(2)} \\ \psi_{i-}^{(3)} \\ \psi_{i-}^{(4)} \\ \psi_{i-}^{(5)} \\ \psi_{i-}^{(6)} \end{bmatrix} = C^{-1} \begin{bmatrix} \psi_{i-3} \\ \psi_{i-2} \\ \psi_{i-1} \\ \psi_i \\ \psi_{i+1} \\ \psi_{i+2} \\ \psi_{i+3} \end{bmatrix}
\tag{B.6}
$$

$$
C = \begin{bmatrix} q_{i-2}^- M_{i-2}^{-1} N_{i-1}^- M_{i-1}^{-1} N_i^- \\ q_{i-1}^- M_{i-1}^{-1} N_i^- \\ q_i^- \\ 1 \quad 0 \quad 0 \quad 0 \quad 0 \quad 0 \quad 0 \\ q_{i+1}^+ M_i \\ q_{i+2}^+ M_{i+1} N_{i+1}^+ M_i \\ q_{i+3}^+ M_{i+2} N_{i+2}^+ M_{i+1} N_{i+1}^+ M_i \end{bmatrix}
\tag{B.7}
$$

$$
q_i^\pm = \begin{bmatrix} 1 & \pm h_i & \frac{h_i^2}{2!} & \frac{\pm h_i^3}{3!} & \frac{h_i^4}{4!} & \frac{h_i^5}{5!} & \frac{h_i^6}{6!} \end{bmatrix}
\tag{B.8}
$$

$$
M_i^{\pm 1} =
\begin{bmatrix}
1 & 0 & 0 & 0 & 0 & 0 & 0 \\
0 & \rho_i^{\pm 1} & 0 & 0 & 0 & 0 & 0 \\
\mp \delta_i & 0 & 1 & 0 & 0 & 0 & 0 \\
0 & \mp \rho_i^{\pm 1} \delta_i & 0 & \rho_i^{\pm 1} & 0 & 0 & 0 \\
\delta_i^2 & 0 & \mp 2\delta_i & 0 & 1 & 0 & 0 \\
0 & \rho_i^{\pm 1}\delta_i^2 & 0 & \mp 2\rho_i^{\pm 1}\delta_i & 0 & \rho_i^{\pm 1} & 0 \\
\mp \delta_i^3 & 0 & 3\delta_i^2 & 0 & \mp 3\delta_i & 0 & 1
\end{bmatrix}
\tag{B.9}
$$

$$
N_i^{\pm} =
\begin{bmatrix}
1 & \pm h_i & \frac{h_i^2}{2!} & \frac{\pm h_i^3}{3!} & \frac{h_i^4}{4!} & \frac{h_i^5}{5!} & \frac{h_i^6}{6!} \\
0 & 1 & \pm h_i & \frac{h_i^2}{2!} & \frac{\pm h_i^3}{3!} & \frac{h_i^4}{4!} & \frac{h_i^5}{5!} \\
0 & 0 & 1 & \pm h_i & \frac{h_i^2}{2!} & \frac{\pm h_i^3}{3!} & \frac{h_i^4}{4!} \\
0 & 0 & 0 & 1 & \pm h_i & \frac{h_i^2}{2!} & \frac{\pm h_i^3}{3!} \\
0 & 0 & 0 & 0 & 1 & \pm h_i & \frac{h_i^2}{2!} \\
0 & 0 & 0 & 0 & 0 & 1 & \pm h_i \\
0 & 0 & 0 & 0 & 0 & 0 & 1
\end{bmatrix}
\tag{B.10}
$$

where $\rho_i = 1$ for the TE waves and $\rho_i = \frac{n_{i+1}^2}{n_i^2}$ for the TM waves, and $\delta_i = k_0^2(n_{i+1}^2 - n_i^2)$.

Appendix C

Calculation of Modal Power and Modal Coefficients in an Arbitrary Field

Any general two-dimensional field $\psi(x, z)$ can be represented as a linear combination of a complete set of orthonormal modes, that is [21]:

$$
\begin{aligned}
\psi(x, z) = \; & \alpha_0 f_0(x)e^{j\beta_0 z} + \alpha_1 f_1(x)e^{j\beta_1 z} + \alpha_2 f_2(x)e^{j\beta_2 z} + \cdots + \alpha_m f_m(x)e^{j\beta_m z} + \cdots \\
& + \alpha_M f_M(x)e^{j\beta_M z} + \int_v \alpha_v f_v(x)e^{j\beta_v z} dv
\end{aligned} \tag{C.1}
$$

where $\alpha_m = $ mth-mode expansion coefficient, $\beta_m = $ mth-mode propagation constant and $\int_v \alpha_v f_v(x)e^{j\beta_v z} dv$ represents an integration over the continuum of all radiation modes. The integer M represents the highest possible order of the guided modes. The modal transverse profiles $\{f_m(x)\}$ describe a set of orthonormal functions over

the transverse coordinate. For a single-mode waveguide ($M = 0$):

$$\psi(x,z) = \alpha_0 f_0(x)e^{j\beta_0 z} + \int_v \alpha_v f_v(x)e^{j\beta_v z}dv \qquad (C.2)$$

At the input end of the polarizer ($z = 0$) the field ψ becomes:

$$\psi(x,0) = \alpha_0 f_0(x) + \int_v \alpha_v f_v(x)dv \qquad (C.3)$$

By using the orthogonality relation between the modal fields, which is expressed as [64]:

$$\int_{-\infty}^{+\infty} \frac{f_m(x)}{K} f_n(x)dx = \begin{cases} 0 & for\ m \neq n \\ \int_{-\infty}^{+\infty} \frac{f_m^2(x)}{K}dx & for\ m = n \end{cases} \qquad (C.4)$$

where K is defined as:

$$K = \begin{cases} n^2(x) & for\ TM\ modes \\ 1 & for\ TE\ modes \end{cases} \qquad (C.5)$$

and $n(x)$ represents the refractive index distribution.

The modal coefficient α_m is given by [21]:

$$\alpha_m = \frac{\int_{-\infty}^{+\infty} \psi(x,0)\frac{f_m(x)}{K}dx}{\int_{-\infty}^{+\infty} \frac{f_m^*(x)f_m(x)}{K}dx} \qquad (C.6)$$

Hence the coefficient of the fundamental mode α_0 is given by:

$$\alpha_0 = \frac{\int_{-\infty}^{+\infty} \psi(x,0)\frac{f_0(x)}{K}dx}{\int_{-\infty}^{+\infty} \frac{f_0^2(x)}{K}dx} \qquad (C.7)$$

The power flowing in the z direction per unit length of the y direction is given by [38]:

$$P_z = \frac{1}{2}\int_{-\infty}^{+\infty} Re(\mathbf{E} \times \mathbf{H}^*)_z dx \qquad (C.8)$$

Appendix D

STF1 Program : Zero Finding

Routine, Eigenvalue Finding

Routine

```
%-------------------------------------------------------------------------------
% Written By : Dr. H. A. Al-Jamid
% Associate Professor, Electrical Engineering Department,
% King Fahd University, Dhahran 31261, Saudi Arabia.
%-------------------------------------------------------------------------------
% zero.m is a zero-finding program based on Muller's method.
% to use it, define the function whos zero is to be found as an M-file
% ( i.e ftest.m) , then run zero.m with the initial guess.
% the ftest.m file may for example be:
%
%    function y=ftest(x);
%    y=x^2-2.001*x+1.001;
%
%    zero('ftest',1.9);
%
% where ftest is the fuction name (must be the same as the M-file name)
```

164

```
% 1.9 is the initial guess.

function b=zero(FunFcn,x2)

nm=30; %input('number of iterations required = ');

low=10^(-8);
h1=-1*10^(-6);
h2=.5*10^(-6);
x1=x2-h2;
x0=x1-h1;
f0=feval(FunFcn,x0);
f1=feval(FunFcn,x1);
f2=feval(FunFcn,x2);
fu=(f2-f1)/h2;
fd=(f1-f0)/h1;
%
%start loop
%
for m=1:nm;
f3=(fu-fd)/(h1+h2);
c=fu+h2*f3;
h1=h2;
pa=c-sqrt(c*c-4*f2*f3);
ma=c+sqrt(c*c-4*f2*f3);
paa=abs(pa);
maa=abs(ma);
if paa>maa
    h2=-2*f2/pa;
else
    h2=-2*f2/ma;
end%
x1=x2;
x2=x2+h2;
f1=f2;
f2=feval(FunFcn,x2);
fd=fu;%
fu=(f2-f1)/h2;
if abs(f2)<low
    zr=x2;
end
    low=min(low,abs(f2));
end
```

```
format long e
[zr feval(FunFcn,zr)]


%                              STF1
%
% This program computes the eigenvalues of guided
% TE and TM modes of a slab waveguide with an arbitrary number of
% layers.
% nps=superstrate refractive index squared. The superstrate is assumed
% to occupy the region x<0.
% nbs=substrate refractive index squared.
% ns=array containing the refractive index squared distribution of the
% layers between the superstrate and the substrate. The first entry
% corresponds to a layer next to the superstarate.
% d is similar to ns, but it contains the width distribution of the
% layers.
% Let TE=1 or any other non-zero number if TE modes are desired
% otherwise let TE=0 for TM modes.

function f=stf1(ne);
global co;
global lo;
global d;

TE = 1;
lambda = 1;
nps = 1^2;
nbs = 3.4^2;
ns = 3.6^2;
d = [0.3];

% Start calculation.

nes=ne*ne;
k0=2*pi/lambda;
asp=k0*sqrt(nes-nps);
l1=k0*sqrt(ns(1)-nes);
rho=1;
if TE==0;rho=ns(1)/nps;end;
a=1;
b=rho*asp/l1;
co=[a b];
m=length(ns);
```

```
for s=2:m;
    l=k0*sqrt(ns(s-1)-nes);
    lp=k0*sqrt(ns(s)-nes);
    t=d(s-1);
    lt=l*t;
    rho=1;
    if TE==0;rho=ns(s)/ns(s-1);end;
    at=a*cos(lt)+b*sin(lt);
    b=rho*(-a*sin(lt)+b*cos(lt))*l/lp;
    a=at;
    co=[co a b];
    lo=[lo lp];
end;

    l=k0*sqrt(ns(m)-nes);
    asb=k0*sqrt(nes-nbs);
    t=d(m);
    lt=l*t;
    rho=1;
    if TE==0;rho=nbs/ns(m);end;

    at=a*cos(lt)+b*sin(lt);
    a=-rho*(-a*sin(lt)+b*cos(lt))*l/asb;
    f=at-a;
```

% Compute the matrix co and lo used for plotting the eigenfields.

```
    co=[1 0 co a 0];
    lo=[asp lo asb];
```

%   STFG

% This program is used to plot the eigenfield of modes. The output
% from STF1 is used for this purpose.

global co; global lo; global d;

np=1000;

% Define the x-coordinates.

```
xl=-abs(log(.01)/lo(1,1));
xhd=abs(log(.01)/lo(length(lo)));
ld=length(d); sd=sum(d);

xd=[];

for i=1:ld; xd=[xd
    sum(d(1:i))];
end;

x=[xl 0 xd xhd+sd];
lx=length(x); on=ones(np,1);

% Compute field and position in the superstrate.

xt=cumsum((x(1)/np)*on);
xt=flipud(xt);
xt=[xt 0];
gf=[xt exp(xt*lo(1))];

% Compute field within the intermediate layers.

for i=2:lx-2;
 xt=cumsum(((x(i+1)-x(i))/np)*on);
 xt=x(i)+xt;
 gf=[gf xt co(i,1)*cos(lo(i)*(xt-x(i)))+co(i,2)*sin(lo(i)*(xt-x(i)))];
end;

% Compute field in the substrate.

xt=cumsum(((x(lx)-x(lx-1))/np)*on);
xt=xt+x(lx-1);
gf=[gf xt co(lx-1,1)*exp(-lo(lx-1)*(xt-sd))];


% Plot modal field vx x.

plot(gf(:,1),(abs(gf(:,2))/max(abs(gf(:,2)))))
```

Appendix E

Improved MOL 3-Point

Approximation

```
%    ***** Written by: Mohammed Zahed Mustafa Khan *****
%    *** This function calculates the Second Derivative Matrix C ***
%    ***** by using the Method of Lines (MoL), 3-Point.*****
%
%    Implements the correct B.Cs. at the Adjacent Points of Interface.
%    using Non-uniform Mesh
%
%    General Purpose for TE and TM mode.
%
%        C = new_3ptapprox(TE,EQ,lambda,n1,h1,M1)
%
%    TE   Mode Selection,
%        TE=1 for TE mode, TE=0 for TM mode.
%
%    EQ=1 or 0 (does'nt effect the results).
%
%    lambda: Wavelength (in micron, dont need to write with e-6).
%
%    n1: Vector for Refractive Indices.
```

```
%
%    h1: Vector array containing Mesh Size distribution in each layer.
%
%    M1: Vector array containing No. of Discretization points in each layer.


function C= new_3ptapprox(TE,EQ,lambda,n1,h1,M1)

%**** Generating n and w of each discretization line****%

clear i n=[];w=[]; M=[];
for i=1:length(n1)
 n=[n n1(i)*ones(1,M1(i))];
 w=[w h1(i)*ones(1,M1(i))];
 M=[M ones(1,M1(i))];
end


%*************** Initializations*************************%

clear j i
h=w./M;                 % Mesh size
nlyr = length(n);       % No. of Layers.
m = sum(M);             % Total number of discretization points
bd = cumsum(M);         % Cumulative Sum of M.
ko = 2*pi/lambda;
kos = ko*ko;

% ************** Matrix C **********************%

C=diag(-2*ones(m,1),0) + diag(ones(m-1,1),1) +
diag(ones(m-1,1),-1); Ctemp=C;

% *****Dividing the C with step size(h)*************%

    clear k
    C=Ctemp(1:M(1),:)/(h(1)^2);
    for k=2:nlyr
        C=[C; Ctemp([(bd(k-1)+1):bd(k)],:)/(h(k)^2)];
    end

% *** Modification in the C Matrix. (Implementing I.C.) ***%

clear i
```

```
for i=2:m-1

    h0=h(i);
    h_p1=h(i+1);
    n0=n(i);
    n_p1=n(i+1);

    Qminus_0=Qminus_matrix(h0,3);
    Qplus_p1=Qplus_matrix(h_p1,3);

    Mplus_0=Mplus_matrix(h0,3,TE,kos,n0,n_p1);

    A=[];
    A(1,:)=Qminus_0;
    A(2,:)=[1 0 0];
    A(3,:)=Qplus_p1*Mplus_0;
    B=inv(A);

% **** Changing the matrix C ****%

    C(i,i-1) = B(3,1);
    C(i,i+0) = B(3,2);
    C(i,i+1) = B(3,3);

end
% ***** End of Function Program *******%
```

Appendix F

Improved MOL 5-Point

Approximation

```
%    ***** Written by: Mohammed Zahed Mustafa Khan *****
%    *** This function calculates the Second Derivative Matrix C ***
%    ***** by using the Method of Lines (MoL), 5-Point.*****
%
%    Implements the correct B.Cs. at the Adjacent Points of Interface.
%    using Non-uniform Mesh
%
%    General Purpose for TE and TM mode.
%
%        C = new_5ptapprox(TE,EQ,lambda,n1,h1,M1)
%
%    TE  Mode Selection,
%        TE=1 for TE mode, TE=0 for TM mode.
%
%    EQ=1 or 0 (does'nt effect the results).
%
%    lambda: Wavelength (in micron, dont need to write with e-6).
%
%    n1: Vector for Refractive Indices.
```

172

```
%
%    h1: Vector array containing Mesh Size distribution in each layer.
%
%    M1: Vector array containing No. of Discretization points in each layer.


function C= new_5ptapprox(TE,EQ,lambda,n1,h1,M1)


%**** Generating n and w of each discretization line****%

clear i n=[];w=[];M=[];

for i=1:length(n1)
    n=[n n1(i)*ones(1,M1(i))];
    w=[w h1(i)*ones(1,M1(i))];
    M=[M ones(1,M1(i))];
end


%*************** Initializations************************%

clear j i
h=w./M;                  % Mesh size
nlyr = length(n);        % No. of Layers.
m = sum(M);              % Total number of discretization points
bd = cumsum(M);          % Cumulative Sum of M.
ko = 2*pi/lambda;
kos = ko*ko;


% ************** Matrix C **********************%

C=diag(-1*ones(m-2,1),-2)+diag(16*ones(m-1,1),-1)+diag(-30*ones(m,1),0)...
    + diag(16*ones(m-1,1),1) +diag(-1*ones(m-2,1),2) ;
Ctemp=C;

%********* Dividing the C with step size(h)********%

C=Ctemp(1:M(1),:)/(12*h(1)^2);
for k=2:nlyr
    C=[C; Ctemp((bd(k-1)+1):bd(k),:)/(12*h(k)^2)];
end
```

```
% **** Modification in the C Matrix. (Implementing I.C.) ****%

for i=2:m-2

    h_m1=h(i-1);
    h0=h(i);
    h_p1=h(i+1);
    h_p2=h(i+2);
    n_m1=n(i-1);
    n0=n(i);
    n_p1=n(i+1);
    n_p2=n(i+2);

    Qminus_m1=Qminus_matrix(h_m1,5);
    Nminus_0=Nminus_matrix(h0,5);
    Mminus_m1=Mminus_matrix(h_m1,5,TE,kos,n_m1,n0);

    Qminus_0=Qminus_matrix(h0,5);

    Qplus_p1=Qplus_matrix(h_p1,5);
    Mplus_0=Mplus_matrix(h0,5,TE,kos,n0,n_p1);

    Qplus_p2=Qplus_matrix(h_p2,5);
    Mplus_p1=Mplus_matrix(h_p1,5,TE,kos,n_p1,n_p2);
    Nplus_p1=Nplus_matrix(h_p1,5);
    Mplus_0=Mplus_matrix(h0,5,TE,kos,n0,n_p1);

    A=[];
    A(1,:)=Qminus_m1*Mminus_m1*Nminus_0;
    A(2,:)=Qminus_0;
    A(3,:)=[1 0 0 0 0];
    A(4,:)=Qplus_p1*Mplus_0;
    A(5,:)=Qplus_p2*Mplus_p1*Nplus_p1*Mplus_0;

    B=inv(A);

%****Changing the matrix C ****%

    if i==2
        C(i,i-1) = B(3,2);
        C(i,i+0) = B(3,3);
        C(i,i+1) = B(3,4);
```

```
            C(i,i+2) = B(3,5);
        else
            C(i,i-2) = B(3,1);
            C(i,i-1) = B(3,2);
            C(i,i+0) = B(3,3);
            C(i,i+1) = B(3,4);
            C(i,i+2) = B(3,5);
        end
end

% ***** End of Function Program *****%
```

Appendix G

Improved MOL 7-Point

Approximation

```
%    ***** Written by: Mohammed Zahed Mustafa Khan *****
%    *** This function calculates the Second Derivative Matrix C ***
%    ***** by using the Method of Lines (MoL), 7-Point.*****
%
%    Implements the correct B.Cs. at the Adjacent Points of Interface.
%    using Non-uniform Mesh
%
%    General Purpose for TE and TM mode.
%
%        C = new_7ptapprox(TE,EQ,lambda,n1,h1,M1)
%
%    TE  Mode Selection,
%        TE=1 for TE mode, TE=0 for TM mode.
%
%    EQ=1 or 0 (does'nt effect the results).
%
%    lambda: Wavelength (in micron, dont need to write with e-6).
%
```

```
%    n1: Vector for Refractive Indices.
%
%    h1: Vector array containing Mesh Size distribution in each layer.
%
%    M1: Vector array containing No. of Discretization points in each layer.


function C= new_7ptapprox(TE,EQ,lambda,n1,h1,M1)


%**** Generating n and w of each discretization line ****%

clear i n=[];w=[];M=[];

for i=1:length(n1)
  n=[n n1(i)*ones(1,M1(i))];
  w=[w h1(i)*ones(1,M1(i))];
  M=[M ones(1,M1(i))];
end



%*************** Initializations*************************%
clear j i
h=w./M;                % Mesh size
nlyr = length(n);      % No. of Layers.
m = sum(M);            % Total number of discretization points
bd = cumsum(M);        % Cumulative Sum of M1.
ko = 2*pi/lambda;
kos = ko*ko;



% ************** Matrix C ********************%

e = ones(m,1);
div = 180;
C = spdiags([2/div*e -27/div*e 270/div*e
        -490/div*e,... 270/div*e -27/div*e 2/div*e], -3:3, m,m);
Ctemp=C;

% **********Dividing the C with step size(h)**********%

    C=Ctemp(1:M(1),:)/(h(1)^2);
    for k=2:nlyr
```

```
        C=[C; Ctemp((bd(k-1)+1):bd(k),:)/(h(k)^2)];
    end

% **** Modification in the C Matrix. (Implementing I.C.) ****%

for i=3:m-3

    h_m2=h(i-2);
    h_m1=h(i-1);
    h0=h(i);
    h_p1=h(i+1);
    h_p2=h(i+2);
    h_p3=h(i+3);
    n_m2=n(i-2);
    n_m1=n(i-1);
    n0=n(i);
    n_p1=n(i+1);
    n_p2=n(i+2);
    n_p3=n(i+3);

    Qminus_m2=Qminus_matrix(h_m2,7);
    Mminus_m2=Mminus_matrix(h_m2,7,TE,kos,n_m2,n_m1);
    Nminus_m1=Nminus_matrix(h_m1,7);
    Mminus_m1=Mminus_matrix(h_m1,7,TE,kos,n_m1,n0);
    Nminus_0=Nminus_matrix(h0,7);

    Qminus_m1=Qminus_matrix(h_m1,7);
    Nminus_0=Nminus_matrix(h0,7);
    Mminus_m1=Mminus_matrix(h_m1,7,TE,kos,n_m1,n0);

    Qminus_0=Qminus_matrix(h0,7);

    Qplus_p1=Qplus_matrix(h_p1,7);
    Mplus_0=Mplus_matrix(h0,7,TE,kos,n0,n_p1);

    Qplus_p2=Qplus_matrix(h_p2,7);
    Mplus_p1=Mplus_matrix(h_p1,7,TE,kos,n_p1,n_p2);
    Nplus_p1=Nplus_matrix(h_p1,7);
    Mplus_0=Mplus_matrix(h0,7,TE,kos,n0,n_p1);

    Qplus_p3=Qplus_matrix(h_p3,7);
    Mplus_p2=Mplus_matrix(h_p2,7,TE,kos,n_p2,n_p3);
    Nplus_p2=Nplus_matrix(h_p2,7);
```

```
        Mplus_p1=Mplus_matrix(h_p1,7,TE,kos,n_p1,n_p2);
        Nplus_p1=Nplus_matrix(h_p1,7);
        Mplus_0=Mplus_matrix(h0,7,TE,kos,n0,n_p1);

        A=[];
        A(1,:)=Qminus_m2*Mminus_m2*Nminus_m1*Mminus_m1*Nminus_0;
        A(2,:)=Qminus_m1*Mminus_m1*Nminus_0;
        A(3,:)=Qminus_0;
        A(4,:)=[1 0 0 0 0 0 0];
        A(5,:)=Qplus_p1*Mplus_0;
        A(6,:)=Qplus_p2*Mplus_p1*Nplus_p1*Mplus_0;
        A(7,:)=Qplus_p3*Mplus_p2*Nplus_p2*Mplus_p1*Nplus_p1*Mplus_0;

        B=inv(A);

% ***** Changing the matrix C *****%

  if i==3
        C(i,i-2) = B(3,2);
        C(i,i-1) = B(3,3);
        C(i,i+0) = B(3,4);
        C(i,i+1) = B(3,5);
        C(i,i+2) = B(3,6);
        C(i,i+3) = B(3,7);
  else
        C(i,i-3) = B(3,1);
        C(i,i-2) = B(3,2);
        C(i,i-1) = B(3,3);
        C(i,i+0) = B(3,4);
        C(i,i+1) = B(3,5);
        C(i,i+2) = B(3,6);
        C(i,i+3) = B(3,7);
  end
end

% ***** End of Function Program *****%
```

Appendix H

The Automated Program

```
% ***** Written by: Mohammed Zahed Mustafa Khan *****
% ***** The Automated Program *****
%
% ***** This Program calculates the Reflectivity, Transmissivity*
% ******and Radiation of the Structure using Method of Lines *****
% ***** using Overlap Integral to calculate Modal Power *****

%****** 'fun' represents the input file **************%


function [] =mainap(fun)
run (fun)
clc;

% Defining the global variables.

global TE EQ lambda ko U V S IS US N IN neff fs ...
    pml_profile npml_sub npml_sup eta_sub eta_sup order;


% Getting the structure vector in the form of matrix

warning off;
```

```
b=zeros(length(st),5);
r = 1; i  = 0;

for k =1:length(st)
    for j = 1:5
        if i==length(st)

            break
        else
            i = i+1;
            if st(i) >=0
                b(r,j)= st(i);
            else
                r = r+1;
                break
            end
        end
    end
end

% 'ws' is the matrix that defines the whole structure.

ws = b(1:r,:); clear b r i j

EQ=0; %Always.

% Defining the reflection and transmission matrices.

reff=[];tran=[];rad=[];

% If the variable 'order' is not defined in the input file, then
% 5-point approximation is used as default.

if length(order)==0
    order=5;
end

% Starting of the loop for the calculation of the
% reflectivity(R or reff),Transmissivity(T or tra) and
% radiation(Ra or rad) of the given structure.

for cc=1:length(lambda1)
```

```
% To find the time taken per wavelength.

ti=cputime;

% Selecting the first wavelength.

lambda=lambda1(cc);
ko=2*pi/lambda;
kos=ko^2;
clear n w M h

% Introducing the PML regions in the index profile
% If PML is not defined in the input file then tangent loss
% profile is used as default.
% Loop for updating the eta value according to the wavelength
% used.

if cc==1
    [n,w,M,h]= new_int_pml(n1,w1,M1,lambda1(cc),0);
else
    [n,w,M,h]= new_int_pml(n1,w1,M1,lambda1(cc),lambda1(cc-1));
end

% Generating the N Matrix for each region.

clear i;
for i=1:length(n(:,1))
    N(:,:,i)=n_matrix_new(n(i,:),M);
end

% Generating the mesh1 matrix of the 1st region
% It is used in calculating the modal power

mesh1=n_matrix_new(sqrt(h),M);
mesh1=transpose(diag(mesh1));

% Finding the U,V,S,IS,IN and US matrices of each region
% 'U' and 'V' are the eigen values and eigen vector matrices.
% 'S' and 'IS' are the sqrt(Q)=U*sqrt(V)*inv(U) and inverse of
% 'S', respectively.'IN' is the inverse of matrix 'N'.
% 'US' matrix is 'S' for TE and IN*S for TM modes.
% 'fs' is the vector that contains the fumdamental mode
%  field values.
```

```
% 'neff' is the variable that is assigned to the
% effective refractive index of each region.

clear i;
for i=1:length(n(:,1))
    [U(:,:,i),V(:,:,i),S(:,:,i),IS(:,:,i),US(:,:,i),...
    IN(:,:,i),neff(i),fs(:,i)]= uv_gen_new(n(i,:),N(:,:,i),h,M);
end;


% Finding the R anf T of the first distinct region, i.e. region-1
% or the semi-infinite strating region, of the structure.
% The single disconitnuity expressions are used.

[R1,T2,R2,T1]=dis_single(US(:,:,ws(1,1)),US(:,:,ws(2,1)));


% Finding the R anf T of the the rest of the structure
% i.e. resr of the regions.
% If the matrix 'ws' contains only three non zero
% elements then it assumes it to be an arbitrary region
% and used single discontinuity expressions to get R and T,
% else it assumes it to be a periodic region and used doubling
% and cascading algorithm to calculate the R and T of that region.
% The loop calculates the R an T of the current part of the
% structures and combines it with the previous available R and T
% using the cascading algorithm.

for i=2:length(ws(:,1))-1
    if ws(i,5)==0
        [R1,T2,R2,T1]=arb(R1,T2,R2,T1,ws(i,:),ws(i+1,:));
    else
        [R1,T2,R2,T1]=periodic(R1,T2,R2,T1,ws(i,:),ws(i+1,:));
    end
end

% Finding the transmitted and reflected field.
A=T2*fs(:,1);
B=R1*fs(:,1);

% If lambda is a single value then the transmitted and reflected
% will be plotted.

if length(lambda1)==1
```

```
        x0=x_axis(n(1,:),M,h);
        xN=x_axis(n(end,:),M,h);

        plot(real(xN),abs(A));
        xlabel('x_axis in \mum');
        ylabel('Field Amplitude');
        title('Transmitted Field');

        plot(real(x0),abs(B));
        xlabel('x_axis in \mum');
        ylabel('Field Amplitude');
        title('Reflected Field');
    else
% If lambda is a not single then the transmissivity, reflectivity
% and Radiation loss will be calculated using overlap
% integral and then plotted against the range of lambda

% Calculating the mode power

        if TE==1
            modepower=fs(:,1)'*(fs(:,1).*mesh1.');
            alphaa=(B'*(fs(:,1).*mesh1.'))/modepower;
            betaa=(A'*(fs(:,1).*mesh1.'))/modepower;
        else
            modepower=fs(:,1)'*(IN(:,:,1)*(fs(:,1).*mesh1.'));
            alphaa=(B'*IN(:,:,1)*(fs(:,1).*mesh1.'))/modepower;
            betaa=(A'*IN(:,:,1)*(fs(:,1).*mesh1.'))/modepower;
        end

% Calculating the R, Ra and T

        reff=[reff (abs(alphaa)^2)];
        tran=[tran (abs(betaa)^2)];
        rad=[rad (1-(abs(alphaa)^2)-(abs(betaa)^2))];
        clc
        tim=cputime-ti;

% Displays the time taken per wavelength and the iteration number.

        disp(cc);disp(tim);

    end
end
```

```
% If lambda is not a single value then plot the
% R,T and Ra with respect to wavelength.

if length(lambda1)~=1

    figure;
    plot(lambda1,reff);
    xlabel('Wavelength in [\mum]');
    ylabel('Fundamental TE Mode Reflectivity');
    title('Fundamental TE Mode Reflectivity of ...
    Infinite Deep Waveguide Gratings');
    grid on;

    figure;
    plot(lambda1,tran);
    xlabel('Wavelength in [\mum]');
    ylabel('Fundamental TE Mode Transmissivity');
    title(' Fundamental TE Mode Transmissivity of ...
    Infnitely Deep Waveguide grating');
    grid on;

    figure;
    plot(lambda1,rad);
    xlabel('Wavelength in [\mum]');
    ylabel('Fundamental TE Mode Radiation');
    title('Fundamental TE Mode Radiation of ...
    Infnitely Deep Waveguide grating');
    grid on;

end

%***************End of the automated program *****************%
```

Appendix I

Functions of the Automated

Program and the Approximations

```
%***************** Start of function 'arb' *******************%

% This is a function that adds an arbitrary discontinuity
% to the given R and Ts

function [R1,T2,R2,T1]= arb(Ra1,Ta2,Ra2,Ta1,w1,w2)

global US

[Rb1,Tb2,Rb2,Tb1]= dis_single(US(:,:,w1(1)),US(:,:,w2(1)));

[R1,T2,R2,T1] = cas_gen_new(Ra1,Ta2, Ra2,Ta1,Rb1,Tb2,
Rb2,Tb1,w1(1),w1(2));

% end of program

%***************** End of Function 'arb' ********************%

%***************** Start of function 'bin_new' ***************%
```

```
%This is a function that generates the weight of the binary
%ones present in the discontinuities

function [wt]= bin_new(ndis)

clear s b m n tmp v;
b=dec2bin(ndis);
b=b -'0';
[m,n] = size(b);
twos = pow2(n-1:-1:0);
tmp=b .* (twos(ones(m,1),:));
tmp(1)=0;
tmp=log2(tmp);
v=find(tmp>0);
tmp=tmp(v);
wt=tmp;
clear s b m n ;
```

%**************** End of Function 'bin_new' ******************%

%**************** Start of function 'cas_gen_new' *************%

```
% This is a function that cascades two discontinuities
% and gives all the four output parameters ie R1, T2, R2, T1.
% The inputs to this function is individual r1,t2 and r2,t1 of
% both the discontinuities (i.e. 8 parameters), the Matrix
% U = S for TE and N^-1S for TM, of the uniform region
% connecting both the discontinuities; and the distance 'd'
% of that uniform region.

function [R1,T2,R2,T1]= cas_gen_new(RA1,TA2, RA2,TA1,RB1,TB2,
RB2,TB1,r,d)

global S U V

I=eye(length(S(:,:,r)));
ESD=U(:,:,r)*diag(exp(j*(diag(V(:,:,r)).^(0.5))*d))*inv(U(:,:,r));

TMP=inv(I-ESD*RA2*ESD*RB1)*ESD*TA2;

R1=RA1+TA1*ESD*RB1*TMP; T2=TB2*TMP;
```

```
clear TMP;

TMP=inv(I-ESD*RB1*ESD*RA2)*ESD*TB1;
R2=RB2+TB2*ESD*RA2*TMP;
T1=TA1*TMP;
```

%***************** End of Function 'cas_gen_new' ***************%

%***************** Start of function 'cas_join_0d' *************%

```
% Function that joins two independent arbitrary discontinuities
% using the cascading algorithm. The distance between the
% discontinuities is assumed to be zero

function [R1,T2,R2,T1]= cas_joining_0d(RA1,TA2, RA2,TA1,RB1,TB2,
RB2,TB1)

global S U V M

I=eye(length(U(:,:,1)));

TMP=inv(I-RA2*RB1)*TA2;
R1=RA1+TA1*RB1*TMP;
T2=TB2*TMP;

clear TMP;
TMP=inv(I-RB1*RA2)*TB1;
R2=RB2+TB2*RA2*TMP;
T1=TA1*TMP;
```

%***************** End of Function 'cas_join_0d' **************%

%***************** Start of function 'cas_periodic_new1' ******%

```
% This is a function that gives the reflection and
% transmission matrices for a periodic pure symmetric
% structures.

function [R1,T2,R2,T1]= cas_periodic_new1(r1,r2,ndis,d0,d1);

global w M h TE EQ lambda ko U V S IS US N IN neff fs ;

% the inputs are, the wavelength lambda, the refractive
```

```
% indices of the waveguide, width of the waveguide regions
% w1,w2, the period of bot the regions d1,d2.

% Adding the other discontinuities
  [wt]= bin_new(ndis);

% Finding the required parameters

I=eye(length(U(:,:,r1)));

ESD0=U(:,:,r1)*diag(exp(j*(diag(V(:,:,r1)).^(0.5))*d0)))...
      *inv(U(:,:,r1));
ESD1=U(:,:,r2)*diag(exp(j*(diag(V(:,:,r2)).^(0.5))*d1)))...
      *inv(U(:,:,r2));

% Finding the reflection and transmission matrices

% for single interface __
%                        |__

[Ra1,Ta2,Ra2,Ta1]= dis_single(US(:,:,r1),US(:,:,r2));

clear Ra2 Ta1 Ta2;

%for double discontinuity __      __
%                            |__|

R=Ra1+(I-Ra1)*ESD1*(-Ra1)*inv(I-(ESD1*Ra1)^2)*ESD1*(I+Ra1);
T=(I-Ra1)*inv(I-(ESD1*Ra1)^2)*ESD1*(I+Ra1); Rd=R;Td=T;

% Saving R and T of one period, if the number of
% discontinuities are odd.

clear x; x=1; if rem(ndis,2)==1
    Ro(:,:,x)=R;
    To(:,:,x)=T;
    x=x+1;
end

% Cascading the double discontinuity for the periodic
% structure

clear k p hh tmp1;
```

```
for k=1:log2(ndis)
    tmp1=inv(I-(ESD0*R)^2)*ESD0*T;
    R=R+T*ESD0*R*tmp1;
    T=T*tmp1;
    [p,hh]=find(wt==k);
    if p==1
    Ro(:,:,x)=R;
    To(:,:,x)=T;
    x=x+1;
    end
end

clear k p hh tmp1;

% Adding the other discontinuities that are
% not in the power of 2

for k=1:x-1
    [R,T]= sym_out_1133(R,T,Ro(:,:,k),To(:,:,k),S(:,:,r1),d0);
end clear k x;

R1=R;
T2=T;

% The other two matrices will be the same due to symmetry.

R2=R1;
T1=T2;

%****** End of Function 'cas_periodic_new1' ***********%

%*********** Start of function 'dis_single' ***********%

% This is a function that gives the four output parameters
% ie R1, T2, R2, T1 of one single discontinuities.
% The inputs to this function are individual R1,T2 and R2,T1
% of both the discontinuities (i.e. 8 parameters),
% the Matrix U = S for TE and N^-1S for TM, of the
% uniform region connecting both the discontinuities;
% and the distance 'd' of that uniform region.

function [R1,T2,R2,T1]= dis_single(US1,SUS2)
```

```
I=eye(length(US1));

R1=(I-inv(US1)*US2)*inv(I+inv(US1)*US2);
T2=2*inv(I+inv(US1)*US2);

R2=-R1;
T1=I+R2;

%*********** End of Function 'dis_single' ***************%

%********** Start of function 'Mminus_matrix' ***********%

% Function that gives the M_minus matrix for the higher order
% approximation.

function Mminus=Mminus_matrix(h,order,TE,kos,n1,n2);

m=[];

z21 = kos*(n2^2-n1^2);

if TE == 1
    r21=1; % for TE mode.
else
    r21=(n2^2)/(n1^2); % For TM Mode.
end

if order==3
    m(1,:)=[ 1 0 0 ];
    m(2,:)=[ 0 (r21)^(-1) 0 ];
    m(3,:)=[ z21 0 1 ];
end
if order==5
    m(1,:)=[ 1 0 0 0 0 ];
    m(2,:)=[ 0 (r21)^(-1) 0 0 0 ];
    m(3,:)=[ z21 0 1 0 0 ];
    m(4,:)=[ 0 ((r21)^(-1))*z21 0 (r21)^(-1) 0 ];
    m(5,:)=[ (z21^2) 0 2*z21 0 1];
end
if order==7
    m(1,:)=[ 1 0 0 0 0 0 0 ];
    m(2,:)=[ 0 (r21)^(-1) 0 0 0 0 0 ];
```

```
        m(3,:)=[ z21 0 1 0 0 0 0 ];
        m(4,:)=[ 0 ((r21)^(-1))*z21 0 (r21)^(-1) 0 0 0 ];
        m(5,:)=[ (z21^2) 0 2*z21 0 1 0 0 ];
        m(6,:)=[ 0 ((r21)^(-1))*(z21^2) 0 2*((r21)^(-1))*...
        z21 0 ((r21)^(-1)) 0 ];
        m(7,:)=[ (z21^3) 0 3*(z21^2) 0 3*z21 0 1];
end

Mminus=m;

%************ End of Function 'Mminus_matrix' ************%

%************ Start of function 'Mplus_matrix' ***********%

% Function that gives the M_plus matrix for the higher order
% approximation.


function Mplus=Mplus_matrix(h,order,TE,kos,n1,n2);

m=[];

z21 = kos*(n2^2-n1^2);

if TE == 1
    r21=1; % for TE mode.
else
    r21=(n2^2)/(n1^2); % For TM Mode.
end

if order==3
    m(1,:)=[ 1 0 0 ];
    m(2,:)=[ 0 r21 0 ];
    m(3,:)=[ -z21 0 1 ];
end

if order==5
    m(1,:)=[ 1 0 0 0 0 ];
    m(2,:)=[ 0 r21 0 0 0 ];
    m(3,:)=[ -z21 0 1 0 0 ];
    m(4,:)=[ 0 -r21*z21 0 r21 0 ];
    m(5,:)=[ (z21^2) 0 -2*z21 0 1];
end
```

```
if order==7
    m(1,:)=[ 1 0 0 0 0 0 0 ];
    m(2,:)=[ 0 r21 0 0 0 0 0 ];
    m(3,:)=[ -z21 0 1 0 0 0 0 ];
    m(4,:)=[ 0 -r21*z21 0 r21 0 0 0 ];
    m(5,:)=[ (z21^2) 0 -2*z21 0 1 0 0 ];
    m(6,:)=[ 0 r21*(z21^2) 0 -2*r21*z21 0 r21 0 ];
    m(7,:)=[ -(z21^3) 0 3*(z21^2) 0 -3*z21 0 1];
end

Mplus=m;


%********** End of Function 'Mplus_matrix' ***************%


%********** Start of function 'n_matrix_new' *************%


%This is a function that generates the n matrix of the waveguide.


function [N]= n_matrix_new(n,M)


nlyr=length(n);
clear q
N=[];


for q=1:nlyr
    N=[N (n(q)^2)*ones(1,M(q))];
end
clear q;
N=diag(N);


%***************** End of Function 'n_matrix_new' ***********%


%***************** Start of function 'new_int_pml' *********%


% This is a function that introduces pml layer on both
% the sides of the waveguide.


function [n_pml,w_pml,M_pml,h_pml]=
new_int_pml(n,w,M,lambda_new,lambda_old)


global pml_profile npml_sub npml_sup eta_sub eta_sup order;
```

```
clear cstart cend;
h=w./M;

% Setting the default values if not given

if length(npml_sub)==0
    if order==5
        npml_sub=10;
    else if order==3
            npml_sub=15;
        else
            npml_sub=8;
        end
    end
end

if length(npml_sup)==0
    if order==5
        npml_sup=10;
    else if order==3
            npml_sup=15;
        else
            npml_sup=8;
        end
    end
end

if length(eta_sub)==0
    eta_sub= 1.35/max(n(:,end));
end

if length(eta_sup)==0
    eta_sup= 1.35/max(n(:,1));
end

%End of default value checking

for k=1:length(n(:,1))
    cstart(k,:)=n(k,1)*ones(1,npml_sup);
    cend(k,:)=n(k,length(n(k,:)))*ones(1,npml_sub);
end

n_pml=[cstart n cend];
```

```
w_pml=[h(1)*ones(1,npml_sup) w
       h(end)*ones(1,npml_sub)];
M_pml=[ones(1,npml_sup) M ones(1,npml_sub)];

clear cstart cend;


if lambda_old==0;
    eta_sub=(eta_sub)*lambda_new/n(1,end);
    eta_sup=(eta_sup)*lambda_new/n(1,1);
else
    eta_sub=(eta_sub*lambda_new/lambda_old);
    eta_sup=(eta_sup*lambda_new/lambda_old);
end

for i=1:npml_sub
    x_sub(i)=(i*pi)/(2*(npml_sub+1));
end for i=1:npml_sup
    x_sup(i)=(i*pi)/(2*(npml_sup+1));
end

if length(pml_profile)==0
    disp('default tan');
    f_sub=tan(x_sub);
    f_sup=tan(x_sup);
elseif  pml_profile=='tan'
    disp('tan');
    f_sub=tan(x_sub);
    f_sup=tan(x_sup);
elseif pml_profile=='sec'
    disp('sec');
    f_sub=sec(x_sub);
    f_sup=sec(x_sup);
elseif pml_profile=='exp'
    disp('exp');
    f_sub=exp(x_sub);
    f_sup=exp(x_sup);
elseif pml_profile=='sin'
    disp('sin');
    f_sub=sin(x_sub);
    f_sup=sin(x_sup);
elseif pml_profile=='sqr'
    disp('sqr');
```

```
        f_sub=(x_sub).^2;
        f_sup=(x_sup).^2;
elseif pml_profile=='cub'
        disp('cub');
        f_sub=(x_sub).^3;
        f_sup=(x_sup).^3;
elseif pml_profile=='lin'
        disp('lin');
        f_sub=(x_sub);
        f_sup=(x_sup);
elseif pml_profile=='unf'
        disp('unf');
        f_sub=ones(1,npml_sub);
        f_sup=ones(1,npml_sup);
end

sub_imag=(eta_sub/npml_sub)*f_sub;
sup_imag=(eta_sup/npml_sup)*transpose(rot90(f_sup));

h_pml=[h(1)+sup_imag*j h h(end)+sub_imag*j];

%********** End of Function 'new_int_pml' **************%

%********* Start of function 'Nminus_matrix' ************%

% Function that gives the N_minus matrix for the higher order
% approximation.


function Nminus=Nminus_matrix(h,order);

n=[];

if order==3
    n(1,:)=[ 1 -h (h^2)/2];
    n(2,:)=[ 0 1 -h ];
    n(3,:)=[ 0 0 1 ];
end

if order==5
    n(1,:)=[ 1 -h (h^2)/2 -(h^3)/6 (h^4)/24];
    n(2,:)=[ 0 1 -h (h^2)/2 -(h^3)/6 ];
    n(3,:)=[ 0 0 1 -h (h^2)/2 ];
```

```
      n(4,:)=[ 0 0 0 1 -h ];
      n(5,:)=[ 0 0 0 0 1];
end

if order==7
   n(1,:)=[ 1 -h (h^2)/2 -(h^3)/6 (h^4)/24 -(h^5)/120 ...
      (h^6)/720];
   n(2,:)=[ 0 1 -h (h^2)/2 -(h^3)/6 (h^4)/24 -(h^5)/120];
   n(3,:)=[ 0 0 1 -h (h^2)/2 -(h^3)/6 (h^4)/24];
   n(4,:)=[ 0 0 0 1 -h (h^2)/2 -(h^3)/6];
   n(5,:)=[ 0 0 0 0 1 -h (h^2)/2 ];
   n(6,:)=[ 0 0 0 0 0 1 -h ];
   n(7,:)=[ 0 0 0 0 0 0 1];
end

Nminus=n;

%********** End of Function 'Nminus_matrix' **************%

%********** Start of function 'Nplus_matrix' *************%

% Function that gives the N_plus matrix for the higher order
% approximation.


function Nplus=Nplus_matrix(h,order);

n=[];

if order==3
     n(1,:)=[ 1 h (h^2)/2];
     n(2,:)=[ 0 1 h ];
     n(3,:)=[ 0 0 1 ];
end

if order==5
     n(1,:)=[ 1 h (h^2)/2 (h^3)/6 (h^4)/24];
     n(2,:)=[ 0 1 h (h^2)/2 (h^3)/6 ];
     n(3,:)=[ 0 0 1 h (h^2)/2 ];
     n(4,:)=[ 0 0 0 1 h ];
     n(5,:)=[ 0 0 0 0 1];
end
```

```
if order==7
    n(1,:)=[ 1 h (h^2)/2 (h^3)/6 (h^4)/24 (h^5)/120 (h^6)/720];
    n(2,:)=[ 0 1 h (h^2)/2 (h^3)/6 (h^4)/24 (h^5)/120];
    n(3,:)=[ 0 0 1 h (h^2)/2 (h^3)/6 (h^4)/24];
    n(4,:)=[ 0 0 0 1 h (h^2)/2 (h^3)/6];
    n(5,:)=[ 0 0 0 0 1 h (h^2)/2 ];
    n(6,:)=[ 0 0 0 0 0 1 h ];
    n(7,:)=[ 0 0 0 0 0 0 1];
end


Nplus=n;


%*********** End of Function 'Nplus_matrix' ****************%


%*********** Start of function 'periodic' ******************%


% This is a function that calculates the R an T of
% overall part by calculating the R an T of the arbitrary
% discontinuity which is assumed to be just after the periodic
% part of the structure, calculates the R and T of the periodic
% part and then joins both R and T to get the R and T of
% the resultant structure.


function [R1,T2,R2,T1]= periodic(Ra1,Ta2,Ra2,Ta1,w1,w2)


global US warning off


[Rb1,Tb2,Rb2,Tb1]=
cas_periodic_new1(w1(1),w1(3),w1(5),w1(2),w1(4));


[R1,T2,R2,T1] = cas_gen_new(Ra1,Ta2,Ra2,Ta1,Rb1,Tb2,
Rb2,Tb1,w1(1),w1(2));


[Rc1,Tc2,Rc2,Tc1] = dis_single(US(:,:,w1(1)),US(:,:,w2(1)));


[R1,T2,R2,T1] = cas_joining_0d(R1,T2,R2,T1,Rc1,Tc2,Rc2,Tc1);


%********** End of Function 'periodic' *********************%


%******* Start of function 'Qminus_matrix' *****************%


% Function that gives the Q_minus matrix for the higher order
% approximation.
```

```
function Qminus=Qminus_matrix(h,order);

n=[];
if order==3
    n=[ 1 -h (h^2)/2];
end
if order==5
    n=[ 1 -h (h^2)/2 -(h^3)/6 (h^4)/24];
end
if order==7
    n=[ 1 -h (h^2)/2 -(h^3)/6 (h^4)/24 -(h^5)/120 (h^6)/720];
end

Qminus=n;


%***************** End of Function 'Qminus_matrix' *******%


%***************** Start of function 'Qplus_matrix' ******%

% Function that gives the Q_plus matrix for the higher order
% approximation.

function Qplus=Qplus_matrix(h,order);

n=[];
if order==3
    n=[ 1 h (h^2)/2];
end

if order==5
    n=[ 1 h (h^2)/2 (h^3)/6 (h^4)/24];
end

if order==7
    n=[ 1 h (h^2)/2 (h^3)/6 (h^4)/24 (h^5)/120 (h^6)/720];
end

Qplus=n;

%************* End of Function 'Qplus_matrix' **********%

%******* Start of function 'sym_out_1133' *************%
```

```
% This is a function that gives the reflection and transmission
% matrices for a periodic pure symmetric structures and the
% resultant is also periodic.Structure 1 is considered to be
% 11 (symmetric by itself) and structure two (symmetric by
% itself)is 33. The resultant is also symmetric.

function [R1,T2]= sym_out_1133(RA,TA,RB,TB,S,d)

% the inputs are, the four matrices of structure 1,
% four matrices of structure 2, the S matric of the region
% joining them and longitudinal distance of that region.

I=eye(length(S));
[Us,Vs]=eig(S);
ESD=Us*diag(exp(j*(diag(Vs)*d)))*inv(Us);

% Since the structure 1 and 2 are symmetric RA1=RA2=RA,
% TA1=RA2,TA ans same for structure 2

TMP=inv(I-ESD*RA*ESD*RB)*ESD*TA;
R1=RA+TA*ESD*RB*TMP;
T2=TB*TMP;

%**************** End of Function 'sym_out_1133' **********%

%**************** Start of function 'uv_gen_new' **********%

% This is a function that calculates the Q matrix, divides
% Q into U and V (eigen pairs), makes all the imaginary part
% of V positive so that the field does not increase in the PML
% region and gives the following outputs U,V,neff,US.

function [U1,V1,S1,IS1,US,IN1,neff1,fs1]= uv_gen_new(n1,N1,h1,M1)

global TE EQ lambda ko order;

% Finding the C1 matrix for First waveguide

if length(order)==0
    C1= new_5ptapprox(TE,EQ,lambda,n1,h1,M1);
elseif order==3
    C1= new_3ptapprox(TE,EQ,lambda,n1,h1,M1);
```

```
elseif order==5
    C1= new_5ptapprox(TE,EQ,lambda,n1,h1,M1);
elseif order==7
    C1= new_7ptapprox(TE,EQ,lambda,n1,h1,M1);
end

kos=ko^2;

clear ne f b
Q1=(C1)+(kos*N1);
[U1,V1]=eig(Q1);
[ne,b]=max(real(diag(V1)));
neff1=sqrt(ne)/ko;neff1;
f=U1(:,b);
fs1=(f/max(abs(f)));

% making all the imaginary terms of V1 positive

clear s
V1=diag(V1);
s=find(imag(V1)<0);
V1(s)=conj(V1(s));
V1=diag(V1);

% Finding the US matrix depending on the TE or TM mode.

S1=U1*diag(diag(V1).^(0.5))*inv(U1);
[US1,VS1]=eig(S1);
clear s
VS1=diag(VS1);
s=find(imag(VS1)<0);
VS1(s)=conj(VS1(s));
VS1=diag(VS1);
S1=US1*VS1*US1^(-1);

IS1=U1*diag(diag(V1).^(-0.5))*inv(U1);

[UIS1,VIS1]=eig(IS1);
clear s
VIS1=diag(VIS1);
s=find(imag(VIS1)<0);
VIS1(s)=conj(VIS1(s));
VIS1=diag(VIS1);
```

```
IS1=UIS1*VIS1*UIS1^(-1);


IN1=diag(diag(N1).^(-1));

if TE==1
    US=S1;
else
    US=IN1*S1;
end
```

%*********** End of Function 'uv_gen_new' ***************%

%*********** Start of function 'x_axis' ****************%

% Function the calculates the transverse distance based on
% the mesh size.

```
function xo1=x_axis(n,M,h);

clear xo;
[temp p]=max(n);
xo=cumsum(h(p)*ones(1,(M(p))));
temp=[0 cumsum(h(p-1)*ones(1,(M(p-1)-1)))];
clear i
for i=p+1:1:length(h)
    xo=[xo xo(end)+cumsum(h(i)*ones(1,(M(i))))];
end
clear i
for i=p-2:-1:1
    temp=[temp temp(end)+cumsum(h(i)*ones(1,(M(i))))];
end

xo1=[(-rot90(temp))' xo];
```

%*********** End of Function 'x_axis' **************%

Appendix J

Input m-file

```
%************ Start of Input file 'example' *************%

clear all;

lambda1=0.7:0.02:3;

npml_sup=4;

npml_sub=8;

eta_sub=0.35;

eta_sup=0.5;

pml_profile='tan';

order=5;

TE=1;

w1=[  1  0.2   0.1   0.05   0.2   0.3   0.15   0.15   3 ];

M1=[  10   7    4     3     7    10    6      6    20];
```

```
n1=[  1     1     1     1     1     3.6   3.6   3.6   3.4;...
      1     1     1     3.6   3.6   3.6   3.6   3.6   3.4;...
      1     1     1     1     3.6   3.6   3.6   3.6   3.4;...
      1     3.6   3.6   3.6   3.6   3.6   3.6   3.6   3.4;...
      1     1     3.6   3.6   3.6   3.6   3.6   3.6   3.4;...
      1     1     1     1     1     1     3.6   3.6   3.4;...
      1     1     1     1     1     1     1     3.6   3.4];

st=[1 [-1] ...
    2 0.05 3 0.05 35 [-1] ...
    4 0.02 5 0.02 35 [-1] ...
    6 0.3 [-1] ...
    7 ];

%********* End of Input file 'example' ***************%
```

Bibliography

[1] S. E. Miller, "Light propagation in generalized lenslike media," *Bell Syst. Tech. Journal*, vol. 44, pp. 2017–2064, 1965.

[2] S. E. Miller, "Integrated optics: an introduction," *Bell Syst. Tech. Journal*, vol. 48, pp. 2059–2069, 1969.

[3] H. Nishihara, M. Haruna, and T. Suhara, *Optical Integrated Circuits*. McGraw-Hill, 1989.

[4] A. K. Ghatak and K. Thyagarajan, *Optical Electronics*. Cambridge University Press, 1989.

[5] C. L. Xu and W. P. .Huang, *Finite-Difference Beam-Propagation Methods for Guided Wave optics*. Progress in Electromagnetics Research (PIER) 11, Elsevier Science Publishing Co., Inc., 1995.

[6] H. M. Masoudi, M. Al-Sunaidi, and J. M. Arnold, "Time-domain finite-difference beam propagation method," *IEEE Photonics Technology Letters*, vol. 11, pp. 1274–1276, Oct. 1999.

[7] R. Scarmozzino, A. Gopinath, R. Pregla, and S. Helfert, "Numerical Techniques for Modeling Guided-Wave Photonic Devices," *IEEE Journal Of Selected Topics In Quantum Electronics,*, vol. 6, No. 1, pp. 150–162, Jan. 2000.

[8] S. T. Chu and S. K. Chaudhrui, *Finite-Difference-Time-Domain Methods for Optical Waveguide Analysis*. Progress in Electromagnetics Research (PIER) 11, Elsevier Science Publishing Co., Inc., 1995.

[9] A. K. Taneja and A. Sharma, "Reflection characteristics of guided wave bragg gratings using the collocation method," *SPIE Proceedings, Internationl conference on fiber optics and photonics*, vol. 3666, pp. 112–119, April 1999.

[10] Q.-H. Liu and W. C. Chew, "Analysis of discontinuities in planar dielectric waveguides : An eigenmode propagation method," *IEEE Transactions on Microwave Theory and Techniques*, vol. 39, pp. 422–430, Mar. 1991.

[11] U. Rogge and R. Pregla, "Method of lines for the analysis of strip-loaded optical waveguides," *Optical Society of America (B)*, vol. 8, pp. 459–463, Feb. 1991.

[12] J. Gerdes and R. Pregla, "Beam-propagation algorithm based on the method of lines," *Optical Society of America (B)*, vol. 8, pp. 389–394, Feb. 1991.

[13] A. Sharma, *Collocation Method For Wave Propagation Through Optical Waveguiding Structures*. Progress in Electromagnetic Research, (PIER) 11, Elsevier Science Publishing Co., Inc., 1995.

[14] M. J. Adams, *An Introduction to Optical Waveguides*. John Wiley and Sons Inc., 1981.

[15] M. N. Akram, "Analysis of anti-resonant reflecting optical waveguide (AR-ROW) grating using the method of lines," Master's thesis, King Fahd University of Petroleum and Minerals, Saudi Arabia, April 2000.

[16] M. A. Khan, "Analysis of metal-clad TM-pass polarizers using the method of lines," Master's thesis, King Fahd University of Petroleum and Minerals, Saudi Arabia, Feb 2001.

[17] A. Yariv, *Optical Electronics*. Saunders College Publishing, 4 ed., 1991.

[18] J. A. Kong, *Electromagnetic Wave Theory*. John Wiley and Sons Inc., 1986.

[19] T. Tamir, ed., *Guided-Wave Optoelectronics*, vol. 26. Springer Series, 2nd ed., 1990.

[20] D. Marcuse, *Theory of Dielectric Optical Waveguides*. Academic Press Inc., 1974.

[21] M. J. Al-Majid, "Method of lines analysis of gaussian beam coupling to the dielectric slab waveguide," Master's thesis, King Fahd University of Petroleum and Minerals, Saudi Arabia, Feb 1994.

[22] M. A. Majid, "Analysis of muti-layer arrow planar waveguide for the evanescent field enhancement in low-index media," Master's thesis, King Fahd University of Petroleum and Minerals, Saudi Arabia, Sep 2001.

[23] Y. P. Chiou and H. C. Chang, "Analysis of optical waveguide discontinuities using pade approximation," *IEEE Photonics Technology Letters*, vol. 9, pp. 964–966, 1997.

[24] C. J. Smartt, T. M. Benson and P. C. Kendall, "Exact analysis of waveguide discontinuities : Junctions and Laser facets," *Electronics Letters*, vol. 29, No. 15, pp. 1352–1353, July 1993.

[25] W. D. Yang and R. Pregla, "Method of lines for analysis of waveguide structures with multidiscontinuities," *Electronics Letters*, vol. 31, p. 892, May 1995.

[26] R. Pregla and W. Yang, "Method of lines for analysis of multilayered dielectric wavegides with bragg gratings," *Electronics Letters*, vol. 29, p. 1962, October 1993.

[27] R. Pregla and E. Ahlers, "Method of lines for analysis of discontinuities in optical waveguides," *Electronics Letters*, vol. 29, p. 1845, October 1993.

[28] A. A. Shittu, "Study of periodic waveguides by the finite-difference time-domain method and the Method of Lines," PhD thesis, King Fahad University of Petroleum and Minerals, Dhahran 31261, Saudi Arabia, September 1994.

[29] A. Goncharenko, S. F.Helfert and R. Pregla, "General analysis of fibre grating structures ," *Journal of Optical Society of America*, vol. 1, p. 25-31, 1999.

[30] S. J. Al-Bader and H. A. Jamid, "Method of lines applied to non-linear guided waves," *Electronics Letters*, vol. 31, pp. 79–85, Feb. 1995.

[31] M. Imtaar and S. J. Al-Bader, "Analysis of diffraction from abruptly-terminated optical fibers by the method of lines," *Journal of Lightwave Technology*, vol. 13, pp. 137–141, Feb. 1995.

[32] Hussain A. Al-Jamid. A new generalized finite-difference higher order approach for the solution of wave equation. *Personal Notes*

[33] Hussain A. Al-Jamid and Muhammad Nadeem Akram, "A new higher-order finite-difference approximation scheme for the method of lines," *Journal of Lightwave Technology*, 19(3):398–404, March 2001.

[34] A. Kornatz and R. Pregla, "Increase in the order of approximation and improvement of the interface condidtions for the method of lines," *Journal of Lightwave Technology*, vol. 11, pp. 249–251, Feb. 1993.

[35] S J Al-Bader and H A Jamid, "Perfectly matched layer absorbing boundary conditions for the method of lines modeling scheme," *IEEE Microwave and Guided Waves Letters*, 8(11):357–359, November 1998.

[36] H. A. Jamid, "Frequency-Domain PML layer based on the complex mapping of space boundary condition treatment," *IEEE Microwave and Guided Wave Letters*, 10:356–358, Sep. 2000.

[37] H. A. Jamid, "Enhanced PML performance using the higher order approximation," *IEEE Transactions on Microwave Theory and Techniques* , to be published in April 2004.

[38] R. Syms and J. Cozens, *Optical Guided Waves and Devices*. Shopenhangers Road, Maidenhead, Berkshire, SL6 2QL, England: McGraw-Hill Book Company Europe, 1992.

[39] A. Yariv, "Periodic structures for integrated optics," *IEEE Journal of Quantum Electronics*, vol. 14, pp. 233–253, Apr. 1977.

[40] W. Streifer, D. R. Scifres, and R. D. Burnham, "Coupling coefficients for distributed feedback single- and double-hetrostructure diode lasers," *IEEE Journal of Quantum Electronics*, vol. 11, pp. 867–873, Nov. 1975.

[41] W. Streifer, D. R. Scifres, and R. D. Burnham, "Coupled wave analysis of dfb and dbr lasers," *IEEE Journal of Quantum Electronics*, vol. 13, pp. 134–141, Apr. 1977.

[42] Y. Yamamoto, T. Kamiya, and H. Yanai, "Improved coupled mode analysis of corrugated waveguides and lasers.," *IEEE Journal of Quantum Electronics*, vol. 14, pp. 245–258, Apr. 1978.

[43] T. Tamir and S. T. Peng, "Analysis and design of grating couplers," *Applied Physics*, vol. 14, pp. 235–254, 1977.

[44] M. T. Wlodarczyk and S. R. Seshadri, "Analysis of grating couplers for planar dielectric waveguides," *Journal of Applied Physics*, vol. 58, pp. 69–87, July 1985.

[45] S. J. Al-Bader and H. A. Jamid, "Mode scattering by a non-linear step-discontinuity in dielectric optical waveguides," *IEEE Transactions on Microwave theory and Techniques*, vol. 44, pp. 218–224, Feb. 1996.

[46] H. A. Jamid and S. J. Al-Bader, "Reflection and transmission of surface plasmon mode at a step discontinuity," *IEEE Photonics Technology Letters*, vol. 9, pp. 220–222, Feb. 1997.

[47] H. A. Jamid and S. J. Al-Bader, "Diffraction of surface plasmon-polaritons in an abruptly terminated dielectric-metal interface," *IEEE Photonics Technology Letters*, vol. 7, pp. 321–323, Mar. 1995.

[48] G. H. Brooke and M. M. Z. Kharadly, "Scattering by abrupt discontinuities on the planar dielectric waveguides ," *IEEE. Trans. Microwave Theory and Tech.*, 30:760-770, May 1982.

[49] T. E.Rozzi, "Rigorous analysis of the step discontinuity in a planar waveguide ," *IEEE. Trans. Microwave Theory and Tech.*, 28(7):809, May 1980.

[50] S. T. Peng and T. Tamir, "TM mode perturbation analysis of dielectric gratings," *Applied Physics*, vol. 7, no. 35, pp. 35–38, 1975.

[51] Y. P. Chiou and H. C. Chang, "Analysis of Optical Waveguide Discontinuities Using the Pade Approximants," *IEEE Photonics Technology Letters*, vol. 9, pp. 964–966, July 1997.

[52] D. C. Flanders and H. Kogelnick, "Grating filters for thin-film optical waveguides," *Applied Physics Letters*, vol. 24, pp. 194–196, Feb. 1974.

[53] K. A. Winick, "Effective-index method and coupled-mode theory for almost-periodic waveguide gratings: a comparison," *Applied Optics*, vol. 31, pp. 757–764, Feb. 1992.

[54] H. A. Jamid and M. N. Akram, "Analysis of Deep Waveguide Gratings: An efficient Cascading and Doubling algorithm in the Method of Lines Framework." *Journal Of Lightwave Technology*, 20(7):1204–1208, July 2002.

[55] J. Ctyroky, S. Helfert and R. Pregla, "Analysis of deep waveguide bragg gratings," *Optical and Quantum Electronics*, pages. 343–358, 1998.

[56] Y. Y. Lu and S. H. Wei, "A New Iterative Bidirectional Beam Propagation Method," *IEEE Photonics Technology Letters*, vol. 14, pp. 1533–1535, Nov 2002.

[57] P. L. Ho and Y. Y. Lu, "A Stable Propagation Method Based on Scattering Operators," *IEEE Photonics Technology Letters*, vol. 13, pp. 1316–1318, Dec 2001.

[58] J. P. Zhang, D. Y. Chu, S. L. Wu, W. G. Bi, R. C. Tiberio, R. M. Joseph, A. Taflove, C. W. Tu and S. T. Ho, "Nanofabrication of 1-D photonic bandgap btructures along a photonic wire," *IEEE Photonics Technology Letters*, vol. 8, No. 4, pp. 491–493, April 1996.

[59] D. J. Ripin, K. Y. Lim, G. S. Petrich, P. R. Villeneuve, S. Fan, E. R. Thoen, J. D. Jonnopoulos, E. P. Ippen and L. A. Kolodziejski, "One-Dimensional photonic bandgap microcavities for strong optical confinement in *GaAs* and *GaAs/Al$_x$O$_x$* semiconductor waveguides," *IEEE Journal of Ligntwave Technology*, vol. 17, No. 11, pp. 2152–2160, Nov. 1999.

[60] T. Hattori, N. Tsurumachi and H. Nakatsuka,"Analysis of optical nonlinearity by defect states in one-dimensional photonic crystals," *Journal of Optical Society of America*, vol. 14, No. 2, pp. 348–354, Feb. 1997.

[61] H. Y. D. Yang , "Finite difference analysis of 2-D photonic crystals," *IEEE Transactions on Microwave Theory and Techniques*, vol. 44, pp. 2688–2694, Dec 1996.

[62] A. Barcz, S. F. Helfert and R. Pregla, "Modeling of 2D photonic crystals using the method of lines," *IEEE conference of ICTON2002*, 2002.

[63] Hussain A. Al-Jamid. Modeling of 2D photonic crystals. *Personal Notes*

[64] T. Nakano, K. Baba, and M. Miyagi, "Insertion loss and extinction ratio of a surface plasmon-polariton polarizer: theoretical analysis," *Journal of Optical Society of America B*, vol. 11, pp. 2030–2035, October 1994.

Vita

Name   : Mohammed Zahed Mustafa Khan.

Nationality : Indian.

Degree   : Bachelor of Engineering in Electronics and Communication
                  (1998-2001).

                : Master of Science in Electrical Engineering (2002-2004).

University   : Osmania University (Muffakham Jah College of Engineering
                  and Technology), Hyderabad, INDIA (1998-2001).

                : King Fahd University of Petroleum and Minreals,
                  Dhahran, SAUDI ARABIA (2002-2004).

Experience : Lecturer in Shadan College of Engineering and Technology,
                  Jawaharlal Nehru Technological University,
                  Hyderabad, INDIA (2001-2002).

                : Research Assistant in E.E. Dept., KFUPM, (2002-2004).